Multiscale Models of the Metalorganic Vapor Phase Epitaxy Process

by

Rajesh Venkataramani

B.S., Chemical Engineering, Computer Science
Cornell University, 1994

M.B.A., Sloan School of Management
Massachusetts Institute of Technology, 2000

ARCHIVES

SUBMITTED TO THE DEPARTMENT OF CHEMICAL ENGINEERING IN PARTIAL FULFILLMENT OF THE REQUIREMENTS FOR THE DEGREE OF DOCTOR OF PHILOSOPHY IN CHEMICAL ENGINEERING
AT THE
MASSACHUSETTS INSTITUTE OF TECHNOLOGY
JUNE 2000

© 2000 Massachusetts Institute of Technology
All rights reserved

Author...
Department of Chemical Engineering
April 20, 2000

Certified by...
Klavs F. Jensen
Lammot du Pont Professor of Chemical Engineering
Thesis Supervisor

Accepted by...
Robert E. Cohen
St. Laurent Professor of Chemical Engineering
Chairman, Committee for Graduate Students

MASSACHUSETTS INSTITUTE OF TECHNOLOGY
JUN 07 2000
LIBRARIES

ARCHIVES

Multiscale Models of the Metalorganic Vapor Phase Epitaxy Process

by

Rajesh Venkataramani

Submitted to the Department of Chemical Engineering
on April 20, 2000 in partial fulfillment of the requirements
for the degree of Doctor of Philosophy in Chemical Engineering

ABSTRACT:

This thesis develops modeling techniques for chemical vapor deposition processes, specifically metalorganic vapor phase epitaxy (MOVPE). The difficulty in creating an overall modeling strategy for the MOVPE process is that important processes occur on a wide range of length and time scales. Gas phase heat and mass transfer affect the flux of species to the surface, while atomic processes affect the morphology of the growing film. In this thesis, new computational models are developed that work on specific length scales, models are linked together, and combined models are used to study the physics of actual deposition processes.

A Kinetic Monte Carlo (KMC) model is developed in order to simulate surface morphology during epitaxial growth. Computational methods, such as binary trees, are used to improve the computational efficiency of the KMC algorithm. To extend the computationally accessible length and time scales, a new parallel algorithm is developed based on ideas from Parallel Discrete Event Simulations (PDES). Superlinear speedup is achieved using this algorithm. The methodology is used along with optimization routines to fit Temperature Programmed Desorption (TPD) spectra to experimental data of methyl desorption off Ga-rich GaAs and determine consistent desorption mechanisms.

Physically based reactor scale models are linked to KMC models to gain an overall understanding of the MOVPE system. Initially reactor models that include surface unknowns are flux-split; the surface model is separated from the gas phase model and linked together through the flux to the surface. It is shown that flux-split models exactly match coupled models and in some cases offer better convergence. This linking methodology is extended with the use of a KMC model for the surface. A test case using GaAs growth is modeled, and both accurate growth rate and surface morphology estimates are achieved using the linked model. Neither model separately could predict both flux and surface morphology, but the linked models can be used to make a range of predictions from gas phase concentrations to surface morphology.

A reactor used for Grazing-Incidence X-ray Scattering (GIXS) experiments is analyzed using the linked model. The linked model matches both gas-phase concentrations and surface morphology estimates in the reactor. The surface model is compared to

experimental GIXS diffuse scattering. The model predicts that the complex reactions on the surface (As dimer and organic group adsorption and desorption from the surface) cause the surface morphology evolution to differ from that observed in molecular beam epitaxy.

Thesis Supervisor: Klavs F. Jensen

Title: Lammot du Pont Professor of Chemical Engineering and Professor of Materials Science

Acknowledgements:

This thesis is the result of support and encouragement from many sources. Many thanks to my thesis advisor, Klavs Jensen, for his guidance and support. In addition to excellent technical guidance, Klavs has truly been a mentor and friend. Others who have helped provide technical guidance include Prof. Tom Kuech, Dr. Harry Moffat, and Dr. Brian Stephenson.

Funding for my studies have come from the Department of Energy Computational Science Graduate Fellowship, National Science Foundation, and Mitsubishi Chemical Corporation. Without these groups help, I would not have had the freedom to explore.

The graduate students in the Jensen group have provided support and technical resources. Many thanks to Seth Rodgers, Ted Mihopoulos, Istvan Lengyel, Dave Quiram, Harsono Simka, Maria Nemirovskaya, Gwang-Soo Kim, I-Ming Hsing, and Vijay Gupta.

During my years at MIT, I have met some amazing people who have become many of my best friends. Thank you all for the dinners, visits, and experiences that we shared.

I would like to dedicate this thesis to my parents and my brother for their support, understanding, and love.

Table of Contents:

CHAPTER 1: RESEARCH MOTIVATION AND BACKGROUND 13

1.1 RESEARCH MOTIVATION 13

1.2 MOVPE PROCESS FOR DEPOSITION OF COMPOUND SEMICONDUCTORS 14

1.2.1 MOVPE reactors 16

1.2.2 Process applications 17

1.3 MODELING THE MOVPE PROCESS 18

1.4 METHODOLOGY FOR LINKING MODELS 22

1.4.1 Microscopic to surface and gas phase 22

1.4.2 Surface to reactor 22

1.5 THESIS GOALS 22

CHAPTER 2: KINETIC MONTE CARLO – THEORY AND IMPLEMENTATION 27

2.1 INTRODUCTION 27

2.2 THEORETICAL JUSTIFICATION 27

2.3 IMPLEMENTATION 29

2.3.1 Simulation Outline 30

2.3.2 Surface Structure 31

2.3.3 GaAs Lattice 32

2.3.4 Hash Tables 33

2.3.5 Picking a transition and Binary Trees 34

2.4 CONCLUSIONS 40

CHAPTER 3: PARALLEL KINETIC MONTE CARLO MODELS 42

3.1 INTRODUCTION 42

3.2 KINETIC MONTE CARLO TECHNIQUE 43

3.3 PARALLELIZATION STRATEGY 49

3.4 RESULTS 55

3.4.1 Correctness 55

3.4.2 Speedup 58

3.4.3 *Synchronization Frequency* ... *61*

3.5 Conclusions ... 63

CHAPTER 4: MONTE CARLO SIMULATIONS OF TEMPERATURE PROGRAMMED DESORPTION ... 68

4.1 Introduction to Temperature Programmed Desorption ... 68

4.2 Review of TPD Modeling Literature ... 69

4.3 Kinetic MC TPD Algorithm ... 70

4.3.1 *Simulating TPD Spectra* ... *76*

4.3.2 *Parallel TPD* ... *83*

4.3.3 *Optimization Algorithms* ... *85*

4.4 Case Study – Methyl Desorption from GaAs ... 88

4.5 Model Results ... 90

4.5.1 *Mechanism Effects* ... *91*

4.5.2 *Optimization Results* ... *100*

4.6 Conclusions ... 105

CHAPTER 5: KINETIC MONTE CARLO MODELS FOR GROWTH PROCESSES ... 109

5.1 Introduction ... 109

5.2 Experimental GaAs ... 111

5.2.1 *Surface Morphology Before and After Growth* ... *111*

5.2.2 *Surface Processes Studied Under Vacuum* ... *114*

5.2.3 *In-situ studies* ... *116*

5.3 Models of the GaAs surface ... 122

5.3.1 *Analytical Models of Surface Growth* ... *123*

5.3.2 *KMC simulations* ... *125*

5.3.3 *Quantum studies of GaAs surfaces* ... *126*

5.4 MOVPE Models of GaAs ... 129

5.4.1 *Model Parameters* ... *130*

5.4.2 *Step Flow versus Island Growth* ... *132*

5.4.3 *MBE versus MOVPE grown films* ... *139*

5.5 CONCLUSIONS 145

CHAPTER 6: LINKING MODELS 154

6.1 INTRODUCTION 154

6.2 THEORY OF LINKED MODELS 154

6.2.1 Flux Split Method – Equation Development 156

6.2.2 Surface Model – Equation Development 157

6.2.3 Separation of Surface and Gas Phase in FEM Models 159

6.3 STEADY STATE SOLUTION AND CONVERGENCE COMPARISON 162

6.4 LINKING TO KMC SURFACE MODELS 166

6.4.1 Reactor Model: 166

6.4.2 Kinetic Monte Carlo Model 168

6.4.3 Linking the Models 170

6.4.4 Monte Carlo Model Comparison 171

6.4.5 Linked Model Comparisons 174

6.5 CONCLUSIONS 178

CHAPTER 7: PUTTING IT ALL TOGETHER-REALISTIC LINKED SIMULATIONS FOR GAAS GROWTH 182

7.1 INTRODUCTION 182

7.2 EXPERIMENTAL RESULTS 183

7.3 MODELS 186

7.4 MODEL RESULTS 190

7.4.1 Reactor Scale Comparisons: 190

7.4.2 Surface Model Comparisons: 193

7.5 CONCLUSIONS 208

CHAPTER 8: CONCLUSIONS AND RECOMMENDATIONS FOR FUTURE WORK 212

8.1 CONCLUSIONS 212

8.1.1 Kinetic Monte Carlo Simulations 212

8.1.2 Multiscale Modeling 213

8.1.3 MOVPE GaAs Growth *214*
8.2 FUTURE WORK 214
8.2.1 Kinetic Monte Carlo Simulations *214*
8.2.2 Multiscale Modeling *216*
8.2.3 Other Systems *216*

List of Figures:

Figure 1. 1: An overview of the chemical vapor deposition process with a cartoon of a typical reactor and the different physical processes occurring in the reactor. 15
Figure 1. 2: A variety of reactor geometries typically used in MOVPE growth. 16
Figure 1. 3: Forecasts for the growth of the GaAs device market. 17
Figure 1. 4: A schematic for a general MOVPE model with user inputs and outputs from the model. Note the length scale variation in the output metrics for the model. 18
Figure 1. 5: Models used to study particular length scales in MOVPE growth. 20

Figure 2. 1: The algorithm for a typical KMC simulation. 30
Figure 2. 2: A schematic of a solid-on-solid surface model. 31
Figure 2. 3: The computational storage structure used to keep track of the zincblende lattice of GaAs. 32
Figure 2. 4: A pictorial representation of a hash table (such as one used to represent surface adatoms) 34
Figure 2. 5: A schematic of how transition rates are stored and chosen in the linear searching algorithm. Each block size corresponds to the magnitude of the rate. ... 36
Figure 2. 6: A representation of the binary tree used to store the transitions. The root node contains average value for the transitions. The left leaf of a node contain all moves with position values less than the average and the right leaf contains all moves with position values greater or equal to the average. 38
Figure 2. 7: The binary tree as a holder of the rates of the transitions. Each node has the sum of all transitions below it on the tree. 38

Figure 3. 1: A flowsheet of the algorithm for the KMC simulation of growth. 45
Figure 3. 2: Computational runtime as a function of surface size simulated in a serial KMC algorithm. 47
Figure 3. 3: Number of total transitions as a function of surface size simulated in a serial KMC algorithm. 48
Figure 3. 4: Computational runtime plotted versus total transitions in a serial KMC algorithm. 48
Figure 3. 5: A cartoon of a simulated surface being split onto processors P0 to P4. 50
Figure 3. 6: An optimistic protocol derived from PDES theory for the simulation of parallel KMC models. The optimism in the models comes from a processor begin able to race ahead in simulation time, but being rolled back to a previous time when necessary. 51
Figure 3. 7: Pictorial representation of ghost sites for processors. Ghost sites are replicated from neighboring processors to ensure the correct environment for adatoms on the boundaries of processors. 53
Figure 3. 8: A pictorial representation of the racing ahead and rollback process of each processor in the parallel algorithm. 54
Figure 3. 9: A comparison between the serial implementation (O) and the parallel implementation (□) at (a) 850 K, (b) 860 K, (c) 870 K, (d) 880 K 57

Figure 3. 10: A comparison between the serial implementation (O) and the parallel implementation (□) of the correlation lengths between islands with respect to temperature. 58
Figure 3. 11: The model was run at temperatures of (O) 800 K and (□) 825 K; A plot of simulation time versus number of processors. 59
Figure 3. 12: The model was run at temperatures of (O) 800 K and (□) 825 K; A plot of speedup versus number of processors. 60
Figure 3. 13: The model was run at temperatures of (O) 800 K and (□) 825 K; A plot of efficiency versus number of processors, (◆) is the efficiency of a model with 512 x 512 Angstrom surface 60
Figure 3. 14: The simulations were run at (O) 825 K, (□) 850 K, and (◆) 875 K. (a) Computational time as a function of the synchronization time; (b) Total number of rollbacks as a function of the synchronization time; (c) Average number of rollbacks as a function of the synchronization time. 62

Figure 4. 1: Algorithm for 'metal' algorithm. The main assumption is that diffusion is much faster than desorption on the surface. 71
Figure 4. 2: Algorithm for the 'semiconductor' algorithm. No assumptions are made on the relative rates of diffusion and desorption on the surface. 72
Figure 4. 3: Equilibration flowsheet for the 'metal' algorithm. 73
Figure 4. 4: Simulation time versus the ratio of diffusion to desorption rates. 74
Figure 4. 5: (a) Peak temperature versus initial coverage of adsorbates; (b) Peak width versus initial coverage of adsorbates. (O) No transition to equilibration, (□) Transition Ratio = 1, (◆) Transition Ratio = 100, (▲) Transition Ratio = 10 76
Figure 4. 6: (a) Peak temperature versus initial starting temperature for the simulation; (b) Peak width versus initial starting temperature for the simulation. 78
Figure 4. 7: (a) Initial rate versus initial temperature for simulation; (b) Initial temperature rise versus initial temperature for simulation. 79
Figure 4. 8: (a) Simulated TPD spectra computed from 5000 adsorbate desorptions; (b) Simulated TPD spectra computed from 50000 adsorbate desorptions 81
Figure 4. 9: (a) Typical error bars in a simulated TPD spectra averaging over a fixed 2 K temperature window; (b) Typical error bars in a simulated TPD spectra averaging over 2.5% of the total desorbed adatoms. 83
Figure 4. 10: Parallel speedup versus number of processors for the master-slave algorithm for the simulation of TPD spectra. Parallel speedup is defined as the simulation time on one processor divided by the simulation time on *n* processors. 85
Figure 4. 11: Optimization methodology to extract kinetic parameters for surface processes from TPD spectra 86
Figure 4. 12: (a) GaAs gallium-rich c(8x2)/(4x2) surface; (b) Methyl covered Ga surface after TMGa adsorption. 88
Figure 4. 13: (a) Experimental TPD spectra of methyl off Ga-rich GaAs[21], the legend is the initial surface coverage for each spectra; (b) Experimental peak temperatures and peak widths as a function of initial coverage of methyl. 89
Figure 4. 14: (a) Simulated TPD spectra of methyl off Ga-rich GaAs using parameters in Table 4.2. 91

Figure 4. 15: Effect of desorption barrier on (a) peak temperature and (b) peak width; (○) 42 kcal desorption barrier, (□) 44 kcal desorption barrier, (◆) 40 kcal desorption barrier.......... 93
Figure 4. 16: Effect of diffusion barrier on (a) peak temperature and (b) peak width; (○) 39.2 kcal diffusion barrier, (□) 50 kcal diffusion barrier, (◆) 30 kcal diffusion barrier.......... 95
Figure 4. 17: Effect of nearest-neighbor barrier on (a) peak temperature and (b) peak width; (○) 2 kcal barrier, (□) 4 kcal barrier, (◆) 1 kcal barrier.......... 97
Figure 4. 18: Effect of surface reconstructions on (a) peak temperature and (b) peak width; (○) base case model, (□) reconstruction model with a repulsive 2 kcal barrier to methyls on the same dimer.......... 99
Figure 4. 19: TPD spectra from optimized desorption and nearest-neighbor barriers (a) 39.2 kcal diffusion barrier, (b) 20 kcal diffusion barrier, (c) 80 kcal diffusion barrier. (blue + is simulated and red light line is experimental).......... 101
Figure 4. 20: Optimized desorption and nearest-neighbor barriers (+) 39.2 kcal diffusion barrier, (o) 20 kcal diffusion barrier, (*) 80 kcal diffusion barrier.......... 102
Figure 4. 21: Surface and contour plot of the error between experimental and simulated spectra at (a) 39.2 kcal diffusion barrier, (b) 20 kcal diffusion barrier.......... 104
Figure 4. 22: Experimental (red line) and simulated (dark blue +) TPD spectra.......... 105

Figure 5. 1: AFM image of GaAs(100) after growth. The surface consists of a series of terraces with a height variation of less than 4 nm. (T.F. Kuech, Univ. of Wisconsin) 109
Figure 5. 2: AFM image of GaAs(100) after growth. The surface consists of mounds and large islands on the surface with a height variation of more than 20 nm. (T.F. Kuech, Univ. of Wisconsin).......... 110
Figure 5. 3: GaAs c(4x4) reconstructed surface. The surface is covered with As dimers. 112
Figure 5. 4: GaAs reconstructed surface; (a) β(2x4), (b) β2(2x4).......... 112
Figure 5. 5: Reactor used for GIXS studies. The reactor consists of two quartz tubes surrounding a heated graphite susceptor. The high energy x-rays enter and exit through a beryllium window near the wafer.......... 116
Figure 5. 6: The crystal truncation rods during a typical growth run at a temperature of 580 °C and growth rate of 5 ML/sec.......... 117
Figure 5. 7: A map of the surface growth modes as a function of flux to the surface and temperature. At high temperatures and low fluxes, step-flow growth is dominant as the adsorbates have high mobility on the surface. At low temperatures and high fluxes, adsorbates have low mobility and island growth is found [33].......... 118
Figure 5. 8: (a) Correlation length as a function of growth rate at a temperature of 813 K; (b) Correlation length as a function of temperature at a growth rate of 5 ML/sec; The correlation length is derived from the diffuse x-ray scattering from the surface.... 119
Figure 5. 9: Relevant length and time scales for a variety of surface modeling techniques. 123
Figure 5. 10: Algorithm for the KMC algorithm to simulate thin film growth.......... 130
Figure 5. 11: (a) Step flow growth – on vicinal surfaces adatoms attach to the steps during growth. This maintains a flat film over time; (b) Island growth (Layer-by-

Layer Growth)– adatoms nucleate and form islands on the surface. Other adatoms attach to the edge of growing islands. 133
Figure 5. 12: Computed x-ray scattering from the surface along with pictures of the model surface. Note the oscillations in the x-ray scattering correspond to each monolayer of growth. 135
Figure 5. 13: Computed x-ray scattering from the surface along with pictures of the model surface. Note the constant signal corresponds to step flow growth whereby adatoms attached of the edge of the steps (as in the pictures of the model surface). 136
Figure 5. 14: The transition from island growth to step flow growth with the increase in temperature. Note how the surface becomes smoother at higher temperatures and fewer islands form on the terraces. (a) 790 K, (b) 800 K, (c) 810 K, (d) 820 K. (e) Oscillations from (a), (b), (d) one same plot 139
Figure 5. 15: Diffusion coefficient computed during (a) MBE growth[104], (b) MOVPE growth[33] using Equation 5.5 141
Figure 5. 16: Configuration of adatoms for nucleation to occur for the circled adatom in (a) Mechanism A, (b) Mechanism B 142
Figure 5. 17: Diffusion coefficients computed from Mechanism A and Mechanism B. Notice the large difference in the magnitude of the coefficient due to only the nucleation mechanism. 143
Figure 5. 18: Transition between step flow and island growth used to derive diffusion coefficients for (o) MOVPE model (□) MBE model. The activation barrier for diffusion is calculated as 45.7 kcal for the MOVPE model and 28.2 for the MBE model. 144

Figure 6. 1: Algorithm for (a) Fully coupled methodology to solve surface and gas phase unknowns in MOVPE reactor simulations; (b) Flux-split methodology whereby the surface problem is separated from the gas phase problem and solved separately, maintaining consistency through the flux of species to the surface; J is the Jacobian, R is the residual, u are the unknowns, y corresponds to the gas phase 160
Figure 6. 2: Jacobian matrix for (a) Fully coupled methodology; (b) Flux-split methodology. Note that the matrix size is slightly smaller in the flux-split methodology, but the bandwidth is similar 161
Figure 6. 3: Comparison of the steady state mole fractions of HF using (+) coupled and (o) flux-split linking methodologies 163
Figure 6. 4: Comparison of the steady state mole fractions of SiF_4 using (+) coupled and (o) flux-split linking methodologies 163
Figure 6. 5: Number of Newton iterations needed for convergence of the surface model as a function of the calls to the surface model. 165
Figure 6. 6: Two dimensional axisymmetric portrayal of reactor used in GIXS experiments[13] 167
Figure 6. 7: Nucleation mechanism for Ga on GaAs(100) surface. The circled adatom is fixed in this configuration 169
Figure 6. 8: Vicinal surface of GaAs(100) studied 170
Figure 6. 9: Comparison of CTR oscillations between (a) simulated and (b) experimental systems 173

Figure 6. 10: Map of growth rate as a function of (a) flux of Ga precursor and (b) temperature; (□) experimental data , (-) simulation results................................. 175
Figure 6. 11: Map of surface morphology as a function of temperature and growth rate, (a) simulated, (b) experimental 177

Figure 7. 1: (a) Time dependent crystal truncation rod for a typical growth run at 580 ° C.; (b) Diffuse scattering for a typical growth run. Note the maximum at the non-zero scattering wavevector, q, occurring at the minimum of the first CTR oscillation. This is a measure of the correlation length of islands on the surface.................... 184
Figure 7. 2: (a) Temperature dependence on the correlation length measured from the diffuse scattering at a growth rate of 5 ML/sec; (b) Growth rate dependence on the correlation length measured from the diffuse scattering at T = 813 K.................. 185
Figure 7. 3: Examples of simulation surfaces used in simulating GaAs(100) (a) singular; (b) vicinal.. 187
Figure 7. 4: Comparisons of experimental and simulated fluorescence of As as a function of distance above wafer. (❍) Experimental at 50 C, (❑) Experimental at 510 C, (●) Simulated at 50 C, (■) Simulated at 510 C. 190
Figure 7. 5: Flood plots of the concentration of As above the wafer (a) 50 ° C; (b) 510 ° C. 191
Figure 7. 6: Flood plot in the GIXS reactor of TEG concentration (mole fraction)....... 192
Figure 7. 7: Comparison of experimental (o) and simulated (□) growth rates in the GIXS reactor. 194
Figure 7. 8: Comparison of features of simulated and experimental CTR and diffuse scattering (q = 0.0374 $Å^{-1}$). Note the CTR oscillates with the onset of layer-by-layer growth and the diffuse scattering oscillates out of phase with the CTR. 197
Figure 7. 9: Correlation length as a function of (a) temperature; (b) growth rate for a wide range of diffusion models. The numbers in the graph give the nearest neighbor barriers for each curve. 199
Figure 7. 10: Correlation length as a function of (a) temperature, (c) The anisotropy of the correlation length as a function of temperature for different diffusion models. The numbers in the plots show the diffusion barrier in the [110] direction for each curve, all plots have a $Es_{[\bar{1}10]}$ = 1.48 eV and a NN = 0.2 eV. 201
Figure 7. 11: Computation of correlation length anisotropy as a function of nearest neighbor energy anisotropy, E_s[110] = 1.4 eV, $E_{s[\bar{1}10]}$ = 1.48 eV; (❍) NN[110] = 0.15 eV, $NN_{[\bar{1}10]}$ = 0.1 eV; (□) NN[110] = 0.2 eV, $NN_{[\bar{1}10]}$ = 0.1 eV; (◆) NN[110] = 0.25 eV, $NN_{[\bar{1}10]}$ = 0.05 eV 202
Figure 7. 12: Surface during growth with inclusion of As dimers on the surface. Note the reduction of dimer density around the islands on the surface, as well as the modified c(4x4) reconstruction on the surface. 204
Figure 7. 13: (a) Simulated RDS signal, (b) Simulated GIXS CTR signal from a growing surface. Note the similarities in the oscillations... 206
Figure 7. 14: Experimental (o) and simulated(□) correlation lengths as a function of temperature. 207
Figure 7. 15: Experimental (o) and simulated(□) correlation lengths as a function of growth rate. 207

Figure 8. 1: Structures grown out of masked areas on the wafer corresponding to different compositions of Ga and Al in AlGaAs[2, 3] 215

List of Tables:

Table 2. 1: Comparison of operation counts for different methods to choose from *k* transitions in KMC simulations. 40

Table 4. 1: Possible physical pathways explaining experimental TPD data 90
Table 4. 2: Base case parameters for TPD simulations 91
Table 4. 3: Parameter changes to base case studied 92
Table 4. 4 :Optimized barriers from 2 parameter optimization using fixed diffusion barriers 100

Table 5. 1: Reaction rates of adsorbed species on GaAs(100) 115
Table 5. 2: Diffusion barriers as estimated by molecular dynamics simulations 129
Table 5. 3: Initial Model of MOVPE surface processes for GaAs(100) growth 131

Table 6. 1: Comparison of computation times between methods 165
Table 6. 2: Gas Phase Mechanism for GaAs growth from TBAs and TEG 168

Table 7. 1: Model I – Ga dynamics only (typical parameters given). 188
Table 7. 2: Model II – Ga, As dimer, and organic dynamics 189

Chapter 1: Research Motivation and Background

The aim of this thesis is to develop multi-scale computational models that describe the metal-organic vapor phase (MOVPE) thin film deposition process. The complexity of the physical phenomena underlying the MOVPE process leads to an approach combining multiple modeling techniques along with experiments in order to understand the process. In this thesis, models of the MOVPE process are developed to better understand the physical phenomena underlying the process, as well as to be used to refine and optimize current reactors. Chapter 1 begins (Section 1.1) with a motivation for studying the MOVPE process. Second (Section 1.2) is an introduction to the MOVPE process which includes a description of the physical processes that occur during thin film deposition. Section 1.3 contains a review of current modeling techniques used to describe the MOVPE process. The next section (Section 1.4) gives a review of how models are currently linked together to form overall process models. This chapter concludes (Section 1.5) with a summary of thesis goals and objectives.

1.1 Research Motivation

The metalorganic vapor phase epitaxy (MOVPE) process is used extensively in the fabrication of compound semiconductors. MOVPE is used commercially to fabricate a variety of semiconductor products ranging from solar cells to cellular phones. In typical production processes, layers of compound semiconductors with carefully controlled band structures and doping levels are built up by vapor deposition. As semiconductor products become more complex, processing issues that affect the material properties (*i.e.* stringent demands on film thickness and impurity concentrations) become increasingly important. Rising costs for building and maintaining semiconductor fabrication units are another factor in the design and optimization of processes.

Predictive models of the MOVPE process are developed in this thesis that can aid in the design and control of MOVPE reactors. Modeling difficulties arise from the complex

nature of the MOVPE process; physical processes occur on widely varying length and time scales. Models have been developed to work on specific time and length scales, but no one modeling strategy is able to simulate the process on all length and time sales. The objective of this research is to develop strategies to link models on varying length and time scales, as to form a coherent process model that can predict both macroscopic and microscopic performance properties of MOVPE systems.

1.2 MOVPE process for deposition of compound semiconductors

MOVPE is generally characterized as a chemical vapor deposition (CVD) process using metalorganic precursors. A typical growth system would deposit GaAs from trimethylgallium (TMG) and arsine with a carrier gas of hydrogen. CVD is a widely used process whereby a thin film is synthesized from gaseous precursors cracking on a heated substrate. On overview of the CVD process is shown in Figure 1.1.

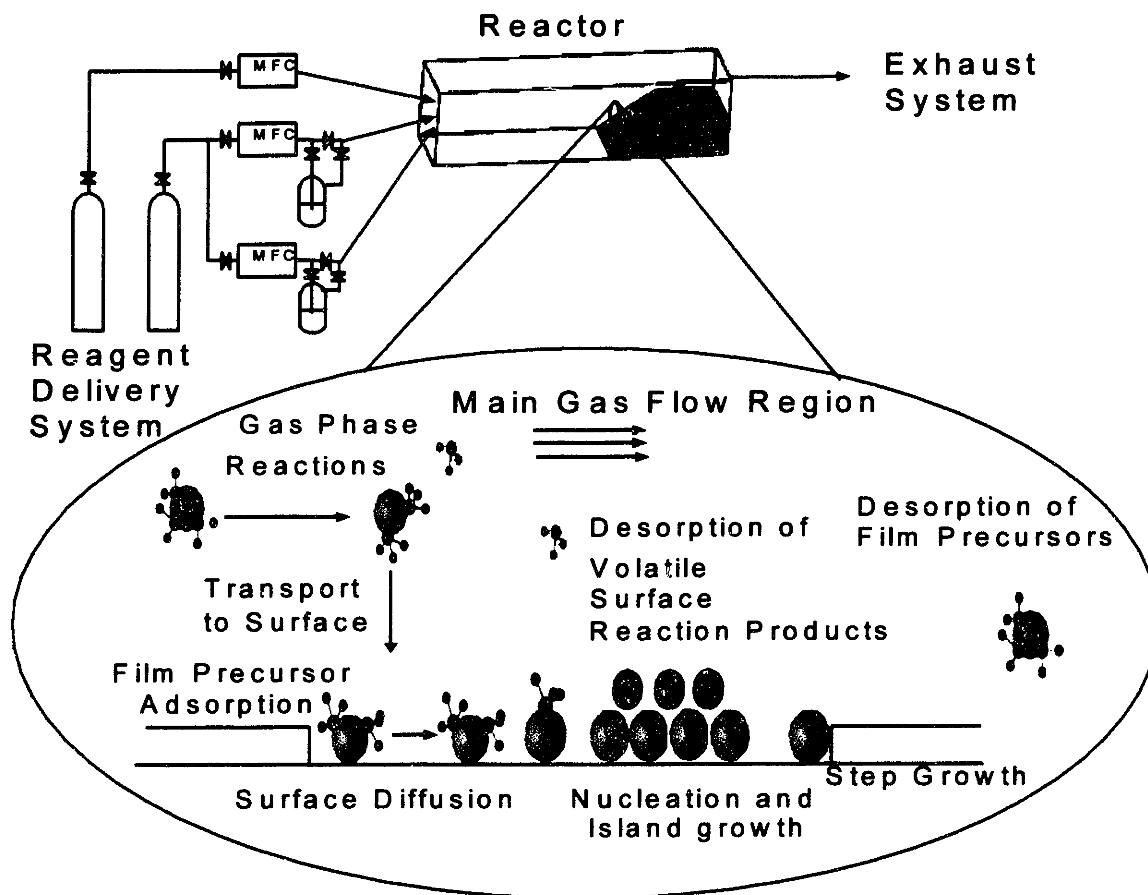

Figure 1. 1: An overview of the chemical vapor deposition process with a cartoon of a typical reactor and the different physical processes occurring in the reactor.

As seen, precursor and carrier gases enter the reactor in the gas phase. As the reactant gases enter into the heated environment of the susceptor, gas phase reactions occur affecting the gas phase species concentration. The mixture of unreacted precursor species and the gas-phase intermediate species are flown over a heated substrate where a portion of the gas-phase species deposits. By-products from surface reactions desorb from the surface into the gas phase, and the resulting mixture of reactants and products in the gas phase leave the system through the reactor exit stream.

On the surface, a whole host of processes occur. Reactant gases adsorb onto the surface. Surface reactions occur and form by-products on the surface. By-products desorb from the surface. Adsorbates can also diffuse on the surface. During the diffusion process, adatoms agglomerate and nucleate to form islands. Adatoms also attach to growing

steps on the surface. Adatoms are entrapped in the lattice and join the growing film. The mechanism of crystal growth plays an important role in the resulting surface morphology.

1.2.1 MOVPE reactors

Due to the complex nature of the MOVPE process, a wide variety of reactor geometries can be used to grow high quality films. A sampling of different reactor geometries is shown in Figure 1.2.

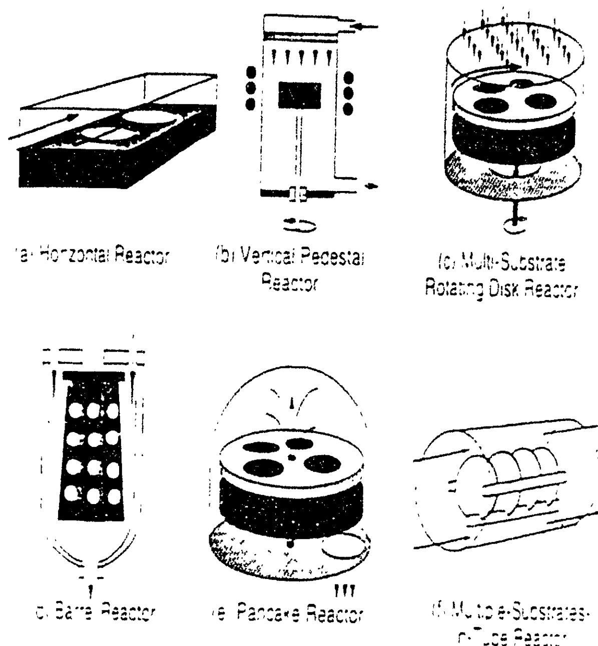

Figure 1. 2: A variety of reactor geometries typically used in MOVPE growth.

The geometry of the reactor along with the operating parameters of the growth process (pressure, temperature, choice of carrier gases) can greatly affect the temperature and flow profiles in the gas phase of the reactor. In turn, the flow profiles affect the distribution and concentration of species adjacent to the surface and can affect the growing film. One objective of this thesis is to link the choice of reactor geometry to the actual surface morphology that occurs during growth processes.

1.2.2 Process applications

The MOVPE process is used widely in the semiconductor fabrication industry in order to produce transistors, lasers, detectors, and circuits in cellular phones. MOVPE is used to deposit III-V and II-VI semiconductors such as GaAs, AlGaAs, InGaP, and GaN. Due to the varying bandgap of these crystals, different color light can be produced and detected. Important applications in many areas such as optical fiber networks and displays are driving the industry to gain a deeper understanding of the physics underlying the process. Forecasts for growth of the GaAs market are shown in Figure 1.3.

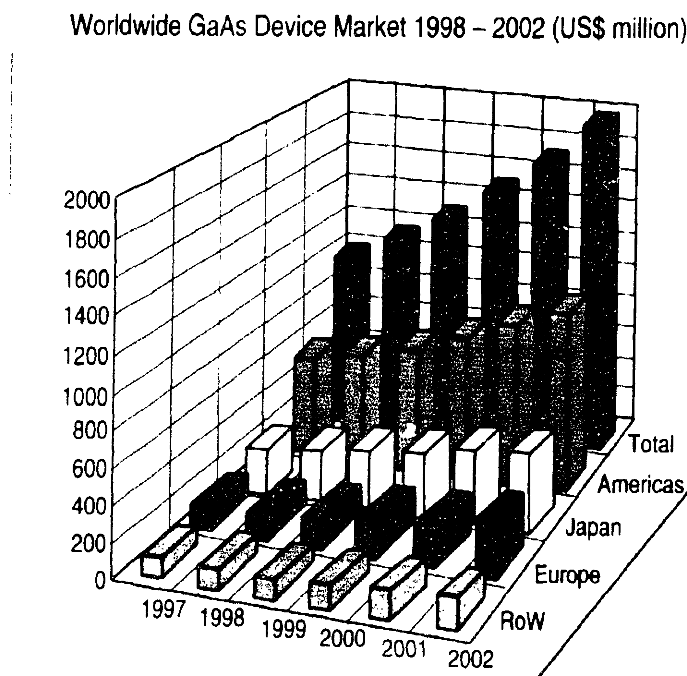

Figure 1. The worldwide GaAs device market over the period 1998 to 2002 showing how it has recently reached billion-dollar status with further good growth anticipated over the forthcoming five year period. (Source: Reed Electronics Research).

Figure 1. 3: Forecasts for the growth of the GaAs device market.

As the market for semiconductors produced by the MOVPE process is expanding, larger reactors are needed to cope with the issue of throughput in the industry. This causes experimental studies to become vastly more expensive for firms, as experimental studies using larger and more wafers are utilizing valuable resources. Models can be used as *a priori* 'experiments' to both design new MOVPE reactors and optimize operating conditions of currently utilized reactors.

1.3 Modeling the MOVPE process

As experimentation in many MOVPE systems are hazardous, difficult, and expensive, models have been used to try and understand the underlying physics in the reactors. A generic model of the MOVPE process would take inputs such as reactor configuration, temperature, pressure, species inlet concentrations, inlet velocities and return predictions for flow profiles, growth rates, film microstructure, and electronic properties of the film. A schematic of this type model is shown in Figure 1.4.

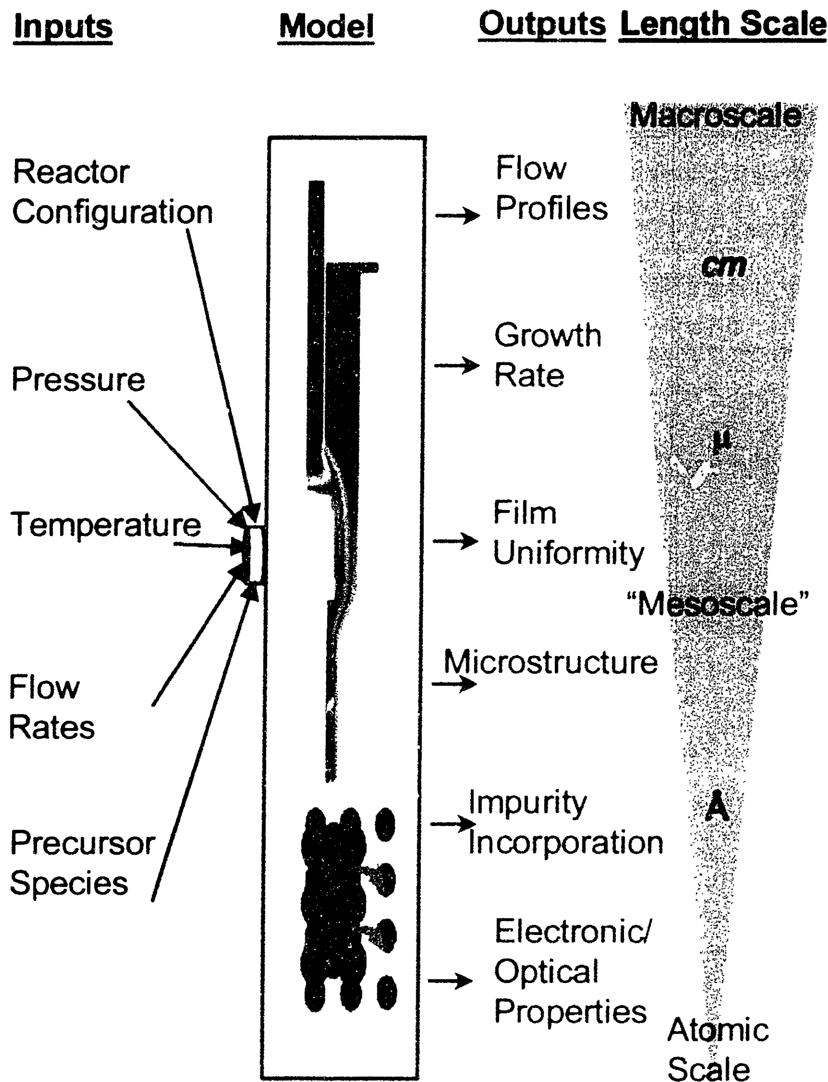

Figure 1. 4: A schematic for a general MOVPE model with user inputs and outputs from the model. Note the length scale variation in the output metrics for the model.

The problem with building such a model is the outputs that need be generated are on a wide range of length and time scales.

The typical film growth process involved multiple length scales, as shown in Figure 1.1: formation of active regions on the submicron to nanometer scale on substrates held in a meter sized deposition chamber. Moreover multiple time scales are involved. Individual diffusion processes and chemical reactions controlling the film growth and defect formation occur on typical atomic time scales of 10^{-13} seconds. In contrast, the growth of the active layer takes $\sim 10^{2}$ seconds and the total processing time for the multilayer structure is $\sim 10^{4}$ seconds.

Process models based on detailed physical understanding (as opposed to empirical data) are becoming necessary to achieve the increasingly higher levels of control of material synthesis required for cost-effective production of sophisticated microelectronics. Prediction of device performance requires understanding of how process conditions (e.g. flow, feed concentration, and temperature) affect the material on the atomic level (e.g. defect concentration and interface abruptness). However, most modeling techniques have focused on particular length and time scales. Shown in Figure 1.5 is a schematic that shows how different length scales are described by various modeling techniques.

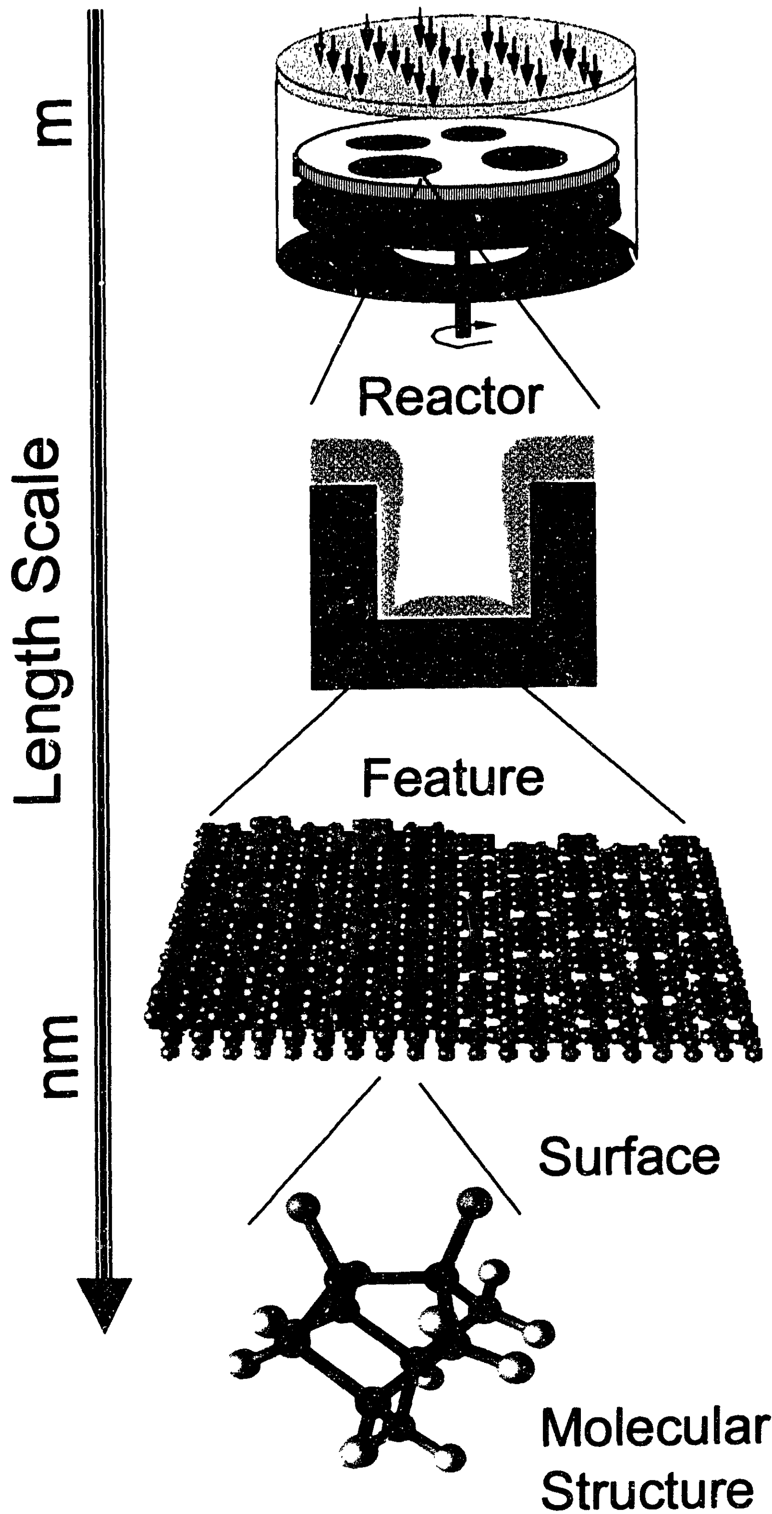

Figure 1. 5: Models used to study particular length scales in MOVPE growth.

However, most models techniques have focused on particular length and time scales; for example, computational fluid dynamics models of the gas transport in the deposition

chamber[1, 2], discrete particle transport models of film morphology evolution on the micron scale[3-5], and Monte Carlo simulations of atomic level surface diffusion and incorporation processes[6, 7]. These models provide useful insights into the underlying physical phenomena, but only at the length and time scales for which they apply. Fundamental molecular models could be developed, in principle, for the entire deposition system, but the needed computational resources would be excessive, if at all available, and results would have no timely impact upon developments in thin film deposition. Macroscopic models can often be solved with less computational efforts, but they fail to resolve phenomena at the microscopic level where the physical assumptions for continuum models breakdown. There is therefore a need to develop efficient multiscale linking approaches that combine cost-effective, physically accurate models of growth phenomena on different length and times. For example, in the case of MOVPE a multiscale linking strategy could include (see Figure 1.5):

- Continuum descriptions of fluid flow, heat and mass transfer combined with detailed gas-phase and surface chemical kinetic mechanisms to predict growth and impurity precursors arriving at the film surface.
- Morphology development at the submicron scale based on precursor arrival rate and microscopic models of surface growth processes.
- Kinetic Monte Carlo simulations of the growth front evolution to provide understanding of mechanisms underlying growth processes and impurity incorporation.
- Molecular dynamics simulations to provide diffusion coefficients and surface rate parameters for the kinetic Monte Carlo simulation
- Quantum chemistry computations of gas-phase and surface thermochemistry and reaction rates.

Additional modeling elements could be included if warranted by the physical situation, such as the inter-diffusion of film constituents and atoms in a multilayer structure.

1.4 Methodology for linking models

In order to gain the predictive power of each of the different length and time scale models, they must be linked together to form a coherent model of the MOVPE process.

1.4.1 Microscopic to surface and gas phase

The link between microscopic models and surface or reactor models is straightforward. The microscopic models can calculate reaction rates and diffusion barriers that are used as inputs into surface and reactor models[7, 8]. Many times the levels of *ab initio* calculations are not accurate, but the energy differences between similar calculations are accurate. This information can be important in determining the relative rates of reactions between competing reactions.

1.4.2 Surface to reactor

A linking between the surface model and the reactor model is important due to the inherent problems with using each model separately. A reactor scale model cannot resolve down to the level of atomic roughness, and therefore cannot give predictions on the morphology of the surface. On the flip side, the surface model does not have a needed input, the flux of species to the surface. Combining the models into a self-consistent formula allows the calculation of the net surface flux to the surface along with a prediction of the surface morphology.

1.5 Thesis Goals

The goal of this thesis is to develop multi-scale models of the MOVPE process. These models consist of linking reactor scale models, surface models, and microscopic models of the MOVPE process. The methodology of handling such multi-scale problems along with a series of case studies exploring the reach and limitations of these modeling techniques are shown. The end goal of this study is to develop models that can be used for *a priori* 'experimentation' of new systems and reactors.

In developing an overall model of a complex process, a series of advances must be made. In this thesis, this consists of

1. Development of improved modeling techniques on particular length and time scales.
2. Developing linking methodologies that combine different length and time scale models into a coherent process model.
3. Using the combined model to better understand the physics of a complex system.

In this thesis, step 1 encompasses Chapters 2 through 5. Step 2 is explored in Chapter 6, and step 3 is shown in Chapter 4 and 7.

In Chapter 2, a surface model, Kinetic Monte Carlo, is explored both from a theoretical and practical view. The theory behind why KMC models are viable representations of the surface and how real time is tracked during the simulation is developed. Computer science techniques, such as hash tables and binary trees are used to speed up the simulation, so realistic surface problems may be addressed.

Parallel computing techniques to speed to computation of the KMC simulations are developed in Chapter 3. Using ideas from the field of Parallel Discrete Event Simulations, techniques to split the problem onto many processors while maintaining correct causality of the simulation is shown. The techniques are shown to greatly enhance the speed of the calculations.

The KMC approach is applied to the problem of modeling Temperature Programmed Desorption (TPD) spectra in Chapter 4. TPD is a commonly used experimental technique used to study adsorbate interactions with surfaces. Analyzing experimental TPD spectra is a challenge due to the many surface processes that can affect the shape of the spectra. Using the KMC approach, the effects of different surface properties such as adsorbate nearest-neighbor interaction, adsorbate islanding, and dynamic surface reconstructions can be modeled directly. These effects can be included in surface mechanisms and directly tested by simulating the spectra for given mechanisms. Chapter 4 elucidates the methodology of simulating TPD spectra as well as a non-linear optimization algorithm to

best fit a mechanism's parameters to experimental data. A case study of methyl desorption from Ga-rich GaAs is shown.

An extension of the surface modeling ideas to surface growth processes is shown in Chapter 5. An introduction to the importance of the surface morphology during growth is given. An overview of the KMC applied to MBE systems is shown, as well as how the approach is applied to MOVPE systems. A modeling approach is outlined that will describe the surface morphology given as an input the flux of species to the surface. Also, simulations are used in order to determine the major differences between MBE and MOVPE growth.

Chapter 6 describes how a simple reactor and surface model can be successfully linked. In order to obtain an overall model of the MOVPE process, the surface morphology must be determined from a given set of reactor conditions. Since reactor scale models cannot give us predictions of surface morphology, a linking of reactor scale and surface models is accomplished. The basic framework for the linking methodology is put forth. The equation set that needs to be coupled is developed in this chapter. A simple example shows both the accuracy and the convergence properties of the linking methodology. An examination of GaAs growth from triethylgallium (TEG) and tertiarybutylarsine (TBAs) is used as a case study to demonstrate the methodology.

In Chapter 7, more detail is given to a surface mechanism used in a KMC approach to the growth of III-V semiconductors. In MOVPE growth, a different mechanism must be pursued to explore the growth of thin films than molecular beam epitaxy (MBE) growth. The handling of the V series compounds on the surface is explored. Direct comparisons to experimental x-ray scattering data are used to validate the model.

A conclusion is presented in Chapter 8 along with various ideas on how to improve the models. The modeling methodology employs a building block approach which can then be improved upon by both increasing the sophistication of the building block models or improving the glue between models.

Bibliography:

1. Jensen, K.F., *Transport phenomena in epitaxy systems*, in *Handbook of Crystal Growth*, D. Hurle, Editor. 1994, Elsevier: Amsterdam. p. 543-599.
2. Kleijn, C.R., *Chemical Vapor Deposition Processes*, in *Computational Modeling in Semiconductor Processing*, M. Meyyappan, Editor. 1995, Artech House: Norwood, MA. p. 97-229.
3. Kersch, A. and W.J. Morokoff, *Transport Simulation in Microelectronics*. Progress in numerical Simulation for Microelectronics, ed. K. Merten and A. Gilg. Vol. 3. 1995: Birkhauser Verlag. 233.
4. Cale, T.S., G.B. Raupp and T.H. Gandy, *Free molecular transport and deposition in long rectangular trenches*. J. Appl. Phys., 1990. **68**: p. 3645-3632.
5. Rey, J.C., L. Cheng, J.P. McVittie and K.C. Saraswat, *Monte Carlo low pressure deposition profile simulations*. J. Vac. Sci. Technol. A, 1990. **9**: p. 1083-1087.
6. Vvedensky, D.D., N. Haider, T. Shitara and P. Smilauer, *Evolution of surface-morphology during epitaxial-growth*. Philisophical Transactions of the Royal Society of London Series A, 1993. **344**(1673): p. 493-505.
7. Ruggerone, P., A. Kley and M. Scheffler, *Microscopic aspects of homoepitaxial growth*. Progress in Surface Science, 1997. **54**(3-4): p. 331-340.
8. Simka, H., B.G. Willis, I. Lengyel and K.F. Jensen, *Computational chemistry predictions of reaction processes in organometallic vapor phase epitaxy*. Prog. Cryst. Growth Charact., 1997. **35**: p. 117-149.

Chapter 2: Kinetic Monte Carlo – Theory and Implementation

Kinetic Monte Carlo simulations are used to model non-equilibrium systems which typically do not have analytic, closed-form solutions. In the first section an introduction to Kinetic Monte Carlo Methods is given in order to understand the type of problems where these methods are used. Section 2.2 contains a theoretical justification of the methodology. Sections 2.3 and 2.4 include an explanation of the serial implementation of the methodology.

2.1 Introduction

Kinetic Monte Carlo methods are used to model non-equilibrium systems using Monte Carlo simulation techniques. A typical example of such a problem is in crystal growth, where the adatom configuration on the surface is a complex function of temperature, flux, and microscopic energetics. Typically, no analytic solution for the dynamics of the crystal morphology can be computed. To understand such problems, Kinetic Monte Carlo (KMC) methods have been developed that simulate the growing film by applying physical 'rules' to a simplified model of the system. From a comparison of these models to experimental results, insight into the crystal growth process can be obtained.

2.2 Theoretical Justification

Monte Carlo simulations are typically used to model equilibrium systems[1], but the growth front evolution of a surface during thin film growth is a dynamic process. Weinberg and co-workers[2-5] have developed methods to study dynamic processes that correspond to the physical 'trajectory' of the system.

To model dynamic processes, the KMC methodology must solve the Master Equation[1] as shown in Equation 2.1,

$$\frac{\partial P(\sigma,t)}{\partial t} = \sum_{\tilde{\sigma}} W(\tilde{\sigma} \to \sigma) P(\tilde{\sigma},t) - \sum_{\sigma} W(\sigma \to \tilde{\sigma}) P(\sigma,t) \qquad (2.1)$$

where $P(\sigma,t)$ is the probability of being in state σ at time t and $W(\sigma \rightarrow \tilde{\sigma})$ is the transition probability to go from state σ to state $\tilde{\sigma}$. To solve the Master Equation, one must choose randomly among the transitions allowable and accept transitions with probability, $W(\sigma \rightarrow \tilde{\sigma})$. The transition probabilities must also be consistent with microscopic reversibility, as shown by Equations 2.2 and 2.3.

$$W(\tilde{\sigma} \rightarrow \sigma)P(\tilde{\sigma}, eqbm) = W(\sigma \rightarrow \tilde{\sigma})P(\sigma, eqbm) \tag{2.2}$$

$$P(\sigma, eqbm) = Z^{-1} e^{-H(\sigma)/k_b T} \tag{2.3}$$

The partition function is shown as Z, H is the Hamiltonian for the system, and $P(\sigma, eqbm)$ is the probability that the system is in state, σ, at equilibrium.

Equations 2.2 and 2.3 do not uniquely specify transition probabilities. Kang and Weinberg[4, 5] have shown different sets of transition probabilities that would eventually lead to the same equilibrium state can arrive to this state via different trajectories. The physical trajectory, the one that corresponds to the physical changes in the system, is needed to model dynamic, non-equilibrium processes. Kang and Weinberg[3] show that Metropolis or Kawasaki dynamics both are solutions to the Master Equation, but do not correspond to the physics of the system during the path to equilibrium. Thus, the transition probabilities must be constructed from rates that have physical meaning.

Fichthorn and Weinberg[2] show that the transition probabilities must be formulated to correspond to the physical rates of the microscopic processes to arrive at the physical trajectory. They also show how the theory of Poisson processes can be used to obtain a relationship between the rates of the transitions and the 'real' time step taken in between MC steps. To obtain the physical trajectory, the transition probabilities should be as in Equation 2.4.

$$W_i = \frac{r_i}{\xi_{max}} \tag{2.4}$$

In Equation 4, W_i corresponds to the transition probability of transition i, r_i corresponds to the rate of transition i, and ξ_{max} corresponds to the maximum rate of a transition in the current state.

The increment of 'real' time corresponding to every MC step, transition, taken is shown in Equation 5.

$$\tau_j = \frac{-1}{\sum_i n_i r_i} \ln(U) \tag{2.5}$$

In Equation 5, τ_j corresponds to the time increment in state j, $\sum_i n_i r_i$ is the sum of all rates in state j, and U is a random number between 0 and 1.

Using the above theory, a simulation can be created that models the evolution of surface morphology. A solid-on-solid (SOS)[6] model can be used to mimic a growing surface. Transitions on the surface, such as adsorption, diffusion, desorption, reaction, and incorporation can be included. If the correct rates are used in the simulation, a direct connection between simulation time and real time can be established. This can allow the direct comparison between experimental results and simulated results for such measures as roughness of surface morphology and rate of desorbing species. The following section will be a more detailed discussion of the implementation of a KMC simulation.

2.3 Implementation

In this section, a typical KMC simulation is described. The typical solid-on-solid surface model used to model the crystal surface is explored. The problem in a straightforward

implementation of a KMC simulation is computational efficiency. To increase the speed of the simulations, we have used computational science techniques to aid in the efficiency of searching lists and searching for the transition to take. These techniques are in the form of hash tables and binary trees.

2.3.1 Simulation Outline

An outline of a typical KMC simulation is shown in Figure 2.1.

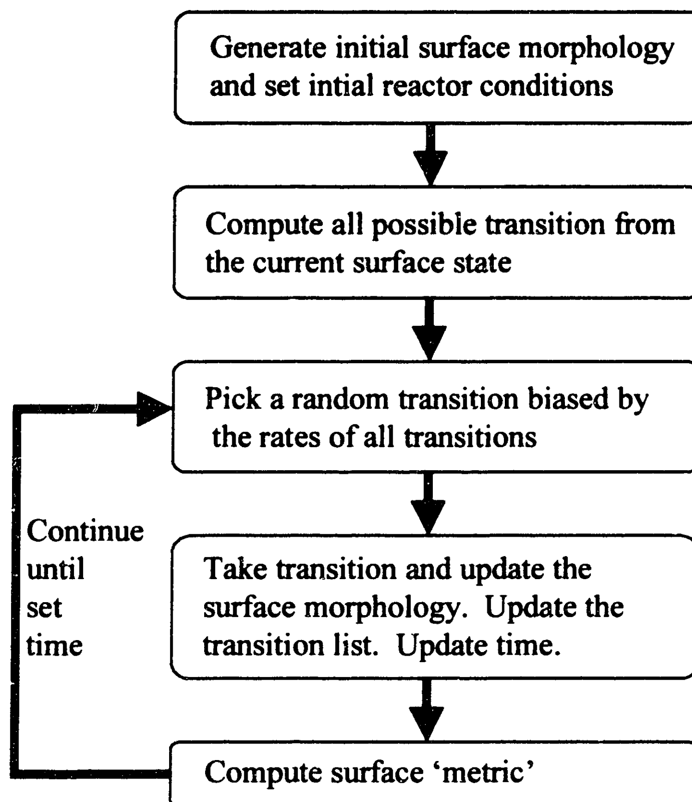

Figure 2. 1: The algorithm for a typical KMC simulation.

Initially, the surface structure and reactor conditions are set. Example initial surface morphologies include singular surfaces or vicinal surfaces with a given miscut. Then, all possible transitions from this surface structure are calculated. A random transition is chosen with probability given by Equation 2.4. A transition is selected and taken. The surface morphology is updated, as well as all old transitions that are not allowed are removed and new transitions that are now possible are added to the overall transition list. Time is updated using Equation 2.5, and different metrics of the surface morphology is

computed (for example surface roughness, a count of the number of dimers on the surface, or the X-ray scattering from a surface). The simulation continues until a given time is reached.

2.3.2 Surface Structure

Typically the surface structure is modeled as a Solid-on-Solid (SOS) model as pioneered by Gilmer[6]. The solid on solid model includes the following assumptions:

- Each adatom occupies a given site on the surface.
- Adatoms diffuse from site to site on the surface.
- No overhangs are allowed for adatoms on the surface.

An example of a simple SOS model is shown in Figure 2.2.

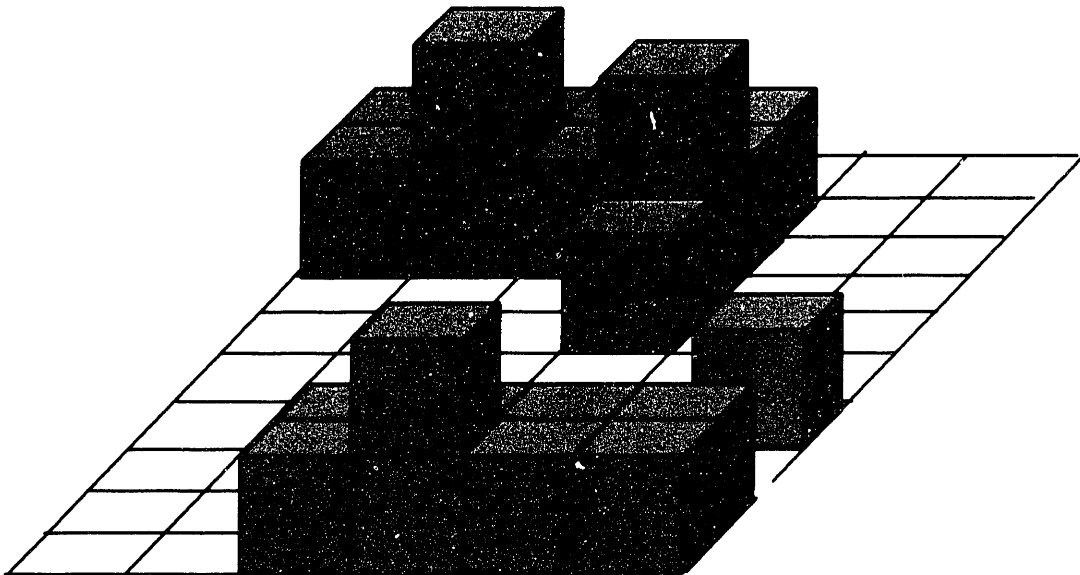

Figure 2. 2: A schematic of a solid-on-solid surface model.

The advantages of a SOS model is the rates of only certain transitions need to be known in order to advance the surface morphology. Only rates of transitions from adatoms going from one site to the next need be known. This is a simple methodology that can allow surface sizes of up to 1 micron^2. The drawback to this approach is that the exact path in space of the transition is not mapped out, as it would be in a methodology where the adatoms were not forced to site on particular sites on the surface. Molecular

dynamics (MD) simulations[7] are an example of this type of methodology, whereby potentials are used in order to exactly map out adatom location in space. The disadvantage of MD simulations is the relatively small surface sizes and time scales computationally accessible. In the end there is a tradeoff between accuracy and size. Larger times and surface sizes necessitate the assumption inherent in SOS models of given surface sites.

2.3.3 GaAs Lattice

The GaAs lattice structure is zincblende; a diamond lattice of Ga intertwined with a diamond lattice of As. In this work, KMC simulations are developed with a lattice model that followed the zincblende GaAs model in a SOS model. Thus, the available sites for Ga and As followed from the relationship to the standard formulation of the GaAs lattice. Figure 2.3 shows the construction of the lattice used for the simulations.

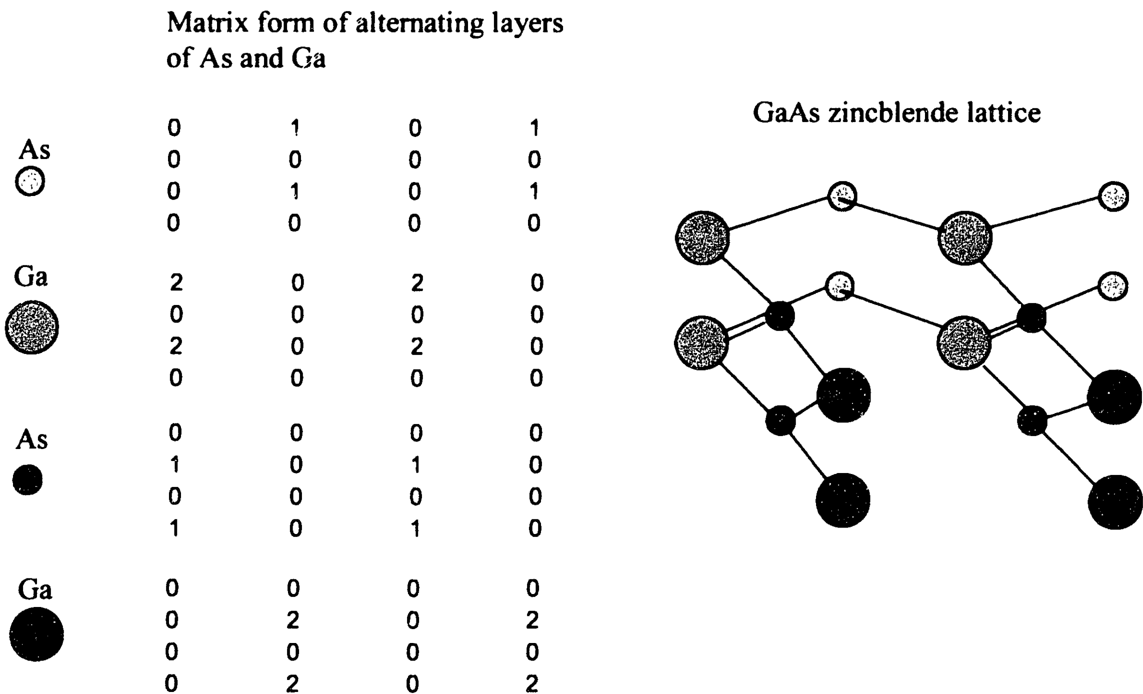

Figure 2. 3: The computational storage structure used to keep track of the zincblende lattice of GaAs.

As shown, the lattice consists of alternating layers of Ga and As occupying the zincblende sites. The lines that are connecting the atoms show bonding. The Ga and As species in the lattice are represented in a three dimensional matrix to aid in the simulation book-keeping of the atomic positions.

2.3.4 Hash Tables

Hash tables are used to aid in searching for available sites, current surface adatoms, and current available moves. In this implementation, there are structures set up for available sites and current surface adatoms that contain information on the *x*, *y*, and *z* positions of the sites or adatoms on the surface as well as the surface species. The difficulty in searching for an available site consists of the problem of searching through an unordered list of *x*, *y*, and *z* positions.

In a list of *x*, *y*, and *z* positions, the universe of possible combinations is large, especially if large surface sizes are run. Also, many of the combinations of *x*, *y*, and *z* positions will not be available sites or be occupied by adatoms. Thus, direct addressing of each structure, the allocation of a memory location for each *x*, *y*, and *z* combination, can occupy large amounts of memory and most of the allocated space will be empty. This leads to the idea of using hash tables[8] to allow for efficient searching of the space.

Hash tables are data structures that map the entire universe of *x*, *y*, and *z* positions to a smaller finite number of keys. This mapping allows searching of the *x*, *y*, and *z* coordinates to occur in a much smaller space (only consisting of the *x*, *y*, and *z* positions that map to a particular key). A pictorial representation of the structure is shown in Figure 2.4 for a hash table representing surface adatoms.

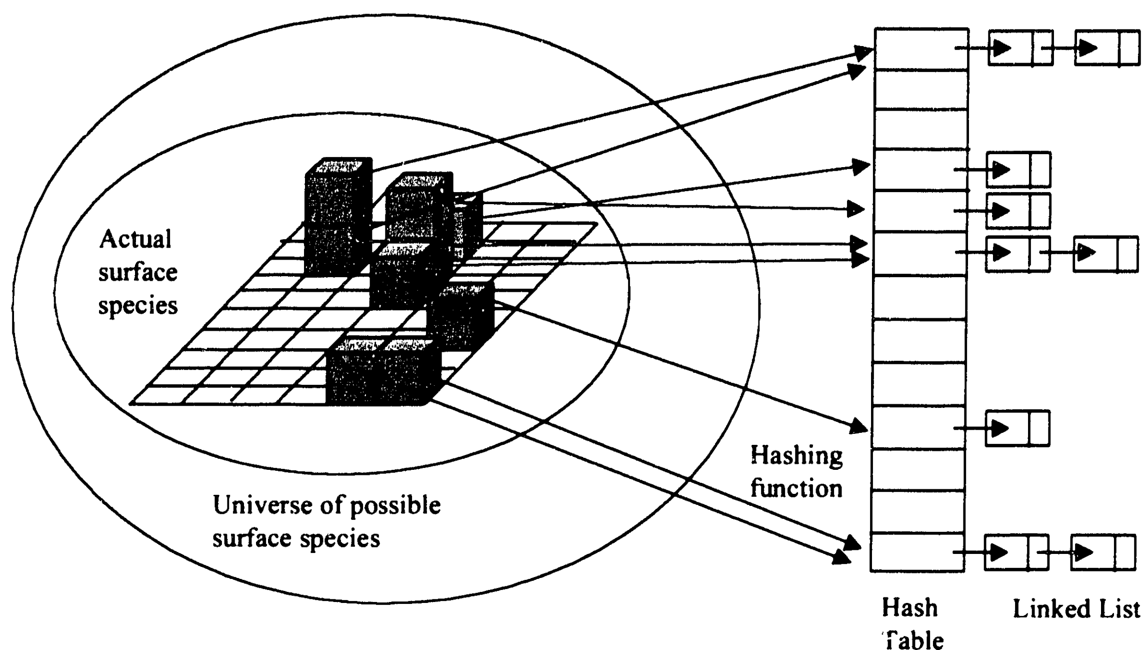

Figure 2. 4: A pictorial representation of a hash table (such as one used to represent surface adatoms)

Shown in Figure 2.4 is a mapping of surface atoms to a hash table. The mapping function of x, y, and z positions to an element of the hash table is done using a hash function. The hash function is picked to disperse the surface atoms among the elements of the hash table. A linked list is created which contains all surface adatoms that hash to the same value, which is linked to the hash table. When searching through the list of surface adatoms given an x, y, and z position, the hash function can be calculated and only the linked list attached to the hash table at the hash function value need be searched. As shown in Cormen, *et al.*,[8], the average case searching time in a hash table is $O(1 + n/m)$, where n is the number of surface adatoms in the list and m is the number of elements in the hash table.

2.3.5 Picking a transition and Binary Trees

In addition to searching for surface adatoms, available sites, and possible transitions, the other main search procedure is to find the next transition to perform. In this section, a

simple version of this procedure will be shown, as well as an update to this procedure using binary trees that greatly increase the efficiency of searching for the correct move.

Transitions are taken according to the probability given in Equation 2.4. The acceptance/rejection implementation of accepting transition is as follows:

1. Pick a random transition from the overall list of transitions from the given surface state.
2. Choose a random number between 0 and 1.
3. Accept the trensition if the random number is greater than the probability given in Equation 2.4, the ratio of the transition rate over the largest transition rate.

The problem with this implementation occurs when there is a large variation between the rates of all transitions. For example, if there were one transition that has a much larger rate than any other transition, the probability of taking that transition would be high. Unfortunately in this scheme, $O(k)$ trials would be taken, where k is the number of attempts before accepting a transition. This is due to the sampling of the many low probability transitions before finding the large rate transition or randomly selecting a low rate transition. To fix this problem, two different sampling schemes were used.

The linear searching sampling scheme agglomerates all the transitions into one large list that is referenced by the partial sum of the rates from the first transition to the transition at a given spot in the list. A sample is shown in Figure 2.5.

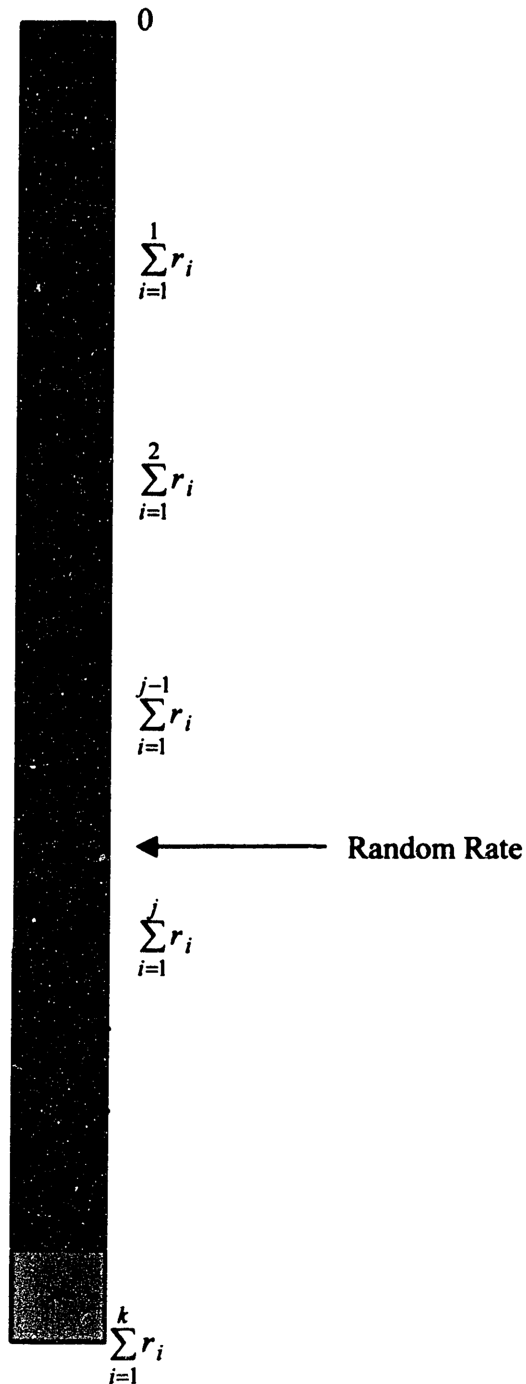

Figure 2. 5: A schematic of how transition rates are stored and chosen in the linear searching algorithm. Each block size corresponds to the magnitude of the rate.

In order to pick a transition, the following steps are taken:

1. A list of all transitions are formed and referenced by the partial sums of the rates for every additional transition.

2. A random rate, ρ, is picked uniformly from the values 0 to $\sum_i r_i$, the sum of all rates.

3. The transition, *j*, is taken when $\sum_{i=1}^{j-1} r_i < \rho < \sum_{i=1}^{j} r_i$, the random rate lies within the range of the partial sum of transition *j*.

This methodology biases the transitions by the same probability as given by Equation 2.4, but only requires one chosen random number. This methodology solves the problem of sampling and rejecting transitions, as a transition is picked for every random number chosen. The problem with this methodology lies in the updating of the partial sums. As transitions can be deleted from the list and added to the list as the surface morphology changes, inner transitions in the list can change. A recalculation of the partial sums from the first changed transition to the last transition is necessary, which leads to $O(k)$ updates at every transition. Also, a binary search is needed in order to find the transition *j* to be taken, which takes another $O(\log_2 k)$ operations.

Another efficient searching scheme is to utilize a binary tree to keep track of all transitions on the surface. Similar to the methodology espoused by Blue and Beichl[9], the binary tree approach has the advantage of both efficient searching and efficient updating. As moves are added to the overall list of transitions, the moves are added to a binary tree. The approach is shown in Figures 2.6 and 2.7.

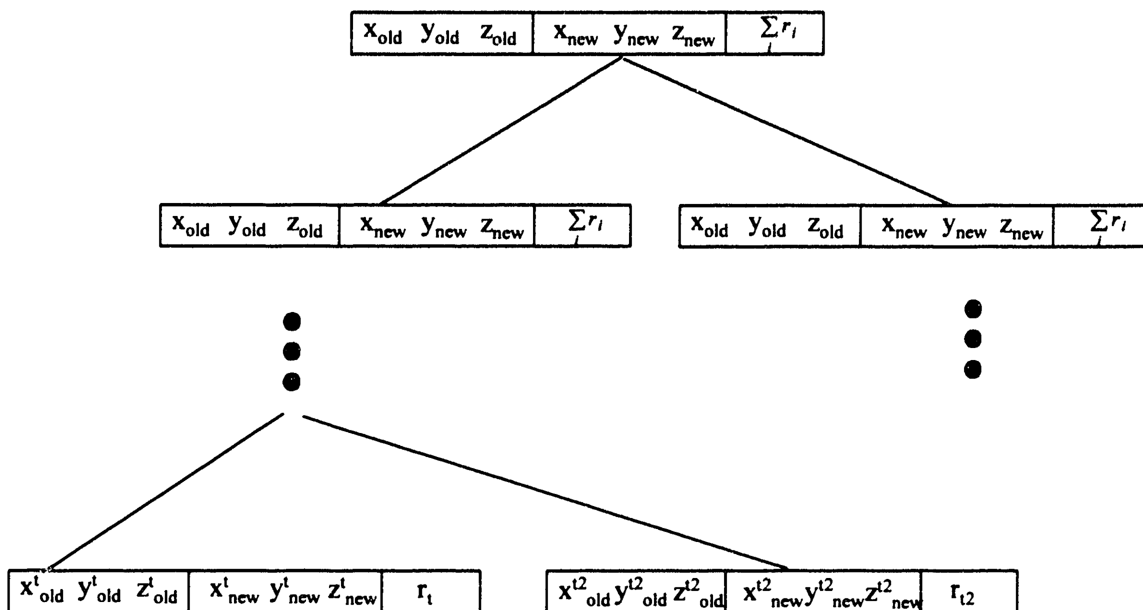

Figure 2. 6: A representation of the binary tree used to store the transitions. The root node contains average value for the transitions. The left leaf of a node contain all moves with position values less than the average and the right leaf contains all moves with position values greater or equal to the average.

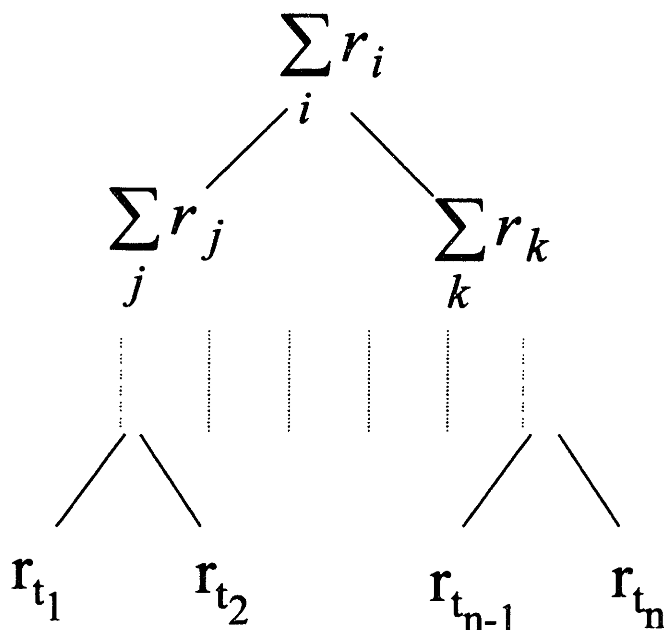

Figure 2. 7: The binary tree as a holder of the rates of the transitions. Each node has the sum of all transitions below it on the tree.

The root node of the tree maintains the sum of all rates in the leave nodes below as well as *x*, *y*, and *z* positions for the beginning and ending sites for a transition. The leaf nodes

of the root node contain the sum of all the rates below itself, as shown in Figure 2.7. The node that branches left contains all transitions that have smaller values of the end site and then beginning site for the transition in the z, x, and y positions compared to the root node. The right branch has transitions with higher values of the end site and beginning site in the z, x, and y positions compared to the root node. At each leaf node of the binary tree, a transition and the related rate is stored. The root node for each branch contains the average of the x, y, and z coordinates of its leaf nodes, as well as the sum of the rates of its leaf nodes.

The benefits of a binary tree include the efficient addition, deletion and searching of transitions. Transitions are added to the binary tree by comparing the transition to be added with the transition at every node. As the transition wends its way down the tree, the transition rate is added to the node, maintaining that every node contains the sum of the rates below it. A new leaf is created for every added transition. Deleting a transition is analogous, as the transition is found by wending down the tree and subtracting the rate of the transition at every node passed. Both addition and deletion of transition from the tree take $O(\log_2 k)$ operations. Searching for the correct move also takes $O(\log_2 k)$ operations. After a random rate is picked from a uniform distribution ranging from 0 to the sum of all rates, the transition is found by examining the leaf nodes of a given root node. If the random rate lies between 0 and the left node sum of rates, then the tree is traversed to the left. Otherwise, the random rate lies between the left node sum of rates and the sum of all the rates, and the tree is traversed to the right branch. This continues recursively until a leaf is found, and the transition at that leaf is taken.

Table 2.1 summarizes the operation count for each method for updating and searching transitions. As shown, the Binary Tree approach dominates the other two methods in updating and searching the transition list. The Linear Searching approach is empirically faster than the Acceptance/Rejection approach, presumably because of a large constant inherent in the Acceptance/Rejection approach.

Table 2. 1: Comparison of operation counts for different methods to choose from k transitions in KMC simulations.

Method	Update Operation Count	Searching Operation Count
Acceptance/Rejection	0	$O(k)$
Linear Searching	$O(k)$	$O(\log_2 k)$
Binary Tree	$O(\log_2 k)$	$O(\log_2 k)$

2.4 Conclusions

Kinetic Monte Carlo is a powerful method that can be used to study dynamic systems. The evolution of thin film morphology is a natural system to be studied by KMC. Physical transitions on the surface, such as adsorption, reaction, diffusion, incorporation, and desorption can be mimicked by KMC simulations. An exact correspondence between real time and simulation time enables the use of KMC simulations to understand experimental surface science and growth experiments.

The difficulty in using KMC simulations is the computational resources needed to solve large problems. This difficulty is alleviated by using techniques developed in computer science, such as hash tables and binary trees, in order to increase the efficiency of the simulation. Also, as the paradigm of high performance computing moves from supercomputers to massively parallel machines, parallel algorithms have been developed for KMC simulations. Chapter 3 contains an exposition of how parallel methods are used to further speed up KMC simulations.

Bibliography:

1. Binder, K., ed. *Topics in Current Physics*. . Vol. 7. 1986, Springer: Berlin.
2. Fichthorn, K.A. and W.H. Weinberg, *Theoretical foundations of dynamical Monte Carlo simulations*. J. Chem. Phys., 1991. **95**: p. 1090-1096.
3. Kang, H.C. and W.H. Weinberg, *Dynamic Monte Carlo with a proper energy barrier: surface diffusion and two-dimensional domain ordering*. J. Chem. Phys., 1989. **5**: p. 2824-2830.
4. Kang, H.C. and W.H. Weinberg, *Dynamic Monte Carlo simulations of surface-rate processes*. Acc. Chem. Res., 1992. **25**: p. 253-259.
5. Kang, H.C. and W.H. Weinberg, *Kinetic modeling of surface rate processes*. Surf. Sci., 1994. **299/300**: p. 755-768.
6. Weeks, J.D. and G.H. Gilmer, Adv. Chem. Phys., 1979. **40**: p. 157.
7. Allen, M.P. and D.J. Tildesley, *Computer Simulation of Liquids*. 1987, Oxford: Clarendon Press.
8. Cormen, T.H., C.E. Leiserson and R.L. Rivest, *Introduction to Algorithms*. 1992, Cambridge, MA: The MIT Press.
9. Blue, J.L., I. Beichl and F. Sullivan, *Faster Monte Carlo Simulations*. Physical Review E, 1995. **51**(2): p. R867-R868.

Chapter 3: Parallel Kinetic Monte Carlo Models

Parallel methods developed from ideas in Parallel Discrete Event Simulations (PDES) are applied to modeling a Kinetic Monte Carlo simulation of thin film growth. The simulated surface is spatially divided onto different processors. Simulations are run on each processor with communication between processors on the boundaries maintaining the correct causality of the overall simulation. Due to the poor scaling of the simulation on one processor, super-linear to linear speedups are achieved. The limitation inherent in the methodology is based on the interaction length on the surface. As the interaction length increases, performance degrades quickly due to increased communication between processors.

An outline of this chapter is as follows. Section 3.1 is an introduction and overview of surface growth simulations and the PDES technique. Following in Section 3.2 is a section on the computational scaling of the KMC simulation. The parallel algorithm development is shown in Section 3.3. Results are included in Section 3.4, and concluding remarks end the chapter. These parallel techniques have been used to greatly speed the calculation of KMC simulations.

3.1 Introduction

One of the limitations in the computational modeling of thin film growth is the size of the surface size simulated. Finite computational resources limit the maximum surface size studied, which is typically small compared to the size of interest. One methodology to increase the feasible surface size is to parallelize the algorithm. In this study, a Kinetic Monte Carlo simulation of the evolution of thin film growth is parallelized using ideas developed from the field of Parallel Discrete Event Simulations (PDES)[1].

Kinetic Monte Carlo simulations can be used to model thin film growth. The technique has been used extensively to examine the surface dynamics of molecular beam epitaxy

(MBE) grown GaAs[2] and CVD grown diamond films[3]. The basic idea in KMC simulations is to simulate thin film growth by modeling the transitions on a surface in discrete steps. These transitions can include adsorption, desorption, reaction, diffusion and incorporation into the growing lattice. The computational complexity arises in the problem when millions to billions of transitions must be taken in order to simulate large scale surface evolution (on the order of micron^2 surface sizes). Serial computations can take days to weeks to run given surface conditions, so parallel methods are developed to speed the computation of the problem.

Theory from parallel discrete event simulations (PDES) is a natural framework to use in order to parallelize KMC simulations. PDES can be defined as simulations where the state changes at discrete time points. Examples of such systems range from battlefield simulations[4] to the simulation of the spread of lyme disease[5-7] to queuing networks[8]. Methods have been developed to attack these problems in varied fields and are used in this case to parallelize KMC simulations.

Parallel methods have been used previously to study KMC simulations. Haider *et al.*[9] have used a spatial discretization to parallelize a KMC simulation. Their algorithm allowed for errors in causality along the processor borders. Beichl *et al.*[10] develop a parallel model with a spatial discretization that uses a variant of a conservative approach to PDES.

3.2 Kinetic Monte Carlo Technique

A solid-on-solid (SOS)[11] model can be used to model a growing surface. Transitions on the surface, such as adsorption, diffusion, desorption, reaction, and incorporation can be included. If the correct rates of these transitions are used in the simulation, a direct connection between simulation time and real time can be established. This can allow the direct comparison between experimental results and simulated results for such measures as roughness of surface morphology and rate of desorbing species.

Fichthorn and Weinberg [12-16]show that the transition probabilities must be formulated to correspond to the physical rates of the microscopic processes to arrive at the physical trajectory. They also show how the theory of Poisson processes can be used to obtain a relationship between the rates of the transitions and the 'real' time step taken in between MC steps. To obtain the physical trajectory, the transition probabilities should be as in Equation 3.1.

$$W_i = \frac{r_i}{\xi_{\max}} \tag{3.1}$$

In Equation 3.1, W_i corresponds to the transition probability of transition i, r_i corresponds to the rate of transition i, and ξ_{max} corresponds to the maximum rate of a transition in the current state.

The increment of 'real' time corresponding to every MC step, transition, taken is shown in Equation 3.2.

$$\tau_j = \frac{-1}{\sum_i n_i r_i} \ln(U) \tag{3.2}$$

In Equation 3.2, τ_j corresponds to the time increment in state j, $\sum_i n_i r_i$ is the sum of all rates in state j, and U is a random number between 0 and 1.

A flowsheet of the simulation technique is shown in Figure 3.1.

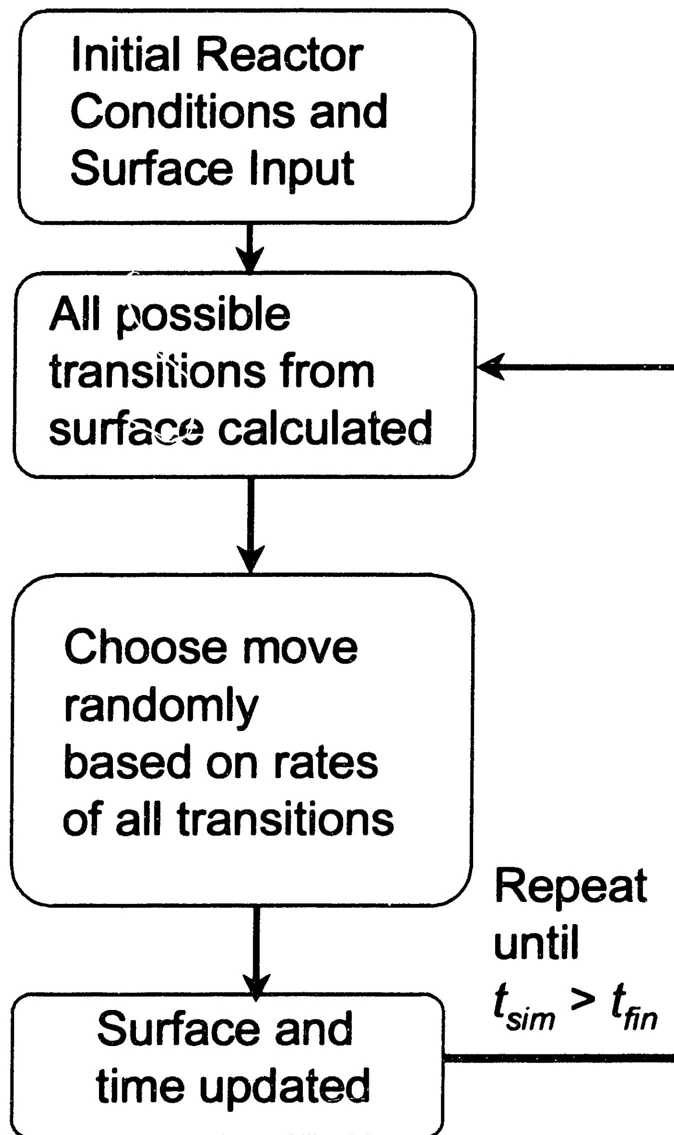

Figure 3. 1: A flowsheet of the algorithm for the KMC simulation of growth.

Given the current surface state, all possible transitions are calculated. A transition is randomly picked with the probability given in Equation 3.1. The transition is taken, and a new surface state is formed. The time increment is calculated using Equation 3.2, and the algorithm loops back until a given stopping time is reached.

The computational complexity lies in picking the transition biased by the probability given in Equation 3.1 and updating the transition list given a state change. As shown by Blue *et al.*[17], a general approach to picking a transition is to store all transitions in a binary tree. Thus picking a transition and updating the tree all scale as $O(\log_2 n)$

operations for n total transitions. Another methodology is to first randomly pick a group of transitions biased by the sum of the entire group's rate divided by the sum of all the rates. Then to pick an individual transition, each one is equally likely, so a uniform distribution can be used to randomly choose the exact transition to accept. This degrades into a binary tree approach as transitions become differentiated (for example, if diffusion rates are dependent on surface configuration due to nearest neighbor interactions, each diffusion transition may have widely different rates).

The computational complexity and memory requirements of a KMC simulation limit the surface size. This limitation is due to the large increases in simulation run-time and memory usage with larger surface sizes. The total time for a simulation is shown in Equation 3.

$$SimTime = \Delta t * N_s \tag{3.3}$$

where Δt is the time per transition and N_s is the number of transitions until a real-time finish time is reached. The number of transitions for a given simulation time is shown in Equation 4,

$$N_s = \frac{T_f}{\left(\dfrac{1}{\sum_i n_i r_i}\right)} \tag{3.4}$$

where T_f is the real time to finish the simulation and the denominator is the average time per transition (as shown in Equation 3.2). As the surface size increases, there are more transitions (n_i increases). The number of transitions can be thought of to scale quadratically with surface size (as the number of free sites increases by the square of the surface size). Thus, the number of transitions until a real time of reached scales as $O(n^{\alpha})$

with the number of transitions. We have already seen that the time per transition scales as $O(log_2 n)$. Thus overall time for a given T_f scales as $O(n^\alpha log_2 n)$.

This is shown empirically in Figure 3.2 to 3.4, as the number of transitions and run time increase with surface size.

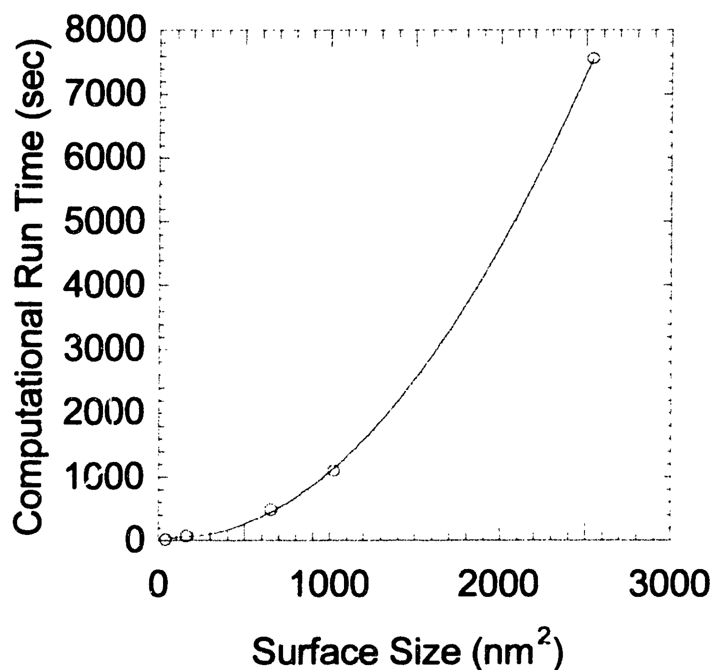

Figure 3. 2: Computational runtime as a function of surface size simulated in a serial KMC algorithm.

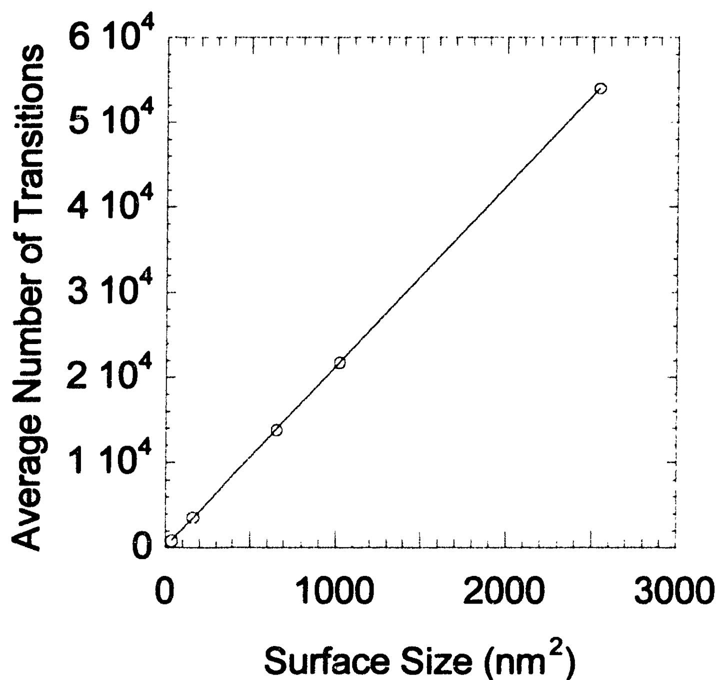

Figure 3. 3: Number of total transitions as a function of surface size simulated in a serial KMC algorithm.

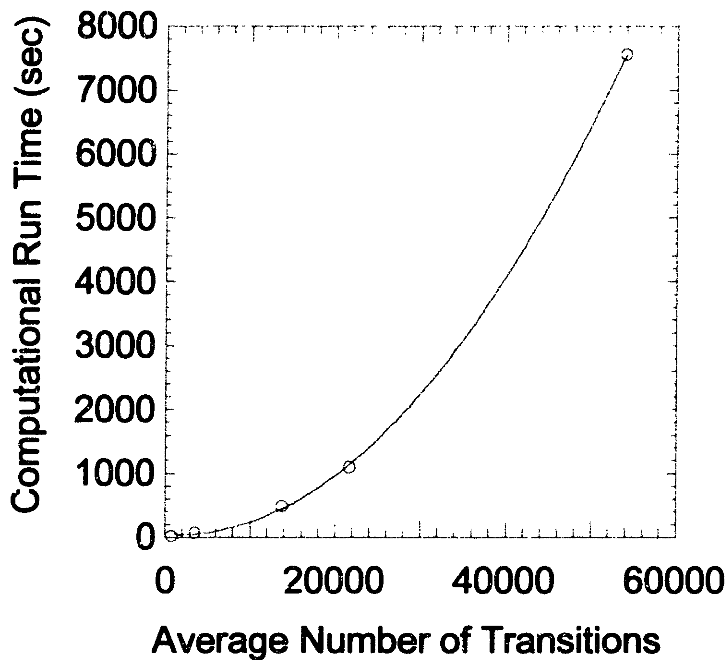

Figure 3. 4: Computational runtime plotted versus total transitions in a serial KMC algorithm.

The problem scales even more poorly as more species (more transitions per surface site) are added to the model. New methods must be developed to run surface sizes in the micron range. Thus, methods to split the problem onto multiple processors are developed.

3.3 Parallelization Strategy

Methods developed for Parallel Discrete Event Simulations (PDES)[1] are applied here to split the KMC problem up spatially over processors. KMC simulations can be classified as Discrete Event (DE) simulations. These are problems where the assumption is that the state of the simulation changes at discrete points in simulated time. The simulation changes state with the occurrence of an event, or a transition in the KMC simulation. PDES refers to methodologies that execute discrete event simulations on multiple processors.

PDES simulations are typically executed by splitting up the problem onto n processors. The split occurs by spatial elements (in battlefield or surface problems) or processing elements (queuing systems). An example of a KMC surface split onto processors is shown in Figure 3.5.

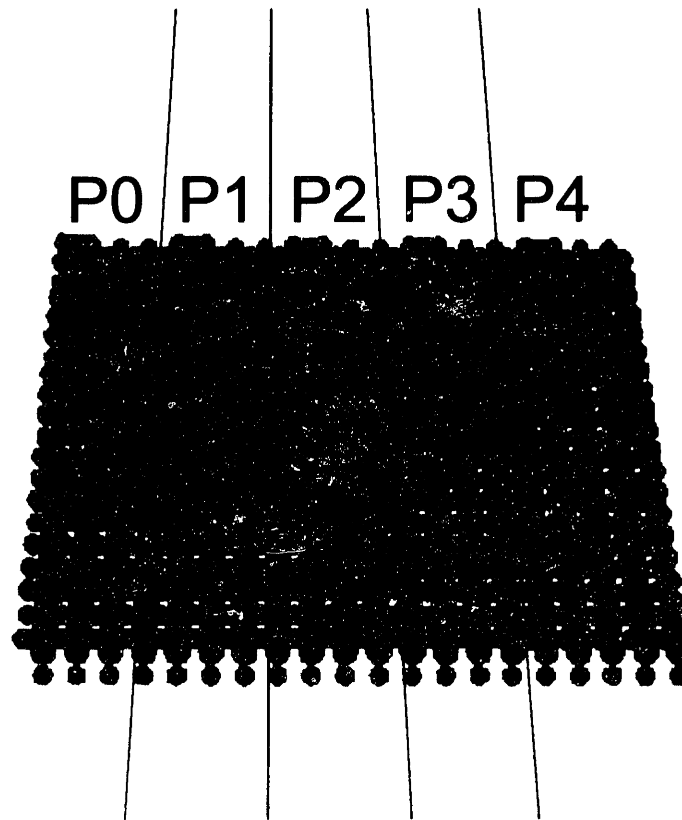

Figure 3. 5: A cartoon of a simulated surface being split onto processors P0 to P4.

Each processor computes in parallel with the information in local residence. Local time is kept for each processor. Messages are passed between processors when events traverse over the spatial elements encompassed by processors.

PDES are difficult due to the sequential nature of the simulation. As events occur in discrete events in time, it is difficult to simulate an event in the future (a transition timestamped T_2) without being worried that a past event (a transition timestamped T_1) would have affected the status of the future transition. An error that occurs due to a smaller timestamped transition affecting the already taken larger timestamped transition is an error in *causality*. The difficulty is to maintain causality during the simulation, as events that occur with smaller timestamps can traverse over to processors whose states have been affected by larger timestamps.

Two basic protocols are used in PDES in order to maintain causality. Conservative protocols allow processors to take events only when causality is maintained.

Conservative protocols force processors to stop until other processors 'catch up' in local time. This maintains causality as an event that traverses from one processor to another will be the smallest timestamped event occurring, with no chance of being affected by a smaller timestamped event. Optimistic protocols work by letting processors 'race' ahead without regard for maintaining causality. When a causality error occurs, the state of the offending processors are *rolled back* to the timestamp of the event. The simulation thus continues with causality maintained.

Since millions to billions of moves are made in a typical KMC simulation of the growth of thin films, the optimistic protocol is used to implement the PDES. Waiting for each processor to make one move at a time, and then synchronizing all the processors would entail more communication than computation, drastically reducing the efficiency of the simulation. The optimistic protocol is shown as a flowsheet diagram in Figure 3.6.

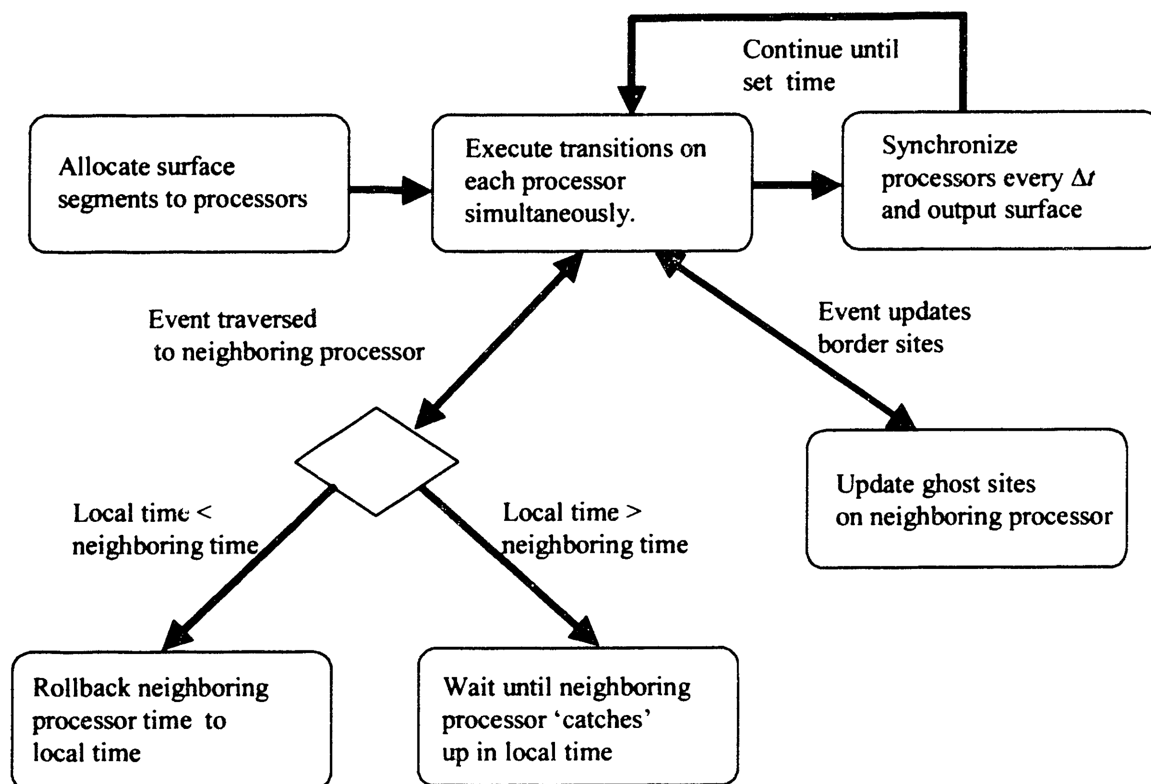

Figure 3. 6: An optimistic protocol derived from PDES theory for the simulation of parallel KMC models. The optimism in the models comes from a processor begin able to race ahead in simulation time, but being rolled back to a previous time when necessary.

Initially, the surface is split into equal sizes and placed on each processor (pictorially represented as in Figure 3.5). If the processors are heterogeneous, surface sizes to be placed on any given processor can be chosen to correspond to the speed of the given processor. Smaller size surfaces can be given to slower processors and vice versa. Optimally, local simulation time on each processor should advance at the same computational speed for every processor.

Each processor works simultaneously in performing moves on its segment of the surface. Local simulation time is kept for each processor. After a given local time is reached, all processors stop at this time and synchronize. This synchronization is to prevent any processor from falling too far behind or ahead the other processors in local time. During the period between synchronizations, each processor completes moves within the encompassing surface. To maintain causality on transitions that include boundary sites (sites that lie at the edges between processors), ghost sites are maintained that include the surface structure of the nearby processors. The ghost sites for processor n are shown in Figure 3.7.

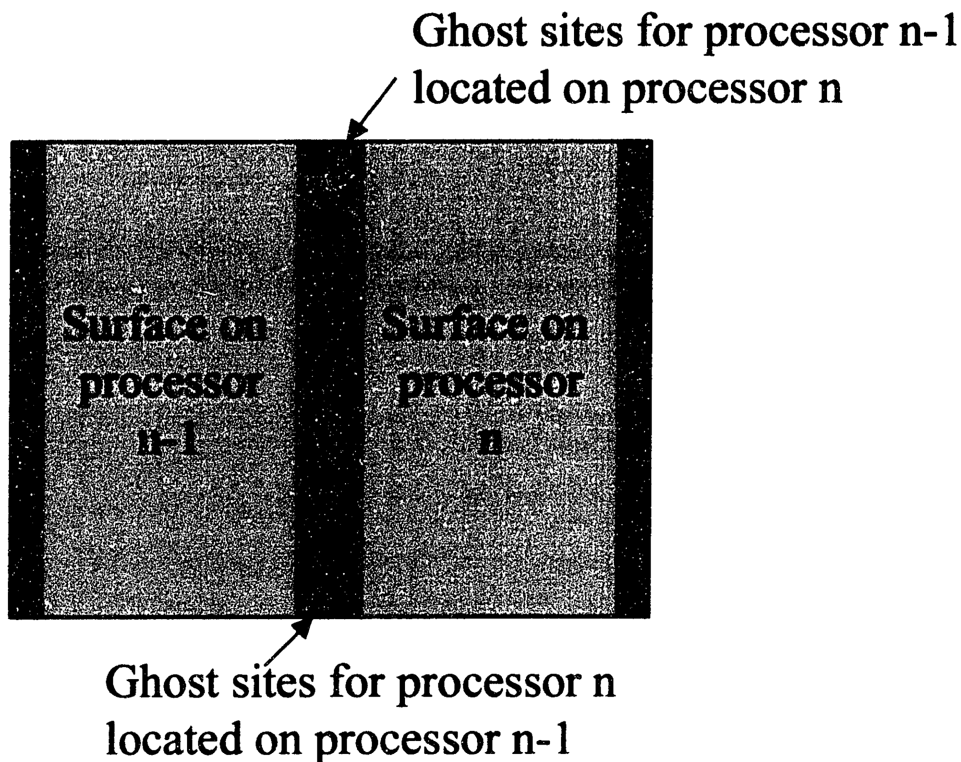

Figure 3. 7: Pictorial representation of ghost sites for processors. Ghost sites are replicated from neighboring processors to ensure the correct environment for adatoms on the boundaries of processors.

When processor *n-1* changes the surface near the boundary of processor *n*, processor *n-1* sends a message to processor *n*. If at this point, processor *n* has a greater simulation time than processor *n-1*, processor *n* rolls back to the simulation time of processor *n-1*. This forces processor *n* to be in the correct state (with all the correct surrounding surface morphology). If processor *n* is at a smaller simulation time than processor *n-1*, processor *n-1* waits until processor *n* catches up and then the move is undertaken. The whole process is shown pictorially in Figure 3.8.

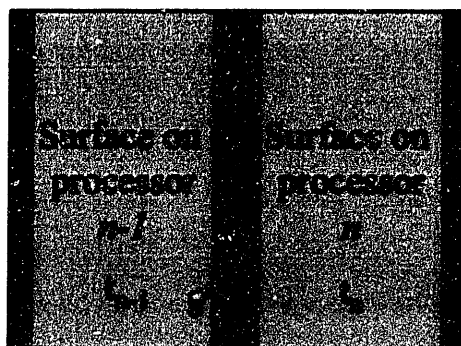

Transition from processor *n-1* inside ghost site are of processor *n*

TIME: $t_{n-1} < t_n$
Processor *n* rolls back to time t_{n-1}. Transition is taken if still valid.

TIME: $t_{n-1} > t_n$
Processor *n-1* waits for processor n to catch up in time.
Transition is taken if still valid.

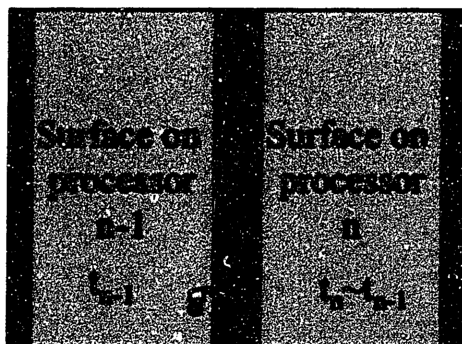

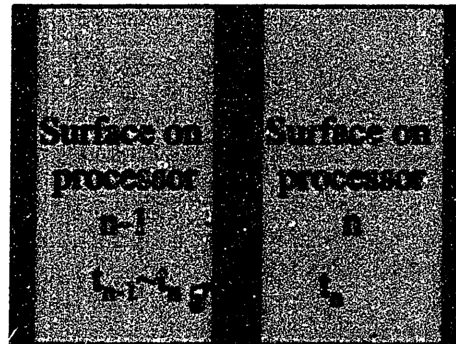

Figure 3. 8: A pictorial representation of the racing ahead and rollback process of each processor in the parallel algorithm.

Thus, messages get passed when the ghost area changes, as well as when adatoms cross from one processor to the other. If the ghost area is large, this can cause excessive communication that will slow down the efficiency of the algorithm. Typically the ghost area should be the size of the interaction length between adsorbates on the surface. The communication does guarantee that each processor 'sees' the correct surrounding surface morphology, and thus guarantees the correctness of the simulation.

To effect rollbacks of the surface, a data structure storing all the moves taken in sequential order is stored in a linked list. When a rollback needs to take place on a

processor, the linked list is traversed back until the simulation time is less than or equal to the simulation time needed for the rollback. This data structure can get large over time (as millions to billions of moves can be made in any given simulation). When the processors synchronize, garbage collecting takes place whereby previous moves that are timestamped less than the synchronization time are deleted from the linked list and the memory freed. This can take place when all the processors are synchronized, as a processor is guaranteed not to roll back further than the simulation time of the slowest processor.

This methodology is related to the space-time approach to PDES developed by Chandy *et al.*[18, 19]. In their approach, the simulation can be viewed as a two-dimensional space-time graph. The simulation fills in each region (space) by splitting up the space and assigning it to a particular processor. Each processor must be cognizant of the boundary conditions for its region and update them in order to complete its task. This methodology is similar to PDES with lazy cancellation (rolling back only after a guarantee of finding an error in causality).

3.4 Results

Performance results are shown for the algorithm. First, the algorithm is tested versus serial implementations in order to show correctness of the algorithm. Then, speedup is shown, as well as cases where speedup can degrade due to the physics of the system.

3.4.1 Correctness

To show the algorithm maintains the right causality of transitions, KMC simulations are run in serial and parallel and compared. More specifically, the on-axis and diffuse x-ray scattering is compared given the same reactor conditions. High-energy x-ray scattering can both give predictions on the overall surface roughness (the on-axis scattering or the crystal truncation rods (CTR)[20]) and the distribution of islands on the surface (diffuse scattering). Thus, a good test of the parallel version of the algorithm is to compare both the on-axis and diffuse scattering from the surface.

The CTR and diffuse scattering is computed from the simulated surface. The exact scattering is computed from the atomic positions by[21, 22],

$$
\begin{aligned}
I &= A(q)A^*(q) \\
A(q) &= \sum_{j=1}^{N_c} f_j(q)\exp(iq \bullet r_j)
\end{aligned}
\tag{3.5}
$$

where I is the intensity of the scattered beam, A is the structure factor, N_c is the number of atoms in the sample, f_j is the atomic scattering factor of atom j, r_j is the position of atom j, and q is the scattering wavevector. The CTR for the simulations is computed at the 110 position which is a bulk forbidden reflection; successive bilayers of GaAs scatter out of phase. This leads to the scattering being extremely sensitive to the top bilayers, so only the scattering from the highest level of the crystal at every site is computed[20].

Shown in Figure 3.9 is a sequence of overall scattering plots for a serial and parallel implementation of the algorithm.

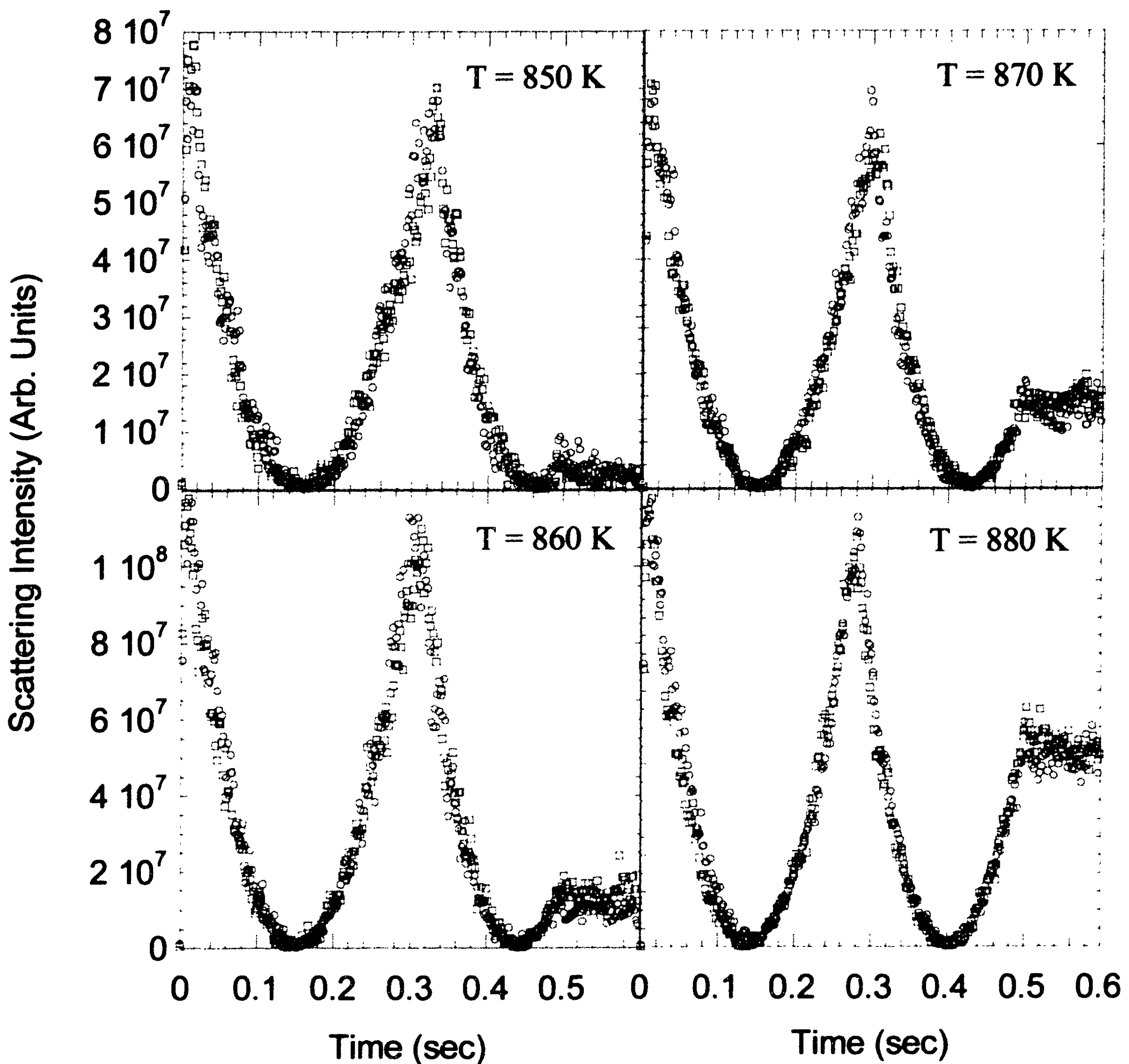

Figure 3. 9: A comparison between the serial implementation (O) and the parallel implementation (□) at (a) 850 K, (b) 860 K, (c) 870 K, (d) 880 K

The oscillations correspond to each bilayer of growth. The surface becomes rough, the bilayers scatter out of phase and produce a low signal. As the islands coalesce, only one bilayer appears, and a large signal is produced from the scattering off the surface. Figure 3.10 shows the diffuse scattering (correlation length) versus temperature.

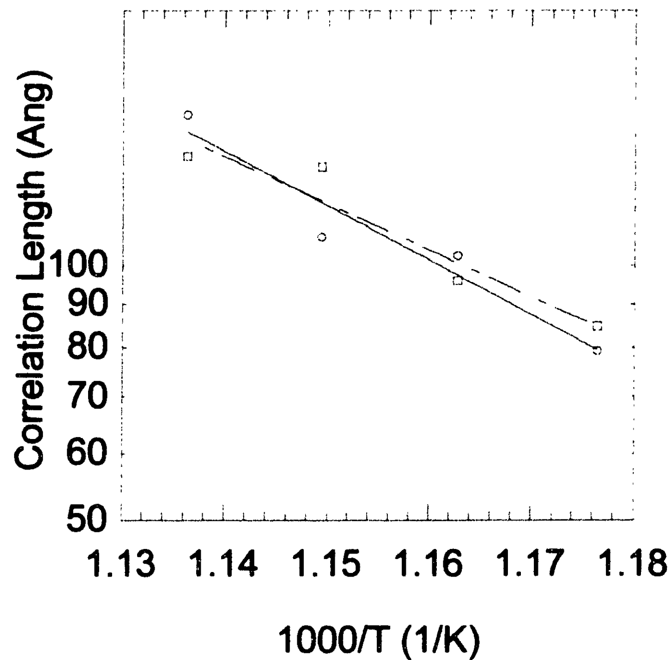

Figure 3. 10: A comparison between the serial implementation (O) and the parallel implementation (□) of the correlation lengths between islands with respect to temperature.

Within the error of the simulation, the curves lie on top of one another.

3.4.2 Speedup

Speedup is calculated by monitoring the computational time to finish one run to a given simulation time. The surface size is 640x640 surface sites which corresponds to 1280x1280 angstroms. The temperature is 800 or 825 K, and the model parameters are typical for MOVPE growth systems. The simulation time, speedup, and efficiency are shown in Figures 3.11-13 running on an IBM SP-2 platform. Speedup is defined in Equation 3.6,

$$S = \frac{t_1}{t_N} \tag{3.6}$$

Where S is the speedup, t_l is the simulation time using one processor, and t_n is the simulation time using n processors. Efficiency is defined as in Equation 3.7,

$$E = N\left(\frac{t_1}{t_N}\right) \tag{3.7}$$

where E is the efficiency and N is the total number of processors used.

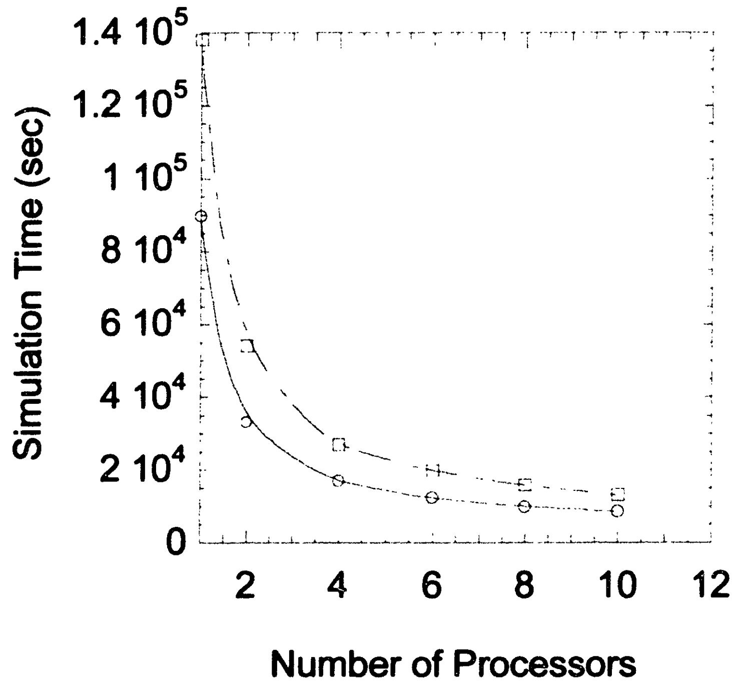

Figure 3. 11: The model was run at temperatures of (O) 800 K and (□) 825 K; A plot of simulation time versus number of processors.

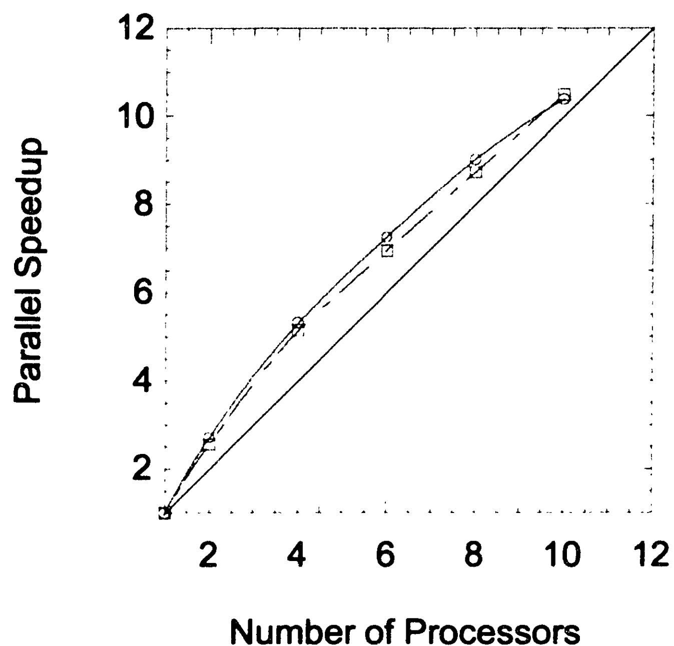

Figure 3. 12: The model was run at temperatures of (O) 800 K and (□) 825 K; A plot of speedup versus number of processors.

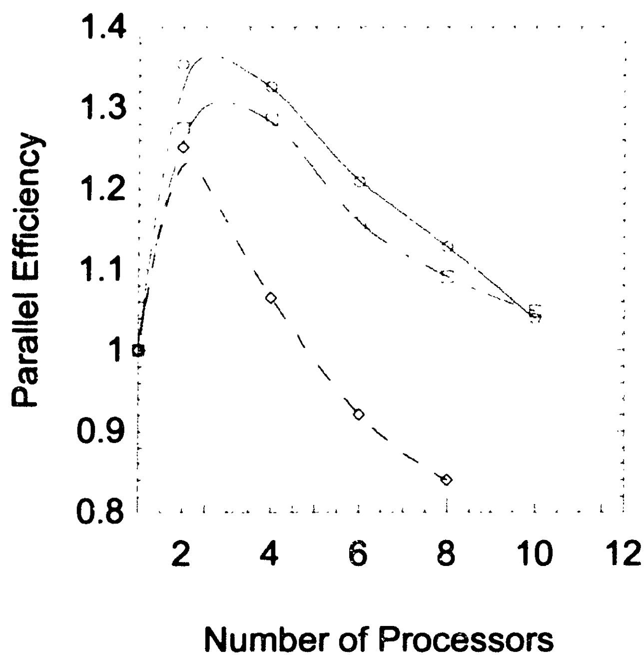

Figure 3. 13: The model was run at temperatures of (O) 800 K and (□) 825 K; A plot of efficiency versus number of processors, (◆) is the efficiency of a model with 512 x 512 Angstrom surface.

An efficiency of 1 implies a speedup proportional to the number of processors. A speedup of greater than one implies a speedup greater than the number of processors and vice versa.

As seen in Figure 3.11 and 3.12, the efficiency for all 10 processors is greater than one. As the efficiency lies above the 45 degree line in Figure 3.12, super-linear speedup is achieved. Due to the poor scaling of the problem on one processor ($O(n^{\alpha}\log_2 n)$), splitting the problem up onto up to 10 processors reduces the problem size on each processor, thus increasing the computational speed of the overall simulation. Extrapolating to more than 10 processors, communication time overtakes the size advantage, as too small of a surface size is placed on each processor. This reduction in speedup is due to slowing of the algorithm from communication between processors overcoming the benefit of a smaller surface on each processor. The shift from superlinear to sublinear speedup can be pushed further out to more processors as the surface size simulated becomes larger. In Figure 3.13, the parallel speedup and efficiency is shown for a 512x512 surface site problem at a temperature of 850 K. Here the efficiency is reduced to below one after the use of 4 processors due to the small sizes on each processor. Temperature also affects the speedup, as at higher temperatures there is more diffusion on the surface, as shown by Figure 3. More diffusion causes a higher probability of adatoms to cross processor boundaries and increases communication. This is offset somewhat by the benefit of performing moves simultaneously on the processors, as at higher temperatures, many diffusion steps would be taken in the serial algorithm before any other transition is taken. Synchronization of the processors can reduce the communication load, as it may reduce the need for rollbacks in the system.

3.4.3 Synchronization Frequency

Changing the synchronization frequency during the simulations does not affect the overall computational run-time of the simulation. Shown in Figure 3.14 is the simulation run time as a function of the synchronization frequency, as well as the average rollback as a function of synchronization frequency.

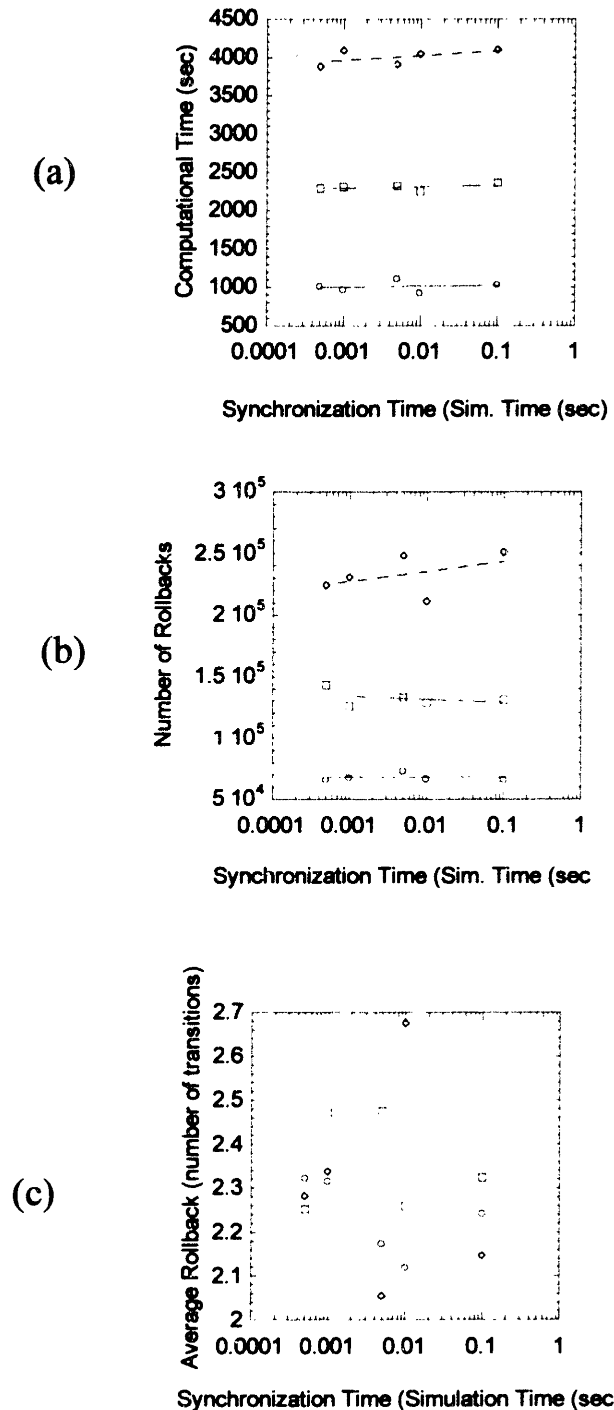

Figure 3. 14: The simulations were run at (O) 825 K, (□) 850 K, and (◆) 875 K. (a) Computational time as a function of the synchronization time; (b) Total number of rollbacks as a function of the synchronization time; (c) Average number of rollbacks as a function of the synchronization time.

As shown, the synchronization frequency does not affect the computational run-time. This is due to the implicit synchronization of processors in the algorithm. As transitions

are tried in the ghost area of each processor, the algorithm forces the nearby processor to be 'synchronized' as the environment for a given transition needs to be at the same time to guarantee the correctness of the transition. This implicit synchronization lessens the impact of the synchronization time on the computational time. An upper bound on the synchronization time is given by memory limitations, since all previous moves are saved until garbage collection is done. The results in the section are from computing on a 4 processor Intel Pentium Pro server.

Temperature affects the computational run-time, as the simulation ends at a specific simulation time. This is shown in Figure 3.14. Increasing the temperature increases the rate of diffusion, thereby reducing the simulation time-step for every transition. Also, the number of rollbacks increases with increasing temperature, as the species diffusion length is longer at higher temperatures. The longer diffusion lengths make it more likely that adsorbates diffuse over processor boundaries and onto other processors, which makes rollbacks more frequent. A plot of average rollbacks show that although the number of rollbacks increase with increasing temperature, the average length of each rollback is similar at all temperatures (all range from 2 to 2.7 moves per rollback). This suggests again that the implicit synchronization of the processors is occurring due to the algorithm.

3.5 Conclusions

A methodology to parallelize KMC simulations has been presented in this chapter. This implementation of the KMC methodology was shown to scale as $O(n^{\alpha}\log_2 n)$, with n being the number of transitions. This poor scaling leads to a limitation in performing simulations at large surface sizes, due to computational constraints. This parallel algorithm splits the surface up onto processors in order to reduce n on each processor, and speed up the overall simulation. In order to keep the boundaries matched, communication between processors must be accomplished. An algorithm is developed in order to guarantee that every adsorbate on the surface 'sees' the correct surface morphology. Unfortunately, the communication is the slow step in the algorithm. As shown by the speedup results, with a surface size on each processor greater than the ghost

area, super-linear speedup is achieved. When too small a surface is simulated on each processor, communication overtakes the benefits of a smaller n on each processor and sub-linear speedup is achieved. The benefits of frequent synchronization are muted, as the algorithm forces an implicit synchronization of the processors. This algorithm works best in simulating large surface sizes with short-range adsorbate interactions.

Bibliography:

1. Fujimoto, R.M., *Parallel Discrete Event Simulation.* Communications of the ACM, 1990. 33(10): p. 30-53.
2. Vvedensky, D.D., N. Haider, T. Shitara and P. Smilauer, *Evolution of surface-morphology during epitaxial-growth.* Philisophical Transactions of the Royal Society of London Series A, 1993. 344(1673): p. 493-505.
3. Srolovitz, D.J., D.S. Dandy, J.E. Butler, C.C. Battaile and Paritosh, *The integrated multiscale modeling of diamond chemical vapor deposition.* Journal of Materials, 1997. 49: p. 42-47.
4. Wieland, F., L. Hawley, A. Feinberg, M. DiLorento, L. Blume, P. Reiher, B. Beckman, P. Hontalas, S. Bellenot and D.R. Jefferson. *Distributed combat simulation and Time Warp: The model and its performance.* in *SCS Multiconference on Distributed Simulation 21.* 1989.
5. Deelman, E. and B.K. Szymanski. *Breadth-first rollback in spatially explicit systems.* in *11th Workshop on Parallel and Distributed Simulation.* 1997. Los Alamitos, CA.
6. Deelman, E., T. Caraco and B.K. Szymanski. *Parallel discrete event simulation of Lyme disease.* in *Pacific Symposium on Biocomputing.* 1995. Singapore: World Scientific.
7. Deelman, E., B.K. Szymanski and T. Caraco. *Simulating Lyme Disease using parallel discrete event simulation.* in *1996 Winter Simulation Conference Proceedings.* 1996. San Diego, CA: SCS Int.
8. Greenburg, A.G., B.D. Lubachevsky and I. Mitrani, *Superfast parallel discrete event simulations.* ACM Transactions on Modeling and Computer Simulation, 1996. 6: p. 107-136.
9. Haider, N., S.A. Khaddaj, M.R. Wilby and D.D. Vvedenky, *Parallel Monte Carlo simulations of epitaxial growth.* Computers in Physics, 1995. 9: p. 85-96.
10. Beichl, I.M., Y.A. Teng and J.L. Blue. *Parallel Monte Carlo Simulation of MBE Growth.* in *9th International Parallel Processing Symposium.* 1995. Santa Barbara, CA.
11. Weeks, J.D. and G.H. Gilmer, Adv. Chem. Phys., 1979. 40: p. 157.
12. Fichthorn, K.A. and W.H. Weinberg, *Theoretical foundations of dynamical Monte Carlo simulations.* J. Chem. Phys., 1991. 95: p. 1090-1096.
13. Kang, H.C. and W.H. Weinberg, *Dynamic Monte Carlo with a proper energy barrier: surface diffusion and two-dimensional domain ordering.* J. Chem. Phys., 1989. 5: p. 2824-2830.
14. Kang, H.C. and W.H. Weinberg, *Dynamic Monte Carlo simulations of surface-rate processes.* Acc. Chem. Res., 1992. 25: p. 253-259.
15. Kang, H.C. and W.H. Weinberg, *Kinetic modeling of surface rate processes.* Surf. Sci., 1994. 299/300: p. 755-768.
16. Kang, H.C. and W.H. Weinberg, *Interface roughening and kinetics of poisoning in a surface reaction.* J. Chem. Phys, 1994. 100: p. 1630-1633.
17. Blue, J.L., I. Beichl and F. Sullivan, *Faster Monte Carlo Simulations.* Physical Review E, 1995. 51(2): p. R867-R868.
18. Chandy, K.M. and R. Sherman. *Space, time, and simulation.* in *Proceedings of the SCS Multiconference on Distributed Simulation 21.* 1989.

19. Chandy, K.M. and J. Misra, *Parallel Program Design, A Foundation.* 1988: Addison-Wesley.
20. Robinson, I.K. and D.J. Tweet, *Surface X-ray Diffraction.* Rep. Prog. Phys., 1992. 55: p. 599.
21. Fuoss, P.H. and S. Brennan, *Surface sensitive X-ray scattering.* Annu. Rev. Mater. Sci., 1990. 20: p. 365-390.
22. Robinson, I.K., *Crystal truncation rods and surface roughness.* Phys. Rev. B, 1986. 33(6): p. 3830-3836.

Chapter 4: Monte Carlo Simulations of Temperature Programmed Desorption

Monte Carlo simulations of Temperature Programmed Desorption (TPD) are performed in order to better understand the desorption mechanisms for adsorbates on semiconductor surfaces. Mechanisms developed from TPD studies can then be used in overall mechanisms of growth, as adsorbate desorption can be the rate-limiting step in MOVPE growth. The outline of this section is as follows. An introduction to the experimental TPD method as well as different modeling techniques to extract information from series of TPD spectra is in Sections 4.1 and 4.2. The KMC TPD algorithm is described in Section 4.3. The methodology is applied in order to understand methyl desorption from GaAs, and a mechanism consistent with experimental results is described in Sections 4.4 and 4.5. Section 4.6 includes concluding remarks that explore the broad applicability of KMC simulations in evaluating experimental results.

4.1 Introduction to Temperature Programmed Desorption

Temperature Programmed Desorption (TPD) is a widely used experimental methodology to determine the interactions of adsorbates on surfaces [1, 2]. TPD has been used to determine surface coverage, activation energies of desorption, and orders of desorption mechanisms. A typical TPD experiment is accomplished as follows:

1. A known concentration of species is allowed to adsorb on a surface. This corresponds to a given coverage of adsorbates on the surfaces. Adsorption occurs at a low temperature.
2. The temperature of the surface is ramped up at a constant rate.
3. The type and concentration of desorbed species is measured.
4. A plot of rate of desorption versus temperature is obtained for all species monitored. Spectra for different initial coverages are obtained in order to understand adsorbate-adsorbate interactions on the surface.

5. The resulting TPD spectra are analyzed in order to determine surface-adsorbate interactions.

A variety of methods have been developed in order to determine the surface coverages, activation energies of desorption, and the reaction order for desorption [3]. Many of these methods rely on analyzing TPD spectra using the simple Arrhenius form for desorption as shown in Equation 4.1,

$$R_d = k(\theta) e^{\frac{-E_d(\theta)}{k_B T}} \theta^n \tag{4.1}$$

where R_d is the desorption rate, θ is the fractional surface coverage, $k(\theta)$ is the coverage dependent pre-exponential, $E_d(\theta)$ is the coverage dependent activation energy, and n is the order of the desorption. Using the simple Arrhenius form for analyzing TPD spectra limits one to model simple desorption processes. Many complex effects, such as adsorbate-adsorbate interactions, dynamic surface reconstructions, and islanding of adsorbates cannot be taken into account using the Arrhenius model. More advanced modeling techniques can be used to examine each of these effects in detail.

4.2 Review of TPD Modeling Literature

A variety of methods have been used to analyze TPD data to obtain activation energy, pre-exponential factor, and order of desorption as a function of adsorbate coverage.[3] These methods primarily use the Arrhenius rate form to analyze the spectra, which limits their use to simple desorption mechanisms.

Statistical and stochastic methods have been developed to extract mechanistic information from TPD spectra. Seebauer[4] has developed a method to calculate a continuous distribution of energy states for desorption from a single TPD spectra. Russell and Ekerdt[5] use statistical methods to fit arbitrary mechanisms to TPD spectra. Non-linear parameter estimation is used to fit the spectra to any model, to evaluate

competing models, and to calculate uncertainties associated with the fitted parameters. Houle and Hinsberg[6] have developed a stochastic method that facilitates the determination of mechanisms and rate constants from TPD spectra. All of these methods extract mechanistic and rate information from TPD spectra, but most do not account for the long range effects of surface morphology on the desorption. Effects that include dynamic surface reconstructions are difficult to include in stochastic and statistical procedures that do not explicitly keep track of the evolving surface morphology during the desorption process.

A variety of MC methods have been used to model desorption from single crystal surfaces. Previously, MC methods have been used to study the effects of adsorbate interactions[7], surface heterogeneity[8, 9], and to compare MC simulations to analytical methods for simulating TPD spectra[10]. These methods do not have a direct connection between MC simulation time and real time. More recently, Fichthorn and Weinberg[11] have developed an algorithm to study surface processes that make a direct connection from MC simulation time to real time. Meng and Weinberg[12] have developed an algorithm to model TPD on metal surfaces, where the assumption is made that the rate of diffusion of adsorbates is much greater than the rate of desorption. This algorithm has been compared to analytical methods and found to directly correspond under limiting conditions[13]. Also, in some cases the MC model can be equivalent to a quasi-equilibrium cluster approximation in limiting cases[14]. The algorithm has also been used to model recombinative TPD[15], and the effect of attractive lateral interactions on TPD spectra[16]. Meng and Weinberg[17] have also simulated TPD spectra under non-equilibrium conditions and have quantitatively elucidated differences between quasi-equilibrium and equilibrium approximations for surface diffusion.

4.3 Kinetic MC TPD Algorithm

The algorithm follows both the experimental procedure and the KMC theory in order to produce simulated spectra that can exactly be compared to experimental spectra. Two complementary algorithms were developed; one to model adsorbates on metal surfaces

and another to model adsorbates on semiconductor surfaces. The main difference between the to models is the assumptions inherent for surface diffusion. On metal surfaces, diffusion is assumed to be fast compared to desorption, so the surface is equilibrated at every MC step. Typical semiconductor surfaces have comparable rates of adsorbate desorption and diffusion[4], so both types of events are simulated in the model. A flow chart of the 'metal' algorithm is shown in Figure 4.1 and the 'semiconductor' algorithm is shown in Figure 4.2.

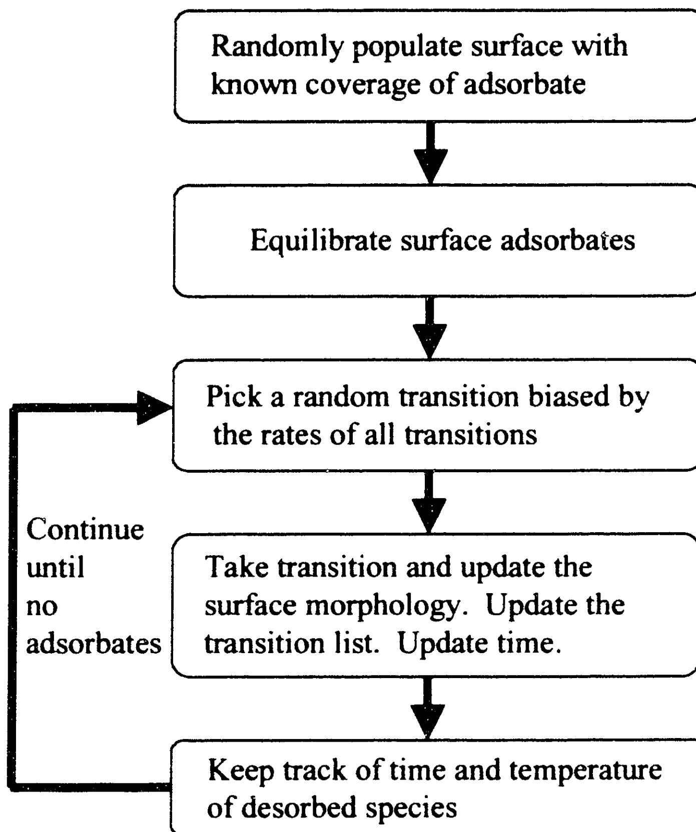

Figure 4. 1: Algorithm for 'metal' algorithm. The main assumption is that diffusion is much faster than desorption on the surface.

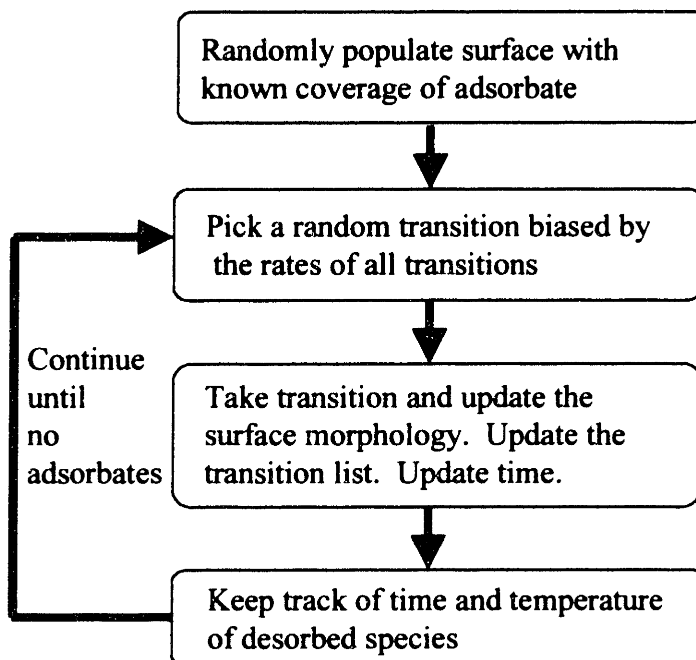

Figure 4. 2: Algorithm for the 'semiconductor' algorithm. No assumptions are made on the relative rates of diffusion and desorption on the surface.

The initial configuration of adsorbate on the surface is dependent on both the adsorption temperature and mechanism. Initially, the approximation is made to populate the surface randomly with adsorbates. This approximation is reasonable since adsorption of species onto the surface is normally done at a low temperature relative to the desorption temperature. The low temperature adsorption reduces the diffusion length of the adsorbates, giving the surface an approximately random initial population.

For the 'metal' algorithm, the next step is to equilibrate the adsorbates on the surface. In Figure 4.1, an equilibration of the surface is done in order to simulate fast diffusion on the surface. This equilibration algorithm is shown in Figure 4.3.

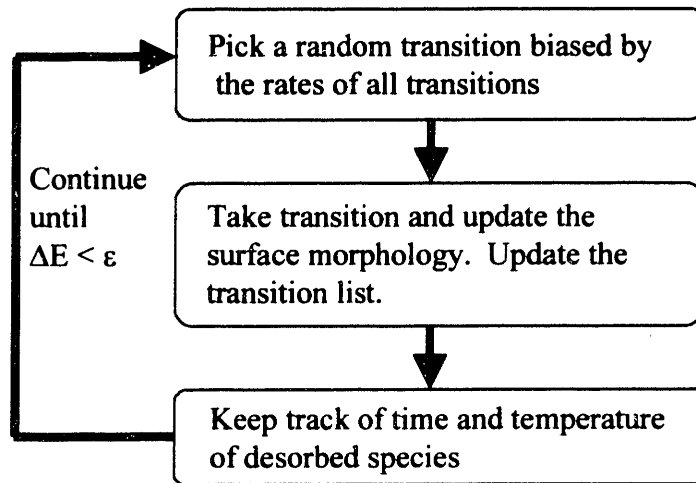

Figure 4. 3: Equilibration flowsheet for the 'metal' algorithm.

The assumption inherent in fast diffusion is that adsorbates will find their equilibrium state on the surface between each MC step in the algorithm. Equilibration is done by randomly selecting a diffusion move on the surface. If the surface energy (mainly determined by the number of nearest neighbor interactions for a given adsorbate) decreases in energy, the diffusion move is accepted. If the overall surface energy is increased, the diffusion step is taken with the probability shown in Equation 4.2.

$$p_i = \frac{\Delta E}{k_B T} \tag{4.2}$$

In Equation 4.2, p_i is the probability of taking diffusion step i and ΔE is the energy difference between the initial and final surface states. Equilibration is continued until the surface is equilibrated (surface energy is minimized).

In both algorithms, the next step is to calculate all transitions from the given state. In the 'metal' algorithm, the transitions are desorption events, while in the 'semiconductor' algorithm, the transitions can consist of desorption, diffusion, and even reaction on the surface. After all transitions are computed, a transition is randomly selected and accepted with the probability given by Equation 2.4. An efficient methodology to accept a transition is given in Chapter 2.4.

The transition is then taken and the surface is updated. Time is incremented as shown in Equation 2.5 and the temperature is increased by the heating rate multiplied by the time increment. In the 'metal' algorithm the surface is then equilibrated at the new temperature and adsorbate distribution on the surface, while in the 'semiconductor' algorithm, new transitions are calculated. The simulations continue until all the adsorbates have desorbed from the surface.

The 'semiconductor' algorithm, as shown in Figure 4.2, is generally the more rigorous approach as desorption, diffusion, and reaction transitions are accounted for explicitly. The problem in using this approach for all systems is when diffusion rates are orders of magnitude greater than desorption rates, simulation run-times increase exponentially. This is the situation when the 'metal' algorithm can be used. To show the approximate switching regime between the two methodologies, a plot of the simulation time versus the ratio of diffusion to desorption rates is shown in Figure 4.4.

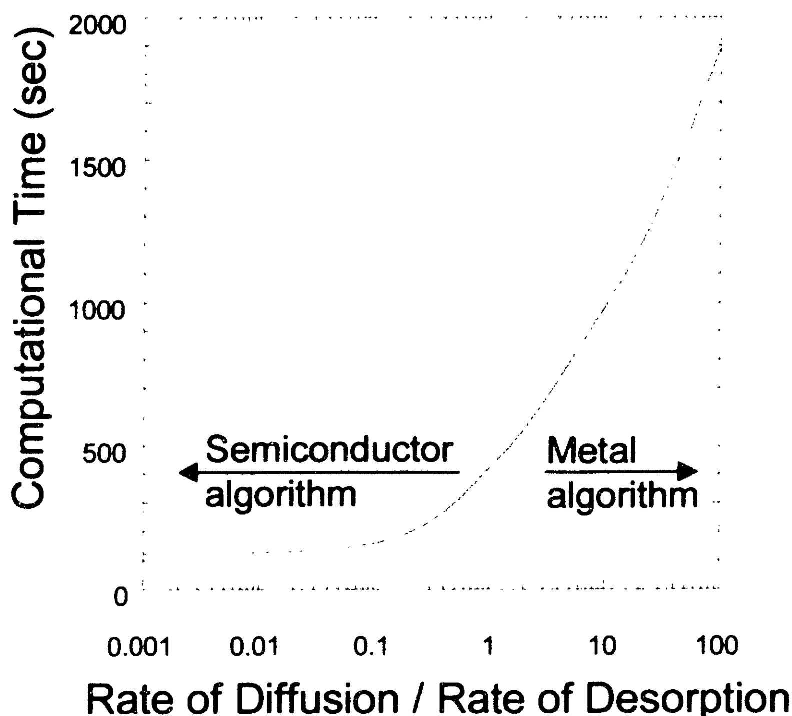

Figure 4. 4: Simulation time versus the ratio of diffusion to desorption rates.

There is a transition between the models, as one can always use the semiconductor algorithm to solve the problem, but the solution will become computationally inefficient

when diffusion is much faster than desorption. A model was developed that nicely switches between the two methodologies when the ratio of diffusion to desorption becomes larger than a given value, which is called the transition ratio. The algorithm switches between the semiconductor algorithm to the metal algorithm when the sum of the rates of the diffusion moves divided by the sum of the rates of desorption moves is greater than the transition ratio. The larger the transition ratio, the more accurate the metal algorithm will be in describing the surface transitions. The peak temperatures and peak widths are plotted using the semiconductor algorithm and transition ratios of 1, 10, and 100 in Figure 4.5.

(a)

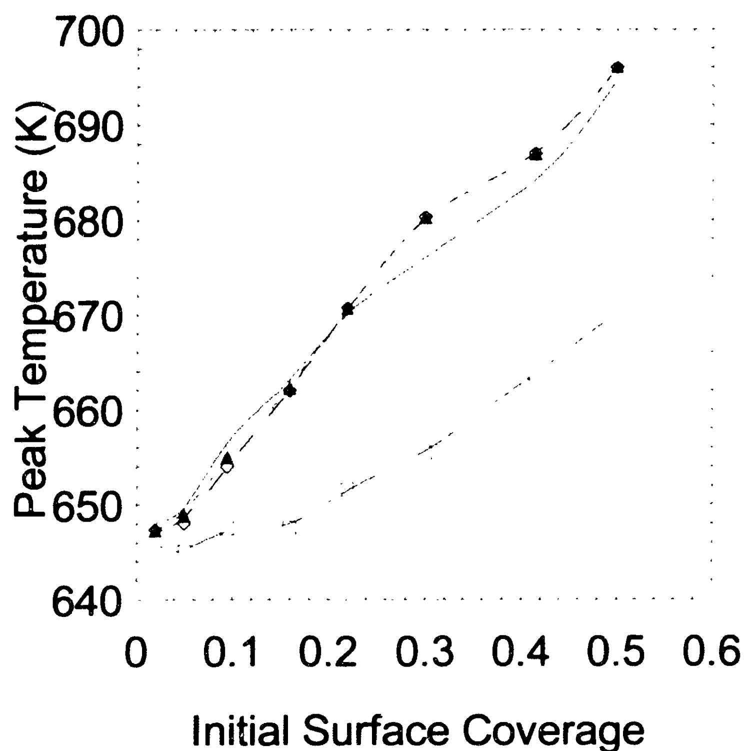

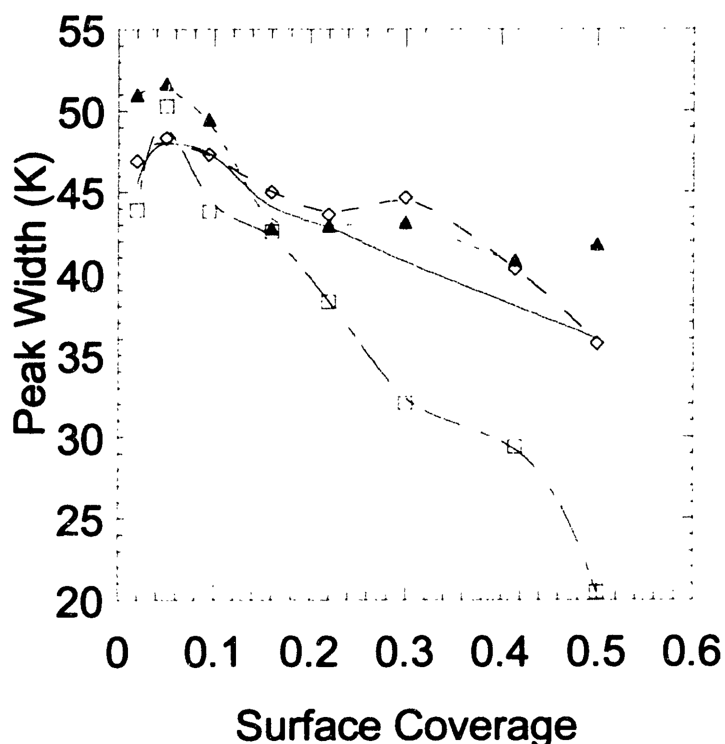

Figure 4. 5: (a) Peak temperature versus initial coverage of adsorbates; (b) Peak width versus initial coverage of adsorbates. (O) No transition to equilibration, (□) Transition Ratio = 1, (◆) Transition Ratio = 100, (▲) Transition Ratio = 10

As seen for large transition ratios (10 and 100), the peak widths and peak temperatures match the solution of the all diffusion case well. The smaller transition ratio case (ratio equal to 1) varies considerably from the other cases; this is due to the poor assumption that diffusion is fast on the surface, even when the rate of diffusion is equal to the rate of desorption on the surfaces.

4.3.1 Simulating TPD Spectra

Several computational issues are important in calculating accurate spectra. The initial temperature is important numerically in order to begin the calculation at a point where the simulation can continue gracefully and to not bias peak widths and peak temperatures. The rate calculation is important in calculating accurate peak widths and peak temperatures. Different averaging schemes to compute accurate rates will be discussed.

4.3.1.1 Initial Temperature:

The simulations are extremely sensitive to the initial temperature. If the initial temperature is set too low, the first few moves will be associated with a time step that is too large. Due to the large time steps, the temperature will be ramped too quickly, which can lead to temperatures that are already above the actual peak temperature. Too high an initial starting temperature, the peak width can be affected, as the initial upward slope of the curve can be at too high of a temperature. Examining the time step of initial moves at a given starting temperature can help ascertain an optimal starting temperature. If the time step is too large, the initial temperature can be increased until the time step is reasonable. A graph of how the initial starting temperatures can affect the peak temperature and peak width is shown in Figures 4.6(a) and (b).

(a)

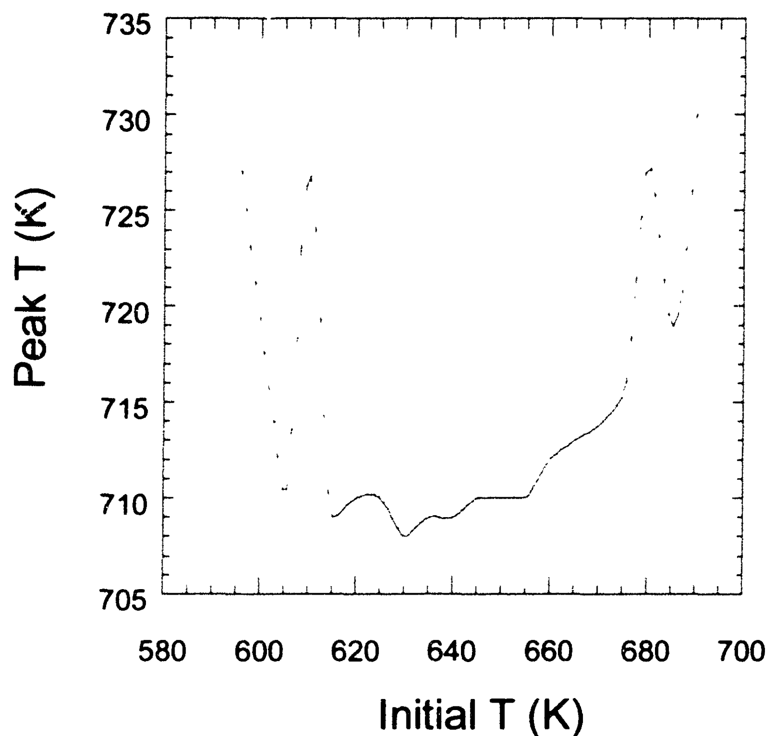

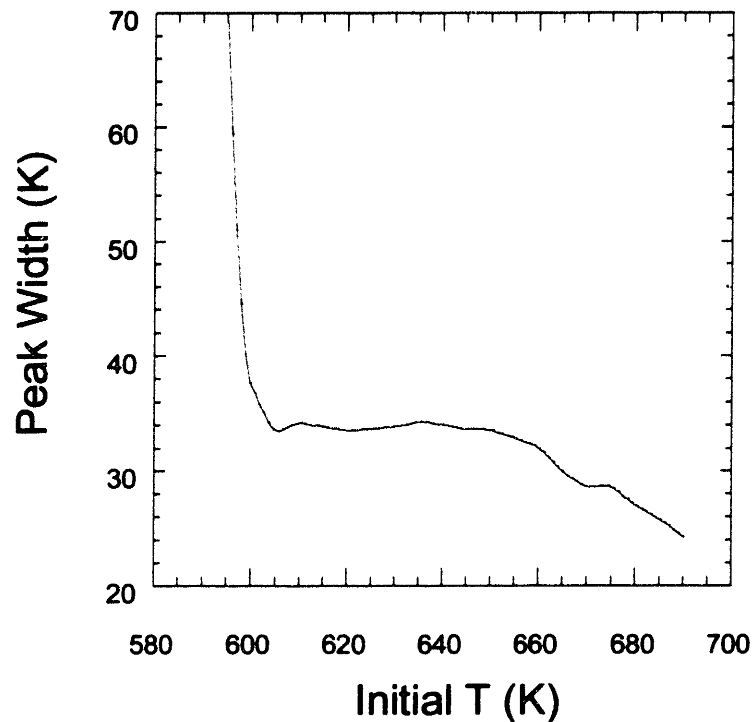

Figure 4. 6: (a) Peak temperature versus initial starting temperature for the simulation; (b) Peak width versus initial starting temperature for the simulation.

The conditions used include 45 kcal for the desorption barrier, and 1×10^{18} and 62.26 kcal for the diffusion pre-exponential and barrier, respectively, with a nearest neighbor energy of 4.6118 kcal for diffusion. The pre-exponential is extremely large in order to make the rate of diffusion comparable to the rate of desorption. The barrier for diffusion was approximated as the literature value for Ga diffusion[18]. The number of adatoms desorbed was set to 6000 and each rate of desorption was calculated over a sequential set of 200 adatoms. The peak temperature and peak widths are fairly constant over the initial temperature range between 620 and 660 K. Below 620 K, the peak temperature increases, as too large a time step is taken initially, and the peak width becomes unphysical. Above 660 K, the peak temperature is pushed up, and the peak width is pushed down, as the starting temperature affects the initial slope of the TPD peak and squeezes the curve. The effects of the initial temperature on the initial rate and initial temperature rises are shown in Figures 4.7(a) and (b).

(a)

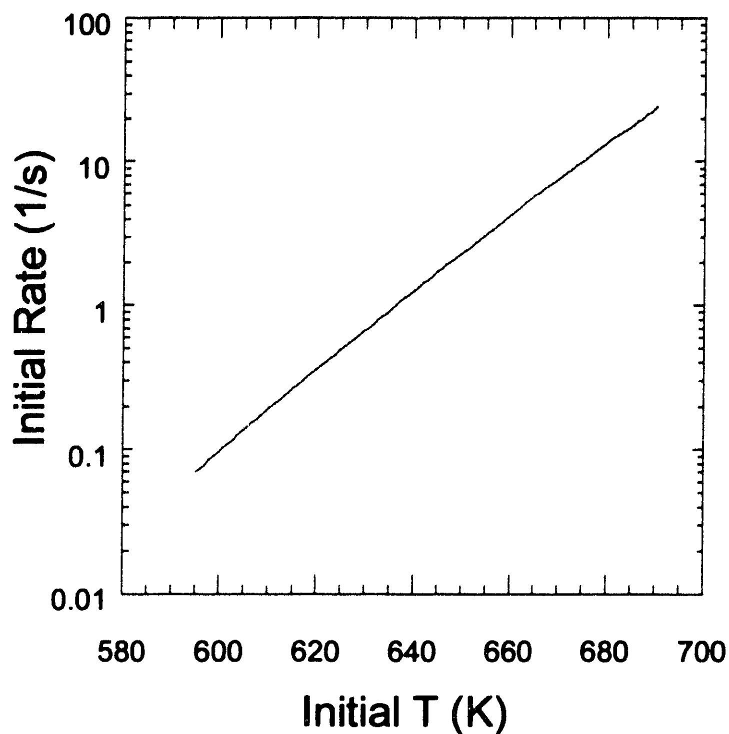

(b)

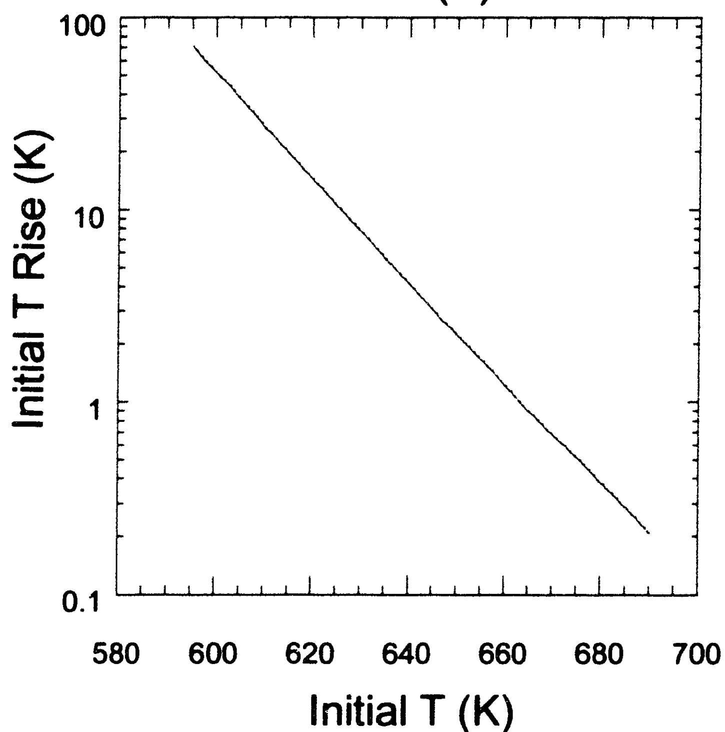

Figure 4. 7: (a) Initial rate versus initial temperature for simulation; (b) Initial temperature rise versus initial temperature for simulation.

In the range where the peak width and peak temperatures are fairly constant, the initial rate is $\mathcal{O}(1)$ which corresponds to an initial temperature rise of ~5 K. This study led to

the addition of a dynamic calculation of the initial temperature based on the initial rates of the system. The initial temperature is calculated as the minimum temperature (+/- 5 degrees) whereby the sum of all rates in the system is greater than 1.

4.3.1.2 Calculating Rate:

From a run of the simulation, the time of each desorption transition can be tracked, and simulated TPD spectra can be formed. The rate of desorption is calculated using Equation 4.3,

$$R_d = \frac{\partial N}{\partial t} \tag{4.3}$$

where R_d is the rate of desorption, ∂N is the number of adatoms desorbing in time ∂t. A plot of the rate of desorption versus temperature can be obtained by calculating the rate of desorption over the course of a simulated heating ramp. As in the case of a typical analysis of experimental data, a cubic spline is used to fit the simulated results. The spectra can be normalized using the area of the largest spectra. Normalized simulated spectra can be compared exactly to experimental spectra to determine if model mechanisms of desorption are consistent with experimental results. Also using the fit, the peak temperature and peak width at half maximum can be computed and used in quantitative comparisons between model predictions and experimental data.

Many simulations can be averaged over in computing the rate. Averaging over many simulations is akin to expanding the surface size and computing the rate of desorption over more desorbed adatoms. This can greatly improve the statistics of the spectra and reduce the noise inherent in stochastic simulations. Shown in Figure 4.8 is a series of spectra over which more adatoms were used in computing the spectra.

(a)

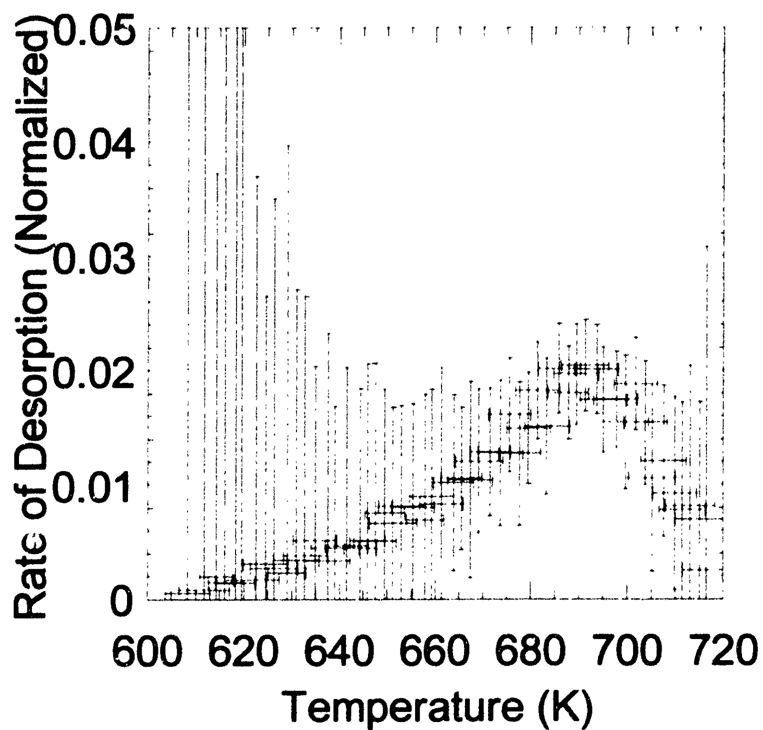

(b)

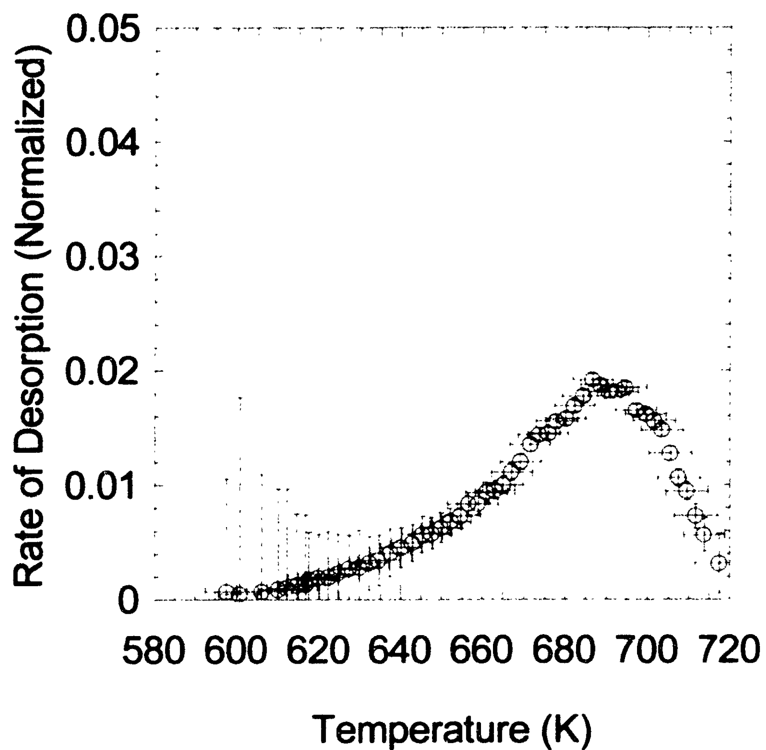

Figure 4. 8: (a) Simulated TPD spectra computed from 5000 adsorbate desorptions; (b) Simulated TPD spectra computed from 50000 adsorbate desorptions.

As seen, the variability is reduced using more adatoms. Averaging can be over the number of adsorbates (keeping the number of adsorbates fixed when computing the rate) or over temperature (averaging over a varied number of adsorbates, but keeping the temperature range fixed for each rate calculation) can be done. Averaging over the number of adsorbates keeps the error in the x-axis constant (rate of desorption), while varies error in the y-axis (temperature). The opposite occurs when averaging over temperature. There is an inherent tradeoff in accuracy of temperature and rate when averaging. Shown in Figure 4.9(a) are typical error bars for averaging over 10000 adatoms using a fixed temperature of 2 K. In Figure 4.9(b), the same simulation is shown but averaged over a fixed percentage of adatoms, 2.5%, in each rate calculation.

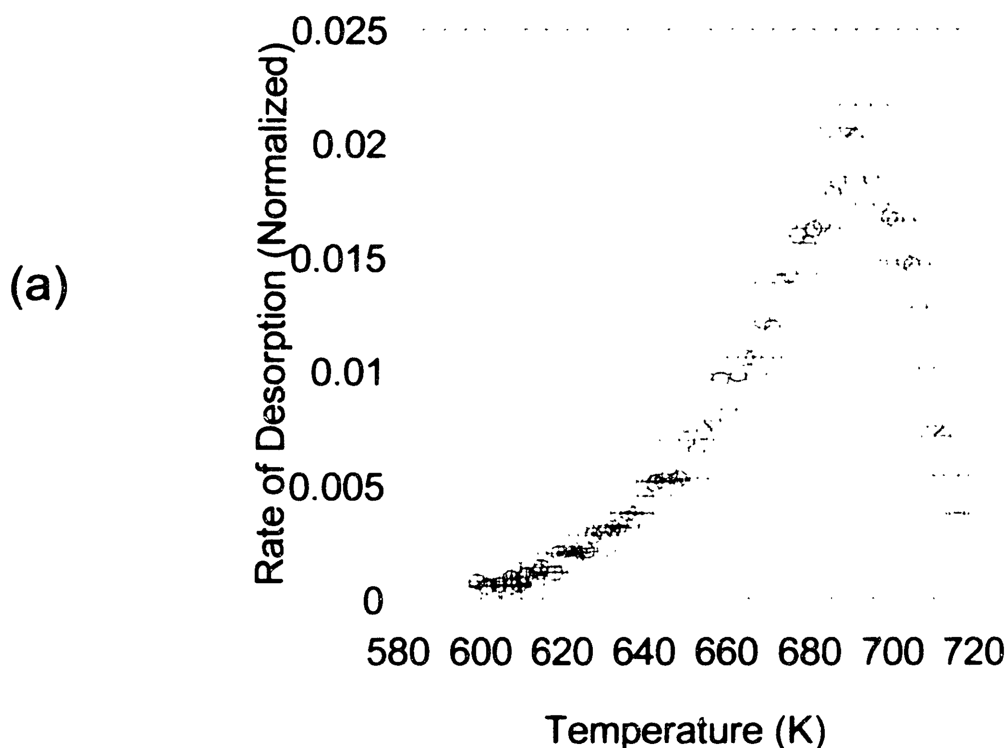

(b)

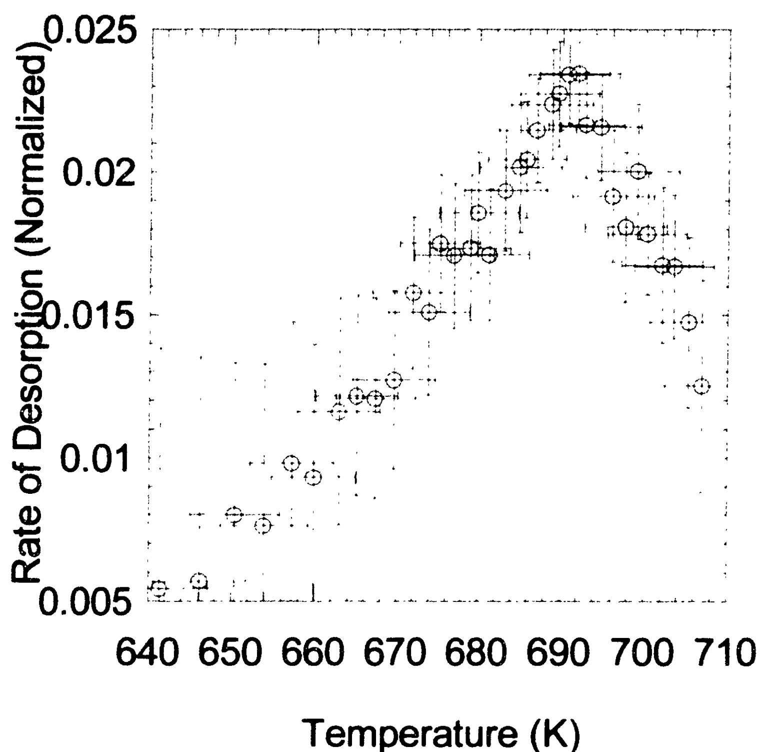

Figure 4. 9: (a) Typical error bars in a simulated TPD spectra averaging over a fixed 2 K temperature window; (b) Typical error bars in a simulated TPD spectra averaging over 2.5% of the total desorbed adatoms.

4.3.2 Parallel TPD

The TPD algorithm is computationally expensive, as many MC steps needs to be accomplished for every simulation. In order to study complicated models (many adsorbates, large surface sizes, many interactions), computational efficiency must be increased. One way of obtaining speedup is to parallelize the algorithm; run the code on many processors.

Parallel versions of the TPD algorithm are developed for the metal algorithm and implemented. From the assumption that the rate of surface diffusion is much faster than the rate of desorption from the metallic surface, the algorithm can be split into two sequential stages. The first stage is the diffusion phase where the surface is relaxed by

diffusion of adsorbates on the surface until a thermodynamic equilibrium of adsorbates on the surface is established. In the second stage, an adsorbate is chosen with probability proportional to its rate of desorption and desorbed from the surface. The stages repeat until all adsorbates are removed from the surface.

A master-slave programming paradigm is used to parallelize the algorithm. Before the simulation begins, the master processor block decomposes the surface and sends a section to each of the slave processors. In the diffusion phase, each slave processor undertakes Monte Carlo steps to simulate the fast diffusion of adsorbates on the surface. Asynchronous communication between slave processors maintains the boundary conditions between slave processors as adatoms diffuse across processors. Before the desorption phase, the slave processors are synchronized by the master. The master processor picks the adsorbate to desorb, updates the surface and restarts the slave processors on the diffusion step. The process is repeated until all adsorbates have desorbed.

Results of the speedup afforded by parallelization are shown in Figure 4.10.

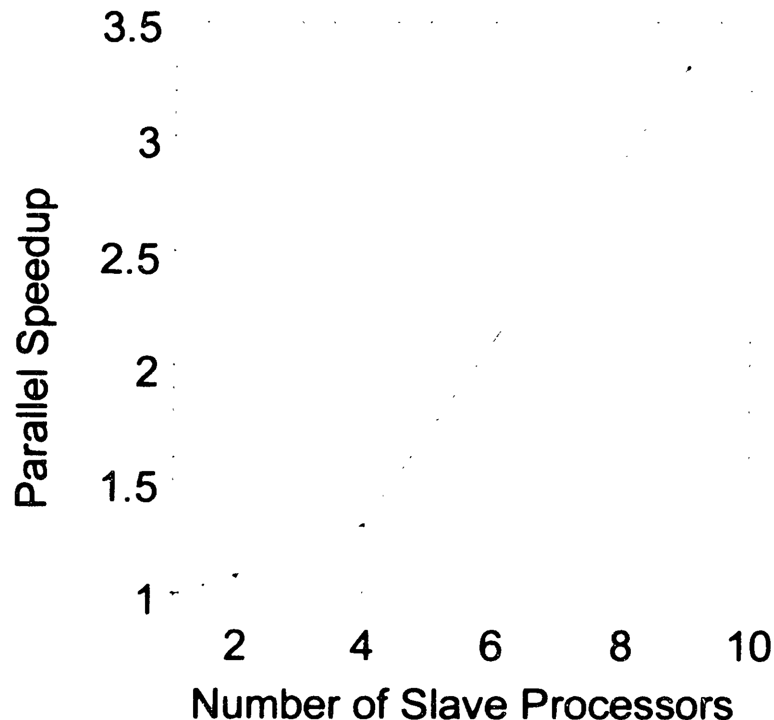

Figure 4. 10: Parallel speedup versus number of processors for the master-slave algorithm for the simulation of TPD spectra. Parallel speedup is defined as the simulation time on one processor divided by the simulation time on *n* processors.

The parallelization of the code shows over a 3-fold speedup with nine processors. The speedup is tested using a code developed with message passing using PVM[19] on an IBM SP-2. The speedup is limited by the desorption step; all processors must wait for the master processor to complete the step before further computation can occur. Nevertheless, this methodology shows promise in speeding up inherently computationally expensive algorithms.

4.3.3 Optimization Algorithms

Optimization methods can be used to find a consistent set of mechanism parameters for a given data set. A methodology is shown in Figure 4.11.

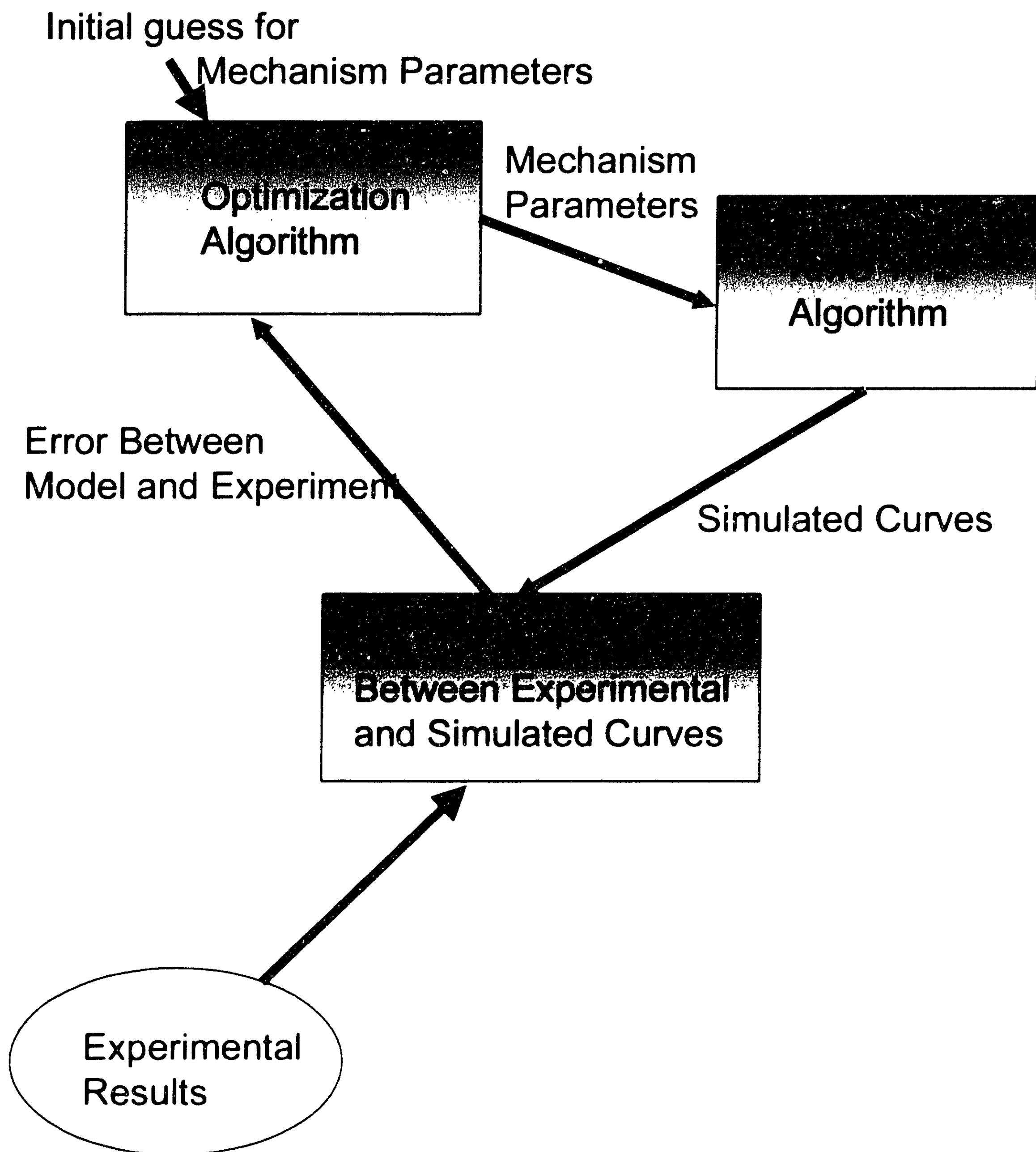

Figure 4. 11: Optimization methodology to extract kinetic parameters for surface processes from TPD spectra.

An initial guess for the mechanism parameters are needed and input into the optimization algorithm. The KMC TPD program is called and a series of simulated spectra are generated. The normalized spectra are compared to the normalized experimental spectra and an error is computed between the two sets of spectra. The error is used by the

optimization algorithm to calculate the next set of mechanism parameters. This process continues until the error is below a set tolerance level.

Powell's algorithm is used to minimize an error function between the model and the data set[20]. This algorithm is used, as it does not need the derivatives of the parameter set. Since the results from the KMC model cannot be derived analytically, the derivatives are impossible to compute analytically. The basic idea in this optimization algorithm is to move in the direction of the solution through the computation of conjugate directions. The conjugate directions are built up through line minimizations along all the dimensions through direct function calls. Basically, these methods use the black box model to compute numerical derivatives to build up a numerical Jacobian. The error is computed as the sum of the squared residuals between the rate of desorption of the normalized data set and the normalized model result, as shown in Equation 4.4.

$$E = \sum_{s=1}^{n} \frac{\left(\sum_{d=1}^{m_s} (r_d^e - r_d^c)^2 \right)}{\sigma_s} \tag{4.4}$$

In Equation 4.4, E is the error, s is the number of spectra, d is a counter that runs from the initial to final temperature at discrete steps, r_d^e is the experimental rate at a given d, r_d^c is the computed rate at a given d, and σ_s is the variability of that experimental run. The variability of each run weights the spectra in computing the error; as the variability of one spectrum decreases, it gets more weight in computing the error.

This methodology will only find a parameter set that is consistent with the data, not the 'true' parameter set. The benefit of this methodology is overall mechanisms can be tested and compared to the data. Thus, the magnitude of surface effects can be efficiently determined given the mechanism.

4.4 Case Study – Methyl Desorption from GaAs

The algorithm described above is used to evaluate proposed pathways for the desorption of methyl from Ga-rich GaAs(100), which has been investigated experimentally by Creighton[21]. The initial surface of GaAs(100) in the experimental TPD study is proposed to be a gallium-rich c(8×2)/(4×2)[22] structure, as shown in Figure 4.12(a).

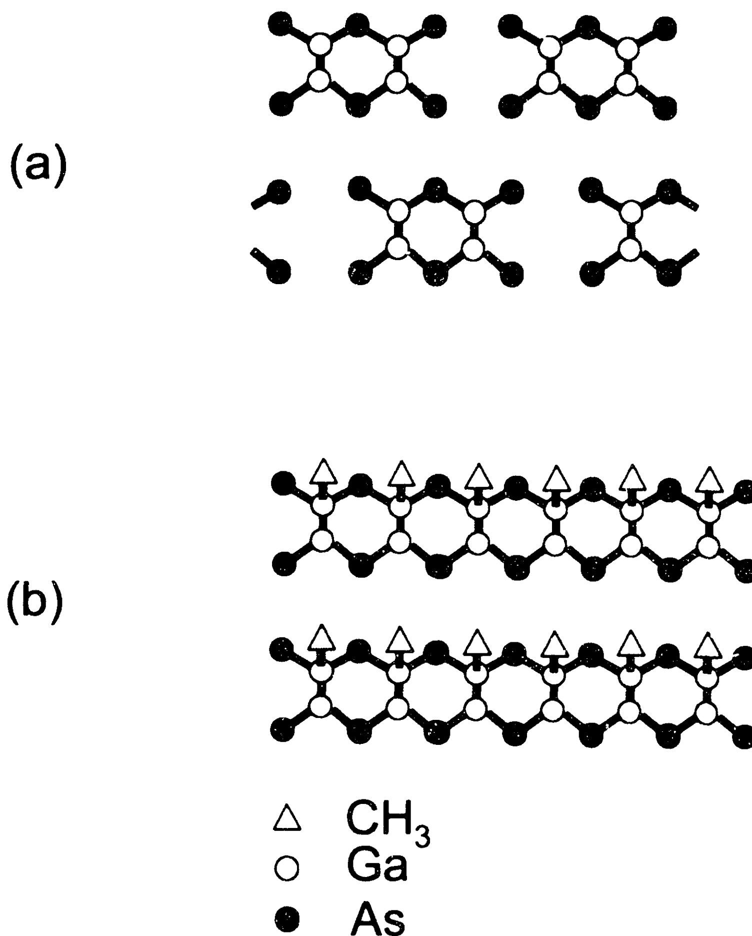

Figure 4. 12: (a) GaAs gallium-rich c(8x2)/(4x2) surface; (b) Methyl covered Ga surface after TMGa adsorption.

Methyl adsorption on the surface stems from the dissociation of trimethylgallium (TMGa). Ga 'holes' exist on the (4×2) surface where there are no Ga atoms on the top surface, corresponding to the missing Ga dimers in Figure 4.12(a). Experimental results[21] indicate that TMGa adsorbs in the Ga 'holes' and dissociates, covering the surface with methyl. This is shown in Figure 4.12(b).

Creighton has found that methyl coverage on the surface is limited to 50%[23] with a (1x2)-CH_3 covered reconstruction. This was confirmed by a (1x2) LEED (low-energy electron diffraction) pattern for this surface. As the methyl groups desorb from the surface, liquid Ga droplets form on the surface and the surface reconstructs back to the (4×2) surface geometry. We have ignored the formation of Ga droplets and have represented the surface after all methyl groups have desorbed.

The experimental data by Creighton for TPD of methyl of Ga-rich GaAs is shown in Figure 4.13.

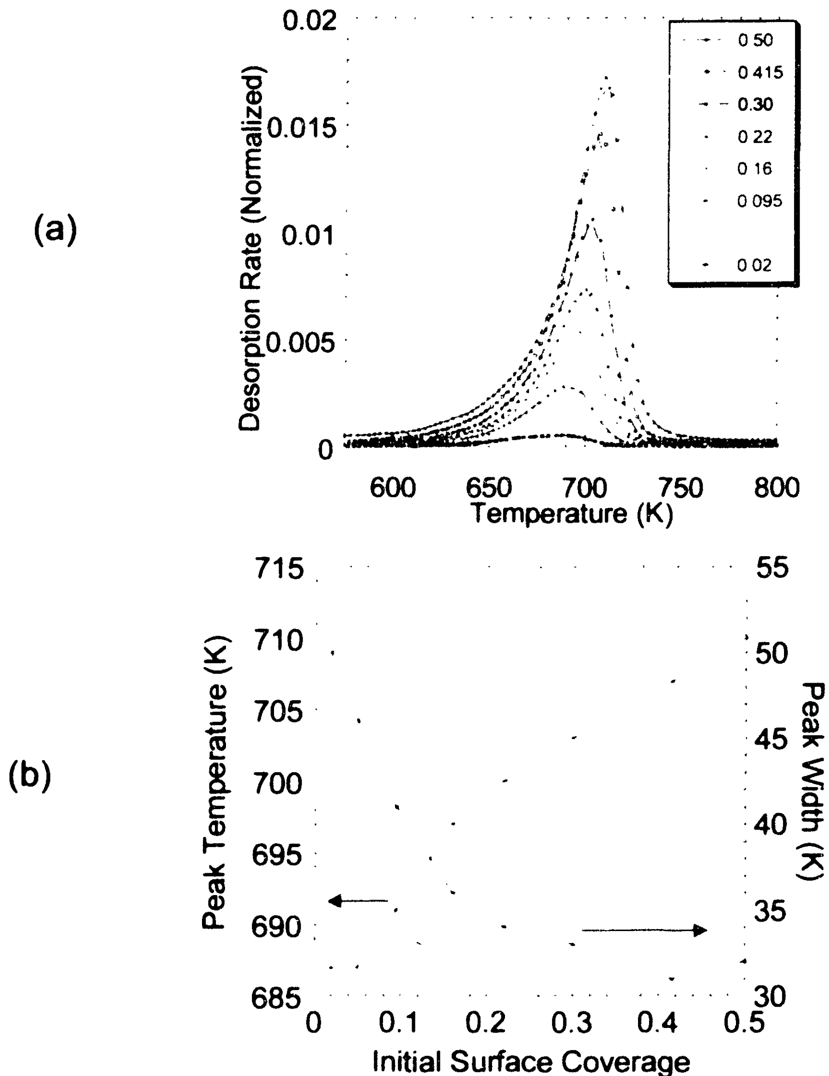

Figure 4. 13: (a) Experimental TPD spectra of methyl off Ga-rich GaAs[21], the legend is the initial surface coverage for each spectra; (b) Experimental peak temperatures and peak widths as a function of initial coverage of methyl.

The larger curves correspond to increasing initial surface coverage of methyl. Figure 4.14 shows how peak temperatures and peak widths change with increasing initial surface coverage of methyl.

Peak temperatures increase with increasing coverage and peak widths narrow with increasing coverage. These results suggest that a variety of surface relaxation processes may be taking place as methyls desorb from the surface. Some hypotheses for the surface dynamics described by the TPD data is summarized in Table 4.1.

Table 4. 1: Possible physical pathways explaining experimental TPD data

Experimental Observation	Possible Physical Explanation
Increase in peak temperature with increasing coverage	Attractive adsorbate interactions
Narrowness of desorption peaks	Formation of 2-D islands Multiple binding sites Surface reconstruction occurring during desorption

Simple Arrhenius type desorption mechanisms might not be sufficient to describe the dynamics of desorption. Thus, KMC methods are used to explore possible desorption mechanisms that can be consistent with the experimental data.

4.5 Model Results

Using the methodology outlined above, the TPD curves for methyl desorption of Ga rich GaAs is studied. Mechanisms are developed in order to understand the experimental data. In Section 4.5.1, the effects of each of the possible parameter changes are shown through changes in the TPD spectra. In Section 4.5.2, non-linear optimization techniques are used to best fit parameters in differing mechanisms. The point is to find plausible mechanisms that fit the data that can bring details of the mechanism out for further simulation and experimentation.

4.5.1 Mechanism Effects

The effects of changes in each of the parameter space are examined. The base case parameters are shown in Table 4.2.

Table 4. 2: Base case parameters for TPD simulations

Transition	Barrier (kcal)
Desorption	42
Nearest Neighbor for Desorption	2
Diffusion	39.2
Nearest Neighbor for Diffusion	2

The adjustable parameters include the desorption barrier, the nearest-neighbor interactions for the desorption barrier, the diffusion barrier, and the nearest-neighbor interactions that affect the diffusion barrier. Figure 4.14 shows the simulated spectra.

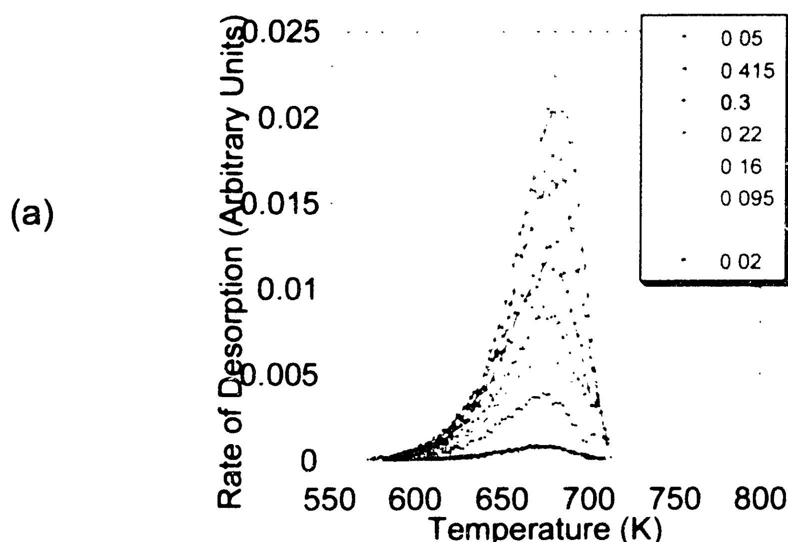

Figure 4. 14: (a) Simulated TPD spectra of methyl off Ga-rich GaAs using parameters in Table 4.2.

The pre-exponential for desorption and diffusion barriers are fixed at 1×10^{13}. The pre-exponential could also be considered as an adjustable parameter, but due to the large correlation between the pre-exponential and the barrier (typically called the compensation effect), the pre-exponential and the barrier are not independent variables. Table 4.3 shows the possible changes to the base case parameters.

Table 4. 3: Parameter changes to base case studied

Parameter	Changes from base case
Desorption Barrier	40-44 kcal
Diffusion Barrier	30-50 kcal
Nearest Neighbor Barrier	1-4 kcal

4.5.1.1 Desorption Barrier:

The desorption barrier in the model is a representation of the zero coverage desorption energy for a methyl. Using techniques such as the Chan-Aris-Weinberg method, Creighton[21] found that the zero coverage activation energy is 43 +/- 1 kcal. The effect of the desorption barrier is to shift the peak temperature up as the desorption barrier rises. The quantitative effect is shown in Figure 4.15.

(a)

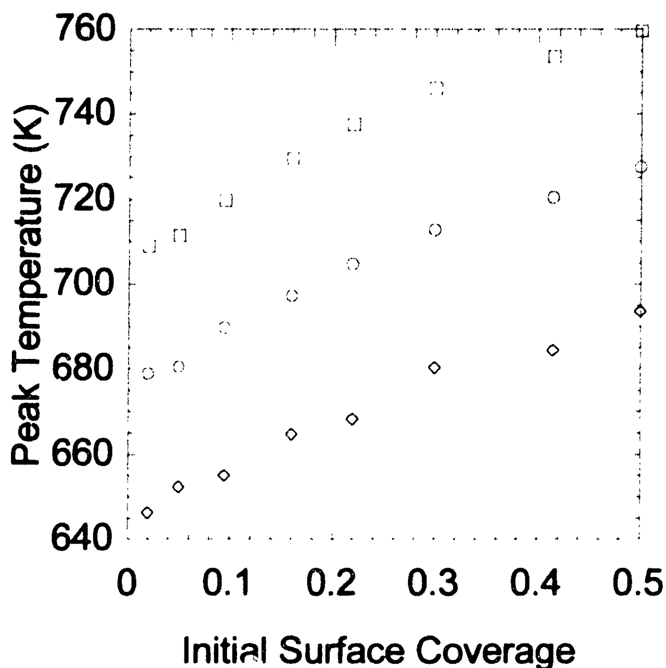

(b)

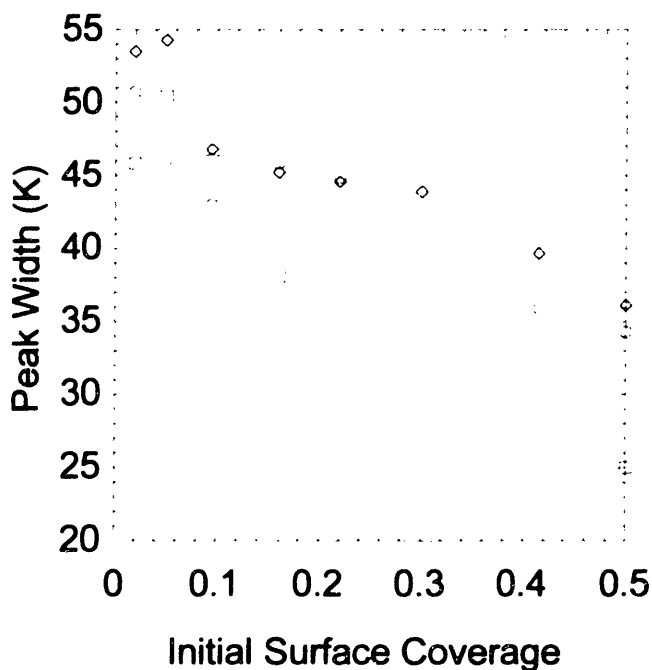

Figure 4. 15: Effect of desorption barrier on (a) peak temperature and (b) peak width; (○) 42 kcal desorption barrier, (□) 44 kcal desorption barrier, (◆) 40 kcal desorption barrier.

As shown, the peak temperature rises as the desorption barrier is increased, but the shape of the curve remains the same. It is very difficult to determine an exact peak width in

both experimental results and simulations, as the peak width is dependent on measuring the exact peak temperature and rate. As shown by Figures 4.7 and 4.8, there is error in computing the rate at the peak temperature. This error magnifies the uncertainty in computing the width at half maximum. The shape of the curves suggests that the desorption barrier does not affect the peak widths.

4.5.1.2 Diffusion Barrier:

The diffusion barrier is a representation of how fast adsorbates can move around on the surface. This is especially important when there is a nearest-neighbor energy for desorption. Fast diffusion increases the chances of island formation, which in turn makes all the effective desorption barriers closer to the same value. This creates a sharpening of the peak (the peak width decreases), as shown in Figure 4.16.

(a)

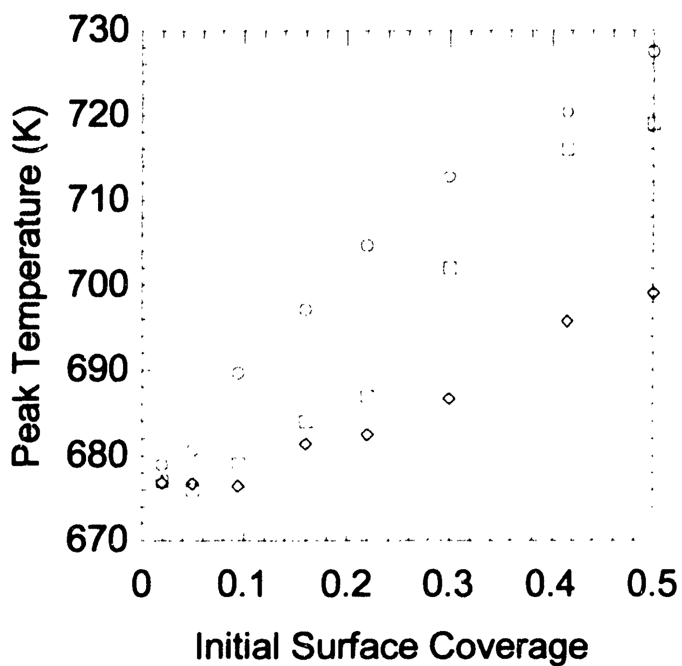

(b)

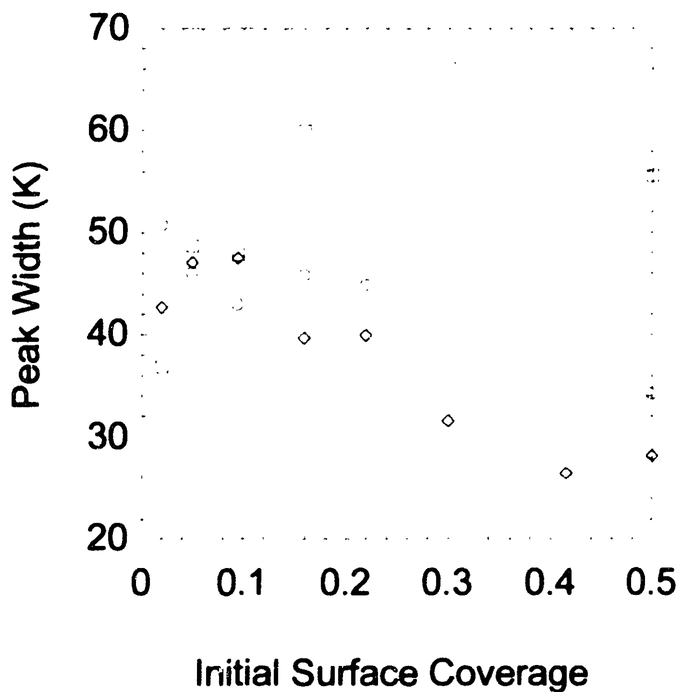

Figure 4. 16: Effect of diffusion barrier on (a) peak temperature and (b) peak width; (○) 39.2 kcal diffusion barrier, (□) 50 kcal diffusion barrier, (◆) 30 kcal diffusion barrier.

The peak temperatures are all similar, even with changing diffusion rate. The peak width for high diffusion rates shows a maximum at intermediate coverage. In this case, the peak width is a measure of the spread of the nearest neighbor barrier. At low coverage, most of the adsorbates do not have a nearest neighbor and diffusion cannot bring the adsorbates closer together. At high temperatures, many of the adsorbates have nearest neighbors, and diffusion does not split up the pairs. At intermediate coverage, there are half of the adsorbates, which have neighbors, and half that do not. This creates a wide distribution of nearest-neighbor interactions, and broadens the peak width.

4.5.1.3 Nearest Neighbor Parameter:

The nearest neighbor parameter is a measure of the lateral attraction between adsorbates on the surface. This attraction can be a measure of the stabilizing force that certain atomic configurations have on the surface. Attractive lateral interactions show up through increasing peak temperatures with increasing initial surface coverage. As the initial surface coverage increases, there is a greater chance of islands, and any attractive interactions will show through an increase in the effective desorption barrier for that spectra. The effect of increasing lateral interactions is shown in Figure 4.17.

(a)

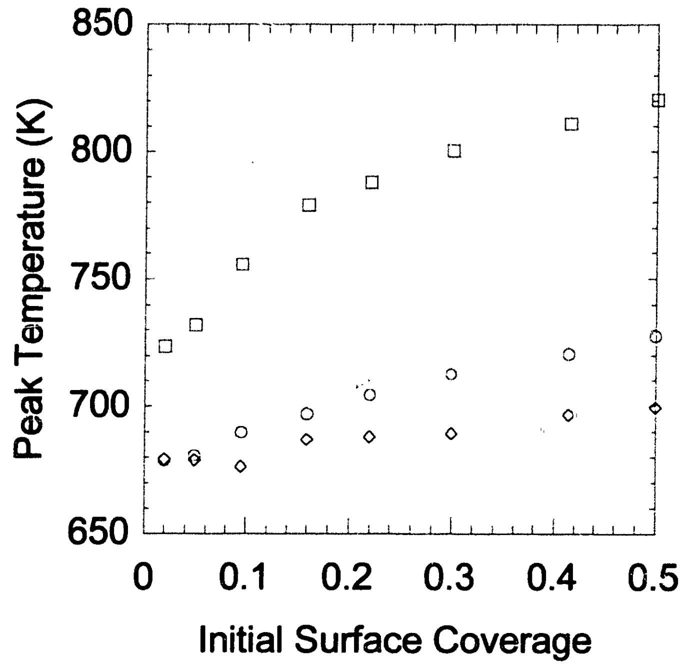

(b)

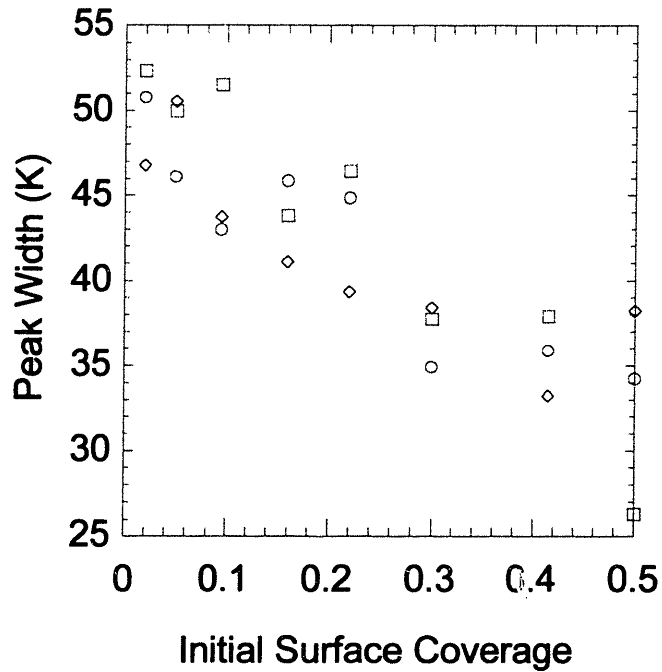

Figure 4. 17: Effect of nearest-neighbor barrier on (a) peak temperature and (b) peak width; (O) 2 kcal barrier, (□) 4 kcal barrier, (◆) 1 kcal barrier.

The peak temperature increases with increasing nearest neighbor barrier, and the slope of the peak temperature increases with respect to surface coverage as the barrier increases. At increasing coverage, the number of interactions increases, and in concert with the nearest neighbor barrier increases the effective nearest neighbor barrier. The peak widths maintain the same shape, following the same general downward trend with increasing coverage.

4.5.1.4 Surface Reconstructions:

Surface reconstructions play an important role in the dynamics of surfaces. Creighton has determined through LEED experiments that methyl on GaAs form a (1x2)-CH_3 reconstruction on the surface[23]. This suggests that there are attractive nearest neighbor energies between methyls on different dimers, while there are repulsive nearest neighbor interactions between methyls on the same dimer (as shown in Figure 4.7(b)). This is included in the nearest neighbor interactions by including a repulsive 2 kcal barrier to methyls on the same dimer. The resulting spectra along with the base case results are shown in Figure 4.18.

(a)

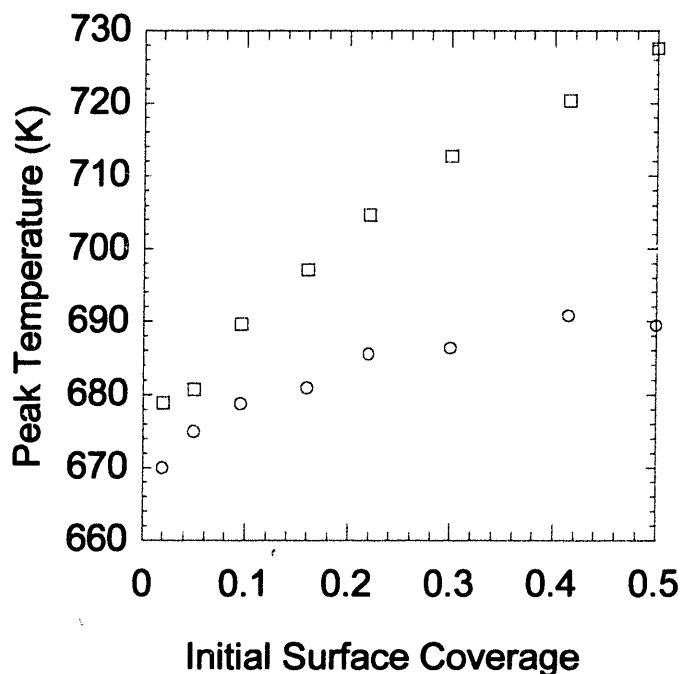

(b)

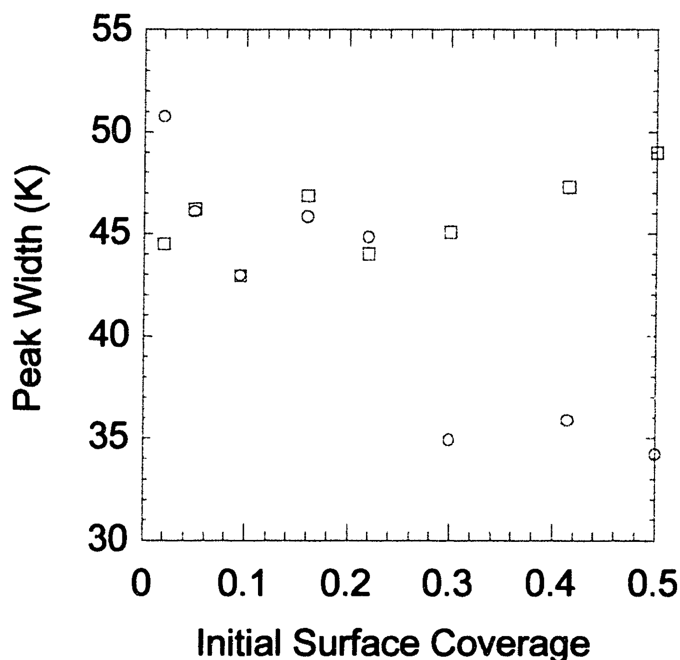

Figure 4. 18: Effect of surface reconstructions on (a) peak temperature and (b) peak width; (O) base case model, (□) reconstruction model with a repulsive 2 kcal barrier to methyls on the same dimer.

The peak temperature does not increase as quickly with increasing coverage in the reconstruction model due to the attractive and repulsive interactions at higher coverage. The peak width is interesting, as it remains level over the entire coverage range. The

distribution of interactions is broad throughout the coverage range. Both attractive and repulsive interactions are felt in both low coverage and high coverage regimes.

4.5.2 Optimization Results

Optimization routines were used in order to determine optimal parameters for a given mechanism as outlined in Section 4.3.3. This procedure does not guarantee that the mechanism is the 'correct' one in comparison to the physics of the surface. This procedure does give a procedure to extract surface barriers from experimental data, given a mechanism.

Optimization was initially done with two floating parameters, the desorption barrier and the nearest neighbor interaction barrier. Since the diffusion barrier is the biggest unknown factor in the model, three separate runs were done at high, low, and comparable diffusion barriers to the desorption barrier in order to determine the effect of diffusion on the spectra. Plots of the tested barrier for the three cases are shown in Figure 4.19 and the results are tabulated in Table 4.4.

Table 4. 4 :Optimized barriers from 2 parameter optimization using fixed diffusion barriers

Desorption Barrier (kcal)	Nearest Neighbor Barrier (kcal)	Diffusion Barrier (kcal)
41.68	1.68	39.2
42.51	2.51	20
42.3	1.3	80

(a)

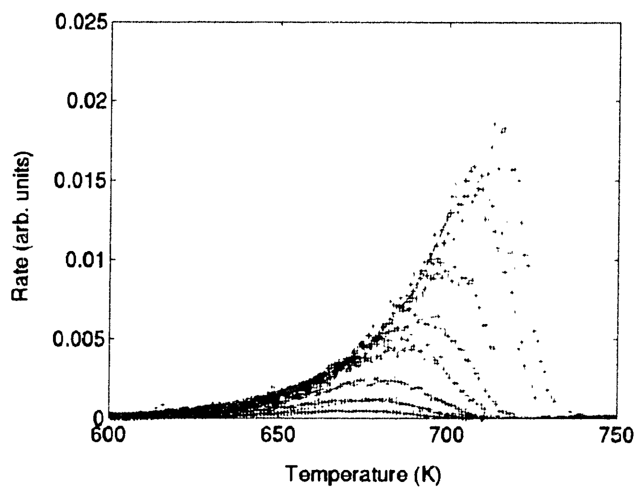

(b)

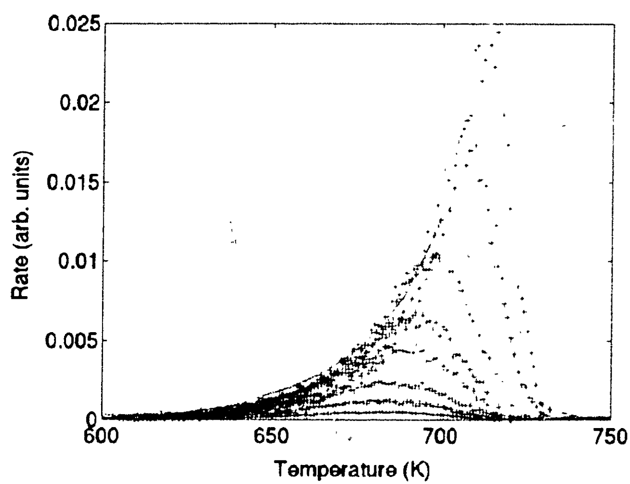

(c)

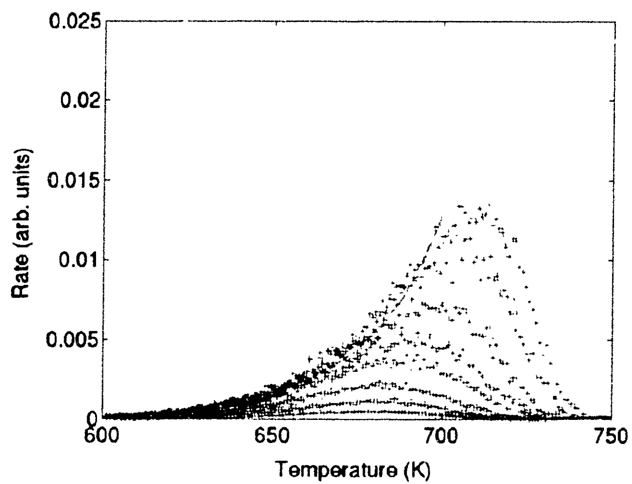

Figure 4. 19: TPD spectra from optimized desorption and nearest-neighbor barriers (a) 39.2 kcal diffusion barrier, (b) 20 kcal diffusion barrier, (c) 80 kcal diffusion barrier. (blue + is simulated and red light line is experimental)

The desorption barriers are fairly consistent over the three optimization runs. The desorption barrier is the zero coverage limit for methyl desorption, so it is not surprising that the nearest neighbor barriers or diffusion barriers affect the value of the desorption barrier. The other two parameters seem to be correlated; with an increasing diffusion barrier, there is a decrease in the nearest neighbor parameter. The peak shift with increasing coverage can be modeled by an attractive nearest neighbor barrier. With fast diffusion, all the adsorbates can cluster into islands, creating a single 'effective' desorption barrier. Slowing diffusion decreases the effect, and the optimized nearest-neighbor barrier broadens the 'effective' desorption barrier . This is seen in Figure 4.19 as the fast diffusion plot has very narrow peak widths compared to experimental (all the adsorbates have the same desorption barrier which means that all the adsorbates had the same local environment), and the slow diffusion plot has a much broader peak widths. Plots of the optimization results are shown in Figure 4.20.

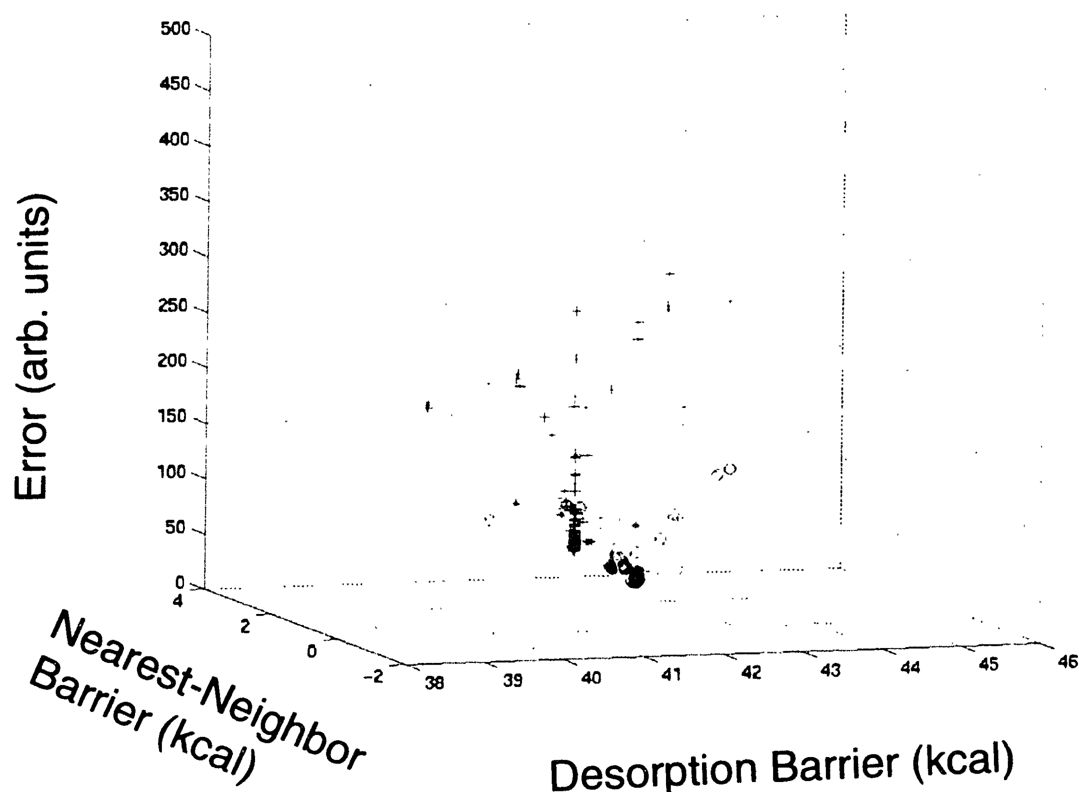

Figure 4. 20: Optimized desorption and nearest-neighbor barriers (+) 39.2 kcal diffusion barrier, (o) 20 kcal diffusion barrier, (*) 80 kcal diffusion barrier.

There is a constant desorption rate, regardless of the starting diffusion barrier. Also, for each diffusion barrier, there seems to be a clear local minima.

To quantify the correlation between parameters, a series of simulations were run in a grid around the desorption and nearest-neighbor barriers at a diffusion barrier of 39.2 kcal. A surface and contour plot of the error is shown in Figure 4.21(a).

(a)

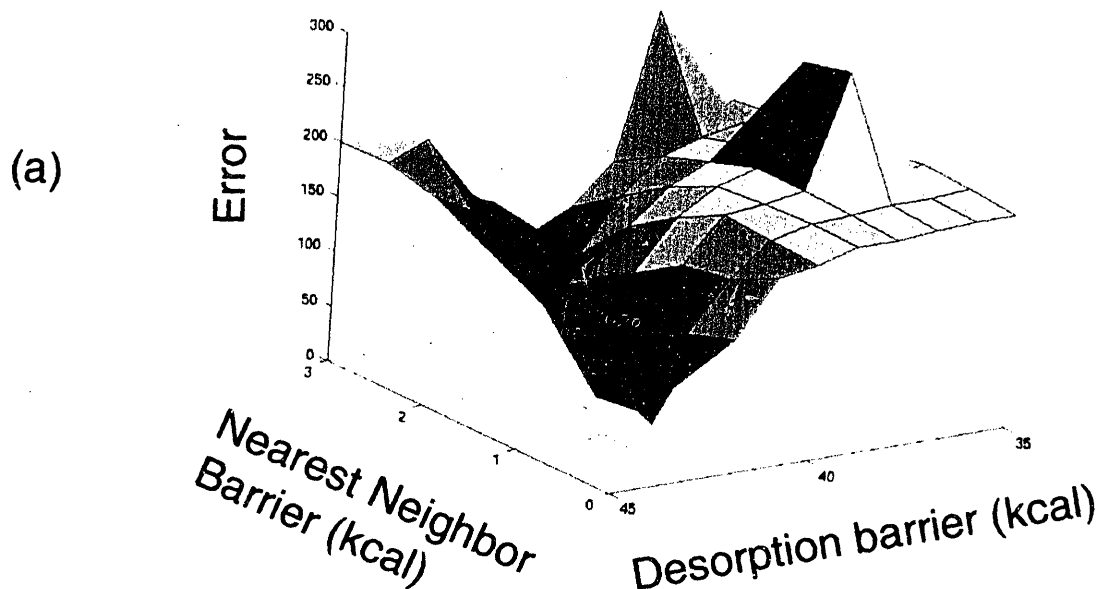

(b)

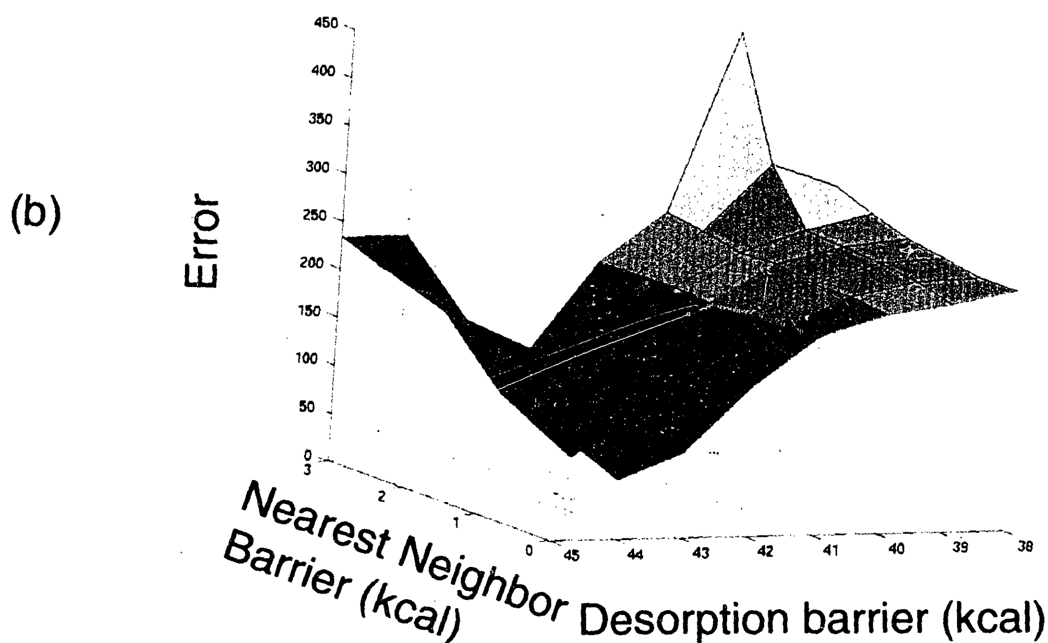

Figure 4. 21: Surface and contour plot of the error between experimental and simulated spectra at (a) 39.2 kcal diffusion barrier, (b) 20 kcal diffusion barrier

Shown is a valley where the computed error is at a minimum that ranges from 40 – 44 kcal and a nearest neighbor barrier ranging from 1-3 kcal. This valley shows the correlation between the desorption and nearest neighbor barriers at this level of the

diffusion barrier. Another valley is seen in Figure 4.21(b) where the diffusion barrier was fixed at 20 kcal. Examining Figure 4.19(a), the correlation between these parameters is due to the computation of the error. The ranges of desorption and nearest-neighbor barriers fit part of the spectra of initial coverages, but not all the spectra. This correlation can be reduced if the diffusion barrier is simultaneously changed.

Similar results were achieved using three floating parameters, desorption, nearest-neighbor, and diffusion barriers. Plots of the resulting spectra are shown in Figure 4.22 for an initial guess of 38 kcal for the diffusion barrier. In this case, the optimization routine searched for local error minima around the initial diffusion rate and found a local optimum at a desorption barrier of 42.69 kcal, a nearest-neighbor barrier of 1.06 kcal, and a diffusion barrier of 38.76 kcal.

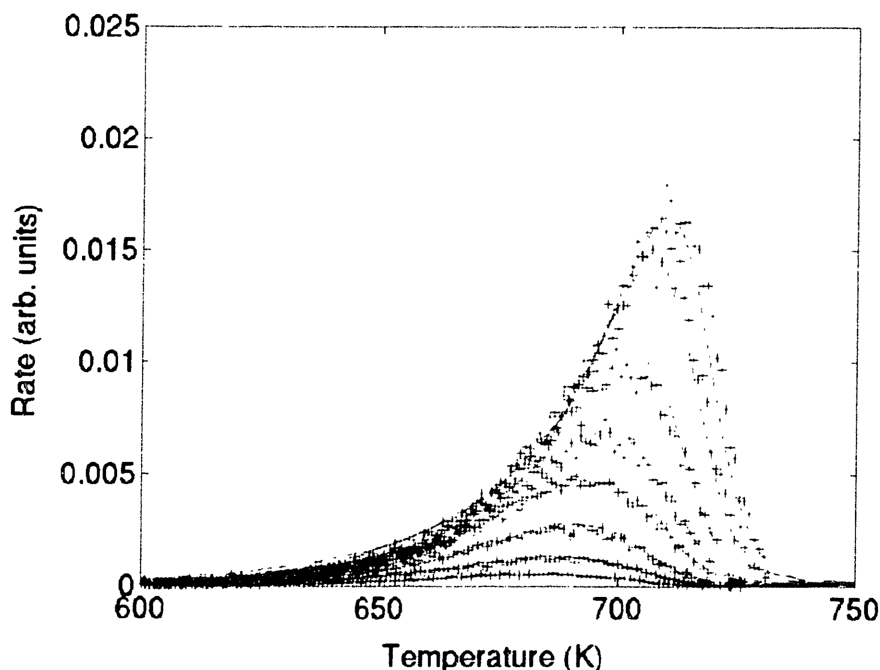

Figure 4. 22: Experimental (red line) and simulated (dark blue +) TPD spectra

4.6 Conclusions

In this section, a methodology was developed to study temperature programmed desorption using KMC simulations. It was shown that multiple modeling methods must

be used, depending on the physics of the surface. For systems where the diffusion rate is slower than or on the same order of the desorption barrier, the diffusion step must be explicitly included in the model. On the other extreme, if the diffusion rate is much smaller than the desorption rate, than a pseudo-equilibrium approximation must be used on the surface in order to complete the simulation in reasonable computational time. A ratio of 1000 for the diffusion to the desorption rate was found to approximate the transition between the two models. An optimization methodology was developed in order to 'fit' entire surface mechanisms to experimental data. This is especially important where the spectra cannot be fitted to typical Arrhenius desorption kinetics. A case study was performed to examine the desorption of methyl from Ga-rich GaAs(100) reconstructions. Effects of changing each of the parameters on the overall spectra were shown. The desorption barrier fixed the initial peak temperature. The nearest-neighbor parameter determined the shift in the peak temperature with increasing initial coverage. The diffusion rate determined the impact of the nearest neighbor interactions. At high diffusion rates, islands formed on the surface increasing the effect of the nearest neighbor interactions, while low diffusion rates blunted the effect. The peak width was determined by a combination of the diffusion and nearest-neighbor barriers. Narrow widths resulted from the adsorbates all having the 'same' local environment, while broader widths came from a distribution of local environments. In this case, the local environment of an adatom corresponded to the number of nearest-neighbors of the average adatom. Finally, optimization methods were used to test different mechanisms. It was found that methyl desorption has a diffusion barrier that is comparable to the desorption barrier with estimated desorption barrier of 41.77 kcal, diffusion barrier of 38.76 kcal, and nearest-neighbor barrier of 1.06 kcal. This section shows the utility of KMC simulations in interpreting experimental data, by running analogous simulations at the exact experimental conditions and testing possible mechanism.

Bibliography:

1. Redhead, P.A., *Thermal desorption of gases.* Vacuum, 1962. **12**: p. 203-211.
2. King, D.A., *Thermal desorption from metal surfaces: A Review.* Surface Sciences, 1975. **47**: p. 384-402.
3. Jong, A.M.d. and J.W. Niemantsverdriet, *Thermal desorption analysis: Comparative test of ten commonly applied procedures.* Surface Science, 1990. **233**: p. 355-365.
4. Seebauer, E.G., *Quantitative extraction of continous distributions of energy states and pre-exponential factors from thermal desorption spectra.* Surface Science, 1994. **316**: p. 391-405.
5. Russell, N.M. and J.G. Ekerdt, *Nonlinear parameter estimation technique for kinetic analysis of thermal desorption data.* Surface Science, 1996. **364**: p. 199-218.
6. Houle, F.A. and W.D. Hinsberg, *Stochastic simulations of temperature programmed desorption kinetics.* Surface Science, 1995. **339**: p. 329.
7. Lombardo, S.J. and A.T. Bell, *A Monte Carlo model for the simulation of temperature-programmed desorption spectra.* Surface Science, 1988. **206**: p. 101-123.
8. Sales, J.L. and G. Zgrablich, *Thermal desorption of interacting molecules from heterogeneous surfaces: application to CO desorption from MgO.* Surface Science, 1987. **187**: p. 1-21.
9. Sales, J.L. and G. Zgrablich, *Thermal desorption of interacting molecules from heterogeneous surfaces.* Phys. Rev. B, 1987. **35**: p. 9520-9528.
10. Sales, J.L., G. Zgrablich and V.P. Zhadonov, *Lattice-Gas model for calculating thermal desorption spectra: Comparison between analytical and Monte Carlo results.* Surface Science, 1988. **210**: p. 208-214.
11. Fichthorn, K.A. and W.H. Weinberg, *Theoretical foundations of dynamical Monte Carlo simulations.* J. Chem. Phys., 1991. **95**: p. 1090-1096.
12. Meng, B. and W.H. Weinberg, *Monte Carlo simulations of temperature programmed desorption.* J. Chem. Phys., 1994. **100**: p. 5280.
13. Weinketz, S., *Dynamic Monte Carlo description of thermal desorption processes.* J. Chem. Phys., 1994. **2**: p. 1632-1637.
14. Weinketz, S. and G.G. Cabrera, *Adsorbate order-disorder effects on recombinative thermal desorption: equivalence between dynamic Monte Carlo simulations and self-consistent cluster approximations.* J. Chem. Phys,, 1997. **106**: p. 1620-1627.
15. Meng, B. and W.H. Weinberg, *Theoretical and simulation studies of recombinative temperature programmed desorption.* J. Chem. Phys., 1994. **102**: p. 1003-1013.
16. Jansen, A.P.J., *Monte Carlo study of temperature-programmed desorption spectra with attractive lateral interactions.* Phys. Rev. B, 1995. **52**: p. 5400-5403.
17. Meng, B. and W.H. Weinberg, *Non-equilibrium effects on thermal desorption spectra.* Surface Science, 1997. **374**: p. 443-453.

18. Seebauer, E.G. and C.E. Allen, *Estimating surface diffusion coefficients.* Progess in Surface Science, 1995. **49**: p. 265-330.
19. Geist, A., A. Beguelin, J. Dongarra, W. Jiang, R. Manchek and V. Sunderam, *PVM: Parallel Virtual Machine, A User's Guide and Tutorial for Networked Parallel Computing*. 1994, Cambridge, MA: MIT Press.
20. Press, W.H., S.A. Teukolsky, W.T. Vetterling and B.P. Flannery, *Numerical Recipes in C: The Art of Scientific Computing.* 1992, New York: Cambridge University Press.
21. Creighton, J.R., *Chemisorption and decomposition of trimethylgallium on GaAs(100).* Surface Science, 1990. **234**: p. 287-307.
22. Biegelsen, D.K., R.D. Bringans, J.E. Northrup and L.E. Swartz, *Surface reconstructions of GaAs(100) observed by scanning tunneling microscopy.* Physical Review B, 1990. **41**: p. 5701-5706.
23. Creighton, J.R., *Accounting for stoichiometry changes on compund semiconductor surfaces.* Journal of Crystal Growth, 1995. **147**: p. 64-73.

Chapter 5: Kinetic Monte Carlo Models for Growth Processes

The development of Kinetic Monte Carlo (KMC) models of surface morphology during GaAs growth is explored. In Section 5.1, the study of thin film growth is motivated. Section 5.2 is a review of important experimental studies used to elucidate pathways for thin film growth of GaAs. Different models for thin film growth are described in Section 5.3. New models developed to understand MOVPE growth are contained in Section 5.4. These new models build upon older models and add MOVPE specific physics. The differences between MOVPE and other thin film growth methods are also developed. Section 5.5 concludes the chapter with a wrap-up of the KMC model and its further applications to other systems.

5.1 Introduction

Thin film growth is an important process in varied applications such as semiconductor processing and coating processes. Morphology evolution during thin film growth is especially important when fabricating multi-layer semiconductor devices, as each the morphology of each successive layer is important to the electrical properties of the entire device. Reactor conditions greatly affect the morphology. Shown in Figures 5.1 and 5.2 are Atomic Force Microscopy (AFM) images of GaAs grown under different reactor conditions[1].

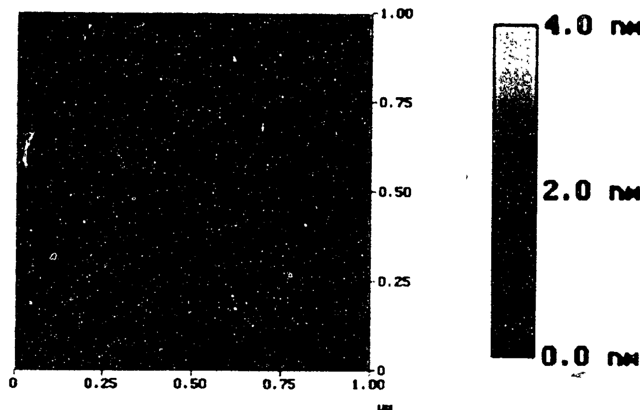

Figure 5. 1: AFM image of GaAs(100) after growth. The surface consists of a series of terraces with a height variation of less than 4 nm. (T.F. Kuech, Univ. of Wisconsin)

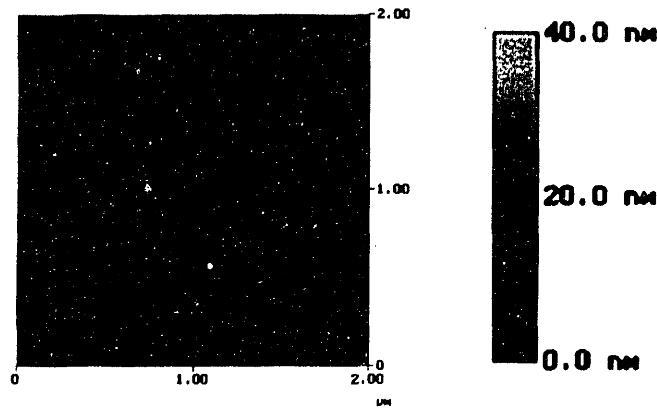

Figure 5. 2: AFM image of GaAs(100) after growth. The surface consists of mounds and large islands on the surface with a height variation of more than 20 nm. (T.F. Kuech, Univ. of Wisconsin)

Notice the order of magnitude difference in surface heights. These large differences in surface smoothness can impact the electrical properties of multi-layer devices, especially in the production of such devices.

In modeling the MOVPE process, an important step is the prediction of surface morphology given reactor conditions. In order to develop such a model, the following steps were undertaken:

- A review of experimental work that focused on understanding surface growth processes. Experimental work focused on surface processes during MOVPE growth is especially difficult as many surface science techniques have been optimized for use under vacuum conditions.
- Models of surface morphology evolution is reviewed in order to understand the benefits and limitations of modeling techniques ranging from continuum to quantum mechanic methods.
- A new KMC model is developed in order to study the growth surface under MOVPE conditions. This model is then tested using experimental grazing incidence x-ray scattering and reflection difference spectrometry results.

The surface model for MOVPE growth has limitations, the main one being that there is no easy way to obtain the flux of species to the surface (a needed input into the model). The net consumption of species can be computed, but only if the needed input of the flux

of species is given. This leads directly into the next chapter where linking methodologies between surface and reactor scale models will be discussed.

5.2 Experimental GaAs

Experimental studies of GaAs can be grouped into three major categories that are of interest in understanding thin film growth:

- Vacuum studies of the surface morphology before and after growth.
- Surface science studies of reactions on the surface (typically done under vacuum or at extremely low pressures).
- In-situ monitors of the surface during growth and general growth studies.

Each of these types of experimental studies can give a different view on the physics occurring during growth. Studies done under vacuum can be very sensitive to the growth morphology and can pick up reaction barriers for select surface reactions. On the other hand, vacuum studies may not be an accurate representation of the surface under growth conditions (high pressures and temperatures). In-situ studies are necessary to understand processes occurring during growth, but many sensitive surface science techniques cannot be used under the harsh environment (high pressures and temperatures) of MOVPE growth.

Another interesting area of research is the comparison of MOVPE growth of GaAs to MBE growth. Due to the different surface reconstructions on a MOVPE grown and MBE grown surface, the surface processes are very different. This leads to different surface morphologies from MOVPE and MBE grown films.

5.2.1 Surface Morphology Before and After Growth

The GaAs surface exhibits many surface reconstructions, depending on the atmosphere and temperature of the exposed GaAs surface. The different surface reconstructions play an important role in the growth of thin films, as each surface reconstruction has a different stochiometry of As to Ga adatoms on the surface, as well as different surface properties. An example of a c(4x4) reconstruction[2] is shown in Figure 5.3.

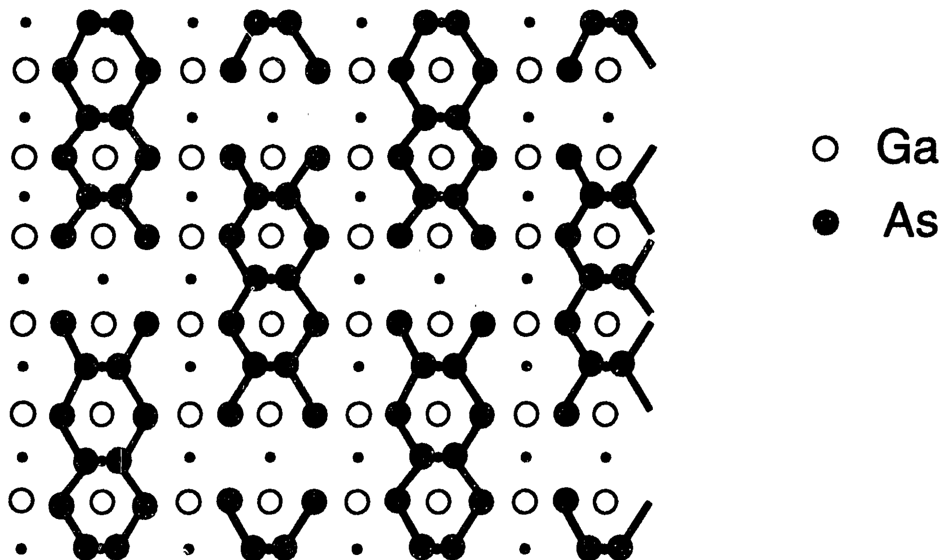

Figure 5. 3: GaAs c(4x4) reconstructed surface. The surface is covered with As dimers.

As will be discussed, a disordered version of the c(4x4) reconstruction has been found to be the surface reconstruction during MOVPE growth[3]. A c(4x4) reconstructed surface has an As coverage of 1.75 monolayers. MBE growth operating conditions produce a β(2x4) or a β2(2x4) reconstruction as shown in Figure 5.4.

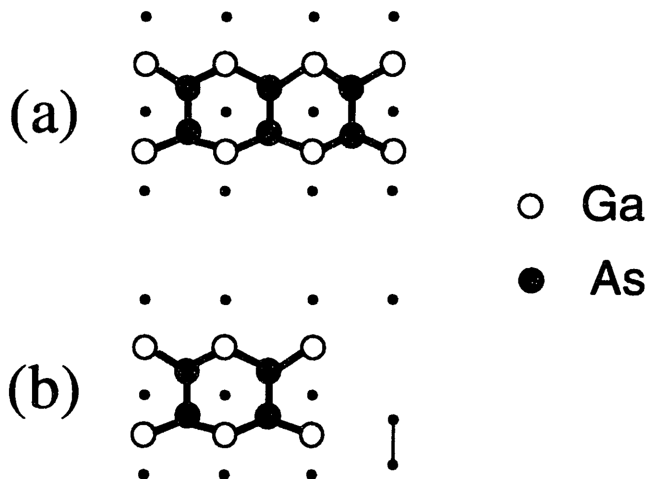

Figure 5. 4: GaAs reconstructed surface; (a) β(2x4), (b) β2(2x4)

These reconstructions only have an As coverage of 0.5-0.75 monolayers. As expected, with increasing As flux to the surface, the reconstruction can change from β(2x4) to c(4x4). The increased As flux in MOVPE systems creates the disordered c(4x4) reconstruction during growth. A thermodynamic picture of GaAs surface phases is given

in Northrup and Froyen[4], who calculated the stability of different reconstructions (energy of the surface) as a function of the chemical potentials of Ga and As.

Two groups, Kasu and Kobashyi[5-7] and Hicks *et al.*[8-11] have grown GaAs using MOVPE and then tried to 'freeze' the surface by stopping growth and cooling the surface at a rapid rate. Then both groups would transfer the samples into a vacuum chamber where a scanning tunneling microscope (STM) is used to examine the morphology of the MOVPE grown film. The fast quenching of the wafer is supposed to freeze the morphology of the surface as to represent the surface during growth. There is great difficulty in accomplishing a quick quench, and the surface morphology during the STM is probably representative of a slightly annealed MOVPE grown surface. Nevertheless, these studies do provide insight into the surface morphology during growth.

Kasu and Kobayashi [5-7] computed the number density of two-dimensional islands on the surface from the STM pictures at different operating conditions. They found the 2D nuclei extend in the [110] direction, which is opposite of MBE growth. It is hypothesized that the surface reconstruction during MOVPE growth plays an important role in this difference. The anisotropy of the islands range from 2.2 at an operating temperature of 530 ° C to 1.3 at 650 ° C. The work was extended in the observation of step bunching of GaAs using the same experimental approach[5, 6, 12, 13].

Hicks *et al.*[8-11] determine that the structure of the surface under MOVPE growth is a disordered c(4x4) reconstruction. The disorder is due to CH_x groups attached to free As adatoms on the surface. They annealed the surface at 350 K and regain the ordered c(4x4) reconstruction. Li and Han also find that the (2x4) reconstruction formed after annealing a MOVPE grown film is similar to a (2x4) reconstruction grown by MBE. This is not surprising, as in a clean film of GaAs, the surface reconstruction is based on the last environment seen by the film. Annealing the film under H_2 at high temperatures leaves the film in the same state as an MBE grown film.

Asai studied the anisotropic lateral growth of GaAs[14] This was accomplished by creating a mesa of GaAs on top of a flat substrate. Under varying reactor conditions (As and Ga flux and temperature), the lateral and vertical growth rates were compared. The lateral growth rate was a factor of 3-5 times as fast as the vertical growth rate. This suggests that adatoms hopped down off the mesa and attached to the edge of the mesa. The fastest growth direction occurred in the [110] direction, and the slowest in the $[\bar{1}10]$ direction. The vertical anisotropy depended on reactor conditions, but the horizontal anisotropy is independent of reactor conditions. Increasing the growth temperature decreased both lateral growth rates. While decreasing As pressure, the [110] growth rate decreased, while the $[\bar{1}10]$ remained constant. This suggests that As on the surface blocks kink sites for Ga, but does not cover the surface and block overall growth.

5.2.2 Surface Processes Studied Under Vacuum

Vacuum studies typically try to determine the mechanism and energetics of surface processes. For example, TPD experiments are done in order to determine the energetics of surface desorption. Laser assisted desorption experiments are similar to TPD, but to better simulate growth temperatures a laser is pulsed onto the surface and the species fragments leaving the surface are determined. Other vacuum studies study adsorption behavior by infrared spectroscopy in order to determine adsorption sites of different precursors. All of these techniques are valuable in determining surface energetics, but the applicability toward surfaces undergoing the harsh conditions of MOVPE growth (high temperatures and pressures) must be determined on a case by case basis.

Banse and Creighton [15] examined the desorption behavior of As on the GaAs surface by TPD. The TPD experiment showed 3 distinct peaks that corresponded to As desorption from the overlayer of As, and in two bursts from 1.00-0.75 monolayer of As and 0.75-0.25 monolayer of As. Adamson *et al.*[16]modeled the TPD spectra and developed a model for As uptake into the thin film. For MOVPE modeling, the interesting parameter is the desorption barrier for As_2/As_4 from the overlayer of As, which is estimated to have a 44 kcal barrier.

McCaulley and Donnelly[17-20] have examined the decomposition of triethylgallium (TEGa) and trimethylgallium (TMGa) adsorbed on GaAs surfaces. Their experiments consisted of adsorbing precursor species on clean GaAs surfaces, heating the surface both thermally or by using a laser under ultra-high vacuum, and measuring the products by a mass spectrometer. Both the type and rate of species desorption was determined. Buchan and Yu[21] used a pulsed molecular beam and time-resolved mass spectrometry to study the pyrolysis of TEGa on GaAs(100) and determined that ethyl desorbs from two different surface sites with different activation energies. Due to the compensation effect, the given reaction rates are not very different. Shown in Table 5.1 is a synopsis of the results.

Table 5. 1: Reaction rates of adsorbed species on GaAs(100)

Reaction	Reaction Rate
C_2H_5(adsorbed) → C_2H_5 (g)	5×10^{11} exp (-32 kcal / (RT))[20] 1×10^{13} exp (-37.5 kcal / (RT)) [22]
C_2H_5(adsorbed) → C_2H_5 (g) (from two sites)	5×10^{8} exp (-17.4 kcal / (RT)) 1×10^{9} exp (-23.9 kcal / (RT)) [21]
CH_3(adsorbed) → CH_3 (g)	1×10^{13} exp (-43 kcal / (RT)) [23]

Li *et al.*[24] and Qi *et al.*[25] determined the adsorption sites for As and Ga precursors on the GaAs surface using infrared spectroscopy. Since infrared spectroscopy must be done under vacuum, the precursors are adsorbed onto different surfaces. On the c(2x8) surface, arsine adsorbed at low temperatures onto second layer Ga adatoms and transferred the H to adjacent As sites. Above 438 K, arsine completely decomposed with the desorption of As_2 and H_2. On the (1x6) surface at high temperatures (above 573 K), arsine transformed the surface into the c(2x8) surface. The results suggest that arsine decomposition on Ga dimers lead to As incorporation into the lattice, and arsine decomposition onto second layer Ga adatoms leads to As_2 formation. Ga precursors adsorb in between the As dimer and transfer a CH_x groups to a nearby As on the surface.

5.2.3 In-situ studies

5.2.3.1 Grazing Incidence X-ray Scattering

Grazing Incidence X-ray Scattering (GIXS)[26, 27] has been used to monitor the surface in-situ during MOVPE growth. GIXS is accomplished by using high energy x-rays (typically from a synchrotron source) that enters into a specially designed reactor. The scattering of the x-rays off the growing semiconductor surface is monitored and both the surface reconstructions on the surface, as well as the correlations between larger structures (such as islands on the surface) can be monitored.

The reactor used to monitor the surface during GaAs growth is shown in Figure 5.5[28].

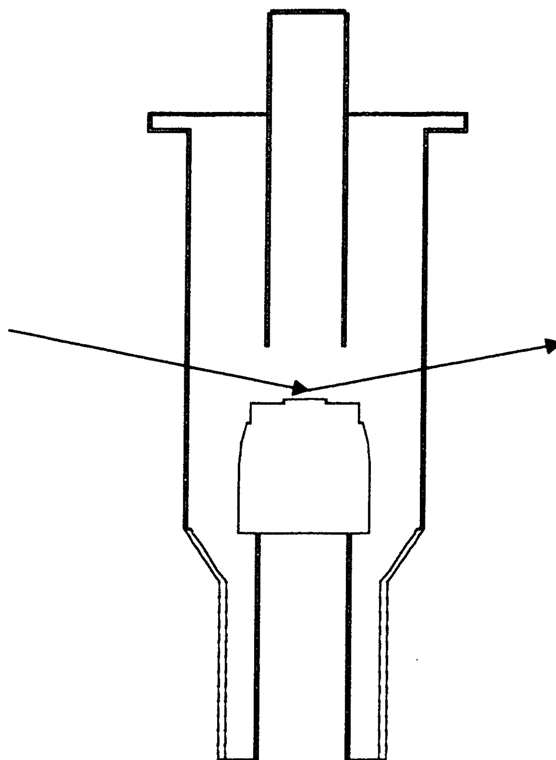

Figure 5. 5: Reactor used for GIXS studies. The reactor consists of two quartz tubes surrounding a heated graphite susceptor. The high energy x-rays enter and exit through a beryllium window near the wafer.

The reactor consists of a smaller quartz tube inside a larger quartz tube. The inner tube has the inlets for the III and V series precursors (typically trimethylgallium or triethylgallium and tertiarybutylarsine) along with a carrier gas (typically hydrogen). The outer tube has an inlet for only carrier gas. This outer tube is used to keep the beryllium

window clean of GaAs deposits in order to allow a portal for the x-rays to enter and exit the reactor.

Experiments were done in order to determine the surface reconstruction during growth[3, 28, 29]. The scattering of the x-rays from the surface can monitor the correlations between atomic positions on the surface. A direct Fourier transform of the scattering data can be used to calculate a Patterson map of the electron density. By using optimization techniques, the positions of atomic species on the surface can be estimated using these Patterson maps. For GaAs, these Patterson maps show that the surface is covered by As dimers during MOVPE growth in a disordered c(4x4) reconstruction.

The scattering can also monitor larger scale structures on the surface. By monitoring the diffraction at a Bragg peak[30], the crystal truncation rods (CTR) can be measured. At the Bragg peak, alternating bilayers of GaAs diffract exactly out of phase, making the scattering extremely sensitive to the top bilayer of the crystal. During layer-by-layer growth, the top bilayer of the GaAs surface becomes half covered with GaAs islands and then the islands coalesce to form the next bilayer. A typical plot is shown in Figure 5.6[31, 32].

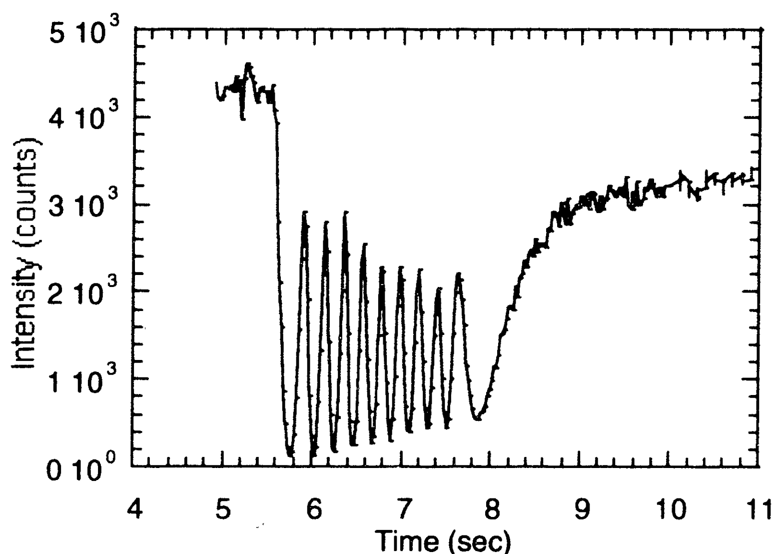

Figure 5. 6: The crystal truncation rods during a typical growth run at a temperature of 580 °C and growth rate of 5 ML/sec.

During this process, the crystal truncation rods oscillate with the roughening and smoothening of the surface. The CTRs disappear during step flow growth on vicinal substrates. The disappearance of CTR oscillations can be used to map out the surface growth mode for given growth conditions (temperature and growth rate). A map of the surface growth modes is shown in Figure 5.7[33].

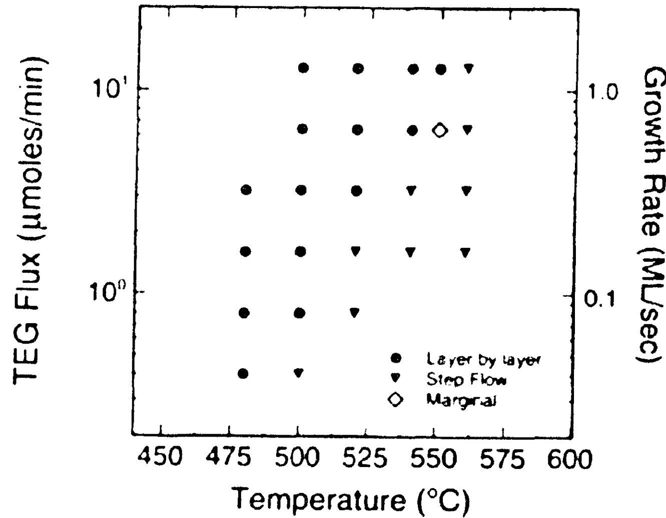

Figure 5. 7: A map of the surface growth modes as a function of flux to the surface and temperature. At high temperatures and low fluxes, step-flow growth is dominant as the adsorbates have high mobility on the surface. At low temperatures and high fluxes, adsorbates have low mobility and island growth is found [33].

The slope of the transition in Figure 5.7 corresponds to an activation energy of 2.7 eV. One of the questions in MOVPE growth is why this transition has such a high activation barrier as compared to MBE growth (which has a barrier computed similarly of 1.58 eV[34]). This high activation barrier has been confirmed in other systems, such as the growth of GaN.

Along with the crystal truncation rods, the off-axis scattering can be monitored. Along with the assumption that the islands are correlated, the off axis scattering can give a measure of the island-island correlation length at half coverage (a minimum in the CTR). This can be measured by monitoring the scattering at a wavevector at positions away from the Bragg peak. A secondary maximum is found that corresponds to the correlation length between islands at half coverage. By monitoring the island-island correlation length as a function of temperature and growth rate, the growth mechanism for MOVPE

can be compared to theoretical models of island growth. The island-island correlation lengths as a function of temperature and growth rate are shown in Figure 5.8[35, 36].

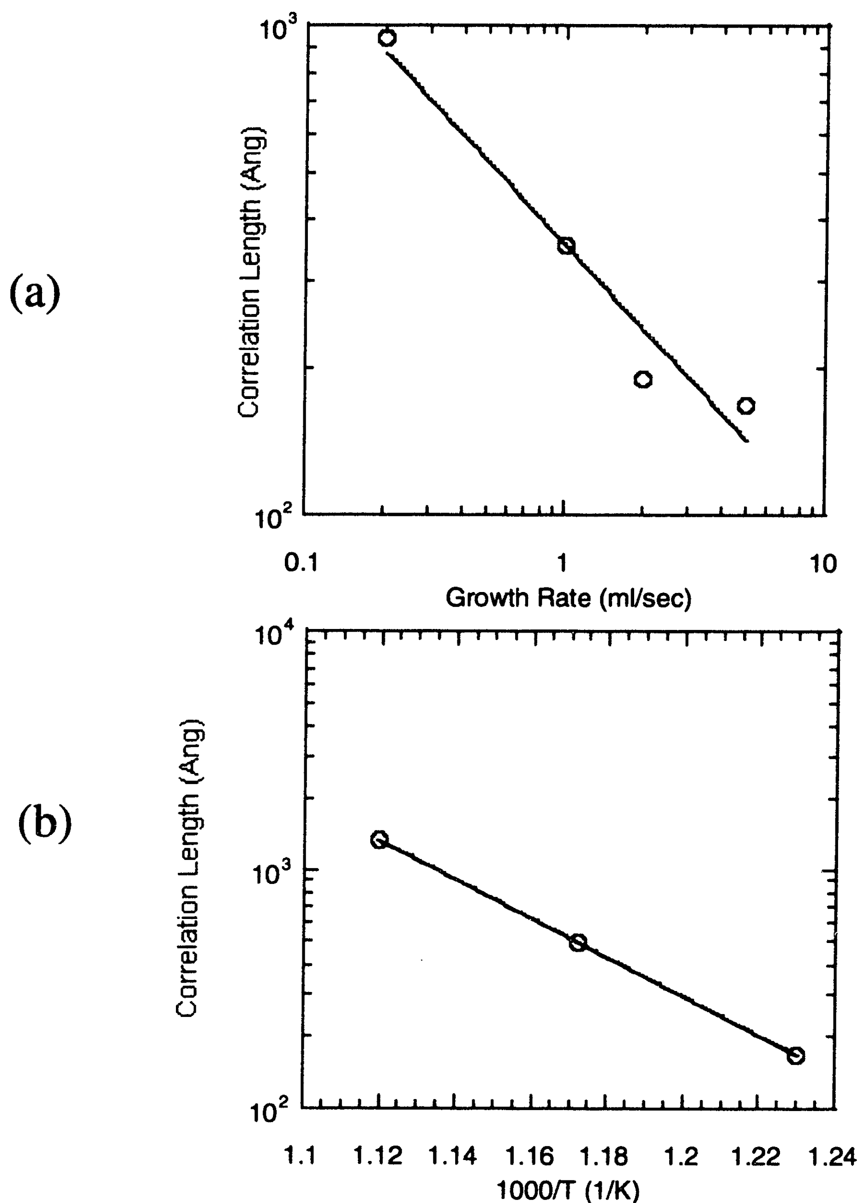

Figure 5. 8: (a) Correlation length as a function of growth rate at a temperature of 813 K; (b) Correlation length as a function of temperature at a growth rate of 5 ML/sec; The correlation length is derived from the diffuse x-ray scattering from the surface.

Thus, the GIXS data represents a method to study the long range order of the surface from an analysis of the growing islands on the surface.

5.2.3.2 Reflection Difference Spectroscopy

Reflection Difference Spectroscopy (RDS) or Reflection Anisotropy Spectroscopy (RAS) is an optical, in-situ technique to monitor surfaces during MOVPE growth. The groups of Aspnes, *et al.*[37-40] and Richter, *et al.*[41, 42] have pioneered this technique to study MOVPE surfaces during growth. In a typical RDS experiment, the difference between the normal incidence reflectance of light polarized parallel and perpendicular to a principal crystallographic axis in the plane of the crystal is measured as a function of time, photon energy, and surface conditions. The results are extremely sensitive to both the chemical and structural state of the surface. Since RDS is an optical probe, it can be used in the harsh environments in MOVPE processing.

RDS has been used to study the surface reconstruction during MOVPE growth. Kamiya *et al.*[43] has characterized different surface reconstructions on GaAs by distinct RDS spectrum. By matching the RDS spectrum with one that has been observed in UHV with a known surface reconstruction, Ploska *et al.*[44] and Wassermeier *et al.*[45] observed a disordered c(4x4) reconstruction covers the GaAs surface under MOVPE conditions. Certain photon energies have been found to be extremely sensitive to the number of As dimers and Ga dimers on the surface. By monitoring these photon energies during MOVPE growth, the growth dynamics can be extracted. The entire RDS spectrum has been analyzed over a range of growth rates and temperatures and three main surface regimes have been found during MOVPE growth[44, 46]. Each regime seems to correspond to the carbon content on the surface, typically from trimethylgallium or triethylgallium, the group III precursor molecules.

Oscillations in photon energies have been found that correspond to layer by layer growth on the GaAs surface[44, 47-50]. It has been hypothesized that the edges of growing islands have a different reconstruction (which include Ga dimers) that the flat terraces (a c(4x4) reconstruction dominated by As dimers). Since the orientation of the Ga and As dimers are perpendicular, the RDS signal from each orientation can be picked up in a specific photon energy. Thus, as islands cover the surface, more Ga rich reconstructions form at the edges of islands. As the islands coalesce, the number of Ga dimers dwindles

until a completely flat surface is formed, which is covered only by As dimers in a disordered c(4x4) reconstruction.

Creighton and Baucom[46] use RDS in a rotating disk MOVPE reactor and a surface science experimental setup. Using both systems, they are able to use the RDS along with surface science techniques to determine the surface species at a variety of temperatures and growth rates. They find that at intermediate temperatures and growth rates, a (1x2)-CH_3 covered surface occurs during growth from the decomposition of TMGa on the surface.

Both RDS and GIXS were performed simultaneously [51, 52] and it was found that the oscillations from both methods correspond to layer-by-layer growth and are in agreement. Interesting is at the conclusion of growth, the RDS signal returns much more quickly to the steady state signal than the GIXS signal does. Since the RDS signal measures Ga and As dimers on the surface, the number of Ga dimers may drop quickly after growth stops. GIXS measures long range order, so the island shapes and densities may still evolve after the flux of Ga atoms has stopped, until the equilibrium structure of islands on the surface has been found.

5.2.3.3 Differences between MBE and MOVPE Growth

Molecular Beam Epitaxy (MBE) and MOVPE growth both produce high quality GaAs films, but the mechanism of film growth is different. For example, the transition between step flow and island growth has been measured in MBE by RHEED and found to correspond to an activation energy of 1.58 eV[34]. This is drastically different than the transition found using RDS and GIXS in MOVPE growth that was found to range from 2.3-2.7 eV[33, 44]. This high activation barrier for the transition between growth modes has also been seen in GaN growth[53]. Also the shape of the islands during STM studies are found to be different in MBE as compared to MOVPE grown films. MBE grown films have islands that are anisotropic and extend further in the $[\bar{1}10]$ direction than the [110] direction. MOVPE grown films have the opposite anisotropy with islands extending in the [110] direction[6]. Also, it was noted that B-type steps are straighter

than A-type steps in MOVPE growth[5]. This is the opposite of MBE growth where A-type steps are relatively straight, while B-type steps are relatively rugged[54]. The cause of such differences in MBE and MOVPE grown films may be the presence of excess As in MOVPE systems. The excess As creates a different surface reconstruction (c(4x4) rather than β(2x4) in MOVPE as compared to MBE), which leads to different diffusion, nucleation, and incorporation differences. KMC simulations are used to determine the nature of such differences between MBE and MOVPE growth.

Another major difference between MBE and MOVPE growth is the processing conditions. MBE temperatures are typically much lower than MOVPE conditions, and the As flux in MBE is much lower than MOVPE As fluxes. The higher temperatures in MOVPE growth are due to the decomposition of the Ga precursors. Stable Ga precursors, such as TEG and TMGa decompose on the surface with the carbon chains leaving the surface. At low temperatures (less than 500 ° C), unintentional carbon incorporation impedes with the electrical properties of the thin film[55]. At these higher temperatures, As precursors desorb from the surface rapidly as shown by Banse and Creighton[15] and Adamson *et al.*[16]. Thus a large As overpressure is needed in MOVPE growth in order to force the As into the thin film during growth. Without enough As in MOVPE growth, the film becomes extremely rough and Ga droplets form on the surface. A stable Ga precursor that decomposes at lower temperatures would allow for lower temperature growth, but a suitable candidate has yet to be found.

5.3 *Models of the GaAs surface*

Models of surface morphology can range from continuum, analytic models to *ab initio* quantum models of surface reactions. The model to use depends on the time and length scale of the needed prediction. An overview of surface modeling techniques and their relevant length and time scales is shown in Figure 5.9.

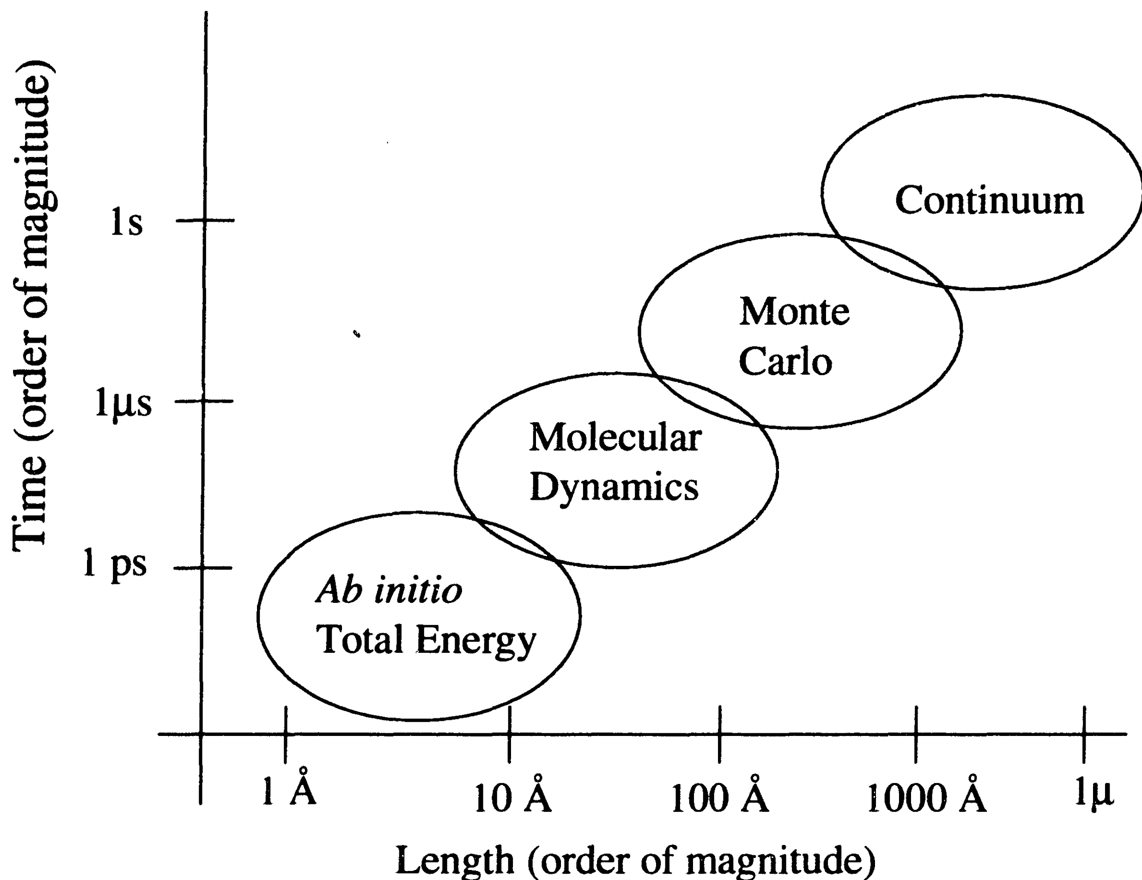

Figure 5. 9: Relevant length and time scales for a variety of surface modeling techniques.

5.3.1 Analytical Models of Surface Growth

Thin film growth has been studied using analytic models. Reviews of these methods are developed in Venables *et al.*[56] and Markov[57]. Surface growth has been modeled by mean-field type approximations which neglects both statistical fluctuations and all spatial degrees of freedom[58]. For modeling growth below a surface coverage of 0.25, rate equations can be developed that describe the average number density of adatoms, $\rho(t)$, and the average number density of immobile islands, $N(t)$.

$$\frac{\partial \rho}{\partial t} = F - D\rho N = 0 \tag{5.1}$$

$$\frac{\partial N}{\partial t} = D\rho^{i+1} - D\rho N^2 \tag{5.2}$$

In Equations 5.1 and 5.2, F is the deposition flux and D is the surface diffusion constant. The term, i, corresponds to the number of adatoms greater than one that are needed to form a critical nucleus on the surface. So the critical nuclei term, i, equaling one corresponds to a critical nuclei of two adatoms. The first term in Equation 5.2 corresponds to the birth of islands and the second term corresponds to coalescence of islands. These equations are only valid for the coverage regime of 0 to 0.25, as coalescence of islands reduces the number density of islands as the monolayer of islands fills in to complete one layer of growth.

From these birth-death equations, scaling laws of how the number of islands on the surface depends on flux and diffusion rate can be extracted. Solution of these equations results in Equation 5.3.

$$N \propto \left(\frac{D}{F}\right)^{-i/(i+2)} \qquad (5.3)$$

This relationship suggests the number density of islands is a result of a competition between diffusion and flux to the surface. As the diffusion rate is increased, the number density of island decreases (due to the negative exponent). Since each adatom is exposed to more of the surface as the diffusion rate increases, each adatom is more likely to attach to a growing nuclei, reducing the number density of nuclei. If the flux to the surface increases, the number density of islands increases, as more adatoms are on the surface at any given time and can find each other faster than they can find a growing nuclei. The exponent reflects the effect of the minimum nuclei size. As the minimum nuclei size increases, the number density of islands on the surface decreases.

This simple model of nucleation can be used to measure the correlation lengths between islands on the surface. The correlation length between islands is shown in Equation 5.4,

$$N \propto L^{-2} \qquad (5.4)$$

where L is the correlation length between islands. This is derived under the assumption that islands are circular, thus the correlation length scales as πr^2 with island size of radius r. As N is smaller, r is larger (smaller number of islands results in each island being larger) and the correlation length scales as r^{-2}. Thus the correlation length can be derived from the diffusion rate and flux to the surface under the assumptions of this model. This simple model describes some of the dynamics of crystal growth, but a description that gives a spatial representation of the surface can be embodied in a KMC simulation.

5.3.2 KMC simulations

KMC models have been used extensively in modeling thin film growth. Many of the analytic models have been tested using KMC models to determine the island density and other surface characteristics given reactor conditions. KMC models have also been used to study real systems, such as the MBE growth of GaAs and other thin films.

5.3.2.1 KMC Models – Theory

KMC methods have been used to validate many of the analytic models for thin film growth that have been developed[59, 60]. Bartelt and Evans[61-63] have studied the nucleation and growth of different shaped islands to understand the behavior of the size, coalescence, and correlations between islands on the surface. Ratsch *et al.*[64, 65] studied island size distributions for KMC models that include nearest neighbor barriers for diffusion. The nearest neighbor barriers included in the diffusion barrier in their simulations allow for nucleation without a critical nucleus size. They find that the exponent in Equation 5.3 is a smoothly varying function of the diffusion rate and nearest neighbor barriers on the surface.

Simulations have also been used in order to derive surface parameters from experimental results, once a given model is known to be consistent with an experimental system. Mo *et al.*[66, 67] computed the activation energy for surface diffusion of Si on Si(001) by measuring the island size distribution by STM studies. Using an analytic model for the

island size distribution and a KMC model, the data was fitted in order to determine the activation energy for surface diffusion of Si, 0.67 eV.

5.3.2.2 KMC Models for GaAs MBE

The surface evolution of MBE grown films have been extensively studied by KMC simulations[68, 69]. KMC models were used extensively to study the GaAs surface by Vvedensky *et al.* [70-74] for MBE systems. The models were solid on solid models with a cubic lattice. A KMC approach was used whereby the Ga adatoms on the surface were tracked and there was initially assumed to be an infinite source of As that would incorporate with probability one when an As site appeared. Nucleation was accomplished using nearest neighbor barriers for Ga diffusion. The first studies were used to interpret oscillations in RHEED experiments that correspond to monolayer growth of GaAs. Layer-by-layer growth corresponded to roughening and smoothing of the surface that matched up exactly with oscillations from the RHEED experiments.[75]. The simulations exactly matched up with the experimental results][34]. Others included the As directly in the model and developed similar models[76]. The model was extended when further experimental STM work was done in order to examine the nucleation behavior on the β(2x4) surface[77]. It was found that Ga adatoms nucleate on top layer of the base reconstruction and not in the trenches of the reconstruction.[78].

5.3.3 Quantum studies of GaAs surfaces

Quantum studies of various levels of accuracy have been done in order to study the GaAs surface during growth. From first-principles density functional theory (DFT) to the use of empirical potentials in molecular dynamics simulations, a range of techniques have been used to study the GaAs surface. A review of quantum techniques used to study epitaxial growth is given in Kaxiras[79].

First principles techniques have been used to study equilibrium structures on the surface, reactions on the surface, and diffusion coefficients of adsorbates on the surface. Moll *et al.*[80] used a first-principles pseudopotential DFT approach to obtain a Wulff plot of the

GaAs equilibrium surface energy as a function of orientation. Northrup and Froyen[4] studied the surface energies of a set of GaAs surfaces by local density approximation. They find that the c(4x4) reconstruction is stable under the As-rich limit. Reactions of hydrogen on the surface have been studied using both cluster calculations and band-structure total energy calculations using the local density approximation[81, 82]. The adsorption of H_2 on the surface is ruled out, but H-atom adsorption is found to occur without breaking the As dimers on As-rich surfaces. Surface diffusion of Ga adatoms on β(2x4) surfaces have been studied by total energy calculations and diffusion has found to be anisotropic with activation barriers ranging from 0.8 to 0.6 eV[83]. Kratzer *et al.*[84] determined a model for nucleation of GaAs on β(2x4) surfaces using DFT methods that disagrees with experimental and KMC work, whereby Ga dimers nucleate in the trenches of the reconstruction. Adsorbates on the β(2x4) surface has been studied using *ab initio* DFT methods in order to examine the adsorption and desorption physics[85]. LePage *et al.*[86] has examined the diffusion barrier on c(4x4) surfaces using *ab initio* calculations and found the barrier to be anisotropic and range from 0.15 to 0.33 eV.

In a series of first-principles calculations, trends in the calculations can be observed. Zhang and Zunger[87] use these trends to develop a methodology called the linear combination of structural motifs. This methodology uses a 'group contribution' approach by building up larger structures through a limited number of structural motifs (for example, tetrahedrally bonded Ga and As). The motif energies are fitted to a series of pseudopotential total-energy calculations. Each motif energy included with a electrostatic term can then be used to calculate the total energy of large surfaces, such as steps, to find the lowest energy structures[88].

First principles calculations were used along with the Electron-Counting Monte Carlo (ECMC) model in order to study surface processes such as adsorption and diffusion of As and Ga on the c(4x4) and β(2x4) surfaces[89-91]. Adsorption, diffusion, and incorporation were studied on the β(2x4) surface and the energetics were found to be coverage dependent. The As_2 adsorption energy drastically increases as the As coverage increases[92]. The diffusion barriers were found to depend on the surface coverage of As

and Ga, and Ga adatoms were found to be more stable attaching to B steps than A steps[93, 94]. For c(4x4) surfaces, the adsorption, desorption and diffusion behavior was again found to be coverage dependent, but in different ways than the β(2x4) surface. The diffusion behavior was reverse that on MBE surfaces, as Ga adatoms were more stable attaching to A steps than B steps[94]. This is what is seen experimentally as a difference between MBE and MOVPE growth[7]. A self-surfactant process was observed from the simulations, as As dimers were found to desorb more quickly (with a lowered barrier) in the presence of Ga adatoms[95]. Desorption of As_2 changes the structure of the surface to allow further Ga species (such as TMGa or TEGa) to adsorb[96] [97]. This is also consistent with experimental data, as As overpressure was not found to affect the lateral growth rates, but it does affect the horizontal growth rates[14].

Molecular dynamics simulations are also used to determine diffusion coefficients of Ga and As on GaAs(001). A methodology has been developed to fit empirical potentials to semiconductor surfaces[98]. Unfortunately, empirical potentials miss many of the electrostatic contributions to the surface energy and using slightly different potentials can lead to vastly different results for diffusion barriers. Palma *et al.*[99] and Salmi *et al.*[100] both compute the diffusion barrier of Ga and As on GaAs(001). Shown in Table 5.2 are the results of their calculations. There is a large discrepancy in their results as different surfaces were modeled and different potentials were used.

Table 5. 2: Diffusion barriers as estimated by molecular dynamics simulations

Adsorbate	Surface	Direction	Barrier (eV)	Pre-exponential (cm^2/s)	Reference
Ga	As terminated	either	0.101	1.637×10^{-5}	[99]
As	As terminated	either	0.077	7.59×10^{-4}	[99]
Ga	β(2x4)	110	2		[100]
Ga	β (2x4)	$[\bar{1}10]$	1.9		[100]
As	β (2x4)	110	1.6		[100]
As	β (2x4)	$[\bar{1}10]$	1.5		[100]
Ga	c(4x4)	110	0.8		[100]
Ga	c(4x4)	$[\bar{1}10]$	1.15		[100]
As	c(4x4)	110	1.55		[100]
As	c(4x4)	$[\bar{1}10]$	1.7		[100]

5.4 MOVPE Models of GaAs

The structure of the KMC algorithm does not change when applying it to growth problems as compared to TPD problems. A flowsheet of the algorithm is shown in Figure 5.10.

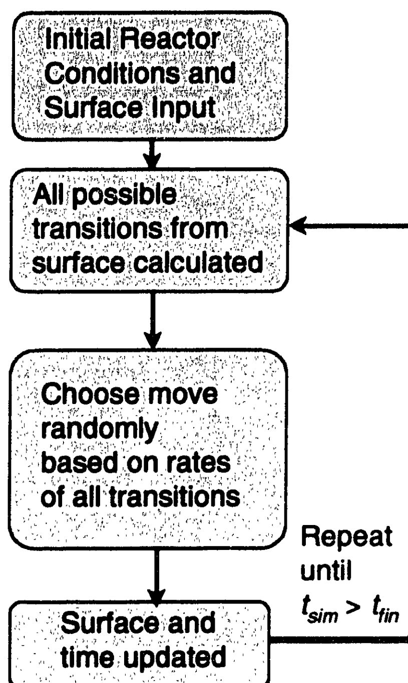

Figure 5. 10: Algorithm for the KMC algorithm to simulate thin film growth.

The differences between models of MOVPE growth and MBE growth occur in the transitions on the surface. As shown by both quantum calculations and experimental results, the MBE surface greatly differs from the MOVPE surface, especially under growth conditions. Thus, a different model must be developed in order to describe the MOVPE surface.

5.4.1 Model Parameters

KMC models with varying parameters where investigated to determine their effectiveness in describing the evolution of surface morphology in MOVPE of GaAs films. An initial model was tested that was similar to MBE models of the surface. This model was extensively tested in Chapter 6. Further refinements to the model included the implementation of the c(4x4) reconstruction on the surface with the inclusion of As_2 dimers on the surface. This model is tested in Chapter 7.

The initial model used the approximation that there is an infinite source of As on the surface that will fill in all available As sites. This assumption was used in MBE simulations, as the Ga flux controlled the growth rate. This should be an even better

assumption in MOVPE simulations, as reactors are typically run 10-50 time excess As precursor (this creates the c(4x4) As rich reconstruction on the surface). Thus, Ga dynamics are the controlling dynamics for growth and the diffusion and incorporation dynamics need to be input into the KMC simulations as rates. Table 5.3 has a list of the transitions and the accompanying rates. Transitions 6-10 in Table 5.3 were used in the simulations, as the other rates are much faster than the rate-limiting steps to growth (diffusion and incorporation).

Table 5. 3: Initial Model of MOVPE surface processes for GaAs(100) growth

	Transition	Rate	Time Constant @ 550 ° C (sec)	Reference
1	$HAs^* + HGa^* \rightarrow H_2 + As^* + Ga^*$	$1.2x10^{17}\exp\left(\frac{-13.8kcal}{RT}\right)$	$3.85x10^{-14}$	[101]
2	$AsH^* + AsH^* \rightarrow 2As^* + H_2$	$1.0x10^{17}\exp\left(\frac{-17kcal}{RT}\right)$	$3.27x10^{-13}$	[101]
3	$C_2H_5Ga^* \rightarrow Ga^* + C_2H_5$	$1.0x10^{9}\exp\left(\frac{-18.5kcal}{RT}\right)$	$8.18x10^{-5}$	[17-20]
4	$(C_2H_5)_2Ga^* \rightarrow C_2H_5Ga^* + C_2H_5$	$5.0x10^{11}\exp\left(\frac{-32kcal}{RT}\right)$	$6.3x10^{-4}$	[17-20]
5	$C_2H_5^* \rightarrow C_2H_5$	$1.0x10^{9}\exp\left(\frac{-18.5kcal}{RT}\right)$	$1.26x10^{-2}$	[17-20]
6	As species flux	Input parameter		
7	Ga species flux	Input parameter		
8	Ga diffusion	$8.0x10^{3}\exp\left(\frac{-64kcal}{RT}\right) cm^2/s$	7.94	[102]
9	$Ga^* \rightarrow Ga$	$1.0x10^{13}\exp\left(\frac{-83kcal}{RT}\right)$	$2.03x10^{9}$	[102]

This model neglects the As dynamics on the surface. Ito and Shiriashi[95] have explored a different mechanism which includes As dimers on the surface which creates the c(4x4) reconstruction found during MOVPE. Their self-surfactant model predicts that As dimers have a lower barrier for desorption when Ga adatoms are in the nearest-neighbor positions. This suggests that As dimers on the surface hinder Ga diffusion, but are likely

to desorb around Ga islands on the surface. These initial dynamics were included in the model by adding As_2 adsorption and desorption into the model. The adsorption rate of As_2 was derived from the concentration of As precursor above the surface. The butyl groups on the TBAs were assumed to desorb quickly from the surface[24]. The desorption rate of As_2 is derived from Adamson. *et al.*[16], who found that the desorption of As dimers from the surface occurs with a barrier of 44 kcal. The self-surfactant effect was included with a nearest-neighbor barrier that decreased the desorption barrier by 4 kcal for every neighbor. This 4 kcal number is derived from the slope of the ECMC simulation by Ito and Shiriashi[95], by scaling their slope by the ratio of the experimental barrier of 44 kcal to their calculated barrier of 98 kcal.

Also, the diffusion barrier for Ga on the surface during MOVPE growth has ranged from 0.04 eV to 2.7 eV[33, 86, 102]. In this model, reasonable parameters were found in Salmi *et al.*[100] for Ga diffusion, and these barrier were used (as shown in Table 5.2).

5.4.2 Step Flow versus Island Growth

The model can be used to determine the different growth modes (given a surface model) as a function of the surface temperature and flux to the surface of precursor species. The growth modes for GaAs include step-flow growth and island growth modes. Both growth modes are shown pictorially in Figure 5.11.

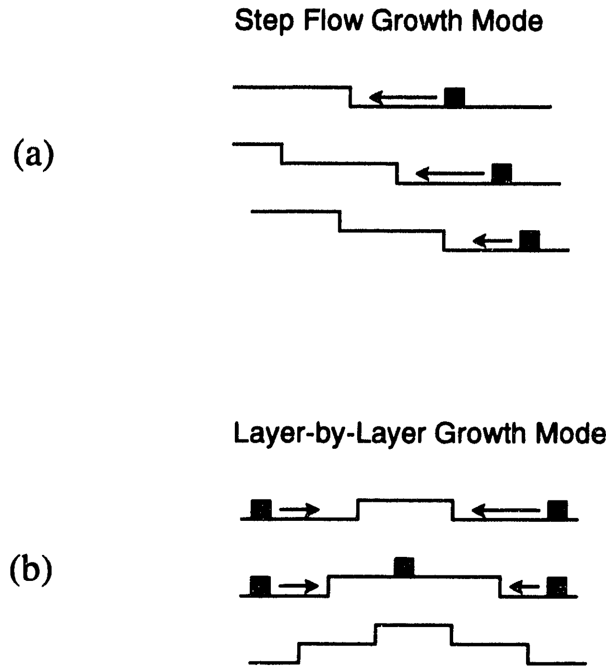

Figure 5. 11: (a) Step flow growth – on vicinal surfaces adatoms attach to the steps during growth. This maintains a flat film over time; (b) Island growth (Layer-by-Layer Growth)– adatoms nucleate and form islands on the surface. Other adatoms attach to the edge of growing islands.

In step flow growth, species are added to a vicinal surface and attach to the step edges rather than nucleating on the terraces. Adatoms diffuse fast enough to find a step edge rather than find each other to nucleate new island on the terrace. In island growth modes, adatoms find each other and nucleate to form islands before finding step edges. Thus, the growth modes are a competition between diffusion (controlled by surface temperature) and flux to the surface. At relatively high temperatures (high diffusion lengths) and a low flux, step flow growth modes prevails, while at relatively low temperatures and high flux rates, island growth modes dominate.

Figure 5.12 shows the oscillations in the x-ray scattering along with the surface morphology in island growth mode at 790 K. Before the beginning of growth, the terraced surface is generally smooth. Since the scattering off the surface only picks up the top bilayer, the resulting signal is relatively strong. As the surface evolves when growth begins, islands appear on the surface. When the surface is half covered with islands, zero scattering results, as the bilayers scatter exactly out of phase. This

corresponds to the first trough in the scattering. Continued growth occurs, and the islands coalesce to form a relatively smooth surface, which corresponds to the second peak in Figure 5.12. This roughening and smoothing process continues until the flux is stopped. Note that the peaks lower in intensity as more monolayers are grown. This corresponds to the overall roughening of the surface during growth. Due to the low temperatures and high flux of this simulation, islands appear on the surface, rather than the free adatoms on the surface attaching to the step edges.

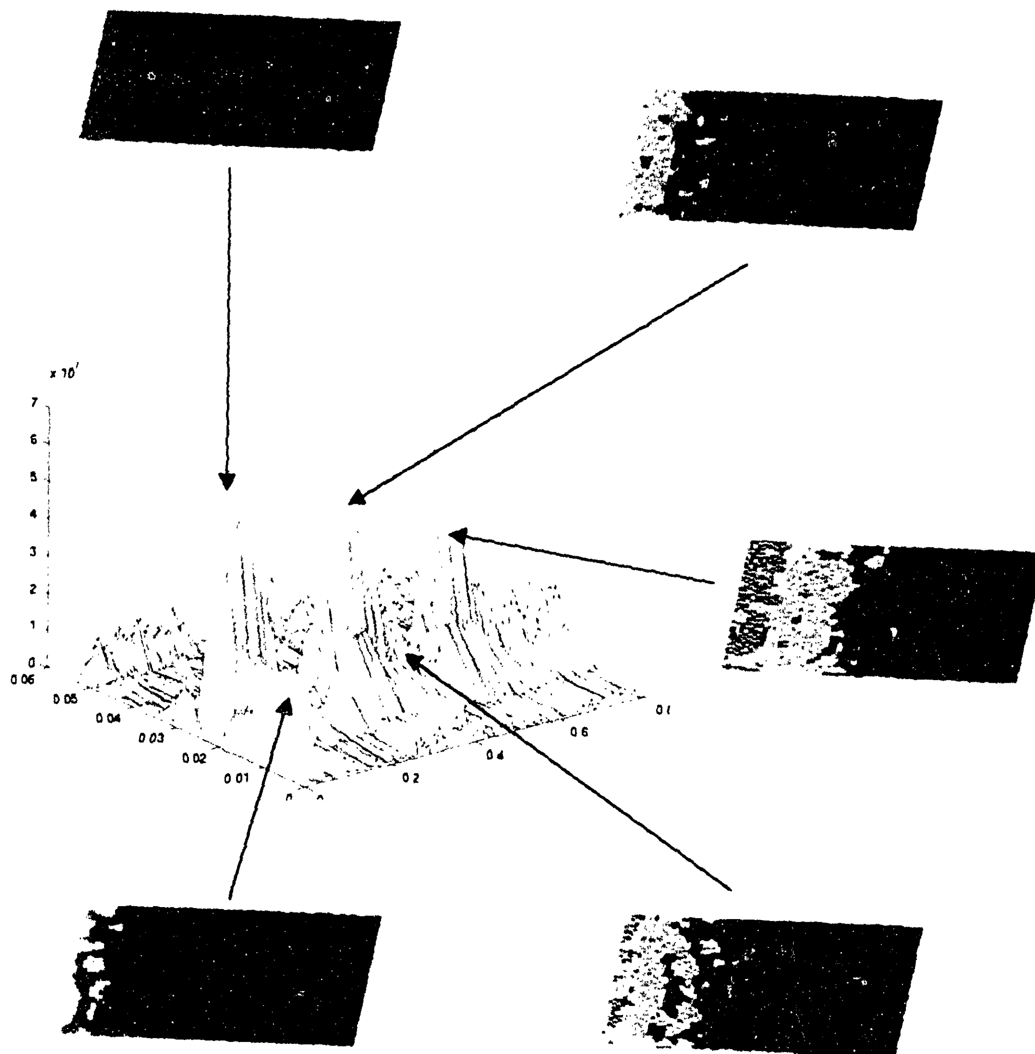

Figure 5. 12: Computed x-ray scattering from the surface along with pictures of the model surface. Note the oscillations in the x-ray scattering correspond to each monolayer of growth.

Figure 5.13 shows the constant x-ray scattering signal along with the surface morphology in step flow mode at 850 K. Before growth, a high scattering signal emanates from the top bilayer. As growth proceeds, the surface remains flat, with the adatoms attaching to the step edges. This does not change the overall morphology of the film, but just shifts

the front. This causes no change in the scattering, as shown by Figure 5.13. A constant signal is generated throughout growth. Much smoother films are produced in step flow mode than island growth modes.

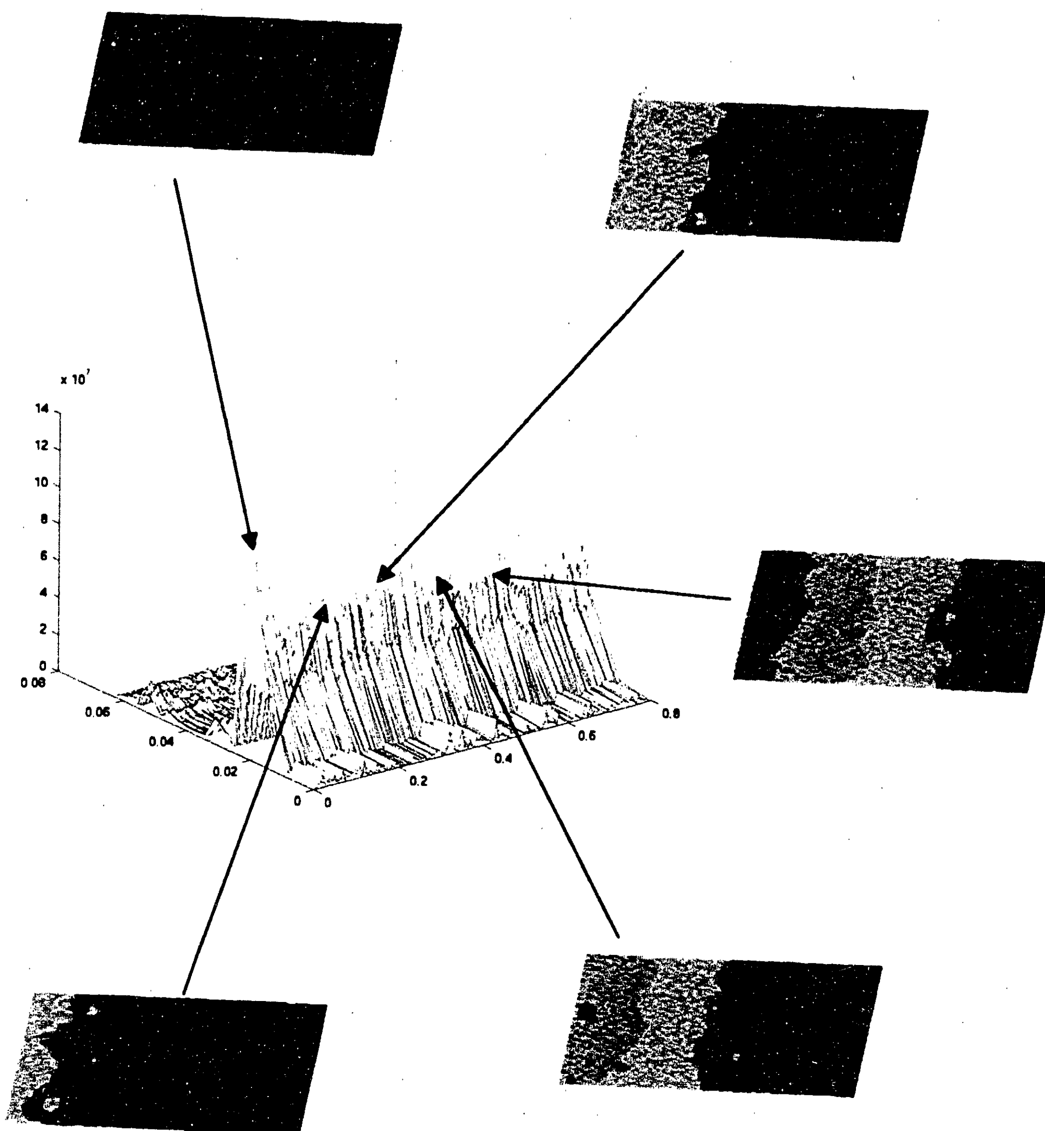

Figure 5. 13: Computed x-ray scattering from the surface along with pictures of the model surface. Note the constant signal corresponds to step flow growth whereby adatoms attached of the edge of the steps (as in the pictures of the model surface).

Experimentally, RHEED, RDS, and GIXS have been used to determine the transition between growth modes. In all three of these in-situ techniques, oscillations have been observed that correspond to island growth mode. The disappearance of oscillations at higher temperatures and lower fluxes correspond to the transition from island growth modes to step flow. Shown in a series of scattering plots and corresponding pictures of the surface in Figure 5.14 is the transition from island growth to step flow growth at a constant flux of 5.0 ML/sec Ga flux and 100 ML/sec As flux to the surface.

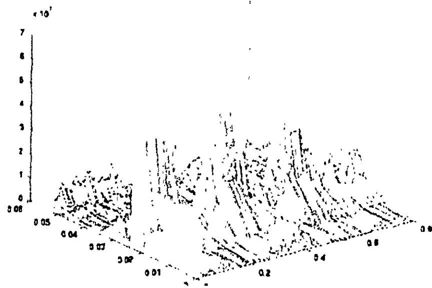

790 K

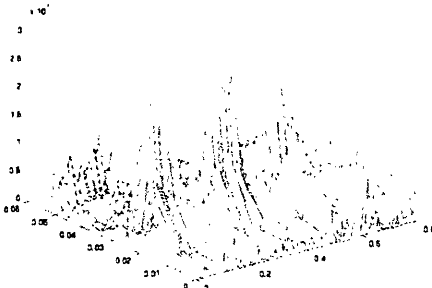

800 K

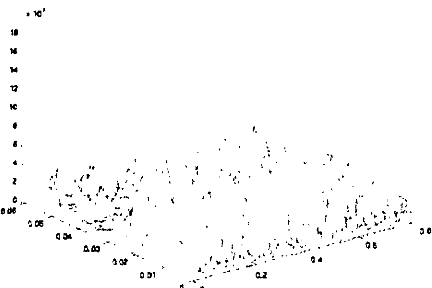

810 K

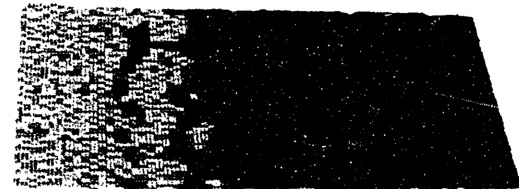

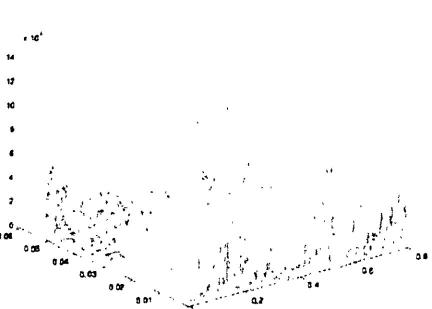

820 K

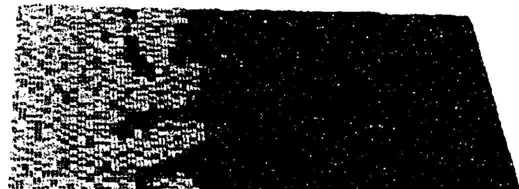

(e)

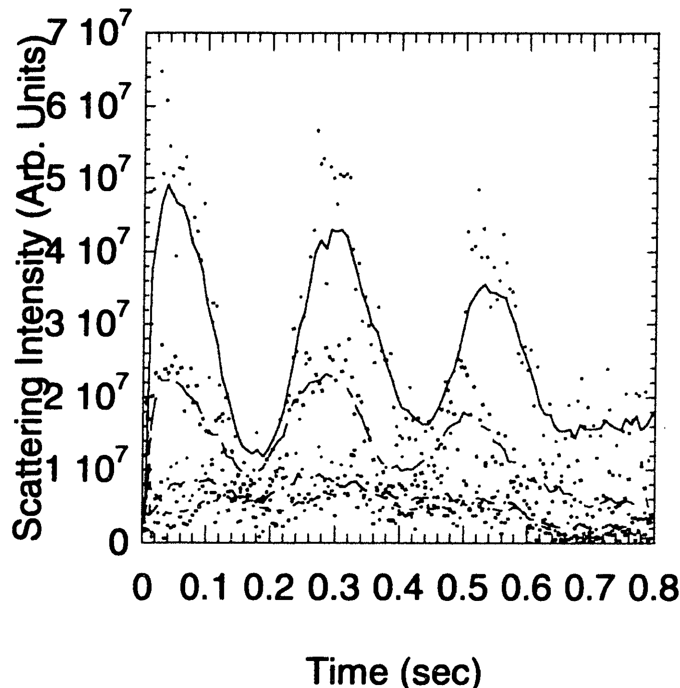

Figure 5. 14: The transition from island growth to step flow growth with the increase in temperature. Note how the surface becomes smoother at higher temperatures and fewer islands form on the terraces. (a) 790 K, (b) 800 K, (c) 810 K, (d) 820 K. (e) Oscillations from (a), (b), (d) one same plot.

As seen, as the temperature is increased, the surface is in general smoother. Also, note that the oscillations in the diffuse scattering become less pronounced as the temperature is increased, and finally becomes constant at high temperatures. This is shown in Figure 5.14 (e). The oscillations occur at a scattering wavevector which exactly corresponds to the two times the terrace length. Since each bilayer scatters exactly out of phase at a Bragg peak, scattering off each terrace cancels the neighboring terrace exactly out at a wavevector of 0. Oscillations occur at a wavevector of exactly two times the terrace length, since the correlation of surface heights are at this length scale. A simulation on a singular surface will have the oscillations at a scattering wavevector of 0.

5.4.3 MBE versus MOVPE grown films

One of the major differences seen in MBE film growth as compared to MOVPE film growth is the transition from step-flow to island are affected differently by changes in temperature. For MBE growth, the slope of the transition is suggested to be the diffusion

barrier, since the average diffusion length must be at least one half the length of a step in order for step flow growth to occur[103]. Typically, Equation 5.5 is used to convert the transition temperature into a diffusion coefficient. In Equation 5.5,

$$x = \sqrt{2Dt} \tag{5.5}$$

x is the terrace length, D is the diffusion coefficient and t is the time for monolayer growth. Unfortunately, this does not take into account the nucleation behavior on the surface. For example, in Figure 5.15, this technique was used to map out the diffusion coefficient for MBE[104] and MOVPE[33].

(a)

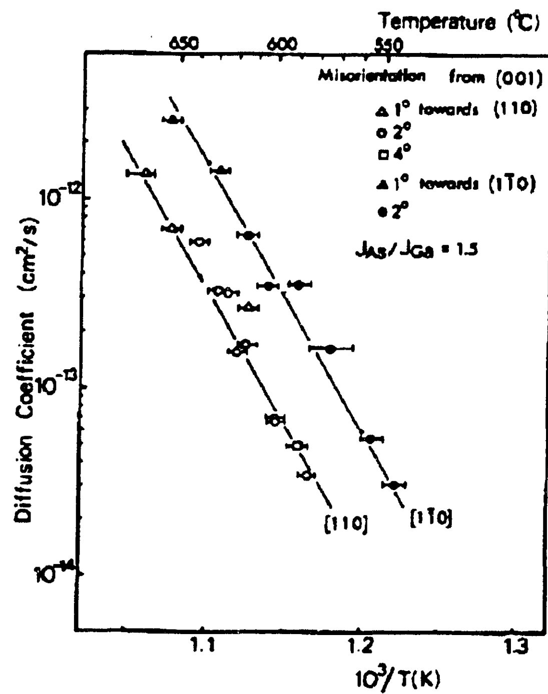

Fig. 3. Diffusion coefficient for [110] and [1$\bar{1}$0] directions. The activation energy is 2.8 eV for both directions.

(b)

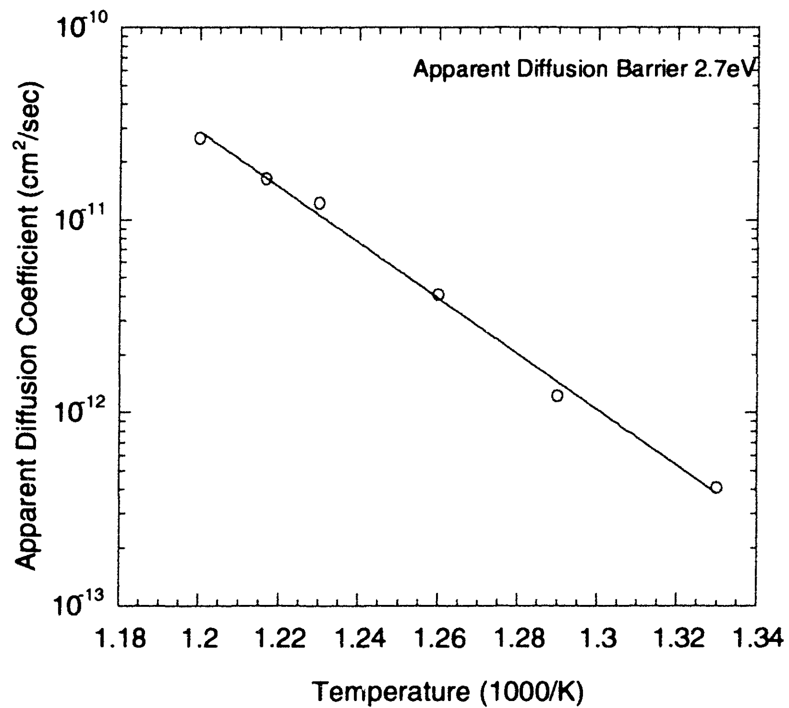

Figure 5. 15: Diffusion coefficient computed during (a) MBE growth[104], (b) MOVPE growth[33] using Equation 5.5.

There is an order of magnitude difference in the diffusion coefficients. This order of magnitude difference could be due to that diffusion is faster on MOVPE surfaces than MBE surfaces. This could be the case, as an MOVPE grown film has a c(4x4) reconstruction, while an MBE grown film has a β(2x4) reconstruction. On the other hand, the surface is 'rougher' on the MOVPE surface, as organic species, As dimers, and hydrogen fly around the surface. Another explanation is that the measured diffusion coefficient and barrier is not a true measurement of diffusion on the surface, but a convolution of diffusion, nucleation, and other reactions on the surface.

As shown in the previous section, the transition between step-flow and island growth can be mapped for a given surface model. To test the idea that nucleation may be drastically different in MBE and MOVPE growth, the same model was used to determine the transition between step-flow and island growth, except the nucleation criteria was changed. The nucleation criterion was based on the morphology of the surface. Mechanism A and Mechanism B nucleated the circled adatom when in the configuration shown in Figure 5.16.

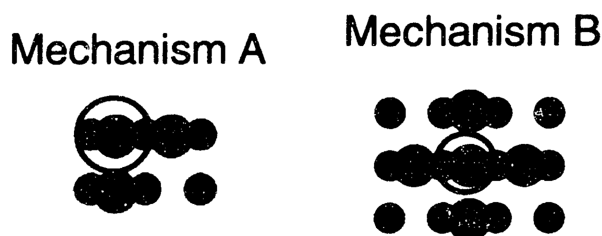

Figure 5. 16: Configuration of adatoms for nucleation to occur for the circled adatom in (a) Mechanism A, (b) Mechanism B

In Mechanism A, the circled adatom is nucleated, and not allowed to diffuse after gaining the trimer configuration. Other adatoms are fixed as they are attached to nucleated adatoms. Mechanism B is similar, except the configuration for a fixed atom is one where

the adatom is surrounded by other Ga adatoms. Both diffusion coefficients were the same as shown in Equation 5.6.

$$D = 8x10^{13}\exp^{(-2.7\ eV/RT)}\ cm^2/s \tag{5.6}$$

Shown in Figure 5.17 are the results of the simulations.

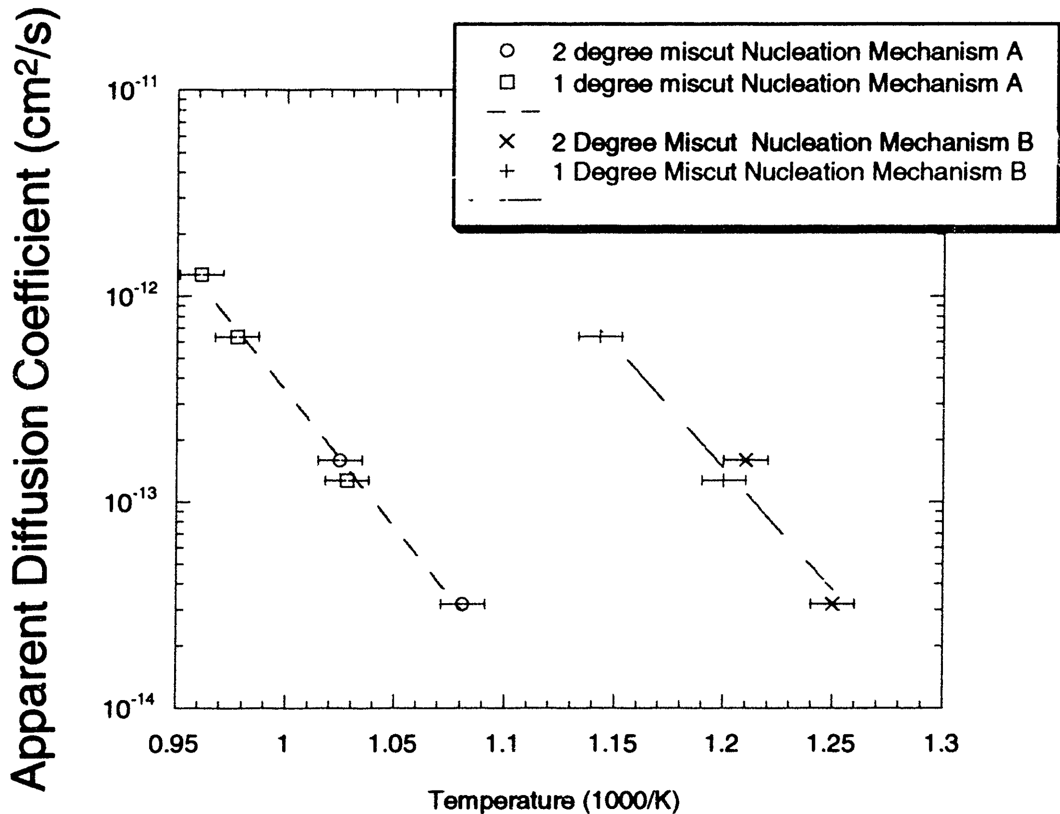

Figure 5. 17: Diffusion coefficients computed from Mechanism A and Mechanism B. Notice the large difference in the magnitude of the coefficient due to only the nucleation mechanism.

The nucleation mechanism plays an extremely large role in determining the apparent diffusion coefficient. Mechanism B has a much higher apparent diffusion coefficient due to the lack of nucleation on the surface (as compared to Mechanism A). This leads to the conclusion that nucleation behavior along with diffusion behavior affect the transition between step flow and island growth. The transition may be even a more convoluted function of surface reactions and diffusion in MOVPE growth.

Using an updated mechanism that includes As_2 adsorption and desorption from the surfaces, the transition behavior can again be examined through simulation. The apparent diffusion barrier is measured from the slope of the transition with respect to inverse temperature. In MBE systems, this slope has been measured from 1.58 eV to 2.8 eV, but it now has been established that 1.58 eV is the correct barrier[34]. As seen in Figure 5.15, the apparent diffusion barrier for MOVPE growth is 2.7 eV. This seems unreasonable as a diffusion barrier, but it may represent a convolution of surface processes. A study was done in order to determine the transition for a model that included 1.3 eV diffusion barriers and a 0.2 eV nearest neighbor attractive barrier as the nucleation model. The apparent diffusion barrier was determined for a model that did not include As_2 adsorption and desorption (a simplified model of an MBE surface), and a model that included the As_2 dynamics with an As flux 100 times that of the Ga flux (a simplified model of a MOVPE surface). Two plots of the transition are shown in Figure 5.18.

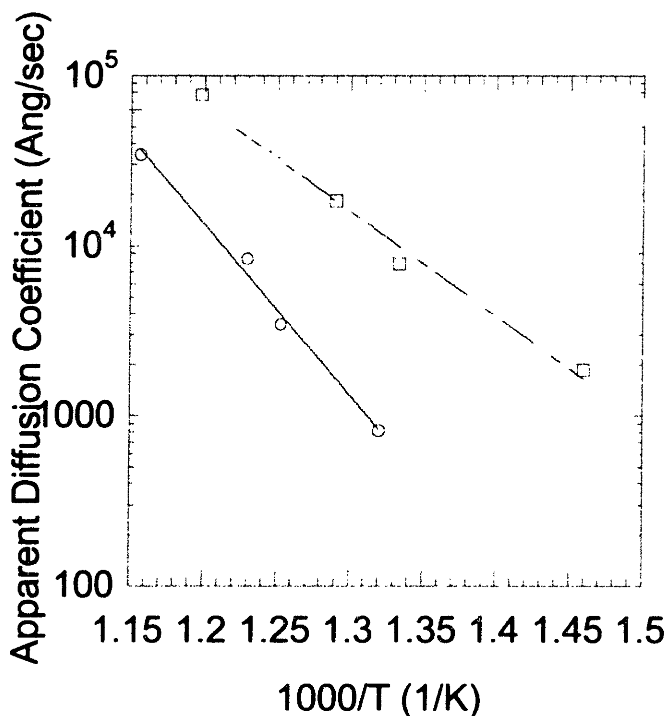

Figure 5. 18: Transition between step flow and island growth used to derive diffusion coefficients for (o) MOVPE model (□) MBE model. The activation barrier for diffusion is calculated as 45.7 kcal for the MOVPE model and 28.2 for the MBE model.

The activation barrier for diffusion computed from the two models varies significantly with the MOVPE barrier being 45.7 kcal and the MBE barrier being 28.2 kcal. The MBE barrier is similar to that of the diffusion barrier in the model, 1.3 eV (29.9 kcal), while the MOVPE barrier is significantly larger. This is due to the As dynamics on the surface. The As dimers on the surface block diffusion sites, which leads to an effective diffusion barrier much larger than that of the input diffusion barrier. This is similar to what is seen in MOVPE growth.

5.5 Conclusions

Thin film growth of GaAs is a complex and important process. Due to the complexity of the many surface reconstructions and growth modes of the surface, experimentation and modeling has been done in order to understand the surface during growth. Experimentally, the surface has been studied using vacuum techniques, STM studies of the surface, and in-situ techniques. Vacuum techniques, such as TPD and Laser assisted desorption have allowed the determination of adsorption and desorption kinetics of adsorbates on the surface. Also, infrared spectroscopy was used in determining adsorption sites for precursors. STM studies were done in order to examine the surface morphology of MOVPE grown films. In-situ studies, such as RDS and GIXS, were used to examine the evolving morphology of the film during growth. Each of the techniques has apiece of the puzzle in developing an overall mechanism for MOVPE growth of GaAs.

Models have been used to understand growth processes. Ranging from analytic models that are used to examine the distribution of islands on the surface to KMC models of surface morphology to quantum calculations of barriers of surface processes, calculations have been used to examine every length and time scale in MOVPE processing. The 'right' model to choose from depends on your choice of predictive metric. Using a combination of experimental and modeling results, a model for the MOVPE growth of GaAs is presented and compared to MBE models of growth. Its is shown that previous techniques oversimplify the analysis of surface processes on MOVPE grown surfaces (such as simple scaling rules), due to the interactions of the precursors on the surface.

Simple comparisons between MBE and MOVPE models show the drastic differences in measured diffusion coefficients can be explained by the addition of the As_2 dynamics on the surface. MOVPE models of surface evolution need to be developed from a combination of experimental and previous modeling efforts.

Bibliography:

1. Li, J. and T.F. Kuech, *Surface morphology of carbon-doped GaAs grown by MOVPE*. J. Crystal Growth, 1997. **170**: p. 292-296.
2. Biegelsen, D.K., R.D. Bringans, J.E. Northrup and L.E. Swartz, *Surface reconstructions of GaAs(100) observed by scanning tunneling microscopy*. Physical Review B, 1990. **41**: p. 5701-5706.
3. Payne, A.P., P.H. Fuoss, D.W. Kisker, G.B. Stephenson and S. Brennan, *GaAs c(4x4) surface structure in organometallic vapor-phase epitaxy*. Physical Review B, 1994. **49**: p. 14427-14434.
4. Northrup, J.E. and S. Froyen, *Structure and thermodynamic stability of GaAs(001) surfaces*. Mat. Sci. Engr., 1995. **B30**: p. 81-86.
5. Kasu, M., N. Kobayashi and H. Yamaguchi, Appl. Phys. Lett., 1993. **63**: p. 678.
6. Kasu, M. and N. Kobayashi, *Scanning tunneling microscopy study of GaAs step structures on vicinal substrate grown by metalorganic chemical vapor deposition*. Jpn. J. Appl. Phys., 1994. **33**: p. 712-715.
7. Kasu, M. and N. Kobayashi, *Surface kinetics of metalorganic vapor-phase epitaxy: Surface diffusion, nucleus formation, sticking at steps*. J. Cryst. Growth, 1997. **174**: p. 513.
8. Li, L., B. Han, S. Gan, H. Qi and R.F. Hicks, *Observation of the atomic structure of GaAs(001) films grown by metalorganic vapor-phase epitaxy*. Surface Science, 1998. **398**: p. 386-394.
9. Li, L., B.-K. Han and R.F. Hicks, *Surface phases of GaAs and InAs (001) found in the metalorganic vapor-phase epitaxy environment*. Applied Physics Letters, 1998. **73**: p. 1239-1241.
10. Han, B.-K., L. Li, Q. Fu and R.F. Hicks, *Structure and composition of the c(4x4) reconstruction formed during gallium arsenide metalorganic vapor-phase epitaxy*. Applied Physics Letters, 1998. **72**: p. 3347-3349.
11. Li, L., B.-K. Han, D. LAw, M. Begarney and R.F. Hicks, *Gallium arsenide and indium arsenide surfaces produced by metalorganic vapor-phase epitaxy*. Journal of Crystal Growth, 1998. **195**: p. 28-33.
12. Kasu, M. and N. Kobayashi, *Equilibrium multiatomic step structure of GaAs(001) vicinal surfaces grown by metalorganic chemical vapor deposition*. Appl. Phys. Lett., 1993. **62**(11): p. 1262-1264.
13. Kasu, M. and T. Fukui, *Multi-atomic steps on metalorganic chemical vapor deposition-grown GaAs vicinal surfaces studied by atomic force microscopy*. Jpn. J. Appl. Phys., 1992. **31**: p. 864-866.
14. Asai, H., *Anisotropic Lateral Growth in GaAs MOCVD Layers on (001) Substrates*. J. Cryst. Growth, 1987. **80**: p. 425-433.
15. Banse, B.A. and J.R. Creighton, *Formation of "super" As-rich GaAs(100) surfaces by high temperature exposure to arsine*. Appl. Phys. Lett., 1992. **60**: p. 856-858.
16. Adamson, S.D., B.K. Han and R.F. Hicks, *Site-specific reaction kinetics for gallium arsenide metalorganic vapor-phase epitaxy*. Appl. Phys. Lett., 1996. **69**: p. 3236-3238.

17. McCaulley, J.A., R.J. Shul and V.M. Donnelly, *Kinetics of thermal decomposition of triethylgallium, trimethylgallium, and trimethylindium adsorbed on GaAs(100).* J. Vac. Sci. Technol. A, 1991. **9**: p. 2872-2886.
18. McCaulley, J.A., V.R. McCrary and V.M. Donnelly, *Laser-Induced Decompoistion of Triethylgallium and Trimethlygallium Adsorbed on GaAs(100).* J. Phys. Chem., 1989. **93**: p. 1148-1158.
19. Donnelly, V.M. and J.A. McCaulley, *Products of thermal decomposition of triethylgallium and trimethylgallium adsorbed on Ga-stabilized GaAs(100).* Surface Science, 1990. **238**: p. 34-52.
20. Donnelly, V.M., *Products of pulsed laser induced thermal decomposition of triethylgallium and trimethylgallium adsorbed on GaAs(100).* J. Vac. Sci. Technol. A, 1991. **9**: p. 2887-2894.
21. Buchan, N.I. and M.L. Yu, *B-Hydride elimination reaction of triethylgallium on GaAs(100) surfaces.* Surface Science, 1993. **280**: p. 383-392.
22. Banse, B.A. and J.R. Creighton, Surface Science, 1991. **257**: p. 221.
23. Creighton, J.R., *Chemisorption and decomposition of trimethylgallium on GaAs(100).* Surface Science, 1990. **234**: p. 287-307.
24. Li, S.H., C.A. Larsen and G.B. Stringfellow, *Decomposition mechanism of trimethylarsine.* Journal of Crystal Growth, 1990. **102**: p. 117-125.
25. Qi, H., P.E. Gee and R.F. Hicks, *Sites for arsine decomposition on GaAs(001).* Surface Science, 1996. **347**: p. 289-302.
26. Robinson, I.K. and D.J. Tweet, *Surface X-ray Diffraction.* Rep. Prog. Phys., 1992. **55**: p. 599.
27. Fuoss, P.H. and S. Brennan, *Surface sensitive X-ray scattering.* Annu. Rev. Mater. Sci., 1990. **20**: p. 365-390.
28. Brennan, S., P.H. Fuoss, J.L. Kahn and D.W. Kisker, Nucl. Instrum. Methods. Phys. Res., Sect. A, 1990. **291**: p. 86.
29. Lamelas, F.J., P.H. Fuoss, D.W. Kisker, G.B. Stephenson, P. Imperatori and S. Brennan, *X-ray scattering analysis of surface structures produced by vapor-phase epitaxy of GaAs.* Phys. Rev. B, 1994. **49**(3): p. 1957-1965.
30. Robinson, I.K., *Crystal truncation rods and surface roughness.* Phys. Rev. B, 1986. **33**(6): p. 3830-3836.
31. Kisker, D.W., G.B. Stephenson, P.H. Fuoss, F.J. Lamelas, S. Brennan and P. Imperatori, *Atomic scale characterization of organometallic vapor phase epitaxial growth using in-situ grazing incidence X-ray scattering.* J. Crystal Growth, 1992. **124**: p. 1-9.
32. Fuoss, P.H., D.W. Kisker, F.J. Lamelas, G.B. Stephenson, P. Imperatori and S. Brennan, *Time-Resolved X-ray Scattering Studies of Layer-by-Layer Epitaxial Growth.* Phys. Rev. Lett., 1992. **69**(19): p. 2791-2794.
33. Kisker, D.W., G.B. Stephenson, P.H. Fuoss and S. Brennan, *Characterization of vapor phase growth using X-ray techniques.* J. Crystal Growth, 1995. **146**: p. 104-111.
34. Shitara, T., D.D. Vvedensky, M.R. Wilby, J. Zhang, J.H. Neave and B.A. Joyce, *Step-density variations and reflection high-energy-diffraction intensity oscillations during epitaxial growth on vicinal GaAs(001).* Physical Review B, 1992. **46**: p. 6815-6824.

35. Fuoss, P.H., D.W. Kisker, G.B. Stephenson and S. Brennan, *In-situ X-ray studies of organometallic vapor phase epitaxy growth.* Mat. Sci. and Eng., 1995. **B30**: p. 99-108.
36. Kisker, D.W., G.B. Stephenson, J. Tersoff, P.H. Fuoss and S. Brennan, *Atomic Scale studies of epitaxial growth processes using X-ray techniques.* J. Cryst. Growth, 1996. **163**: p. 54.
37. Aspnes, D.E., *Optical properties of thin films.* Thin Solid Films, 1982. **89**: p. 249-262.
38. Aspnes, D.E., *Real-time surface and near-surface optical diagnostics for epitaxial growth.* Mat. Res. Soc. Symp. Proc., 1994. **324**: p. 3-14.
39. Aspnes, D.E., *Observation and analysis of epitaxial growth with reflectance-difference spectroscopy.* Materials Science and Engineering, 1995. **B30**: p. 109-119.
40. Aspnes, D.E., *Real-time optical diagnostics for epitaxial growth.* AIP Conference Proceedings, 1996. **378**: p. 216-234.
41. Zettler, J.-T., *Characterization of epitaxial semiconductor growth by reflectance anistotropy spectroscopy and ellipsometry.* Prog. Crystal Growth and Charact., 1997. **35**: p. 27-98.
42. Zettler, J.-T., M. Pristovsek, T. Trepk, A. Shrebtii, E. Steinmetz, M. Zorn and W. Richter, *Reponse of the surface dielectric function to dynamic surface modifications: application of reflectance anisotropy spectroscopy and spectroscopic ellipsomentry.* Thin Solid Films, 1997.
43. Kamiya, I., D.E. Aspnes, L.T. Florez and J.P. Harbison, *Reflectance-difference spectroscopy of (001) GaAs surfaces in ultrahigh vacuum.* Phys. Rev. B, 1992. **46**: p. 15894-15904.
44. Ploska, K., M. Pristovsek, W. Richter, J. Jonsson, I. Kamiya and J.-T. Zettler, *Metalorganic Vapour Phase Epitaxial Growth on Vicinal GaAs (001) Surface Studied by Reflectance Anisotropy Spectroscopy.* Phys. Stat. Sol., 1995. **152**: p. 49.
45. Wassermeier, M., J. Behrend, J.-T. Zettler, K. Stahrenberg and K.H. Ploog, *In-situ spectroscopic ellipsometry and reflectance difference spectroscopy of GaAs(001) surface reconstructions.* Appl. Surf. Sci., 1996. **107**: p. 48-52.
46. Creighton, J. and K. Baucom, *Reflectance-difference spectroscopy of adsorbate-covered GaAs(100) surfaces: a combined surface science and in-situ OMVPE study.* Surface Science, 1998. **409**: p. 372-383.
47. Zettler, J.-T., J. Rumberg, K. Ploska, K. Stahrenberg, M. Pristovsek, W. Richter, M. Wassermeier, P. Schutzendube, J. Behrend and L. Daweritz, *Reflectance Anisotropy Oscillations during MOCVD and MBE growth of GaAs(001).* Phys. Stat. Sol. (a), 1995. **152**: p. 35-47.
48. Kamiya, I., D.E. Aspnes, H. Tanaka, L.T. Florez, E. Colas, J.P. Harbison and R. Bhat, *Real time in situ observation of (001) GaAs in OMCVD by refelctance difference spectroscopy.* Appl. Surf. Sci., 1992. **60/61**: p. 534-543.
49. Jonsson, J., K. Deppert and L. Samuelson, *Real-time monolayer growth oscillations detected by RD at pressures up to LP-MOVPE.* J. Cryst. Growth, 1992. **124**: p. 30-36.

50. Reinhardt, F., W. Richter, A.B. Muller, D. Gutsche, P. Kurpas, K. Ploska, K.C. Rose and M. Zorn, *GaAs surface control during metalorganic vapor phase epitaxy by relfectance anisotropy spectroscopy.* J. Vac. Scti. Technol. B, 1993. **11**: p. 1427-1430.
51. Kamiya, I., L. Mantese, D.E. Aspnes, D.W. Kisker, P.H. Fuoss, G.B. Stephenson and S. Brennan, *Optical characterization of surfaces during epitaxial growth using RDS and GIXS.* J. Cryst. Growth, 1996. **163**: p. 67-77.
52. Kisker, D.W., G.B. Stephenson, I. Kamiya, P.H. Fuoss, D.E. Aspnes, L. Mantese and S. Brennan, *Investigation of the Relationship between Reflectance Difference Spectroscopy and Surface Structure Using Grazing Incidence X-Ray Scattering.* Phys. Stat. Sol. (a), 1995. **152**: p. 9-21.
53. Stephenson, G.B., J.A. Eastman, C. Thompson, O. Auciello, L.J. Thompson, A. Munkholm, P. Fini, S.P. DenBaars and J.S. Speck, *Observation of growth modes during metal-organi chemical vapor deposition of GaN.* Applied Physics Letters, 1999. **74**: p. 3326-3328.
54. Pashley, M.D., K.W. Haberern and J.M. Gaines, Appl. Phys. Lett., 1991. **58**: p. 406.
55. Kuech, T.F. and J.M. Redwing, *Carbon doping in metalorganic vapor phase epitaxy.* J. Crystal Growth, 1994. **145**: p. 382-389.
56. Venables, J.A., G.D.T. Spiller and M. Hanbrucken, *Nucleation and Growth of Thin Films.* Rep. Prog. Phys., 1984. **47**: p. 399-459.
57. Markov, I.V., *Crystal Growth for Beginners.* 1995, River Edge, NJ: World Scientific.
58. Zangwill, A., *Scaling Description of Sub-Monolayer Epitaxial Growth.* Mat. Res. Soc. Proc., 1993. **280**: p. 121.
59. Family, F. and J.G. Amar, *Kinetics of epitaxial growth and roughening.* Materials Science and Engineering, 1995. **B30**: p. 146-166.
60. Amar, J.G., F. Family and P. Lam, *Dynamic scaling of island-size distributions and percolation in a model of submonolayer molecular-beam epitaxy.* Physical Review B, 1994. **50**: p. 8781-8797.
61. Bartelt, M.C. and J.W. Evans, *Nucleation and growth of square islands during deposition: sizes, coalescence, separations, and correlations.* Surface Science, 1993. **298**: p. 421-431.
62. Evans, J.W. and M.C. Bartelt, *Irreversible island formation during deposition: separation distributions and diffraction profiles.* Surface Science Letters, 1993. **284**: p. L437-L443.
63. Li, Y., M.C. Bartelt, J.W. Evans, N. Waelchli, E. Kampshoff and K. Kern, *Transition from one- to two-dimensional island growth on metal (11) surfaces induced by anisotropic corner rounding.* Physical Review B, 1997. **56**: p. 12539-12543.
64. Ratsch, C., P. Smilauer, A. Zangwill and D.D. Vvedensky, *Submonolayer epitaxy without a critical nucleus.* Surface Science Letters, 1995. **329**: p. L599-L604.
65. Ratsch, C., A. Zangwill, P. Smilauer and D.D. Vvedensky, *Saturation and scaling of epitaxial island densities.* Physical Review Letters, 1994. **72**: p. 3194-3197.

66. Mo, Y.W., J. Kleiner, M.B. Webb and M.G. Lagally, *Activation energy for surface diffusion of Si on Si(001): A scanning-tunneling-microscopy study.* Physical Review Letters, 1991. **66**: p. 1998-2001.
67. Pimpinelli, A., J. Villain and D.E. Wolf, *Surface diffusion and island density.* Physical Review Letters, 1992. **69**: p. 985-986.
68. Orme, C. and B.G. Orr, *Surface Evolution During MBE Growth.* Surface Review and Letters, 1997. **4**: p. 71-105.
69. Pal, S. and D.P. Landau, *Monte Carlo simulation of MBE growth on vicinal surfaces.* Computational Materials Science, 1996. **6**: p. 176-181.
70. Vvedensky, D.D. and S. Clarke, *Recovery kinetics during interrupted epitaxial growth.* Surface Science, 1990. **225**: p. 373-389.
71. Vvedensky, D.D., N. Haider, T. Shitara and P. Smilauer, *Evolution of surface-morphology during epitaxial-growth.* Philisophical Transactions of the Royal Society of London Series A, 1993. **344**(1673): p. 493-505.
72. Smilauer, P. and D.D. Vvedensky, Phys. Rev. B, 1993. **48**: p. 17603.
73. Itoh, M., G. Bell, A. Avery, T. Jones, B. Joyce and D. Vvedenskey, *Island nucleation and growth on reconstructed GaAs(001) surfaces.* Physical Review Letters, 1998. **81**(3): p. 633-636.
74. Clarke, S. and D.D. Vvedensky, *Growth kinetics and step density in reflection high-energy electron diffraction during molecular-beam epitaxy.* J. Appl. Phys., 1988. **63**: p. 2272.
75. Clarke, S. and D.D. Vvedensky, *Origin of Reflection High Energy Electron Diffraction Intensity Oscillations during Molecular Beam Epitaxy: A Computational Modeling Approach.* Physical Review Letters, 1987. **58**: p. 2235-2238.
76. Heyn, C. and M. Harsdorff, *Simulation of GaAs growth and surface recovery with respect to gallium and arsenic surface kinetics.* Phys. Rev. B, 1997. **55**: p. 7034.
77. Avery, A.R., H.T. Dobbs, D.M. Holmes, B.A. Joyce and D.D. Vvedensky, *Nucleation and Growth of Islands on GaAs Surface.* Phys. Rev. Lett., 1997. **79**: p. 3938.
78. Vvedensky, D.D., M. Itoh, G.R. Bell, T.S. Jones and B.A. Joyce, *Island nucleation and growth during homoepitaxy on GaAs(001)-(2x4).* Journal of Crystal Growth, 1999. **201/202**: p. 56-61.
79. Kaxiras, E., *Review of atomistic simulations of surface diffusion and growth on semiconductors.* Computational Materials Science, 1996. **6**: p. 158--172.
80. Moll, N., A. Kley, E. Pehlke and M. Scheffler, *GaAs equilibrium crystal shape from first principles.* Physical Review B, 1996. **54**: p. 8844-8855.
81. Nonoyama, S., Y. Aoyagi and S. Namba, *Ab Initio Cluster Study of the Interaction of Hydrogen with the GaAs(100) Surface.* Jpn. J. Appl. Phys., 1992. **31**: p. 1298-1302.
82. Miyamoto, Y. and S. Nonoyama, *First-principle calculations of molecular- and atomic-hydrogen reactions on As-terminated GaAs(100) surfaces.* Phys. Rev. B, 1992. **46**: p. 6915-6921.
83. Kley, A., P. Ruggerone and M. Scheffler, *Novel diffusion mechanism on the GaAs(001) surface: The role of adatom-dimer interaction.* Physical Review Letters, 1997. **79**: p. 5278-5281.

84. Kratzer, P., C.G. Morgan and M. Scheffler, *Model for nucleation in GaAs homoepitaxy derived from first principles.* Physical Review B, 1999. **59**: p. 15246-15252.
85. Goringe, C.M., L.J. Clark, M.C. Payne, I. Stich, J.A. White, M.J. Gillan and A.P. Sutton, *The GaAs(001)-(2x4) surface: Structure, chemistry , and adsorbates.* Journal of Physical Chemistry B, 1997. **101**(9): p. 1498-1509.
86. LePage, J., M. Alouani, D. Dorsey, J. Wilkins and P. Blochl, *Ab initio calculation of binding and diffusion of a Ga adatom on the GaAs (001) -c(4x4 surface.* Physical Review B, 1998. **58**(3): p. 1499-1505.
87. Zhang, S.B. and A. Zunger, *Method of linear combination of structural motifs for surface and step energy calculations: application to GaAs(001).* Physical Review B, 1996. **53**: p. 1343-1356.
88. Zhang, S.B. and A. Zunger, *Predicted structures and stabilities of the surface A grooves and double bilayer height steps on the GaAs(001)-2x4 surface.* Journal of Crystal Growth, 1996. **163**: p. 113-121.
89. Ohno, T., *Theoretical study of atomic structures and dynamics on semiconductor surfaces.* Thin Solid Films, 1996. **272**: p. 331-344.
90. Ito, T., *Recent progress in computer-aided materials design for compound semiconductors.* J. Appl. Phys., 1995. **77**(10): p. 4845-4886.
91. Shiraishi, K., *First-principles calculations of surface adsorption and migration on GaAs surfaces.* Thin Solid Films, 1996. **272**: p. 345-363.
92. Shiraishi, K. and T. Ito, *First principles study of arsenic incorporation on a GaAs(001) surface during MBE growth.* Surf. Sci., 1996. **357-358**: p. 451-454.
93. Ito, T. and K. Shiraishi, *Theoretical investigations of initial growth process on GaAs(001) surfaces.* Surface Science, 1997. **386**: p. 241-244.
94. Ito, T. and K. Shiraishi, *A theoretical investigation of migration potentials of Ga adatoms near step edges on GaAs(001)-c(4x4) surface.* Jpn. J. Appl. Phys., 1996. **35**: p. L1016-L1018.
95. Shiraishi, K. and T. Ito, *Ga-adatom induced As rearrangement during GaAs epitaxial growth: Self-surfactant effect.* Physical Review B, 1998. **57**: p. 6301.
96. Ito, T. and K. Shiraishi, *Theoretical investigations of adsorption behavior on GaAs(001) Surfaces.* Japanese Journal of Applied Physics - Part 1, 1998. **37**: p. 4234-4243.
97. Ito, T. and K. Shiraishi, *Electron counting Monte Carlo simulation of the structural change of the GaAs(001)-c(4*4) surface during Ga predeposition.* Japanese Journal of Applied Physics - Part 2, 1998. **37**: p. 262-264.
98. Ito, T., K.E. Khor and S.D. Sarma, *Systematic approach to developing empirical potentials for compound semiconductors.* Physical Review B, 1990. **41**: p. 3893-3896.
99. Palma, A., E. Semprini, A. Talamo and N. Tomassini, *Diffusion constant of Ga, In, and As adatoms on GaAs(001) surface: Molecular dynamics calculations.* Materials Science and Engineering B, 1996. **37**: p. 135-138.
100. Salmi, M.A., M. Alatalo, T. Ala-Nissila and R.M. Nieminen, *Energetics and diffusion paths of gallium and arsenic adatoms on flat and stepped GaAs(001) surfaces.* Surface Science, 1999. **425**: p. 31-47.
101. Mokwa, W., D. Kohl and G. Heiland, Phys. Rev. B, 1984. **29**: p. 6709.

102. Seebauer, E.G. and C.E. Allen, *Estimating surface diffusion coefficients.* Progess in Surface Science, 1995. **49**: p. 265-330.
103. Markov, I., *Surface energetics from the transition from step-flow growth to two-dimensional nucleation in metal homoepitaxy.* Physical Review B, 1997. **56**: p. 12544-12552.
104. Ohta, K., T. Kojima and T. Nakagawa, Journal of Crystal Growth, 1989. **95**: p. 71-78.

Chapter 6: Linking Models

In this chapter, linking of macro-scale finite element models with micro-scale Kinetic Monte Carlo models will be described. As a variety of models describe the different length and time scales in MOVPE growth, linking methodologies are developed to combine the models into a coherent process model. This process model can then be used to do *a priori* modeling of a system to determine optimal operating parameters. An introduction and review of linking methodologies are given. In Section 6.2, finite element models of MOVPE reactors are separated into gas phase and surface models. The separated model is tested for both accuracy and convergence properties in Section 6.3. Section 6.4 extends the linking to a different surface model, a KMC model for the growth of GaAs. Gas phase and surface predictions for the growth of GaAs are shown. Section 6.5 is a conclusion to the topic with an overview of linking methods.

6.1 Introduction

Considerable efforts have been devoted to develop physical models and simulation strategies within each length and time scale regime[1-3]. In this chapter, the focus is on linking methodologies between reactor models and surface models. The reactor scale model will be explored in detail, focusing in on how reactor scale models use surface scale models as a boundary condition. A case study will be shown removing the surface problem from the reactor model and solving both models in a concurrent fashion. This separation then can be extended to use various surface models. Kinetic Monte Carlo models of the surface of GaAs are then used along with reactor models as a model system to show the flexibility of this modeling methodology.

6.2 Theory of Linked Models

The premise in separating the surface model from the reactor scale model is that surface processes occur on a widely different time and length scale than the gas phase fluid flow

and reactions. Many simulations of CVD processes include the surface as a set of partial differential equations and include the gas phase and surface unknowns together in an overall solution vector. Thus the gas phase and surface unknowns are solved together. Other approaches invert the surface problem and couple the two problems through their expressions for flux of gas-phase species to the surface.

There are advantages and disadvantages to flux-splitting the problem. Separation of the gas phase and surface problems allows the use of a variety of models for the surface problem. Since the surface sub-problem has physical underpinnings, insights into its behavior (i.e. bounds on solution components) may be invoked to make its solution easier and more reliable when separated from the gas phase problem. For example, many surface and gas-phase chemical mechanisms have multiple solutions, with solution branches occurring in negative gas-phase or surface-phase species concentration regimes. These solutions are unphysical, but exist mathematically. By separating the surface-phase mechanism and ensuring that surface-phase concentrations are positive definite, the convergence properties of the entire problem may be improved. In a practical note, separation of the problem leads to a constant number of solution components at every grid node, a much easier coding task than if the number of unknowns differ from element to element.

The disadvantage of separating the problem lies in the additional computational time necessary in solving the problem. Typically the surface model will take more computational time to solve when a separate model is solved, rather than if the set of partial differential equations describing the surface-phase are solved along with the gas phase solution vector. A case study using SPIN[4] will show both the advantages and disadvantages of flux-splitting the MOVPE problem.

There have been attempts to link reactor and surface models. Srolovitz *et al.*[5] use a sequential approach to link reactor scale fluxes to surface models describing diamond deposition by chemical vapor deposition. In this approach, the reactor scale fluxes were computed initially and used as inputs into the surface model. Vlachos[6] extends this by

directly coupling simple surface models in order to determine the effect of gas phase fluxes on surface morphology. Rodgers and Jensen[7] also couple reactor and surface models for the application of etching and deposition of contact holes and vias in semiconductor processing. In this problem, the surface morphology evolves over time affecting the fluxes coming out of the surface model, which in turn affects the gas phase concentrations.

6.2.1 Flux Split Method – Equation Development

Both the coupled and flux-split modeling approaches start from the same basic equations. The flux-split method connects the gas phase and surface problems through the boundary condition on the gas-phase species flux at the surface. The gas-phase species conservation equations may be simply stated as in Equation 6.1,

$$\rho\frac{\partial Y_k}{\partial t}+\rho\mathbf{u}\bullet\nabla Y_k=\rho D_k\nabla^2 Y_k+F(\mathbf{Y},\frac{\partial\mathbf{Y}}{\partial n}) \tag{6.1}$$

Where Y_k is the mass fraction of gas-phase species k, $\mathbf{Y}$ is the vector of all gas phase species mass fractions, $d\mathbf{Y}/dn$ is the gradient of mass fraction vectors normal to the surface, facing into the surface. The boundary condition is shown in Equation 6.2,

$$\mathbf{n}\bullet(j_k+\rho\mathbf{u}Y_k)=-\dot{s}_k(\mathbf{Y},\theta,\mathbf{X}^{\mathbf{b}},t)W_kM \tag{6.2}$$

$$k=1,\ldots,N_g$$

where j_k is the diffusive mass flux of gas-phase species k, θ is the concentration of surface species, $\mathbf{X}^{\mathbf{b}}$ is the vector of bulk mole fractions, t is the time, $\mathbf{n}$ is the outward-facing normal to the gas phase (facing into the surface). The molar production rate of gas phase of species k due to surface reactions, $\dot{s}_k$, is generally a complicated function of gas-phase mole fractions, surface species concentration, bulk mole fractions, temperature and pressure. The molecular weight is shown as W_k. The morphological area function is shown as M (assumed as one in our case). In undulating or patterned surface morphologies, M can change from one. Under certain conditions, M can be a complex function of reactor conditions, and as shown by Rodgers and Jensen{Rodgers, 1998 #149}, different linking methods must be developed to solve this interesting problem.

To obtain the macroscopic flux of a gas-phase species, one integrates the microscopic surface flux term, $\dot{s}_k$, over the microscopic area and then divides by the macroscopic area. The term, $n \bullet j_k$, is related to the gradient of the mass fraction of k in the direction of the surface normal, and for binary systems reduces to Equation 6.3. For multi-component systems or systems with thermal diffusion, it can be a quite complex function.

$$-\rho D_k \frac{\partial Y_k}{\partial n} = n \bullet j_k \tag{6.3}$$

The second expression on the left-hand side of Equation 6.2 is the Stefan velocity component. It can be found by summing Equation 6.2 over all gas phase species to yield Equation 6.4,

$$n \bullet j_k = -\dot{s}_k W_k - \left[\sum_{k=1}^{N_g} \dot{s}_k W_k \right] Y_k \tag{6.4}$$

To close the conservation equations for gas phase species an expression for the surface production rates due to surface reactions, $\dot{s}_k(Y,\theta,\mathbf{X}^{\mathbf{b}},t)$ must be obtained.

To determine $\dot{s}_k(Y,\theta,\mathbf{X}^{\mathbf{b}},t)$, a surface model must be solved at each surface node. This model can be general in nature and can range from a simple, closed-form expression for the surface production to separate complex models. In this study we will compare the flux-split methodology with the coupled methodology using a set of partial differential equations to describe the dynamics of the surface.

6.2.2 Surface Model – Equation Development

The typical surface model used in reactor models is a set of partial differential equations describing the surface species. This derivation is taken from the Surface Chemkin[8] description of the surface. The starting point for the derivation of these equations comes

from the time-dependent conservation equations. Equation 6.5 describes the change in total mass of surface species k with respect to time,

$$\frac{\partial}{\partial t}\left(A c_k^s W_k\right) = A W_k \dot{s}_k(\mathbf{Y},\theta), \qquad k = K_s^f,\ldots,K_s^l \tag{6.5}$$

where c_k^s is the surface concentration of the kth surface species (mole cm^{-2}), A is the microscopic surface area (treated here as a constant), K_s^f is the first surface species in the first surface phase, and K_s^l is the last surface species in the last surface phase. The concentration of surface species is broken down further into the surface site fraction of surface species k, θ_k, and surface site density of phase n on which species k is defined, Γ_n, using Equation 6.6,

$$c_k^s = \frac{\Gamma_n \theta_k}{\sigma_k} \tag{6.6}$$

where σ_k is defined as the number of surface sites the kth surface species covers. There is the possibility that the value of Γ_n changing over time (i.e. surface sites of type n may be created or destroyed as part of the surface mechanism). This leads to additional variables for the surface problem of Γ_n. An expression for the surface site fractions may be obtained by plugging Equation 6.6 into Equation 6.5.

$$\Gamma_n \frac{\partial \theta_k}{\partial t} + \theta_k \frac{\partial \Gamma_n}{\partial t} = \sigma_k \dot{s}_k(\mathbf{Y},\theta) \qquad k = K_s^f,\ldots,K_s^l \tag{6.7}$$

Equation 6.7 does not fully specify the surface site fractions, since for any valid surface mechanism, Equation 6.8 also holds true.

$$\frac{\partial \Gamma_n}{\partial t} = \sum_{k=K_s^f(n)}^{k=K_s^l(n)} \sigma_k \dot{s}_k \tag{6.8}$$

In Equation 6.8, n specifies the phase for each of the surface species. Equation 6.8 is the surface site conservation equation, and is used to determine the production rate of surface

sites for phase *n*. An additional requirement must be added so that all the surface site fractions for each surface phase must sum to one:

$$\sum_{k=K_s^f(n)}^{K_s^l(n)} \theta_k = 1 \tag{6.9}$$

Equation 6.9 has been incorporated into the equation set by the replacement of one of the surface site species in the conservation equation, Equation 6.7, with Equation 6.9 for each surface phase. The equation to be replaced is set to the one corresponding to the surface species with the largest site fraction. This leads to a reduction in numerical round-off errors.

For deposition, the relative growth rates can be used to provide for an equation for the bulk mole fractions, $\mathbf{X^b}$. Equation 6.11 represents the bulk mole fractions for all bulk species in bulk phase *n*,

$$X_k^b = \frac{\max(\dot{s}_k^b(\mathbf{Y},\theta,X_k^b),0)}{G_n} \text{ where } G_n = \sum_{k=K_b^f(n)}^{K_b^l(n)} \max(\dot{s}_k^b,0) \tag{6.10}$$

where G_n is the total growth rate of bulk phase *n*.

The equations to be solved in the surface problem are encompassed by Equations 6.7, 6.8, 6.9, and 6.10. The unknowns consist of θ_k , Γ_n, and $\mathbf{X^b}$. The steady-state problem is obtained by dropping all time derivatives from Equations 6.7 and 6.8.

The solution of the surface problem is accomplished using Placid, a routine developed in MPSalsa[9]. Placid uses a damped Newton's method to relax the surface problem. The relaxation method uses an extremely conservative time-stepping algorithm.

6.2.3 Separation of Surface and Gas Phase in FEM Models

Both the coupled and flux-split problems actually solve the same equation set. The coupled approach adds the unknowns from the surface problem into the global unknown

solution vector and solves the entire gas and surface phase problem. The flux-split methodology solves the surface problem separately from the gas phase problem. The surface solver takes the gas-phase concentrations at the surface as input and returns the gas-phase fluxes. The gas-phase problem then uses the gas phase species surface fluxes as a boundary condition for the gas-phase species continuity equation in the residual calculation.

A schematic for both methodologies is shown in Figure 6.1.

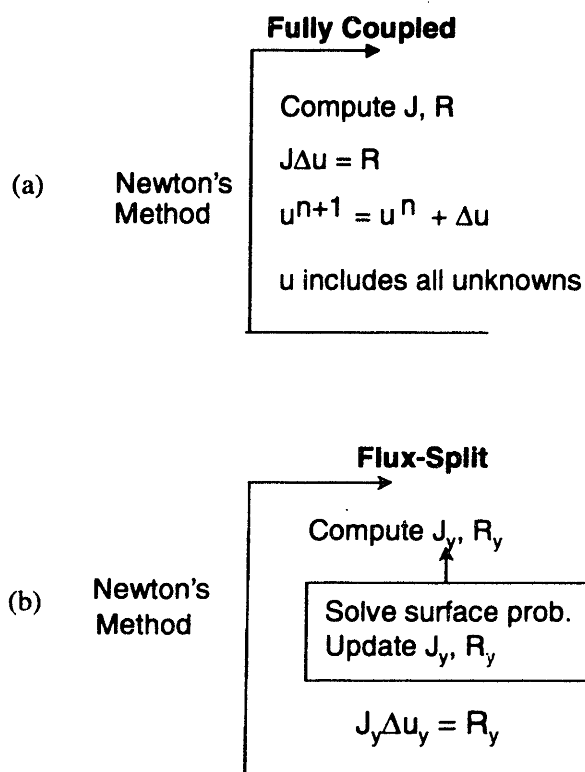

Figure 6. 1: Algorithm for (a) Fully coupled methodology to solve surface and gas phase unknowns in MOVPE reactor simulations; (b) Flux-split methodology whereby the surface problem is separated from the gas phase problem and solved separately, maintaining consistency through the flux of species to the surface; *J* is the Jacobian, *R* is the residual, *u* are the unknowns, *y* corresponds to the gas phase.

As seen in the coupled method, all the unknowns are lumped and solved together. In the flux-split methodology, the surface problem is solved separately and used as the flux boundary condition. The Jacobian stencil in the Newton's method to solve the overall set of partial differential equations is shown in Figure 6.2.

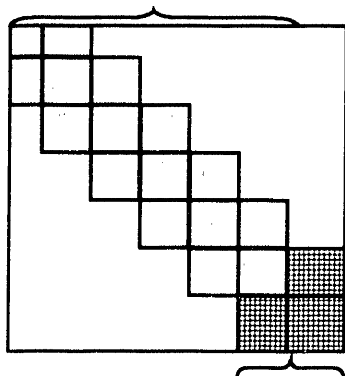

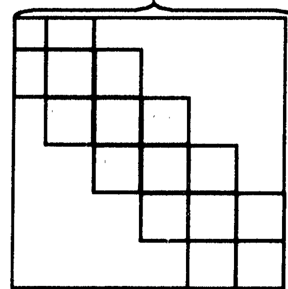

Figure 6. 2: Jacobian matrix for (a) Fully coupled methodology; (b) Flux-split methodology. Note that the matrix size is slightly smaller in the flux-split methodology, but the bandwidth is similar.

The coupled problem has a slightly larger matrix problem to solve since both gas and surface phase unknowns are included. The cost to invert the Jacobian matrices is almost the same, since the bandwidth of the two matrices is typically the same. Only if the number of surface unknowns is larger than the number of unknowns in the gas-phase problem is the bandwidth larger for the coupled problem.

The flux-split method is closely associated with a subblock-solution method for a linear system. In that method, a linear system is considered to be broken up into two parts, as shown by Equation 6.11. Each subblock has its own set of solution components, X1 and X2. The matrix is then split up into 4 subblocks, with the off-diagonal subblocks representing the interaction terms between the subblocks.

$$\begin{bmatrix} A_{11} & A_{12} \\ A_{21} & A_{22} \end{bmatrix} \begin{bmatrix} X_1 \\ X_2 \end{bmatrix} = \begin{bmatrix} B_1 \\ B_2 \end{bmatrix} \tag{6.11}$$

The second block can be inverted and presolved if X_1 is known through Equation 6.12,

$$X_2 = A_{22}^{-1}[B_2 - A_{21}X_1] \tag{6.12}$$

Thus the first subblock matrix problem becomes Equation 6.13,

$$[A_{11} - A_{12}A_{22}^{-1}A_{21}]X_1 = B_1 - A_{12}A_{22}^{-1}B_2 \tag{6.13}$$

The flux-split method links the two subblocks at the non-linear solver level. Therefore, Equation 6.12 and 6.13 is not fully representative of the matrix problem in the flux-split method.

6.3 Steady State Solution and Convergence Comparison

The steady state solution for the coupled problem and the flux-split problem are compared for a few representative reaction mechanisms to test that the methods produce the same solution. A simple study is done to compare the convergence properties of the two methods.

A mechanism for the deposition of SiN[10] is used to compare the two solution methods. The mechanism includes 17 gas-phase species, 33 gas-phase reactions, 6 surface-phase species, 2 bulk phase species, and 6 surface-phase reactions. The comparison was done using SPIN, a code that solves for the species, temperature, velocity profiles, and deposition rates in a steady-state one-dimensional rotating disk or stagnation-point flow reactor. Solutions for the steady-state mole fractions of HF and SiF_4 using both methods are shown in Figures 6.3 and 6.4.

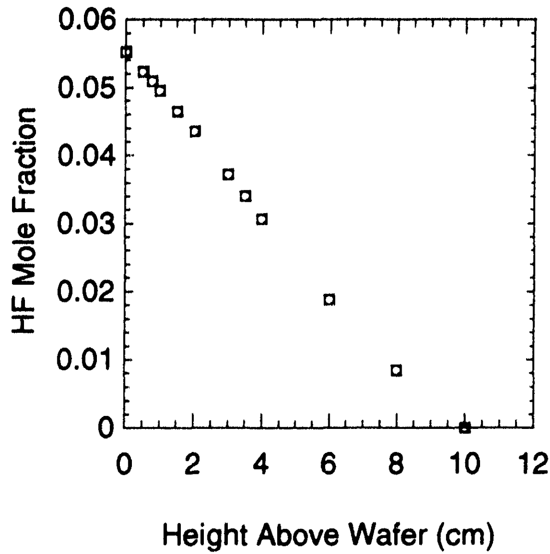

Figure 6. 3: Comparison of the steady state mole fractions of HF using (+) coupled and (o) flux-split linking methodologies.

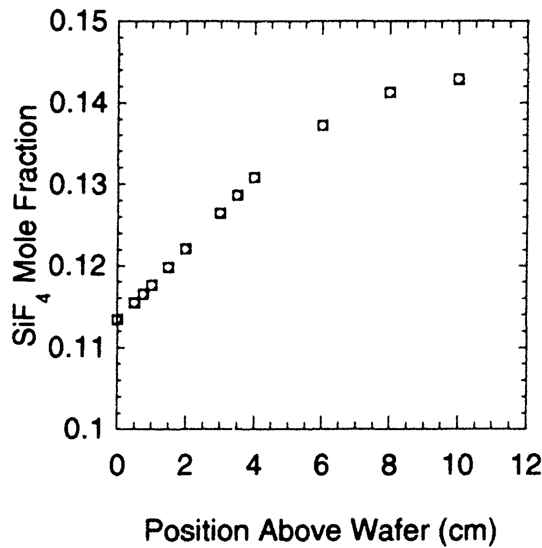

Figure 6. 4: Comparison of the steady state mole fractions of SiF_4 using (+) coupled and (o) flux-split linking methodologies.

As the comparisons show, the two methods produce the exact same solution.

Convergence properties for the two methods are compared by supplying poor initial guesses and checking whether the methods converge to a solution. The mechanism used to test the convergence properties of the two methods is one used to model GaAs

deposition from $Ga(CH_3)_3$ and AsH_3 with H_2 as a carrier gas[11]. The mechanism includes 17 gas phase species, 6 surface species, 2 bulk species, 24 gas-phase reactions, and 38 surface reactions.

The initial guesses for the surface site fractions are very important for the coupled problem. Empirically, we have found cases where poor initial guesses for the surface unknowns prohibits the coupled problem from converging to a solution, regardless of how good the gas phase initial guesses. The poor initial guess for the surface site fractions consist of equal fractions for each species, whereas the true solution has one species that is very high in concentration compared to the others. The problem with the same (poor) set of initial guesses is solved successfully using the flux-split method. Poor initial guesses for the surface species do not hinder the flux-split method from converging to a correct steady-state solution. Given either method poor guesses for the gas phase and good guesses for the surface phase lead to convergence in both methods. The surface model's relaxation method for solving the surface problem (based on a false transient algorithm) pushes the surface concentrations into appropriate physically realistic regime, regardless of the initial guess.

Transit time stepping must be done in the surface model to relax the surface problem before a steady state solution can be found. Typically, this only needs to be done the first time the surface model is called, as further calls to the surface model have similar gas phase concentrations and do not change the surface site fractions greatly. This is shown in Figure 6.6, as the number of Newton iterations taken per call to the surface model decreases sharply after the first few calls to the surface model.

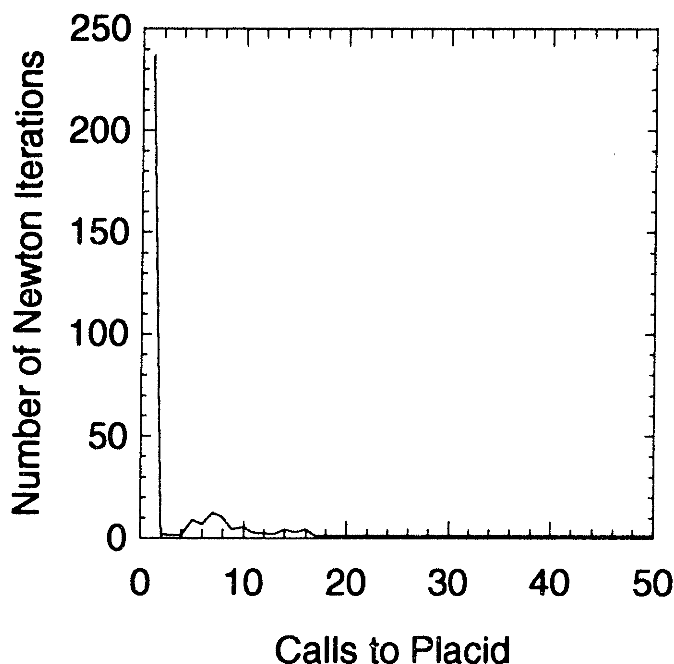

Figure 6. 5: Number of Newton iterations needed for convergence of the surface model as a function of the calls to the surface model.

There is a trade-off in using the separated method, as more work is done in solving the surface problem separately than is done in the coupled method. As shown above, the extra work is used to solve problems with poor surface guesses that could not be solved using the coupled method. A comparison in run times for solving the problem with good initial and gas phase guesses in shown in Table 6.1.

Table 6. 1: Comparison of computation times between methods

Method	Time in Surface Model (sec)	Time for Matrix Solve (sec)	Time for Matrix Fill (sec)	Total Time (sec)	Total Residual Evaluations
Coupled	0.0	113.49	99.419	311.95	14134
Separated	203.96	365.64	377.82	682.81	15970

A substantial amount of work is done in the surface model to solve the surface problem for every residual calculation. This behavior is reflected in the greater total time needed for convergence using good initial guesses.

6.4 Linking to KMC surface models

Using the same linking methodology, realistic reactor scale models can be linked to KMC models of growing films to predict both macroscopic and microscopic features in the growth. In this section, both the reactor scale and surface model will be described, as well as the linking between the models. Then, results of the model will be compared to experimental GIXS results. The main point of this section is to show that each model run separately would not be able to predict important features of the growth, but linked the models can make predictions on various length scales.

6.4.1 Reactor Model:

The set of differential equations describing mass transfer, heat transfer, and chemical mechanisms in the reactor is solved by discretizing the reactor domain and solving for unknowns using the Finite Element Method (FEM). The methodology is described in detail in Fotiadis *et al.*[12] Partial differential equations describing heat and mass transfer are solved to generate the flow and temperature fields in the reactor. The flow and temperature fields along with the chemical mechanism are then used in solving for species concentrations throughout the reactor. The separation of solving the flow and temperature fields before solving for the species concentration profile in the reactor assumes that the heat of reaction due to chemical reactions in the gas phase do not affect the flow and temperature fields. This is a good assumption for many MOVPE systems, as the concentration of the reacting species is normally extremely dilute compared to the concentration of the carrier gas. From the concentration profiles in the reactor, the flux to the surface of reactive precursors can be estimated to compute growth rate and uniformity of the film.

In this work, a reactor designed by Kisker, Fuoss, Stephenson, and Brennan[13] is modeled. Shown in Figure 6.6 is a two-dimensional axisymmetric diagram of the reactor.

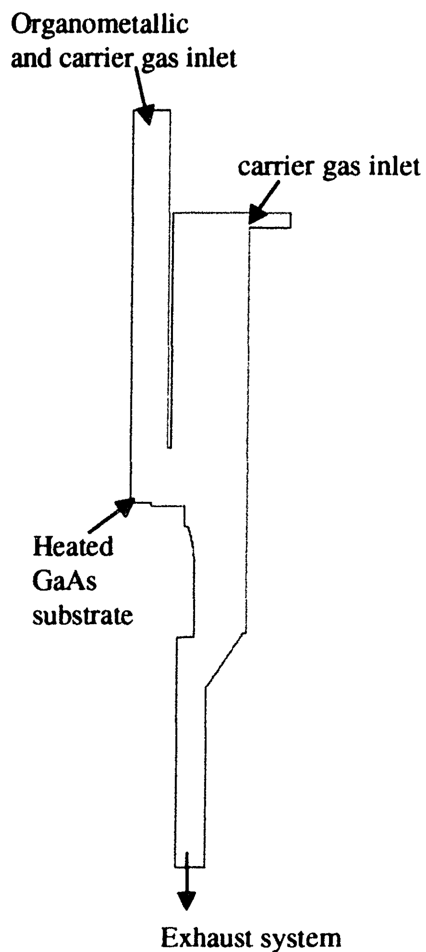

Figure 6. 6: Two dimensional axisymmetric portrayal of reactor used in GIXS experiments[13].

A simplified gas phase mechanism for the precursors, triethylgallium (TEG) and tertiarybutylarsine (TBAs), is shown in Table 6.2.

Table 6. 2: Gas Phase Mechanism for GaAs growth from TBAs and TEG.

	Reaction	Rate	Reference
1	$C_4H_9AsH_2 \rightarrow i\text{-}C_4H_8 + AsH_3$	$1.7x10^{14}\exp\left(\frac{-48.5kcal}{RT}\right)$	[14]
2	$(C_2H_5)_3Ga \rightarrow (C_2H_5)_2GaH + C_2H_4$	$1.2x10^{14}\exp\left(\frac{-37kcal}{RT}\right)$	[15]
3	$(C_2H_5)_2Ga \rightarrow (C_2H_5)\ GaH_2 + C_2H_4$	$1.2x10^{14}\exp\left(\frac{-37kcal}{RT}\right)$	[15]
4	$(C_2H_5)Ga \rightarrow GaH_3 + C_2H_4$	FAST	

Diffusion and thermal diffusion coefficients were determined through the usual group contribution methods.

6.4.2 Kinetic Monte Carlo Model

In this work, the KMC method is used to model the evolution of the GaAs surface during MOVPE growth using TEG and TBAs. Table 5.3 has a list of the transitions and accompanying rates. Transitions 6-9 in Table 5.3 were used in the simulations, as the other rates are much faster than the rate-limiting steps to growth (diffusion and incorporation). Inherent in the growth mechanism is the assumption that Ga is the limiting reagent, so As is assumed to incorporate fast compared to Ga. This is usually assumed for MOVPE of GaAs as most reactors are operated As rich.

The only other input parameters to the KMC model are the anisotropic barriers to incorporating at an up or down step and the nucleation mechanism. It has been hypothesized that this anisotropic barrier to incorporation leads to step bunching[16, 17].

Both parameters have been extracted through comparison to X-ray diffraction data[18, 19]. The anistropic barriers have been extracted through comparison to the degradation in the oscillating signal for layer-by-layer growth. The overall roughening of the surface during growth could cause this degradation. The difference between incorporating at an up step (hopping across a terrace to incorporate at a step edge) and a down step (hopping down from a ledge to incorporate) is estimated as 2.2 kcal. This estimate was obtained by varying the barrier and determining the overall degradation of the signal. Too large of a barrier difference leads to a smoothing of the surface (no degradation of the signal) , while too small leads to a coarsening of the surface. The nucleation mechanism was derived from the comparison of the island formation with the diffuse scattering[18, 19]. The diffuse scattering provides an estimate of the correlation length, the average distance between islands on the surface. Nucleation occurs in the model when specific configurations of Ga atoms arrange on the surface, as shown in Figure 6.7.

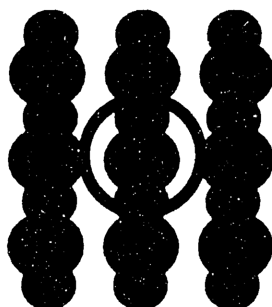

Figure 6. 7: Nucleation mechanism for Ga on GaAs(100) surface. The circled adatom is fixed in this configuration.

Nucleation occurs when a Ga adatom is surrounded by other Ga adatoms. Then, the center Ga adatoms is fixed (as shown by the circle in Figure 6.7). After nucleation, the center Ga adatom is fixed, and other adatoms can incorporate around it. Incorporation occurs when an adatom has at least 1 other incorporated atoms as a nearest neighbor and also has at least 2 total adatoms as nearest neighbors.

To study the GaAs system, one terrace is modeled. The model system is shown in Figure 6.8.

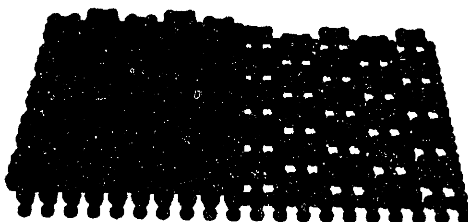

Figure 6. 8: Vicinal surface of GaAs(100) studied.

The terrace length is computed using the initial miscut of the surface. Periodic boundary conditions are used to limit edge effects. A step is introduced in the middle of the system to allow for step-flow motion.

6.4.3 Linking the Models

The FEM and MC models are connected through the flux of species to the substrate. The MC model uses the flux given by the FEM as inputs, and returns the computed flux. The FEM uses the flux calculated by the MC model as a boundary condition at the substrate. The solutions of both problems are iterated until a consistent flux to the surface is determined. The FEM uses a Newton's method to solve for the gas phase species unknowns. In the Newton's method, a Jacobian (direction matrix) and residuals (error terms for each unknown) are calculated analytically using the partial differential equations describing the chemistry of the system. At the elements near the substrate, species fluxes from the surface are needed. When the surface fluxes are needed, the Monte Carlo code is called and a flux is computed and sent back to the FEM code. The Jacobian is updated by numerically differentiating the surface fluxes to obtain the derivatives of fluxes with respect to the unknown species. This method of solving the surface problem separately from the gas phase problem and linking through the boundary

conditions of both models allows the use of any model for the surface problem. This methodology is exactly the same one developed in Section 6.2.

To minimize running the computationally expensive MC code, a set of procedures has been developed. A set of partial differential equations representing the surface processes can be used as a surface model, which can then be fully coupled to the partial differential equations representing the gas-phase. By solving this problem, a steady state gas phase solution is obtained. Using this steady state solution as an initial guess in the "linked" model minimizes the number of MC runs needed in converging the Newton's Method. Also, a table of fluxes at varying conditions is stored to minimize the running of the MC code.

6.4.4 Monte Carlo Model Comparison

The MC model is used to determine the transition between step flow and island-growth (layer-by-layer) modes. During step-flow growth modes, the majority of the Ga adatoms incorporate at a terrace edge. Island growth occurs when islands nucleate and coalesce on terraces. Normally step flow growth is preferred, as flatter films are generally produced. The growth mode is determined through a complex function of temperature, flux of adatoms to the surface, and initial miscut of the crystal. Temperature affects the diffusion length of the adatoms on the surface. The flux of species affects the total surface concentration of adatoms on the surface, which affects the probability of island nucleation. The initial miscut of the crystal determines the average initial terrace length. If the diffusion length of an adatom is larger than the terrace length and there are fewer adatoms on the surface than needed for nucleation, adatoms will incorporate at kink sites on terrace edges and step-flow growth will occur. If adatoms cannot reach terrace edges before nucleating or incorporating on islands in the middle of a terrace, then island-growth modes arise.

Experimental studies have determined the growth mode by examining the X-ray scattering from the surface in MOVPE reactors off the surface. The X-ray scattering is

monitored at a Bragg peak[20, 21]. At this peak, the bilayers of GaAs scatter exactly out of phase with the adjacent bilayers. A smooth surface corresponds to one bilayer of scattering; as the surface roughens during island growth, the bilayers scatter out of phase with each other and a low scattering signal is recorded. This X-ray scattering signal can be interpreted as a measure of the roughness of the surface. During island growth, there is an oscillation in the X-ray intensity as the surface roughens during the nucleation of islands on the surface, and smoothes during the coalescence of the islands. Step-flow growth produces a constant X-ray intensity, as the overall roughness of the surface remains constant during growth.

MC simulations can determine the transition by computing the variance of the surface height over the growth period. Oscillations in this measure of surface roughness would correspond to island growth and a constant signal would correspond to step-flow growth. A comparison of the oscillations in the X-ray intensity for an experimental and corresponding simulated system is shown in Figure 6.9.

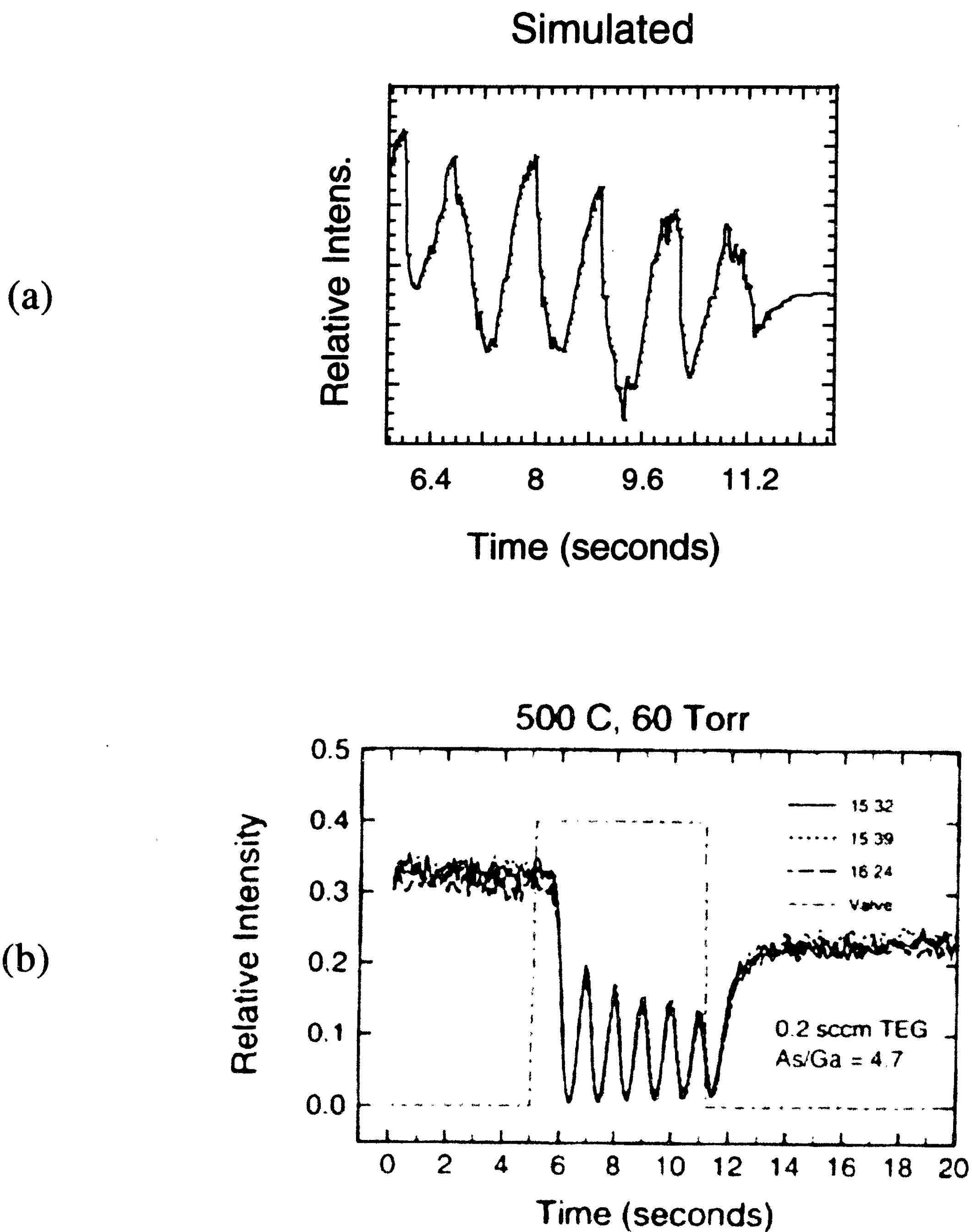

Figure 6. 9: Comparison of CTR oscillations between (a) simulated and (b) experimental systems.

The simulated signal matches the frequency of the experimental signal. As the simulated signal is a measure of the surface roughness in the system, as more monolayers are grown, the maximum roughness of the surface increases. This is shown by the

decreasing minimums in each of the oscillations. The experimental signal does not show this decrease, as the degree of roughness of the surface is not measured.

6.4.5 Linked Model Comparisons

Through linking the models, predictions on both the macroscopic gas phase and the "mesoscopic" surface can be made. The linked model is compared to experimental growth rate experiments for the growth of GaAs from TEG and TBAs. In the experiments, TEG and TBAs are flowed into the reactor (shown in Figure 6.5) and react on a heated substrate. The growth rate is monitored by in-situ X-ray scattering, and the number of oscillations of the X-ray intensity gives the number of monolayers of GaAs grown. The linked model is used to simulate the exact operating conditions of the reactor.

A comparison of growth rate with changing inlet flux is shown in Figure 6.10(a). The simulated growth rates exactly match the experimental measurements. The straight line in Figure 6.10 shows that the growth is mass transport limited. For a given flux to the surface, the temperature is varied, and the experimental and simulated growth rate is shown in Figure 6.10(b).

(a)

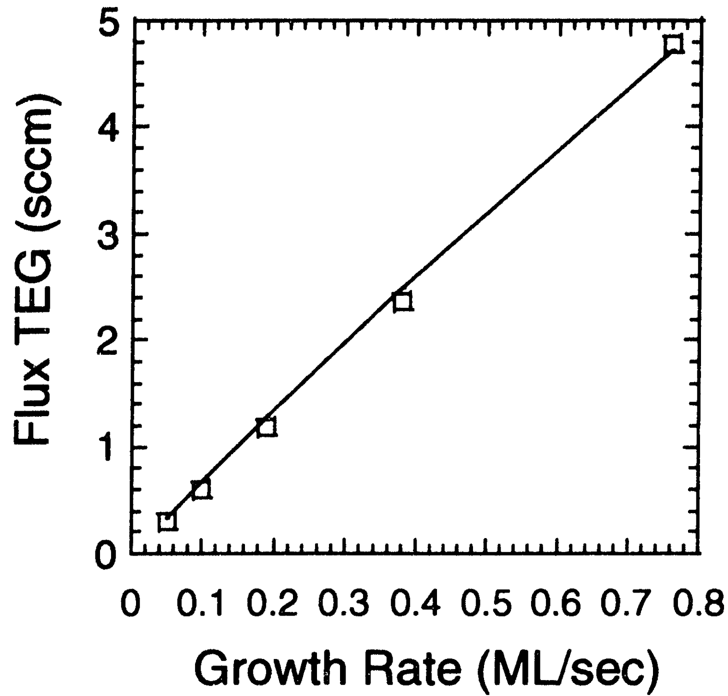

(b)

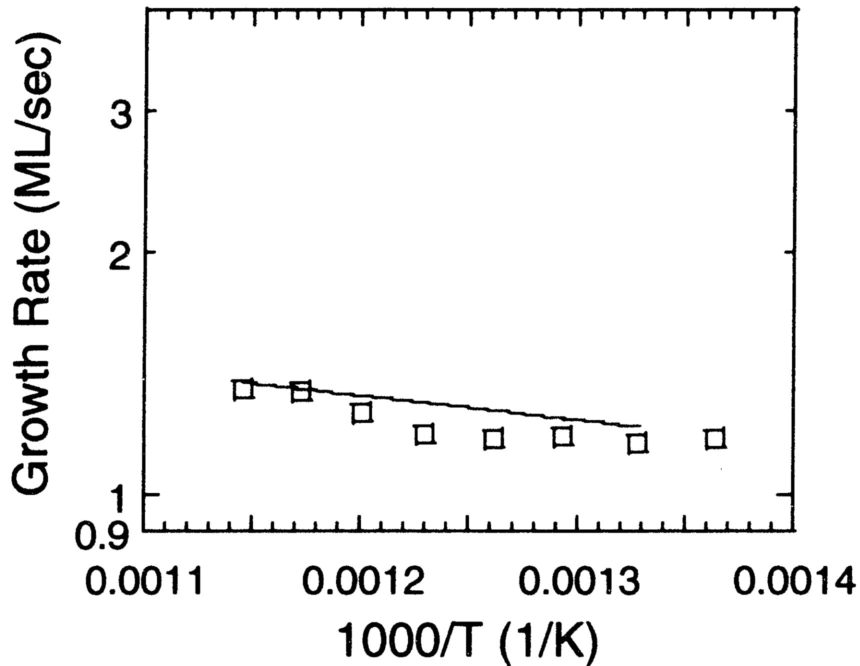

Figure 6. 10: Map of growth rate as a function of (a) flux of Ga precursor and (b) temperature; ( ) experimental data , (-) simulation results.

Again, the simulated growth rates match the experimental growth rates closely. It is interesting that a mass transport limited system has a slope corresponding to an activation

energy of 4 kcal. From the simulations, this slope is due to the increased diffusion of species at higher temperature, which increases the concentration of precursors at the surface, leading to higher growth rates. These flow effects on the growth rate cannot be determined unless a reactor scale model is used. Monte Carlo simulations of the evolution of surface morphology cannot be input the correct flux of species to the surface without the use of these reactor simulations.

The morphology of the surface during and after growth cannot be determined by FEM, but can be determined by Monte Carlo simulations. By linking the MC simulation to the FEM, the growth mode can be determined at various operating regimes. Shown in Figure 6.11 are the experimental and simulated mappings of growth modes with changing flux and temperature.

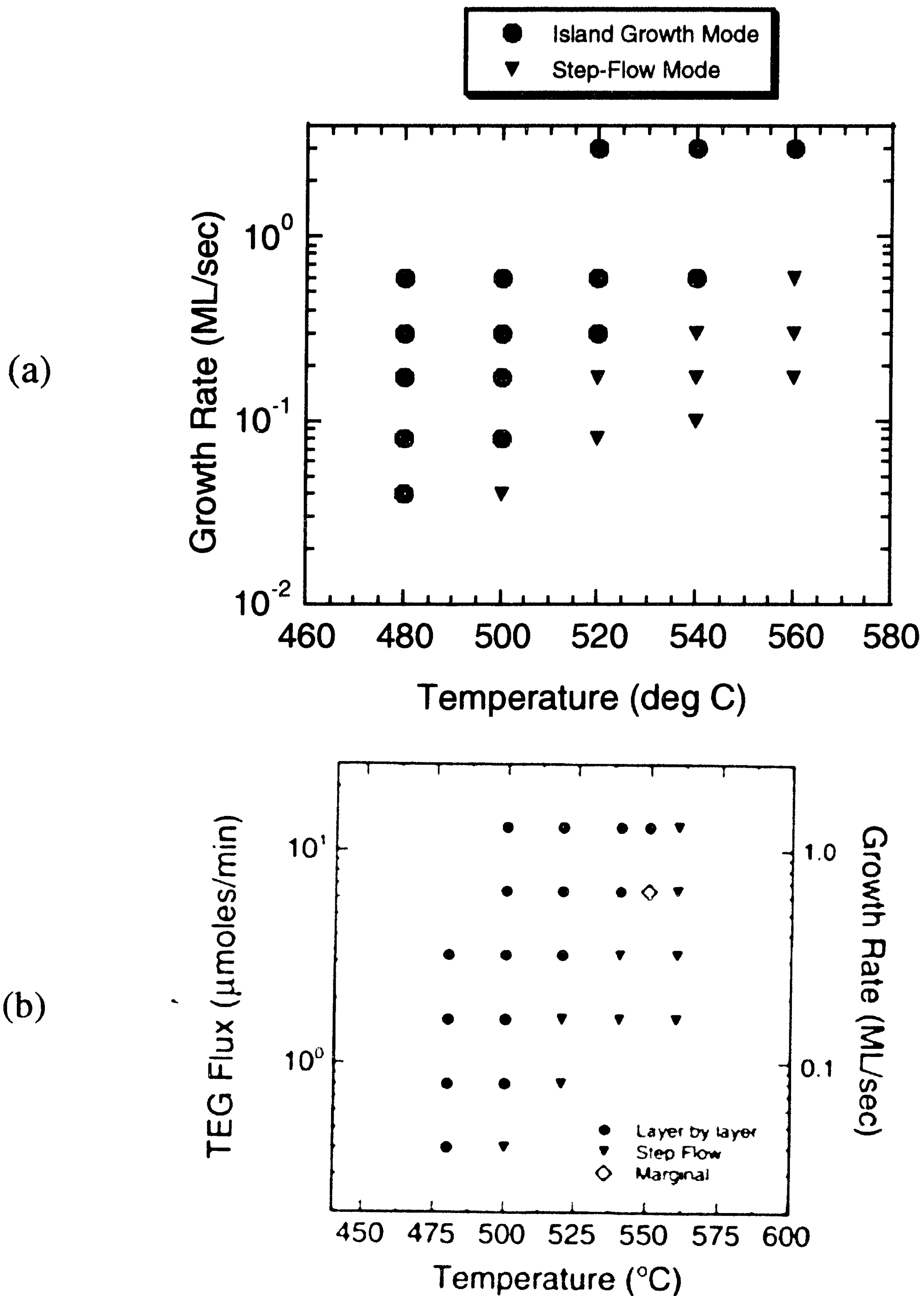

Figure 6. 11: Map of surface morphology as a function of temperature and growth rate, (a) simulated, (b) experimental

Good agreement is found with the experimental and simulated results, except at high temperatures and growth rates. The model does not include the breaking up of islands, and at high temperatures and growth rates, the breaking off of adatoms from the lattice may be significant.

There are some deficiencies to this model, specifically in the KMC surface model. The diffusion barrier used, 2.7 eV, is much larger than typical diffusion barriers found on semiconductor surfaces. This barrier, although measured experimentally[22], is probably an effective barrier for diffusion. This effective barrier may be made up of a sequence of reaction and diffusion steps on the surface. As shown in Chapter 7, a more rigorous model that includes As dimers on the surface will be needed in order to determine smaller surface structures. When effective barriers are used, large-scale surface structures can be determined (such as growth mode) but smaller scale structures on the surface (such as island density) can be determined only by using microscopic inputs. This again brings up the point that the inputs to the model must be on the same scale as the outputs for the model.

6.5 Conclusions

Surface and gas phase models for MOVPE growth are linked through their flux boundary condition at the edge of the growing wafer. The methodology for linking includes flux-splitting the models. It was shown that flux-splitting exactly matches a coupled model. The benefits of flux-splitting the problem include better convergence when poor initial guesses for the surface unknowns are given. Also, any surface model can be used; all that is needed is a model that takes incoming fluxes and solves for the resulting flux. The disadvantages of flux-splitting the problem include longer simulation run-times.

The methodology was tested on a case study of GaAs growth using TEG and TBAs. Using a realistic reactor geometry, the linked model was able to predict both macroscopic features of the film (such as growth rate), as well as microscopic details (growth mode on the surface). The benefit of such linked models is the ability to make predictions on

multiple length scales. Using each model separately, one would not be able to predict both growth rate and morphology. The reactor scale model cannot predict the morphology of the film, and the surface model needs as an input, the flux of gas phase species to the surface.

Bibliography:

1. Jensen, K.F., *Transport phenomena in epitaxy systems*, in *Handbook of Crystal Growth*, D. Hurle, Editor. 1994, Elsevier: Amsterdam. p. 543-599.
2. Vvedensky, D.D., M. Itoh, G.R. Bell, T.S. Jones and B.A. Joyce, *Island nucleation and growth during homoepitaxy on GaAs(001)-(2x4).* Journal of Crystal Growth, 1999. **201/202**: p. 56-61.
3. Simka, H., B.G. Willis, I. Lengyel and K.F. Jensen, *Computational chemistry predictions of reaction processes in organometallic vapor phase epitaxy.* Prog. Cryst. Growth Charact., 1997. **35**: p. 117-149.
4. Kee, R.J., G.H. Evans and M.E. Coltrin, *SPIN - One Dimensional Laminar Spinning-Disk Reactor Code*, . 1996, Sandia National Laboratories: Livermore, CA.
5. Srolovitz, D.J., D.S. Dandy, J.E. Butler, C.C. Battaile and Paritosh, *The integrated multiscale modeling of diamond chemical vapor deposition.* Journal of Materials, 1997. **49**: p. 42-47.
6. Vlachos, D.G., *The role of macroscopic transport phenomena in film microstructure during epitaxial growth.* Applied Physics Letters, 1999. **74**: p. 2797-2799.
7. Rodgers, S.T. and K.F. Jensen, *Multiscale Modeling of CVD Processes.* J. Appl. Phys., 1998. **83**: p. 524-530.
8. Rupley, F., *Surface Chemkin*, . 1996, Sandia National Laboratories: Livermore, CA.
9. Moffat, H.K., *MPSalsa*, . 1996, Sandia National Laboratories: Albuquerque, NM.
10. Melius, C.F. and P. Ho, *Theoretical study of the thermochemistry of molecules in the Si-N-H-F system.* J. Chem. Phys., 1991. **95**: p. 1410-1419.
11. Salinger, A.G., J.N. Shadid, S.A. Hutchinson, G.L. Hennigan, K.D. Devine and H.K. Moffat, *Analysis of gallium arsenide deposition in a horizontal chemical vapor deposition reactor using massively parallel computations.* Journal of Crystal Growth, 1999. **203**: p. 516-533.
12. Fotiadis, D.I., S. Kieda and K.F. Jensen, J. Crystal Growth, 1990. **102**: p. 441.
13. Brennan, S., P.H. Fuoss, J.L. Kahn and D.W. Kisker, Nucl. Instrum. Methods. Phys. Res., Sect. A, 1990. **291**: p. 86.
14. Larsen, C.A., N.I. Buchan, S.H. Li and G.B. Stringfellow, J. Crystal Growth, 1989. **94**: p. 663.
15. Lee, P.W., T.R. Omstead, D.R. McKenna and K.F. Jensen, J. Crystal Growth, 1987. **85**: p. 165.
16. Kasu, M. and T. Fukui, *Multi-atomic steps on metalorganic chemical vapor deposition-grown GaAs vicinal surfaces studied by atomic force microscopy.* Jpn. J. Appl. Phys., 1992. **31**: p. 864-866.
17. Kasu, M. and N. Kobayashi, *Equilibrium multiatomic step structure of GaAs(001) vicinal surfaces grown by metalorganic chemical vapor deposition.* Appl. Phys. Lett., 1993. **62**(11): p. 1262-1264.
18. Kisker, D.W., G.B. Stephenson, P.H. Fuoss, F.J. Lamelas, S. Brennan and P. Imperatori, *Atomic scale characterization of organometallic vapor phase*

epitaxial growth using in-situ grazing incidence X-ray scattering. J. Crystal Growth, 1992. **124**: p. 1-9.

19. Kisker, D.W., G.B. Stephenson, P.H. Fuoss and S. Brennan, *Characterization of vapor phase growth using X-ray techniques.* J. Crystal Growth, 1995. **146**: p. 104-111.
20. Robinson, I.K. and D.J. Tweet, *Surface X-ray Diffraction.* Rep. Prog. Phys., 1992. **55**: p. 599.
21. Robinson, I.K., *Crystal truncation rods and surface roughness.* Phys. Rev. B, 1986. **33**(6): p. 3830-3836.
22. Seebauer, E.G. and C.E. Allen, *Estimating surface diffusion coefficients.* Progess in Surface Science, 1995. **49**: p. 265-330.

Chapter 7: Putting it all together-Realistic Linked Simulations for GaAs Growth

This chapter is the capstone of the thesis; many of the methodologies developed in chapters 1 through 6 are used to simulate a realistic system. The system studied is a reactor used by Kisker *et al.*[1] for GIXS experiments. This system allowed a quantitative comparison of both gas phase concentrations and surface morphologies. Section 7.1 is an introduction to the system and the modeling methodologies. A review of the experimental setup and results are contained in 7.2. The models are briefly reviewed in 7.3 and the resulting gas-phase and surface predictions are elucidated in section 7.4. Conclusions are in Section 7.5.

7.1 Introduction

Understanding the microscopic surface processes that occur in semiconductor growth during MOVPE is critical in order to determine reactor processing conditions to grow high quality films. Due to the extreme conditions encountered in MOVPE (high pressures and temperatures), an in-situ study of the surface during growth is difficult. In-situ studies of GaAs growth during MOVPE have been done using grazing incidence x-ray scattering (GIXS)[2] and reflectance difference spectroscopy (RDS)[3]. Also, ex-situ methods, such as scanning tunneling microscopy[4] and atomic force microscopy[5] have been performed in order to understand the surface morphology during growth. Experimental and theoretical work has been reviewed in Chapter 5.

In this work, GIXS is applied for the in-situ study of the vapor phase epitaxial growth of GaAs using organometallic sources. Surface kinetics will be derived from the literature and used to compare simulated and experimental growth morphologies. The difficulty in producing a single model describing MOVPE is inherent in the complex nature of the process; physical processes occur on a variety of length and time scales. Heat and mass transport in the gas phase occurs on the length scales of millimeters, while surface

processes occur on the length scale of nanometers. A combination of modeling techniques will be used to analyze the system; models describing the heat and mass transport in the gas phase of the reactor will be linked to models of the evolving surface morphology. Linking methodologies have been developed in Chapter 6.

In this chapter, the KMC model developed for MOVPE surfaces is used in conjunction with a reactor scale model that mimics the exact reactor used in the GIXS experiments. This allows a quantitative comparison between gas phase concentrations, growth rates, and surface morphology.

7.2 Experimental Results

The experimental system has been described previously[1, 2, 6, 7]. The experimental runs were done using triethylgallium and tertiarybutylarsine in a carrier gas of H_2 at a pressure of 60 torr. The crystal truncation rod (CTR)[8] and the in-plane diffuse scattering was observed as a function of time. Shown in Figure 7.1(a) is the time dependent CTR for a typical growth run at 580 ° C. The CTR shows the familiar oscillations of roughening and smootning that corresponds to layer-by-layer growth. Each oscillation corresponds to one bilayer of GaAs growth. Shown in Figure 7.1(b) is a typical diffuse scattering map monitored in the $[\bar{1}10]$ direction. The well-defined maximum at $\Delta q = 0.02$ $Å^{-1}$ is a measure of the island-island correlation length on the surface when the surface is half covered with islands (at a minimum in CTR intensity). At half coverage of islands, the correlation length between islands should be similar to the island size in that direction. The temperature and flux dependence of the island-island correlation length can be seen in Figure 7.2. The diffuse scattering was monitored in the [110] direction and the correlation lengths were found to be between 2 and 3 times higher in this direction than in the $[\bar{1}10]$ at 540 ° C and 0.2 ML/sec. suggesting anisotropy in surface diffusion processes.

(a)

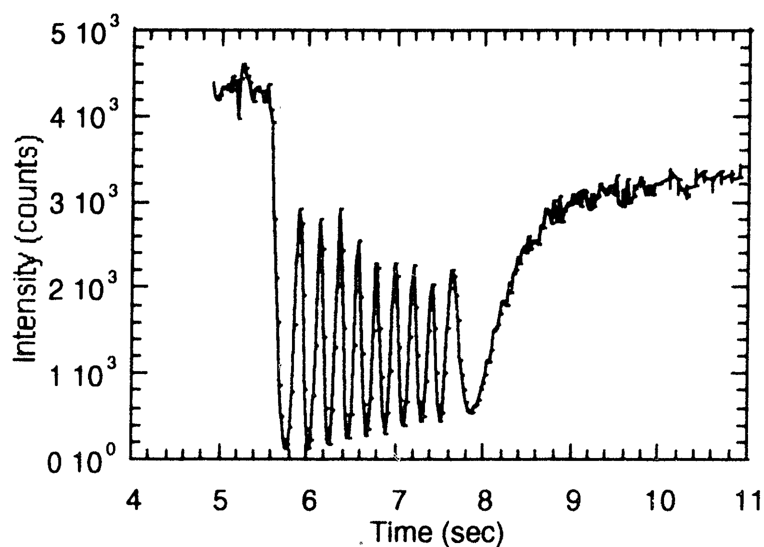

(b)

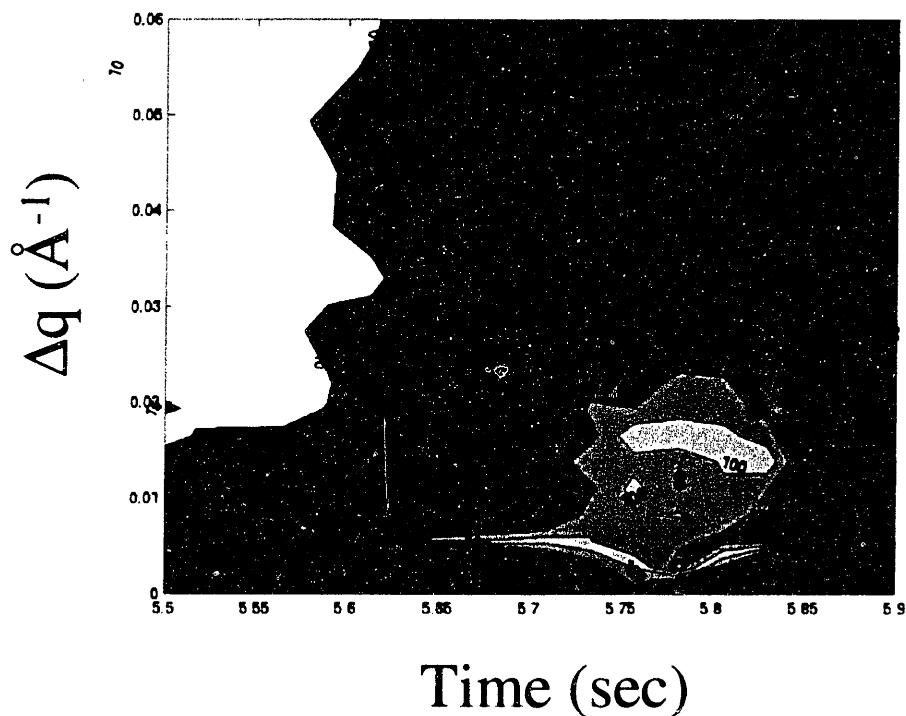

Figure 7. 1: (a) Time dependent crystal truncation rod for a typical growth run at 580 ° C.; (b) Diffuse scattering for a typical growth run. Note the maximum at the non-zero scattering wavevector, q, occurring at the minimum of the first CTR oscillation. This is a measure of the correlation length of islands on the surface.

(a)

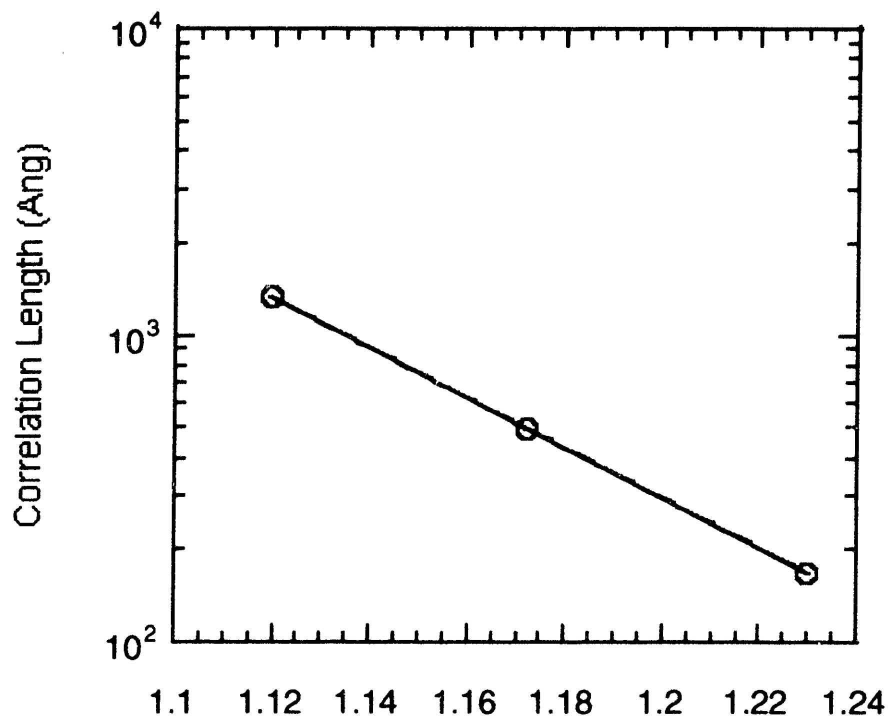

(b)

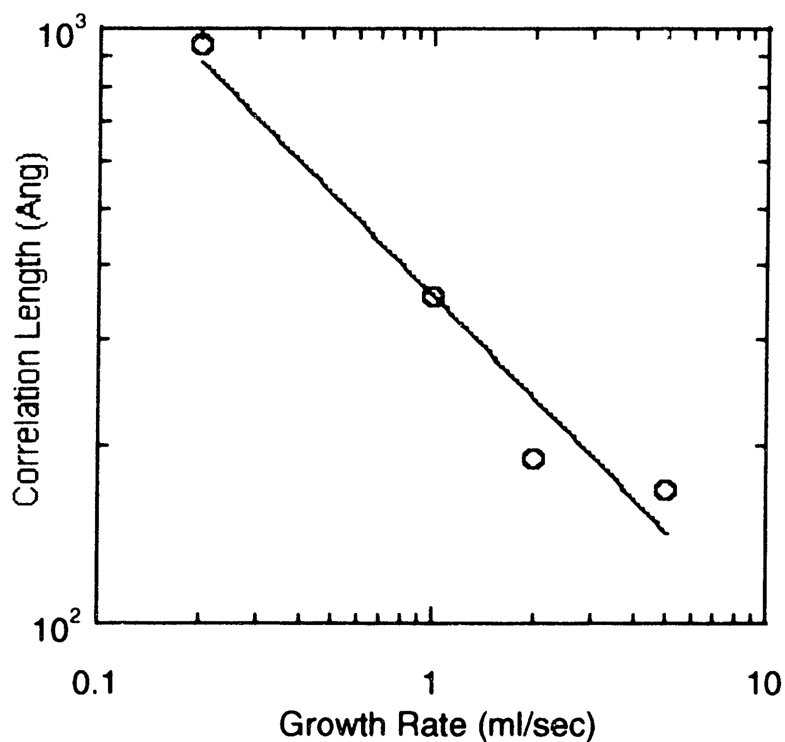

Figure 7. 2: (a) Temperature dependence on the correlation length measured from the diffuse scattering at a growth rate of 5 ML/sec; (b) Growth rate dependence on the correlation length measured from the diffuse scattering at T = 813 K.

7.3 Models

In order to understand the experimental data, reactor scale models are linked to models of the evolving surface morphology. The reactor scale model consists of a set of non-linear partial differential equations describing mass transfer, heat transfer, and the chemical mechanism in the reactor. The equations are solved over the reactor domain using the Finite Element Method (FEM). The methodology is described in detail in Fotiadis *et al.*[9] The gas-phase chemical mechanism for the precursors used is simplified from Mountziaris[10] and Ingle[11]. The reactor models are important in order to determine the correct flux of precursors to the substrate; many MOVPE reactors have complex flow and temperature fields that can affect the transport of growth species to the surface.

A Kinetic Monte Carlo (KMC) approach[12] is used to model the evolution of the surface morphology during growth. A modified solid-on-solid (SOS) model is used to represent the surface which takes into account the zincblende crystal structure of GaAs. Either singular or vicinal substrates are used as the initial surface, as shown in Figure 7.3.

(a)

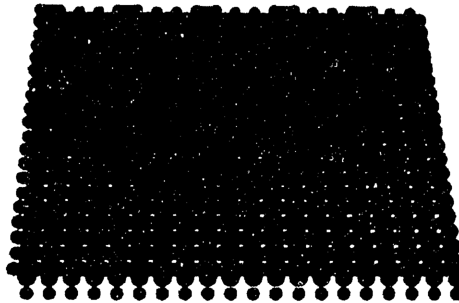

(b)

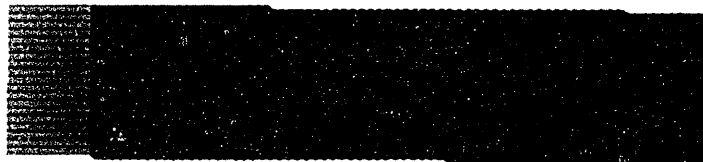

Figure 7. 3: Examples of simulation surfaces used in simulating GaAs(100) (a) singular; (b) vicinal.

The surface consists of 2D lattice sites whose separation is 0.4 nm, and each successive bilayer is shifted to match the zincblende crystal structure. A host of processes can modify the surface morphology, including adsorption of species, diffusion of species on the surface, surface reactions, and incorporation of species into the lattice. The methodology is similar to that used for simulating MBE growth of GaAs[13-15] and MOVPE growth[4].

Two different surface models were tested. Model I includes adsorption and diffusion of Ga species on the surface. In this model, As is ignored and assumed to incorporate immediately when an As site is available. The assumption is typically made in MOVPE grown GaAs, as the As is 10-40 times in excess of the Ga precursors during growth. The model is summarized in Table 7.1.

Table 7. 1: Model I – Ga dynamics only (typical parameters given).

Transition	Rate
Ga Adsorption	flux from reactor scale model
Ga Diffusion	$R_d = 1x10^{13} * \exp(-E_d/RT)$ $E_d = 1.3 + \#NN_{110} * 0.2 + \#NN_{\bar{1}10} * 0.2$

The important input parameters to the model are the rates of each of the transitions. Diffusion of Ga adatoms on the surface is given by Equation 7.1,

$$R_d = 1x10^{13} * \exp(-E_d/RT)$$
$$E_d = E_s + \#NN_{110} E_{N110} + \#NN_{\bar{1}10} E_{N\bar{1}10} \tag{7.1}$$

where R_d is the rate of diffusion and E_d is the activation barrier for diffusion. The activation barrier for diffusion can be anisotropic, as E_s, which is the diffusion of an adatom on a bare surface, can be a function of the direction of movement of the adatom. Also, the diffusion barrier for an adatom is affected by the number of lateral nearest neighbors, as $\#NN_{110}$ and $\#NN_{\bar{1}10}$ are the number of nearest neighbors of an adatom in the [110] and [$\bar{1}$10] directions respectively, and by the anisotropy of the nearest neighbor energies, as shown by E_{N110} and $E_{N\bar{1}10}$. Incorporation in the lattice occurs when adatoms are surrounded by other adatoms and As is added to the layer above. Incorporation is reversible, as adatoms can break away from nuclei.

Model II includes adsorption, diffusion, reaction of organic species, and As_2 adsorption and desorption. Only Ga species and As dimers on the surface are considered during growth, with As adatoms added to the surface immediately if a growth As site is available. This assumption is justified by the high V/III ratios usually used in MOVPE for growing GaAs films. The c(4x4) As rich reconstruction is automatically added to terraces on the surface by As_2 dimer adsorption desorption, as shown by GIXS studies[16]. The As_2 kinetics were derived from Adamson *et al.*[17] who modeled the desorption kinetics of arsenic species from GaAs(100). In modeling growth of GaAs from triethylgallium and tertiarybutylarsine, the reaction rates of the organic species on the surface must be considered in MOVPE growth. The As precursor is assumed to react

quickly to form As on the surface, with both organic species and H_2 desorbing from the surface[10]. The desorption of ethyl from the surface was entered as one of the transitions on the surface. The desorption of Ga adatoms from the surface is negligible compared to diffusion and incorporation. The final transition is the adsorption rate of species to the surface, and this is the link to the reactor scale model. Model II is summarized in Table 7.2.

Table 7. 2: Model II – Ga, As dimer, and organic dynamics

Transition	Rate	Reference
Ga flux	from model	Reactor scale model
As flux	from model	Reactor scale model
As dimer desorption	44 kcal - 8 kcal*# Ga adatoms - 4 kcal* # next nearest neighbor As adatoms	[17, 18]
$CH_5Ga(*) \rightarrow CH_5\ (g) + Ga(*)$	37.5 kcal	[19]
Ga diffusion - [110] direction	0.9 eV + 0.4 eV * # Ga adatom [110] direction + 0.2 eV * # Ga adatom $[\bar{1}10]$direction	[20]
Ga diffusion - $[\bar{1}10]$ direction	1.1 eV + 0.4 eV * # Ga adatom [110] direction + 0.2 eV * # Ga adatom $[\bar{1}10]$direction	[20]

The linkage between the reactor scale FEM model and the surface KMC model is through the flux of species to the surface. Methods have been developed to link the models that range from separating both models completely and using the flux from the FEM model as an input into the KMC model to embedding the KMC model into the FEM model as the boundary condition at the surface. Linking the models is needed for any type of predictive modeling of surface morphology; given reactor dimensions and operating conditions, the FEM code calculates the flux to the surface that the KMC code uses to predict morphologies. In this study, the KMC model was embedded in the Newton iteration of the reactor scale model, as shown in Chapter 6. This leads to a strong linking between the models through the flux boundary conditions and aids in convergence of the reactor scale model.

7.4 *Model Results*

Due to the flexibility of the linked models, both macroscale gas phase concentrations and microscale surface morphology can be compared.

7.4.1 Reactor Scale Comparisons:

To validate the reactor model, simulated TBAs concentrations are compared to experimental X-ray fluorescence data[1, 6]. In the experiments, the reactor was moved vertically past a stationary synchrotron beam. The fluorescence rate, a measure of the number density in the gas phase, was measured at heights above the GaAs substrate. The experiments consisted of flowing TBAs through the reactor, and measuring the As Kα fluorescence from the gas phase. The experimental and corresponding simulation results are shown in Figure 7.4.

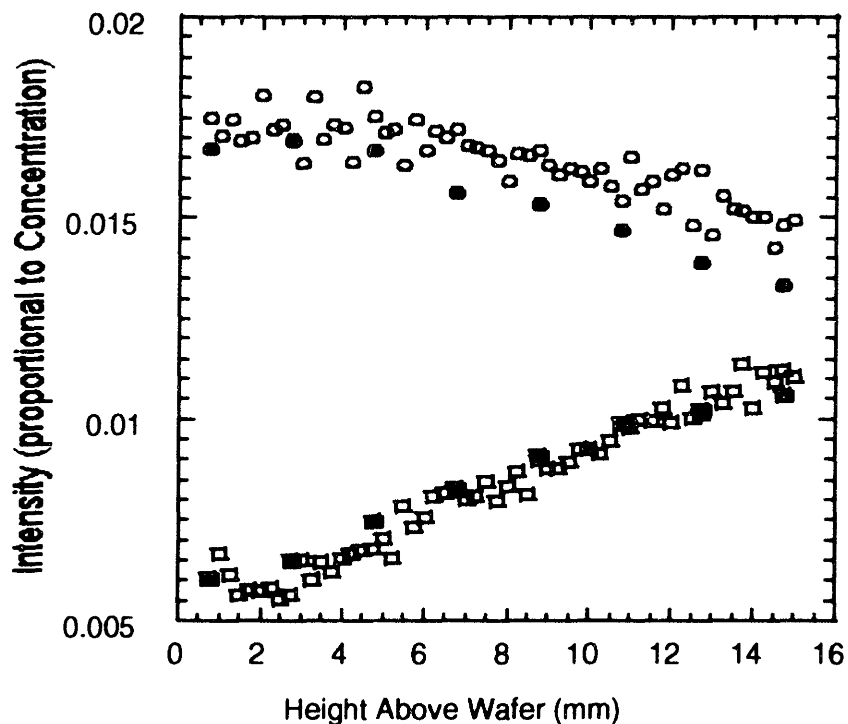

Figure 7. 4: Comparisons of experimental and simulated fluorescence of As as a function of distance above wafer. (O) Experimental at 50 C, (❑) Experimental at 510 C, (●) Simulated at 50 C, (■) Simulated at 510 C.

The simulations accurately predict the gas phase concentration of As in the reactor. Shown in Figure 7.5 are flood plots of the concentration of As precursors. In the low temperature (50 C) case, there is a maximum in concentration near the substrate.

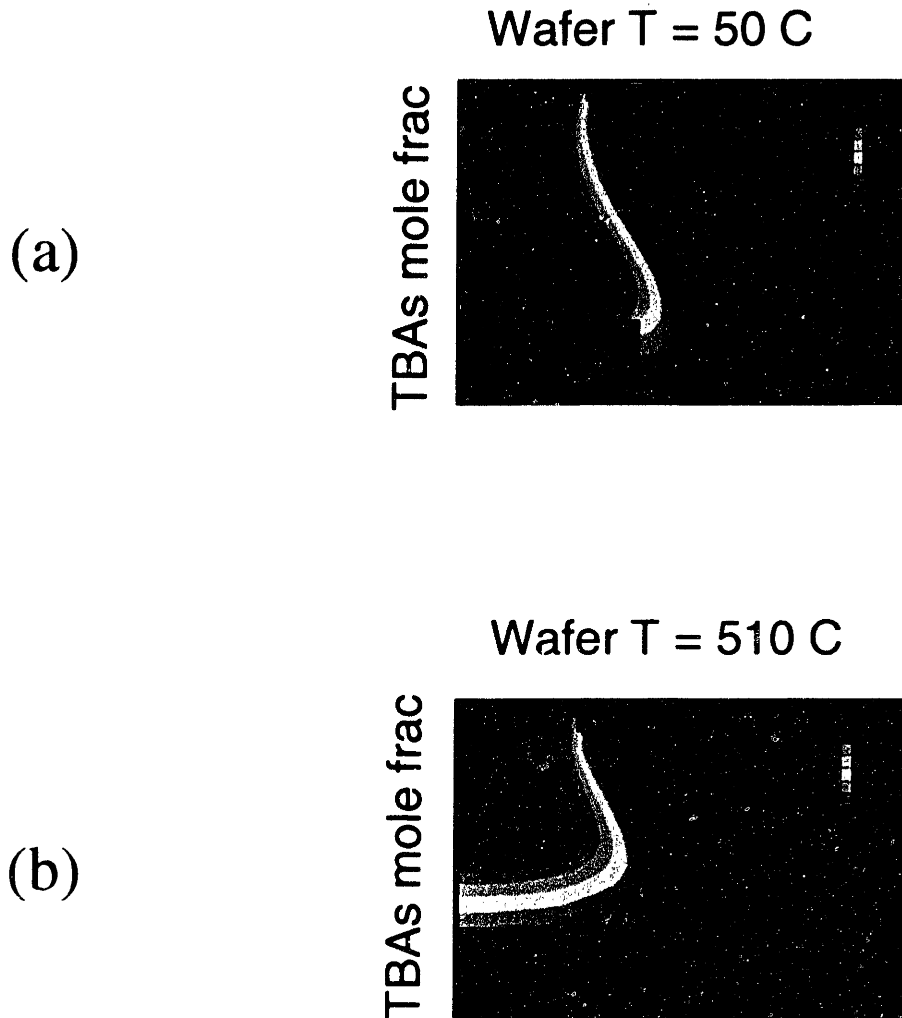

Figure 7. 5: Flood plots of the concentration of As above the wafer (a) 50 ° C; (b) 510 ° C.

The slow fluid velocities near the surface coupled with the lack of thermal diffusion away from the surface (due to the small thermal gradient) leads to a build up of As near the surface. The high temperature case (510 C) shows the opposite result. There is a significant decrease in the density of the gas near the heated substrate and therefore a decrease in the concentration of As-species. Also, thermal diffusion of the larger As species (compared to the smaller H_2 carrier gas) away from the hot substrate explains some of the decrease in concentration. The matching experimental and simulated results confirm the accuracy of the gas phase FEM model.

During growth processes, the temperature and flow profiles affect the concentration of growth precursors above the surface. A typical TEG concentration profile in the reactor is shown in Figure 7.6.

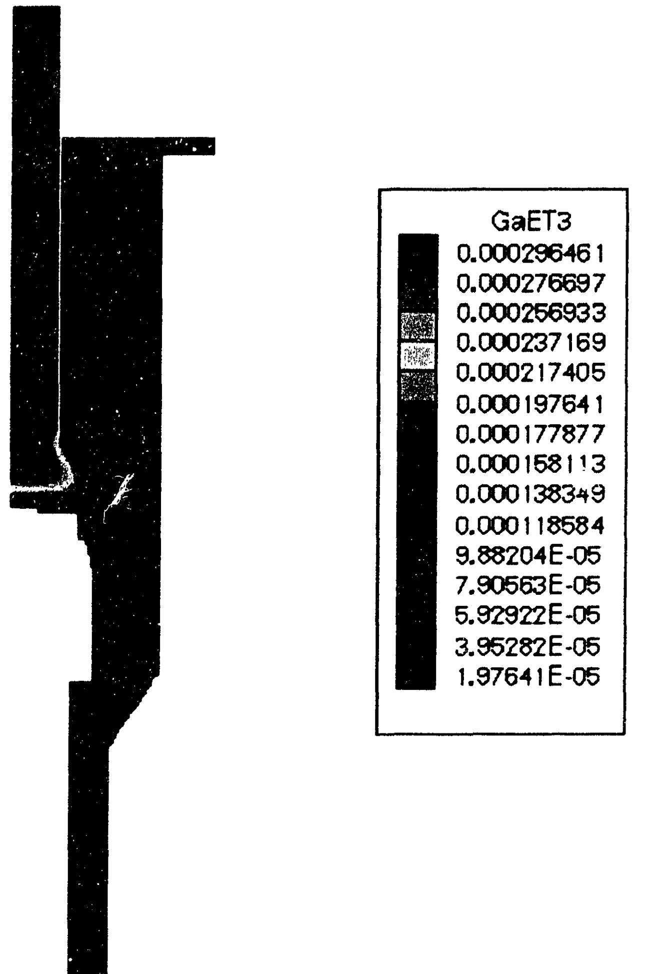

Figure 7. 6: Flood plot in the GIXS reactor of TEG concentration (mole fraction).

As seen by the concentration profiles, the TEG reacts on the surface, with the resulting depletion of concentration seen above the wafer. Also, a considerable flow of precursors never 'sees' the wafer and flows directly into the inlet. This underscores the importance of the gas phase reactor model in determining the correct flux of species to the wafer.

7.4.2 Surface Model Comparisons:

In comparing the model with the experimental results, different length scales can be compared. The growth rate can be compared on the micron scale, the growth mode can be compared on the nanometer scale, and the correlation length between islands can be compared on the order of hundreds of angstroms.

7.4.2.1 Growth Rate:

The growth rate can be compared using the linked model. By embedding the KMC model into the Newton steps, the growth rate can be determined from the KMC simulation as a function of the flux to the surface from the reactor scale model. This has been previously shown in Chapter 6, where the simulated and experimental growth rates matched using the linked model. A comparison of growth rate as a function of flux of Ga to the surface is shown in Figure 7.7 (using Model II). The model matches experimental growth rate measurements. A slight overestimate of the growth rate by the model is due to a finite size effect of the KMC model. Smaller than realistic size KMC models were used in the linking simulations in order to run the simulations in reasonable computation times. Due to the high diffusion rates, islands were formed more quickly on the surface than on a larger simulated surface. These islands created more available sites for adsorption that increased the effective growth rate. Moving to larger surfaces gives a more accurate growth rate measure. Nevertheless, this is again a validation of the reactor scale model, as this confirms the correct flux of precursors to the growth surface.

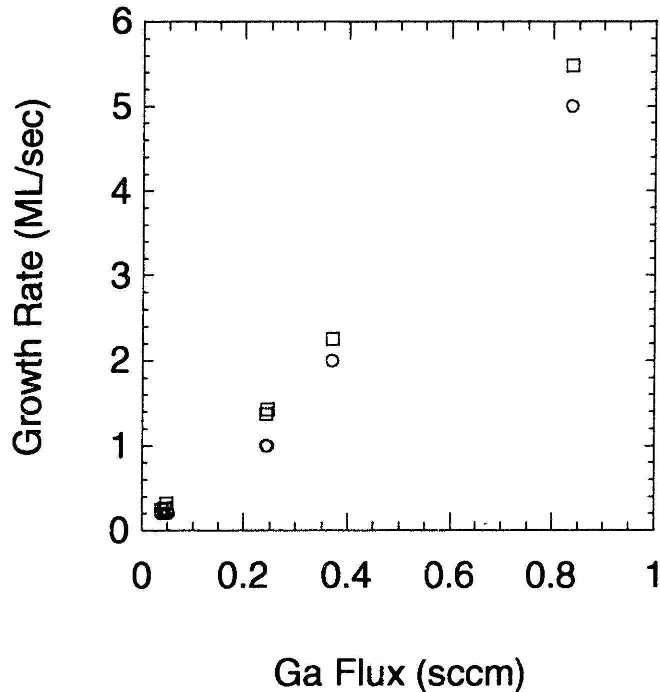

Figure 7. 7: Comparison of experimental (o) and simulated (□) growth rates in the GIXS reactor.

7.4.2.2 Correlation Length:

An interesting development in the experimental results is the temperature and growth rate dependence on the correlation length on the surface. Surface mobility is dependent on the temperature, growth rate, and surface. A comparison of these results to similar MBE results shows that Ga adatoms in MOVPE growth appear to be more mobile than in MBE growth, and also have a much larger dependence on temperature and growth rate. Computed from the transition from island growth to step flow growth, the apparent activation barrier for diffusion was computed as 2.3 to 2.7 eV from GIXS and RDS experiments in MOVPE growth[1, 3], while only from 1.3-1.58 eV for MBE surfaces[21]. These aggregate numbers are 'lumped' in that they are a function of many variables (miscut, temperature, growth rate). A better comparison is one between island sizes (correlation length) on the surface as a function of temperature and growth rate. This can be studied through both analytic models and KMC models of surface growth.

7.4.2.2.1 Analytic Models:

From standard nucleation theory[22], the correlation length should scale as in Equation 7.2, where D is the diffusion length, J is the flux to the surface, l_c is the correlation length, N_s is the number density of islands, and χ is an exponent that depends on the minimum number of atoms that form a stable nuclei.

$$N_s \propto l_c^{-2} \propto \left(\frac{D}{F}\right)^{-\chi} \tag{7.2}$$

The assumptions in the model include isotropic diffusion and irreversible attachment of the adatoms to the surface. The exponent, χ, can be computed from the experimental plot, Figure 7.2(b), but this leads to an unphysical value for χ of greater than 1, which implies an infinite number of atoms as the critical nucleus. Kisker[23] used the same approach to show that the critical number of atoms in order to form a nuclei should be very large (~25 atoms). The difficulty in applying these models to the GIXS experiments is the standard nucleation model is only directly applicable to the pre-coalescence regime, while the scattering measures the correlation lengths at half coverage of islands on the surface. This may be the reason for the unphysical value of the exponent. The assumptions in this model can be relaxed if a KMC model is used to represent the surface.

7.4.2.2.2 KMC Models:

To compare to the experimental scattering results, the CTR and diffuse scattering is computed from the simulated surface. The exact scattering is computed from the atomic positions by,

$$\begin{aligned} I &= A(q)A^*(q) \\ A(q) &= \sum_{j=1}^{N_c} f_j(q)\exp(iq \bullet r_j) \end{aligned} \tag{7.3}$$

where I is the intensity of the scattered beam, A is the structure factor, N_c is the number of atoms in the sample, f_j is the atomic scattering factor of atom j, r_j is the position of atom j, and q is the scattering wavevector[24]. The CTR for the simulations is computed at the [110] positon which is a bulk forbidden reflection; successive bilayers of GaAs scatter out of phase. This leads to the scattering being extremely sensitive to the top bilayers, so only the scattering from the highest level of the crystal at every site is computed. The diffuse scattering is computed in both the [110] and $[\bar{1}10]$ directions from the [110] position in order to examine the anisotropy of the islands on the surface. Predicted CTR and diffuse scattering are shown in comparison to the experimental diffuse scattering data.

The model scattering in Figure 7.8 shows the same features as the experimental scattering; oscillations in the CTR that correspond to layer-by-layer growth and oscillations in the diffuse scattering that are out of phase with the CTR. The initial signal for the CTR is different in the experimental and simulated surface, as the experimental surface had an As flux to the surface at all times. This created some disorder on the surface that lowers the initial signal. The simulated surface started with a clean surface (as shown by the high signal) and started both As and Ga fluxes at the same time. During growth the scattering shows the same features.

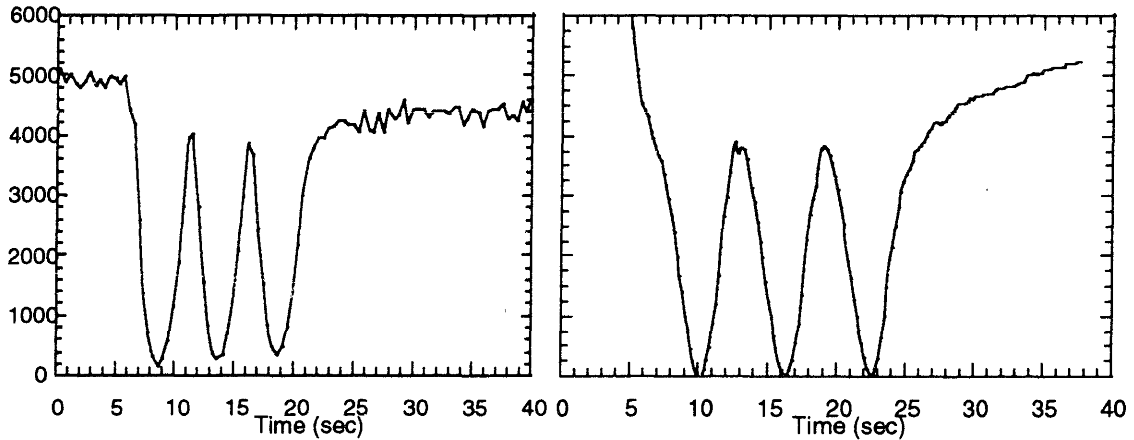

(a)

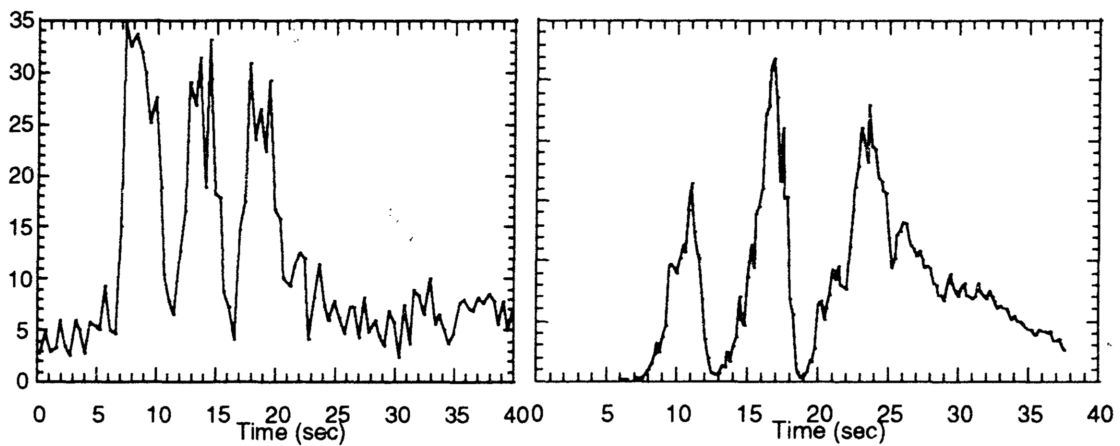

(b)

Figure 7. 8: Comparison of features of simulated and experimental CTR and diffuse scattering (q = 0.0374 Å^{-1}). Note the CTR oscillates with the onset of layer-by-layer growth and the diffuse scattering oscillates out of phase with the CTR.

7.4.2.2.3 Testing Model I:

Using the direct comparison between model and experiments, surface models are tested to explore the trends in correlation length on the surface as a function of temperature and

growth rate. Each of the simulated conditions is run on surface sizes of 512 by 512 angstroms or larger. First, simple MBE type diffusion models are used without As_2 adsorption and desorption.

Figure 7.9 shows a set of simulated runs with isotropic diffusion and nearest neighbor barriers. Similar results were obtained using a range of diffusion and nearest neighbor barriers. The temperature dependence of the simulated correlation lengths is less than the dependence of the experimental correlation lengths. The growth rate dependence of the correlation lengths is influenced by the nearest neighbor parameters. For this parameter range, the lower the nearest neighbor energies, the more strongly the correlation lengths of islands depend on the flux to the surface. Lower nearest neighbor energies imply a higher number of adatoms to form a stable nuclei . This suggests that the experimental slope of -0.57 for the growth rate dependence on correlation length is consistent with the idea that a large number of adatoms are needed for a critical nucleus in MOVPE growth. This can be contrasted to recent STM studies for MBE growth, where pairwise addition of 2 Ga adatoms to a critical nucleus of 2 adatoms is seen for GaAs(001) growth[25]. The dependence of temperature and growth rate on the correlation lengths is not consistent with the data in Model I.

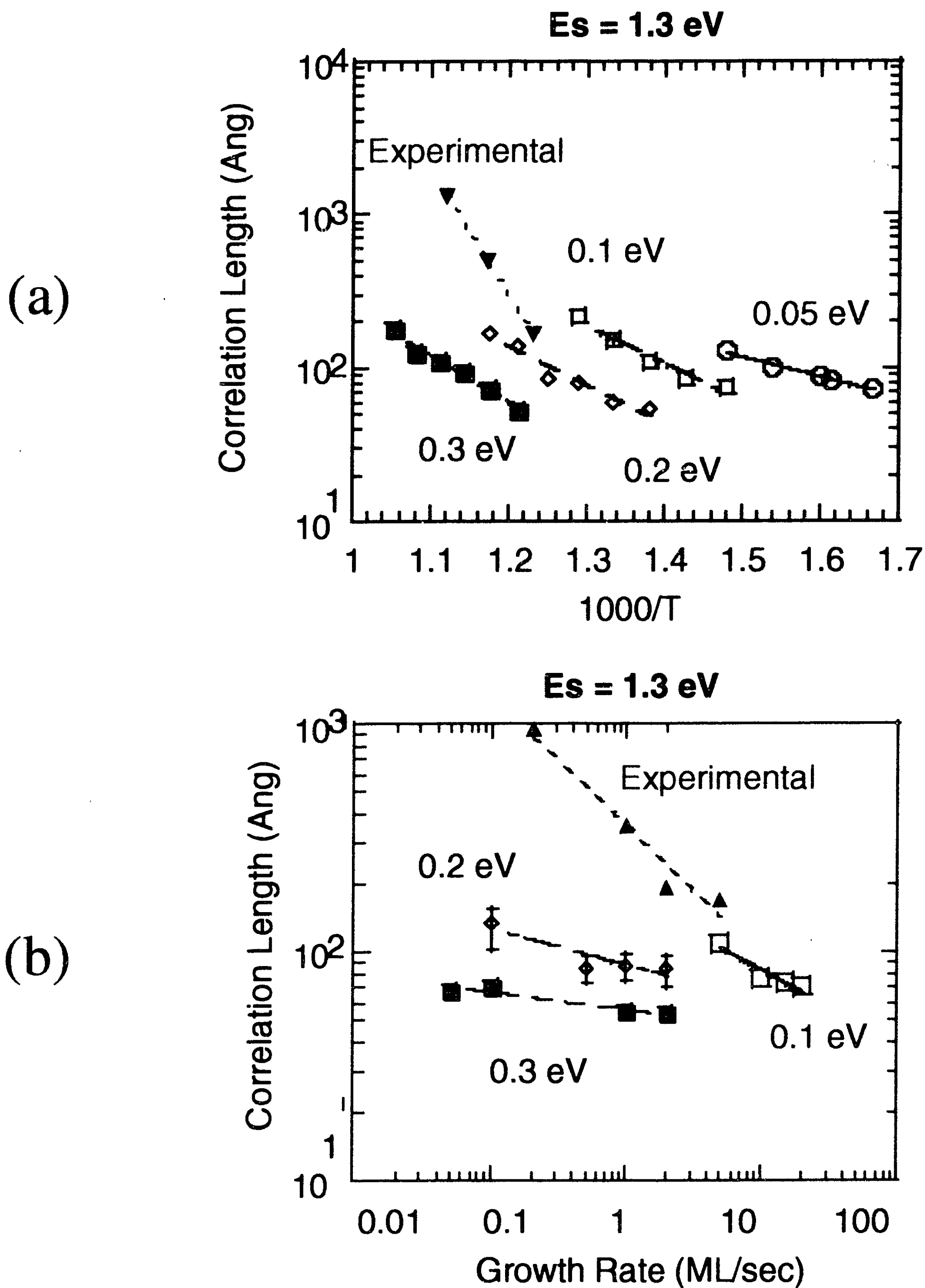

Figure 7. 9: Correlation length as a function of (a) temperature; (b) growth rate for a wide range of diffusion models. The numbers in the graph give the nearest neighbor barriers for each curve.

From STM studies of MOVPE GaAs growth[4], islands are longer in the [110] direction than the $[\bar{1}10]$ direction, and the experimental diffuse scattering results are consistent

with this result. This leads us to examine the effects of surface diffusion anisotropy to the model. In Figure 7.10, the degree of anisotropy of the diffusion coefficient, E_s, is studied.

The temperature dependence is similar to that using isotropic diffusion. It is to note that the dependence on growth rate is constant over the range of anisotropies studied. This seems to imply that the nearest neighbor parameters control the growth rate dependence of the correlation length. Over the entire range of anisotropies studied, the maximum ratio of correlation lengths in the [110] to the $[\bar{1}10]$ direction is ~1.4, lower than the experimental values. A plot of the ratio of the correlation lengths in the [110] and $[\bar{1}10]$ direction is shown in Figure 7.10(c). Differences in anisotropy of the diffusion barrier do not change the anisotropy of the islands to a degree anticipated due to the breaking off of adatoms from nucleated islands in the fast diffusion direction. The adatoms diffuse over to the edges of nuclei faster in the [110] direction, but also break off at a higher rate than do adatoms in the $[\bar{1}10]$ direction.

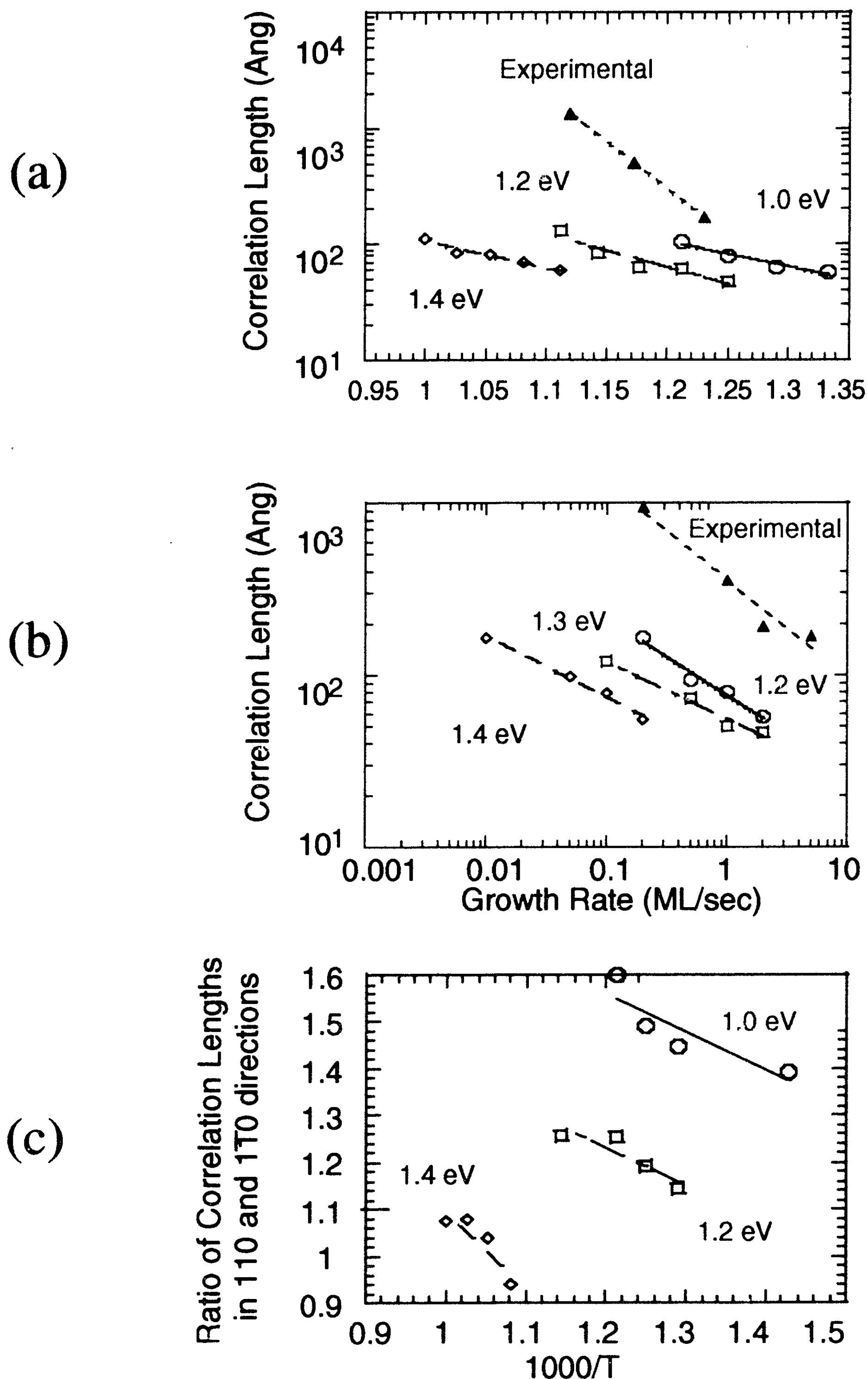

Figure 7. 10: Correlation length as a function of (a) temperature, (c) The anisotropy of the correlation length as a function of temperature for different diffusion models. The numbers in the plots show the diffusion barrier in the [110] direction for each curve, all plots have a Es$[\bar{1}10]$ = 1.48 eV and a NN = 0.2 eV.

STM studies have also shown that A steps on MOVPE grown surface are much rougher than B steps[26]. Also, quantum chemical calculations have found that diffusion away from A steps is slower than diffusion away from B steps on a c(4x4) reconstructed surface [27]. The degree of anisotropy is also studied for the nearest neighbor energies. The dependence of correlation length for temperature and ratio of correlation lengths in the two directions are shown in Figure 7.11. Anisotropy in the nearest neighbor energies have a large effect on the anisotropy of islands, but as the anisotropy increases, the temperature dependence of the correlation lengths in the $[\bar{1}10]$ direction decreases.

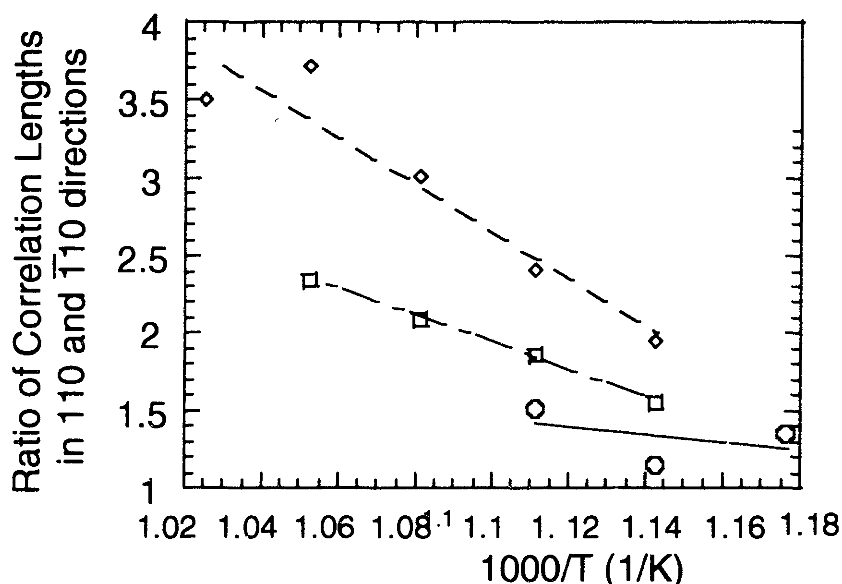

Figure 7. 11: Computation of correlation length anisotropy as a function of nearest neighbor energy anisotropy, $E_s[110]$ = 1.4 eV, $E_s[\bar{1}10]$ = 1.48 eV; (O) NN[110] = 0.15 eV, NN$[\bar{1}10]$ = 0.1 eV; ( ) NN[110] = 0.2 eV, NN$[\bar{1}10]$ = 0.1 eV; (◆) NN[110] = 0.25 eV, NN$[\bar{1}10]$ = 0.05 eV

The simple Model I does not include the physics necessary to model the MOVPE surface during growth. Unless an unphysical activation barrier for diffusion is used (as in Chapter 6), the surface morphology evolution cannot be correctly modeled. Even though a range of parameter values is used, none fits the data. This behavior suggests that additional physical phenomena are occurring on the surface during MOVPE growth. This emphasizes a theme of this work; data and parameters are needed on the same length scale as the predictions. In this case, there is a need for microscopic data in order to build

microscopic models. Thus in Model II, surface chemistry is added in order to test if the added physical detail can explain the GIXS data.

7.4.2.2.4 Model II – inclusion of surface chemistry dynamics:

Models that include As_2 adsorption and desorption and organic groups on the surface are tested. Payne *et al.*[28] showed that the GaAs(100) surface is covered with As dimers with a coverage of 50-75% of the surface in a c(4x4) reconstruction. The As dimers do not impede the adsorption of the Ga species, as experimental results show no dependence on the overall growth rate with increasing As precursor flux. The transitions used in the simulations are summarized in Table 7.2.

The important features of the model include the nearest neighbor barriers for As_2 desorption. This causes a modified c(4x4) reconstruction to appear on the surface with sufficient As flux to the surface, as shown in Figure 7.12.

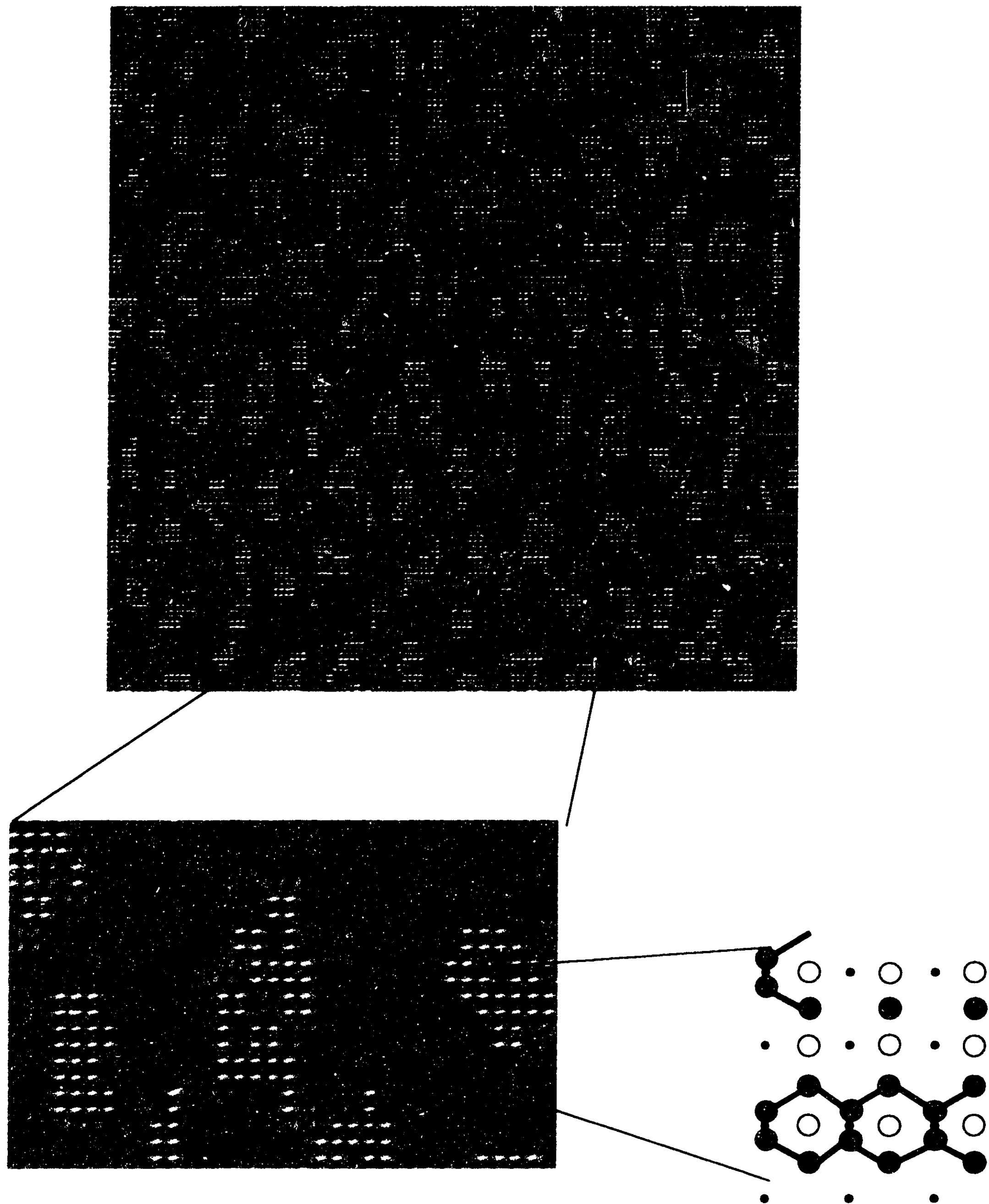

Figure 7. 12: Surface during growth with inclusion of As dimers on the surface. Note the reduction of dimer density around the islands on the surface, as well as the modified c(4x4) reconstruction on the surface.

Also, the As dimers cover roughly 50% of the surface. This reconstruction on the surface allows for roughly 50% of the surface to always be available for Ga precursors to adsorb, and causes a zero dependence on the As flux, as seen experimentally [29]. The nearest neighbor barrier for As desorption is derived from Shiriashi and Ito[18], as an example of

the self-surfactant affect of Ga on the surface. The self surfactant effect appears in Figure 7.12 with the lack of As dimers around islands on the surface. Another important features is the barrier for ethyl desorption is included in the model, as its time constant at growth temperatures is on the same order of magnitude as the diffusion barrier. The diffusion barrier and nearest neighbor barrier for diffusion are extracted from an MD study of the GaAs c(4x4) surface[20]. Both the diffusion barrier and nearest neighbor barriers are anisotropic and consistent with experimental studies[4] and theoretical calculations[30, 31].

The surface model was directly linked to the reactor scale to compute flux to the KMC models. The growth rates match with experimental growth rates, as shown in Figure 7.7. The GICS scattering was computed from the growing surface and computed to a measure of the RDS signal. As explored in Chapter 5, RDS is an in-situ optical probe of the surface. It has been hypothesized that the oscillations in the RDS signal in certain photon energies is due to the As and Ga dimers on the surface[32-34]. The model picks this up, as shown in Figure 7.13. The number of As dimers on the surface is plotted as a function of time along with the GIXS CTR. Both show the oscillations with roughening and smoothing of the surface.

(a)

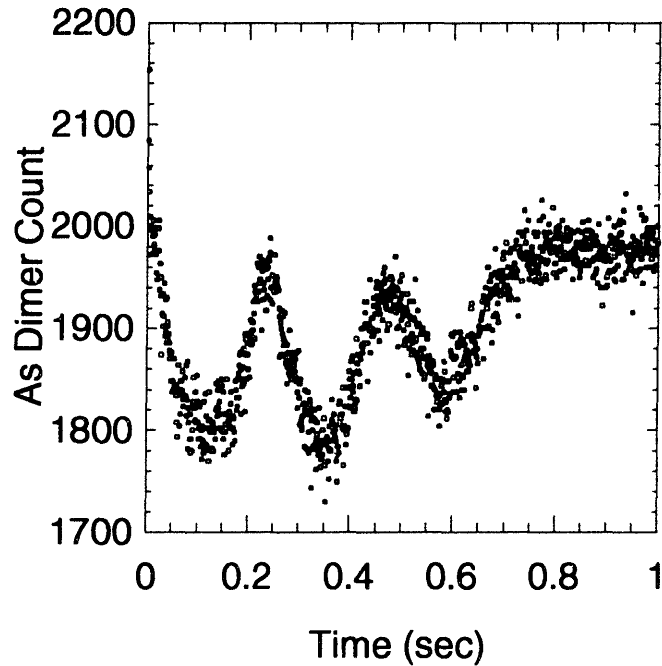

(b)

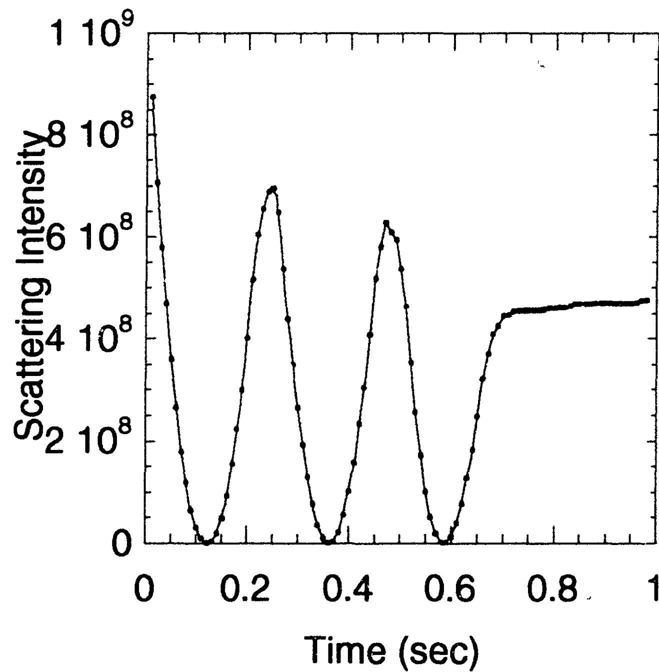

Figure 7. 13: (a) Simulated RDS signal, (b) Simulated GIXS CTR signal from a growing surface. Note the similarities in the oscillations.

A comparison of the experimental and simulated correlation lengths will respect to temperature and growth rate is shown in Figure 7.14 and 7.15.

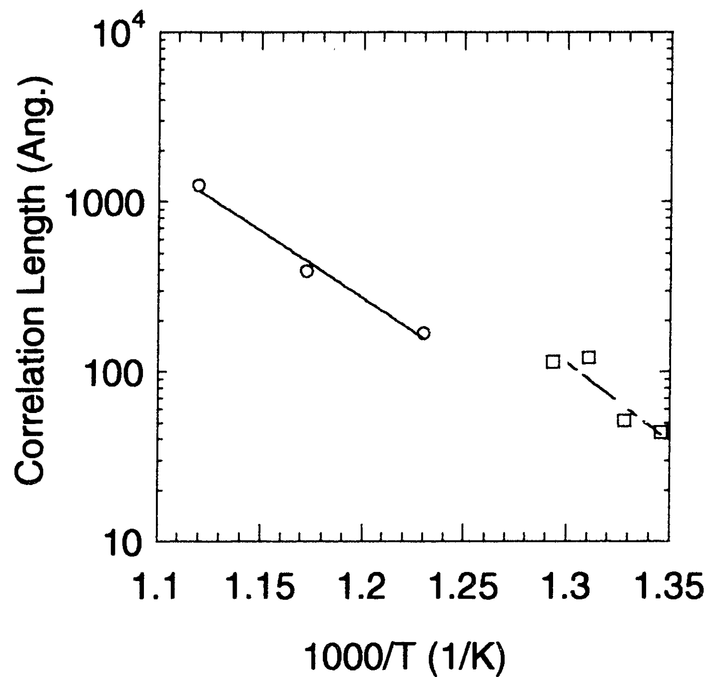

Figure 7. 14: Experimental (o) and simulated(□) correlation lengths as a function of temperature.

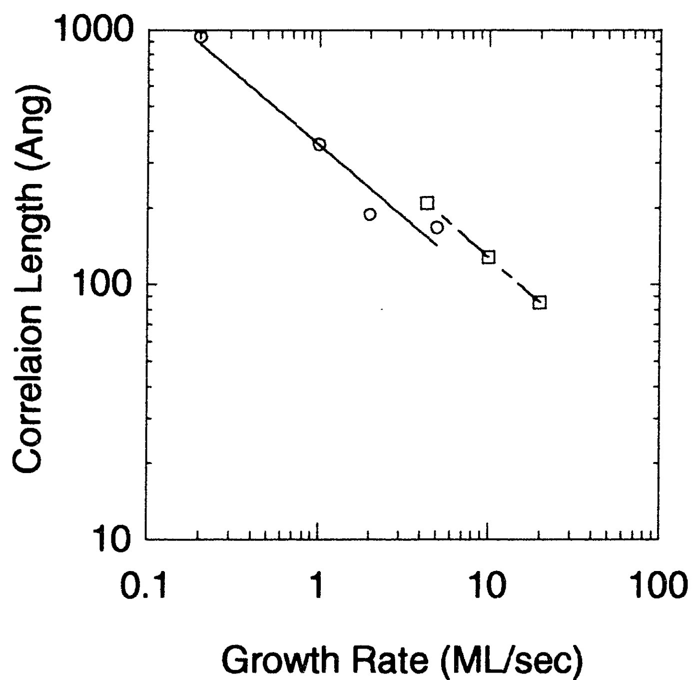

Figure 7. 15: Experimental (o) and simulated(□) correlation lengths as a function of growth rate.

As shown, the model has a much higher dependence on the temperature than the MBE-type models. Since the barrier measured by the correlation length dependence on temperature is a convolution of barriers, the effective dependence on temperature is high in MOVPE growth. In the model, the temperature dependence is a convolution of the barrier for ethyl desorption, diffusion, and As_2 desorption. If the transitions were independent, the effective barrier would be the sum of the individual barriers. There seems to be some 'correlation' between the barriers, as the effective barrier is less than the sum, but the correlation is small. This can be explained, as in the early stages of growth all three barriers must be overcome in order for islands to form. Later stages of growth proceeds with some percentage of the Ga precursors adsorbing near islands, bypassing the diffusion barrier and the As_2 desorption barrier. Other adsorbates land near islands, and due to the self surfactant effect, have a clear path to an island, unimpeded by As dimers. The convolution of all these processes forms the effective barrier on the surface.

7.5 Conclusions

In this work, GIXS experiments were performed in-situ during MOVPE growth of GaAs to characterize the surface morphology during growth. The temperature and flux dependence of the correlation lengths was found at half coverage. Standard nucleation theory is not directly applicable to the experiments, so a combination of FEM and KMC simulations were done in order to understand the surface processes during growth. The surface seems to be characterized by a large critical nuclei size and anisotropic diffusion and/or nearest neighbor barriers. The many surface processes occurring during MOVPE growth may explain the high measured activation energy for the step-flow to island growth transition. Desorption of organics, adsorption and desorption of As on the surface, and anisotropic surface diffusion all play a role in the high 'effective' barrier for diffusion on the surface. The linked models were shown to predict the flux of species to the surface correctly and can be used to predict surface morphologies given reactor conditions.

Bibliography:

1. Kisker, D.W., G.B. Stephenson, P.H. Fuoss and S. Brennan, *Characterization of vapor phase growth using X-ray techniques.* J. Crystal Growth, 1995. **146**: p. 104-111.
2. Fuoss, P.H., D.W. Kisker, F.J. Lamelas, G.B. Stephenson, P. Imperatori and S. Brennan, *Time-Resolved X-ray Scattering Studies of Layer-by-Layer Epitaxial Growth.* Phys. Rev. Lett., 1992. **69**(19): p. 2791-2794.
3. Ploska, K., M. Pristovsek, W. Richter, J. Jonsson, I. Kamiya and J.-T. Zettler, *Metalorganic Vapour Phase Epitaxial Growth on Vicinal GaAs (001) Surface Studied by Reflectance Anisotropy Spectroscopy.* Phys. Stat. Sol., 1995. **152**: p. 49.
4. Kasu, M. and N. Kobayashi, *Surface kinetics of metalorganic vapor-phase epitaxy: Surface diffusion, nucleus formation, sticking at steps.* J. Cryst. Growth, 1997. **174**: p. 513.
5. Li, J. and T.F. Kuech, *Surface morphology of carbon-doped GaAs grown by MOVPE.* J. Crystal Growth, 1997. **170**: p. 292-296.
6. Fuoss, P.H., D.W. Kisker, G.B. Stephenson and S. Brennan, *In-situ X-ray studies of organometallic vapor phase epitaxy growth.* Mat. Sci. and Eng., 1995. **B30**: p. 99-108.
7. Kisker, D.W., G.B. Stephenson, P.H. Fuoss, F.J. Lamelas, S. Brennan and P. Imperatori, *Atomic scale characterization of organometallic vapor phase epitaxial growth using in-situ grazing incidence X-ray scattering.* J. Crystal Growth, 1992. **124**: p. 1-9.
8. Robinson, I.K., *Crystal truncation rods and surface roughness.* Phys. Rev. B, 1986. **33**(6): p. 3830-3836.
9. Fotiadis, D.I., S. Kieda and K.F. Jensen, J. Crystal Growth, 1990. **102**: p. 441.
10. Mountziaris, T.J., S. Kalyanasundaran and N.K. Ingle, *A reaction-transport model of GaAs growth by metalorganic chemical vapor deposition using trimethyl-gallium and tertiary-butyl-arsine.* J. Crystal Growth, 1993. **131**: p. 283-299.
11. Ingle, N.K., C. Theodropoulos, T.J. Mountziaris, R.M. Wexler and F.T.J. Smith, J. Crystal Growth, 1996. **167**: p. 543.
12. Kang, H.C. and W.H. Weinberg, *Kinetic modeling of surface rate processes.* Surf. Sci., 1994. **299/300**: p. 755-768.
13. Clarke, S. and D.D. Vvedensky, *Origin of Reflection High Energy Electron Diffraction Intensity Oscillations during Molecular Beam Epitaxy: A Computational Modeling Approach.* Physical Review Letters, 1987. **58**: p. 2235-2238.
14. Clarke, S. and D.D. Vvedensky, *Growth kinetics and step density in reflection high-energy electron diffraction during molecular-beam epitaxy.* J. Appl. Phys., 1988. **63**: p. 2272.
15. Heyn, C. and M. Harsdorff, *Simulation of GaAs growth and surface recovery with respect to gallium and arsenic surface kinetics.* Phys. Rev. B, 1997. **55**: p. 7034.
16. Lamelas, F.J., P.H. Fuoss, D.W. Kisker, G.B. Stephenson, P. Imperatori and S. Brennan, *X-ray scattering analysis of surface structures produced by vapor-phase epitaxy of GaAs.* Phys. Rev. B, 1994. **49**(3): p. 1957-1965.

17. Adamson, S.D., B.K. Han and R.F. Hicks, *Site-specific reaction kinetics for gallium arsenide metalorganic vapor-phase epitaxy.* Appl. Phys. Lett., 1996. **69**: p. 3236-3238.
18. Shiraishi, K. and T. Ito, *Ga-adatom induced As rearrangement during GaAs epitaxial growth: Self-surfactant effect.* Physical Review B, 1998. **57**: p. 6301.
19. Donnelly, V.M. and J.A. McCauliey, *Products of thermal decomposition of triethylgallium and trimethylgallium adsorbed on Ga-stabilized GaAs(100).* Surface Science, 1990. **238**: p. 34-52.
20. Salmi, M.A., M. Alatalo, T. Ala-Nissila and R.M. Nieminen, *Energetics and diffusion paths of gallium and arsenic adatoms on flat and stepped GaAs(001) surfaces.* Surface Science, 1999. **425**: p. 31-47.
21. Shitara, T., D.D. Vvedensky, M.R. Wilby, J. Zhang, J.H. Neave and B.A. Joyce, *Step-density variations and reflection high-energy-diffraction intensity oscillations during epitaxial growth on vicinal GaAs(001).* Physical Review B, 1992. **46**: p. 6815-6824.
22. Zangwill, A., *Scaling Description of Sub-Monolayer Epitaxial Growth.* Mat. Res. Soc. Proc., 1993. **280**: p. 121.
23. Kisker, D.W., G.B. Stephenson, J. Tersoff, P.H. Fuoss and S. Brennan, *Atomic Scale studies of epitaxial growth processes using X-ray techniques.* J. Cryst. Growth, 1996. **163**: p. 54.
24. Robinson, I.K. and D.J. Tweet, *Surface X-ray Diffraction.* Rep. Prog. Phys., 1992. **55**: p. 599.
25. Avery, A.R., H.T. Dobbs, D.M. Holmes, B.A. Joyce and D.D. Vvedensky, *Nucleation and Growth of Islands on GaAs Surface.* Phys. Rev. Lett., 1997. **79**: p. 3938.
26. Kasu, M., N. Kobayashi and H. Yamaguchi, Appl. Phys. Lett., 1993. **63**: p. 678.
27. Ito, T. and K. Shiraishi, *A theoretical investigation of migration potentials of Ga adatoms near step edges on GaAs(001)-c(4x4) surface.* Jpn. J. Appl. Phys., 1996. **35**: p. L1016-L1018.
28. Payne, A.P., P.H. Fuoss, D.W. Kisker, G.B. Stephenson and S. Brennan, *GaAs c(4x4) surface structure in organometallic vapor-phase epitaxy.* Physical Review B, 1994. **49**: p. 14427-14434.
29. Asai, H., *Anisotropic Lateral Growth in GaAs MOCVD Layers on (001) Substrates.* J. Cryst. Growth, 1987. **80**: p. 425-433.
30. Ito, T. and K. Shiraishi, *Theoretical investigations of adsorption behavior on GaAs(001) Surfaces.* Japanese Journal of Applied Physics - Part 1, 1998. **37**: p. 4234-4243.
31. Ito, T. and K. Shiraishi, *Electron counting Monte Carlo simulation of the structural change of the GaAs(001)-c(4*4) surface during Ga predeposition.* Japanese Journal of Applied Physics - Part 2, 1998. **37**: p. 262-264.
32. Zettler, J.-T., J. Rumberg, K. Ploska, K. Stahrenberg, M. Pristovsek, W. Richter, M. Wassermeier, P. Schutzendube, J. Behrend and L. Daweritz, *Reflectance Anisotropy Oscillations during MOCVD and MBE growth of GaAs(001).* Phys. Stat. Sol. (a), 1995. **152**: p. 35-47.
33. Zettler, J.-T., M. Pristovsek, T. Trepk, A. Shrebtii, E. Steinmetz, M. Zorn and W. Richter, *Response of the surface dielectric function to dynamic surface*

modifications: application of reflectance anisotropy spectroscopy and spectroscopic ellipsomentry. Thin Solid Films, 1997.

34. Zettler, J.-T., *Characterization of epitaxial semiconductor growth by reflectance anistotropy spectroscopy and ellipsometry.* Prog. Crystal Growth and Charact., 1997. **35**: p. 27-98.

Chapter 8: Conclusions and Recommendations for Future Work

8.1 Conclusions

Various computational methods can be useful in describing and predicting physical phenomena. Computational methods such as Monte Carlo simulations, optimization techniques, and numerical solutions to partial differential equations are all used in this thesis to model a complex system. Unfortunately, one technique is not sufficient in modeling all the detail inherent in physical systems. In the MOVPE process, we showed that phenomena that can greatly affect the growth process are on widely different length and time scales. In this thesis, we developed models, linked models, and used the linked models to better understand the physics of the complex MOVPE system.

8.1.1 Kinetic Monte Carlo Simulations

Kinetic Monte Carlo simulations are developed in this thesis to model the TPD process and growth processes. This modeling technique has shown the flexibility to exactly model experimental results due to the direct connection between real time and Monte Carlo steps. The technique is computationally expensive, so different techniques from computer science were used in order to speed the computation. Hash tables and binary trees were used in keeping track of the surface and quickly picking the next transition to take.

Parallel techniques were also used to speed the calculation. In TPD simulations, a master-slave approach was used to parallelize the diffusion step in algorithm. A speedup of over 3 times on 9 processors was achieved. The growth model was parallelized using a new algorithm developed in this thesis that is a variant of a parallel discrete event simulation. The surface was split onto the processors and growth initiated on each processor simultaneously. Due to the poor scaling of the algorithm on one processor (empirically about n^2), the algorithm achieves superlinear speedup when there is a large enough surface on each processor. Superlinear speedup and a large enough parallel machine allows the computation of micron size surfaces in reasonable runtimes. Also, the algorithm runs on all tested platforms (SGI Origin 2000, IBM SP-2, and Intel Pentium

Server). As serial processors become faster, the algorithm will allow the computation of even larger surfaces. The algorithm allows the modeling of problems that are inaccessible with current computing technology.

TPD models were developed that can model any surface mechanism. The difficulties in modeling all mechanisms are inherent when rates on the surface are of widely different magnitudes. In TPD simulations, when the desorption and diffusion rates are different by orders of magnitude, different methods must be used in order to simulate the spectra in reasonable runtime. The thesis developed a model that robustly switches between modeling techniques when the assumption of fast diffusion leading to a quasi-equilibria of adsorbates on the surface is met. The algorithm was used extensively in modeling methyl desorption off GaAs(100). In conjunction with the TPD algorithm, an optimization scheme was developed to quantitatively determine parameters for surface mechanisms. This allows researchers to test surface mechanisms and determine if the mechanisms are consistent with experimental findings.

KMC simulations have been shown to be flexible in studying a variety of experimental techniques; an exact comparison between the model and experiments can be made. The main difficulty in using the models is the computational expense leads to restrictions on the system size studied. This was alleviated by the development of parallel techniques. The methodologies have been used to study GaAs(100) growth and TPD systems.

8.1.2 Multiscale Modeling

Multiscale modeling techniques were developed in this thesis that linked realistic surface morphology models to reactor scale models. Different models must be used in order to match the needed predictions; for example, reactor scale models are described by sets of partial differential equations that represent the macroscopic conservation equations and surface models can be represented by adatoms hopping on a defined lattice in a KMC simulation. A reactor scale model cannot predict surface morphology and the KMC simulations cannot predict gas phase concentrations. Only both models used together can make predictions on both macroscopic and microscopic length scales. The models were

linked together by matching fluxes inside the Newton iteration of the reactor scale model. It was shown that this methodology has better convergence properties than a combined methodology, with the tradeoff of longer runtimes. The technique was used to make realistic predictions on the surface morphology and gas phase concentrations during GaAs(100) growth.

8.1.3 MOVPE GaAs Growth

A new model was developed for GaAs(100) MOVPE growth. This model explicitly kept track of As dimers on the surface and included the As dynamics. This was different than previous MBE models, which ignored the As species due to the Ga species being growth limiting. In MOVPE growth, Ga is also the limiting reagent to growth, but it was shown that the As dynamics play a role in the evolution of surface morphology. The As dimers on the surface block diffusion and access to growing islands. This leads to a large temperature dependence on the correlation length between islands on the surface (much larger than in MBE growth). The model may have broad applicability to MOVPE systems; recently GaN growth was shown to also have this large temperature dependence on the transition between growth modes[1].

8.2 Future Work

The methodologies in this thesis allow the simulation of many systems that were previously inaccessible. Better methods can be developed in modeling surfaces through a modified KMC simulator and better linking methodologies can be developed through methods used in linking air and ocean models from global climate change. These methodological advances can lead to multi-scale modeling over the entire range of length scales from macroscopic reactor simulations to the prediction of the electrical and optical properties of the thin film.

8.2.1 Kinetic Monte Carlo Simulations

Large scale KMC simulations have been developed in this thesis. The simulations on a fixed lattice can be extended to new surfaces, such as the GaAs(111). Concurrent simulations of multiple surface structures can lead to simulations of grain growth on

semiconductor surfaces. Shown in Figure 8.1 is experimental work of the growth of novel AlGaAs structures.

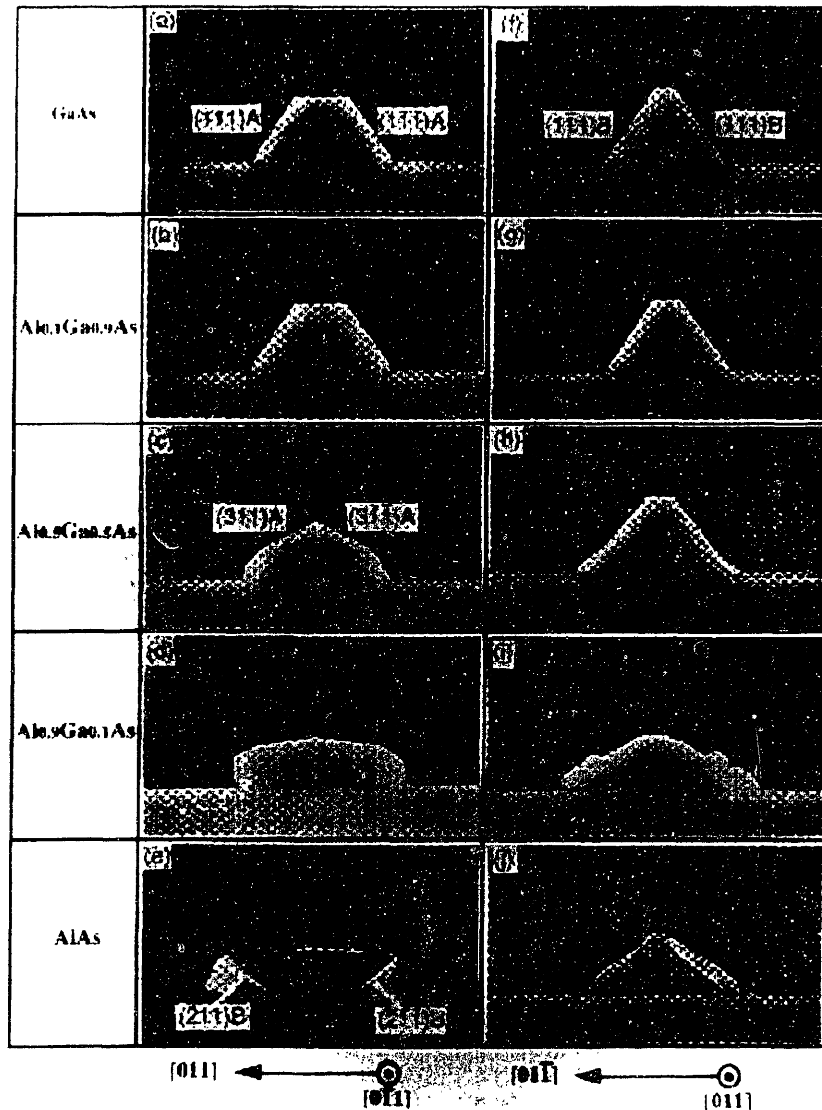

Figure 8. 1: Structures grown out of masked areas on the wafer corresponding to different compositions of Ga and Al in AlGaAs[2, 3].

The drawback to KMC simulations is the adatoms are forced onto a pre-determined lattice. The benefit of KMC simulations over MD simulations is that longer length and time scales are accessible. A new methodology may be developed that is a hybrid between MD and KMC simulations. For example, after every KMC step is taken, a MD potential can be used to move adatoms off their lattice sites. This movement can affect future KMC transitions. In this way, interstitials may be modeled. A sliding scale can be

attached to the simulation to change the degree of MD or KMC in the model. For example, some parts of the surface may need more MD steps due to many interstitials, while other parts of the surface may be relaxed and KMC moves may be the most efficient method to change the surface structure. Exciting theoretical work in this area remains to be developed.

8.2.2 Multiscale Modeling

One of the themes of this work and much of the work being done in multi-scale modeling is methodologies from other academic fields can be applied to problems in chemical engineering. One such example is the linking of air and ocean models in global climate change models. Since such models are extremely expensive to run, linking methodologies have been developed that use the structure of the problem to minimize running of each model[4]. In the ocean-air linking, ocean temperature fields change at a much longer time scale than air models that can be used in smart methods to link the models.

The other area of multiscale modeling that can be extended is a push into smaller length scales. After the surface morphology of a given system can be predicted, models can be used to simulate the device performance from these films. With such models, device performance characteristics can be directly traced back to reactor conditions. A whole array of models must be used in this case. The advancement of quantum chemical techniques is another driver that will allow the predictions of properties on smaller length scales.

8.2.3 Other Systems

Other physical systems can be modeled using the same basic methods. A simple extension is the modeling of AlGaAs with the larger surface sizes enabled by the parallel technology. Segregation of Al and Ga on the surface can be studied, as well as multi-layer structures. Another example is InAs islands on GaAs. The larger surface that are accessible to be simulated can lead to a better understanding of island formation on the surface, as well as why island morphology is drastically different between MOVPE and MBE growth.

In addition to MOVPE growth, the methodology can be extended into other physical systems that are similar. For example, heterogeneous catalysis has many of the same characteristics of MOVPE growth. Heat and mass transfer and chemical reactions in the gas phase occur in both systems. Surface processes play an important role in determining the gas phase concentrations in both cases, and the surface evolves over time. Also, many areas in biology can be modeled using many of the same techniques. For example, the transport of viruses through the body can be modeled on many different length scales (macroscale through blood and microscale through cells). Interdisciplinary research in this area seems to be a fruitful direction.

Bibliography:

1. Stephenson, G.B., J.A. Eastman, C. Thompson, O. Auciello, L.J. Thompson, A. Munkholm, P. Fini, S.P. DenBaars and J.S. Speck, *Observation of growth modes during metal-organi chemical vapor deposition of GaN.* Applied Physics Letters, 1999. **74**: p. 3326-3328.
2. Shimoyama, K., N. Hosoi, K. Fujii and H. Gotoh, *Facet growth of AlxGa1-xAs with HCL gas by metalorganic vapor phase epitaxy.* Journal of Crystal Growth, 1994. **145**: p. 283-290.
3. Shimoyama, K., S. Nagao, Y. Inoue, K. Kiyomi, N. Hosoi, K. Fujuii and H. Gotoh, *Fabrication of quantum wire structures by in-situ gas etching and selective-area metalorganic vapor phase epitaxy regrowth.* Journal of Crystal Growth, 1994. **145**: p. 734--739.
4. Voss, R. and R. Sausen, *Techniques for asynchronous and periodically synchronous coupling of atmosphere and ocean models. II. Impact of variability.* Climate Dynamics, 1996. **12**: p. 312-323.

THESIS PROCESSING SLIP

FIXED FIELD: ill. ______ name ______

index ______ biblio ______

COPIES: (Archives) Aero Dewey Eng Hum

Lindgren Music Rotch (Science)

TITLE VARIES: ▶☐ ______

NAME VARIES: ▶☐ ______

IMPRINT: (COPYRIGHT) ______

COLLATION: ______

ADD: DEGREE: ______ ▶ DEPT.: ______

SUPERVISORS: ______

NOTES:

cat'r: date:

page:

▶ J178

▶ DEPT: Chem. Eng.

▶ YEAR: 2000 ▶ DEGREE: Ph. D.

▶ NAME: VENKATARAMANI, Rajesh